Master of Science Thesis

A Validation Study of the Coupled Aero-Thermal Flow through a Target-Type Thrust Reverser

To Determine the Wall Temperature Distribution on a Thrust Reverser Door

K.M.L. Knoben

28 April 2015

Aerodynamics

Faculty of Aerospace Engineering

TU Delft

Delft University of Technology

A Validation Study of the Coupled Aero-Thermal Flow through a Target-Type Thrust Reverser

To Determine the Wall Temperature Distribution on a Thrust Reverser Door

Master of Science Thesis

For obtaining the degree of Master of Science in Aerospace Engineering at Delft University of Technology

K.M.L. Knoben

28 April 2015

Faculty of Aerospace Engineering · Delft University of Technology

DELFT UNIVERSITY OF TECHNOLOGY
DEPARTMENT OF AERODYNAMICS

The undersigned hereby certify that they have read and recommend to the Faculty of Aerospace Engineering for acceptance the thesis entitled **“A Validation Study of the Coupled Aero-Thermal Flow through a Target-Type Thrust Reverser”** by **K.M.L. Knoben** in fulfillment of the requirements for the degree of **Master of Science**.

Dated: 6 May 2015

Supervisors: ______________________________________

Dr. ir. B.W. van Oudheusden

____

Dr.ir. A.H. van Zuijlen

____

Dr.ir. R.Vos

____

Ir. M.I.M. de Vries

Preface

This report documents the master thesis project which is the final required project upon graduating as a Master of Science in Aerospace Engineering from the TU Delft, The Netherlands. The project is carried out at Rolls-Royce Deutschland Ltd & Co KG, location Dahlewitz, Germany.

The report is written in such a way that some fundamental background knowledge in the field of aerodynamics and turbomachinery is required. The report has a logical order in which the project scope and used background theory are described first, followed by the results and conclusions of the research project.

I would like to thank my two supervisors from the TU Delft and Rolls-Royce Deutschland, Dr. Ir. Alexander van Zuijlen and Dr. Gero Schieffer, for their advice and encouragement to bring the project to a successful end. I also would like to thank Hubert Dengg of Rolls-Royce Deutschland for his advice on the coupled aero-thermal simulations. Last but not least I would like to thank Dr. Bianca Deinert, group leader of the Installations Aerodynamics group, for giving me the opportunity to carry out my internship and master thesis project at Rolls-Royce Deutschland.

Finally, I would like to thank my parents for giving me the opportunity to study and their support in every possible way during this time.

Kjeld Knoben

9 April 2015, Berlin

Abstract

This abstract describes the research performed to predict the wall temperature distribution on the door of a target-type thrust reverser by means of coupled aero-thermal simulations. The research is performed to obtain the degree of Master of Science in Aerospace Engineering from the Technical University of Delft. The project is carried out at Rolls-Royce Deutschland Ltd & Co KG.

The main function of a thrust reverser is to decrease the ground-roll distance during landing or an aborted take-off. The thrust reversers are not allowed to be used during certification but add an extra element of safety during these critical flight phases.

Target-type thrust reversers are an integral part of the exhaust system and reverse both the core and bypass-duct flow during deployment. The doors have to withstand high pressure loadings and temperatures causing the doors to become heavy, expensive and maintenance prone. Optimising the doors for pressure loadings and thermal resistance can save cost, weight and fuel burn.

Previous work at Rolls-Royce Deutschland has shown that CFD simulations are not accurate enough to be used for the optimisation for thermal resistance. The goal of this research is therefore to improve the accuracy of the wall temperature prediction on the reverser door by performing coupled aero-thermal simulations. First, the flow topology of the flow around the TRU with a satisfactory level of convergence and accuracy is determined by making use of the Ansys Fluent solver. Second, the coupled aero-thermal simulations are performed by making use of a feasible and validated coupling technique.

Validation test cases characteristic for the flow topology around the thrust reverser were found from the literature and used to determine a suitable research strategy. From this validation study was found that the SST k-ω turbulence model was the preferred model. Unfortunately no solution was obtained with the SST k-ω model for the TRU simulations. The only model which gave flow solutions was the Realizable k-ε turbulence model. Structured meshes were shown to be less dissipative in areas where variations in velocity directions are high like mixing and vortical flows. A high boundary layer resolution mesh was shown to have a negative influence on the mesh quality. Both the mesh resolution near the wall and mesh quality are important parameters to ensure convergence of the CFD simulations. Therefore, a compromise needs to be found.

The experiments used to validate the simulation data are performed on a 1:5 scaled thrust reverser model. To obtain a converged and accurate flow solution three main cases were investigated. The influence of the boundary conditions, mesh and scaling of the geometry were evaluated. From this study can be concluded that a converged solution is found for the simulations performed on a semi-structured mesh. The accuracy of this solution is reasonable with a maximum error in modelled pressure and temperature values of 7% and 22% respectively. The maximum error in temperature values was reduced from 32% on a hybrid mesh to 22% by using a semi-structured mesh.

For future research it is recommended to perform a simulation on a non-simplified geometry. In this research project the door-actuator and door-actuator-void were taken out of the geometry. Also a 360° geometry should be tested. It is believed that by constraining the mixing flow at the 180° symmetry plane can cause wrong wall temperature predictions. Next to these recommendations it is highly recommended to obtain a flow solution with the SST k-ω turbulence model.

A coupled CFD/FE analysis method is used to couple the fluid domain to the solid domain. The solid domain is also modelled by the Ansys Fluent solver. The validation test cases showed that the solid mesh has no influence on the accuracy of the temperature prediction. The y^+ value of the fluid mesh however has shown to have an influence on the solution accuracy.

Also for the coupled aero-thermal simulations three main cases were investigated. The influence of the prescribed non-coupled walls boundary conditions, ambient temperature and CFD simulation convergence were investigated. From this study can be concluded that the maximum error in temperature values for the non-coupled simulations of 32% was reduced to 15% for the coupled simulations. Also by prescribing a temperature profile at the non-coupled walls instead of a constant temperature as boundary condition, the error in temperatures in some regions of the door decreased from 24% to 2%. It was shown that the convergence of the coupled simulation is dominated by the convergence of the CFD simulation.

For future research it is recommended to investigate the possibility to couple all TRU door walls with the CFD simulation. This because it was observed that a considerable improvement is obtained by using temperature profiles instead of constant temperatures as boundary conditions for the non-coupled walls.

Table of Contents

List of Figures

List of Tables

Nomenclature

Abbreviations

AR	Aspect ratio	$[-]$
BC	Boundary condition	$[-]$
BPD	Bypass-duct	$[-]$
CASM	Convergence acceleration for stretched meshes	$[-]$
CC	Curvature correction	$[-]$
CFD	Computational fluid dynamics	$[-]$
CFL	Courant-Friedrichs-Lewy	$[-]$
CG	Centre of gravity	$[-]$
CPU	Central processing unit	$[-]$
ER	Expansion ratio	$[-]$
FDS	Flux difference splitting	$[-]$
FE	Finite element	$[-]$
FNPR	Fan nozzle pressure ratio	$[-]$
FNTR	Fan nozzle temperature ratio	$[-]$
FOD	Foreign object damage	$[-]$
HOTR	High order term relaxation	$[-]$
HTC	Heat transfer coefficient	$[W/m^2 \cdot K]$
JICF	Jet in a cross flow	$[-]$
LES	Large eddy simulation	$[-]$
LDV	Laser Doppler velocimetry	$[-]$
PS	Pressure split	$[-]$
RANS	Reynolds averaged Navier-Stokes	$[-]$
RRD	Rolls-Royce Deutschland Ltd & Co KG	$[-]$
RSM	Reynolds stress transport model	$[-]$
SA	Spalart-Allmaras	$[-]$
SST	Shear stress transport	$[-]$
TRU	Thrust reverser unit	$[-]$
TS	Temperature split	$[-]$

Greek symbols

γ	Specific heat ratio	$[-]$
δ	Boundary layer thickness	$[m]$
δ_{ij}	Kronecker delta	$[-]$
ε	Turbulence dissipation	$[J/kg \cdot s]$
θ	Angle	$[°]$
κ	Von Kármán constant	$[-]$
μ	Dynamic viscosity	$[kg/m \cdot s]$
μ_t	Turbulent viscosity	$[kg/m \cdot s]$
ν_T	Kinematic eddy viscosity	$[m^2/s]$
ρ	Density	$[kg/m^3]$
τ	Wall shear stress	$[Pa]$
τ_{ij}	Reynolds-stress tensor	$[Pa]$
$\widetilde{\varphi}_i$	Favre-Reynolds averaged scalar variable	$[-]$
φ_i''	Favre-Reynolds averaged scalar variable fluctuation	$[-]$.
ω	Specific turbulence dissipation rate	$[1/s]$
$\mathit{\Omega}_{ij}$	Mean rate-of-rotation tensor	$[rad/s]$

Roman symbols

$c_{b_\#}$	Spalart-Allmaras turbulence model coefficients	$[-]$
c_i	Vector from cell centroid to adjacent cell centre	$[-]$
c_p	Specific heat capacity at constant pressure	$[J/kg \cdot K]$
c_v	Specific heat capacity at constant volume	$[J/kg \cdot K]$
d	Diameter	$[m]$
e	Internal energy	$[J]$
$f_\#$	Spalart-Allmaras turbulence model coefficients	$[-]$
$\vec{f_i}$	Vector from cell centroid to face centroid	$[-]$
h	Enthalpy	$[J]$
h	Heat transfer coefficient	$[W/m^2 \cdot K]$
h	Height/Step height	$[m]$
k	Turbulent kinetic energy	$[J/kg]$
k	Thermal conductivity	$[W/m \cdot K]$
l	Characteristic length	$[m]$
l_{turb}	Turbulent length scale	$[m]$
$\dot{m}$	Mass flow	$[kg/s]$
$\vec{n}$	Direction vector	$[-]$
p	Pressure	$[Pa]$
q	Heat flux	$[W/m^2]$
q_g	Internal heat generation rate per unit volume	$[W/m^2]$

Roman symbols (continued)

q_{T_i}	Turbulent heat flux vector	$[W/m^2]$
r	Radius	$[m]$
r^*	Throat radius	$[m]$
s	Distance	$[m]$
t	Time	$[s]$
t_{ij}	Viscous stress tensor	$[Pa]$
u^+	Non-dimensional velocity for near-wall turbulence modelling	$[-]$
u_i	Velocity component	$[m/s]$
$\widetilde{u_\iota}$	Favre-Reynolds averaged velocity component	$[m/s]$
u_i''	Favre-Reynolds averaged velocity component fluctuation	$[m/s]$
v_i	Ideal velocity	$[m/s]$
x	x-Position	$[m]$
x_i	Position component	$[m]$
y	y-Position	$[m]$
y^+	Non-dimensional distance for near-wall turbulence modelling	$[-]$
A	Area	$[m^2]$
$\overrightarrow{A_\iota}$	Face normal vector	$[-]$
C^+	Constant for calculating u^+	$[-]$
$C_{\#}$	Realizable k-ε turbulence model coefficients	$[-]$
$C_D A$	Effective nozzle area	$[in^2]$
C_μ	Emperical constant Realizable k-ε turbulence model	$[-]$
C_f	Skin friction coefficient	$[-]$
C_p	Pressure coefficient	$[-]$
C_p	Specific heat capacity at constant pressure	$[J/kg \cdot K]$
C_{T_x}	Reversed thrust coefficient in x-direction	$[-]$
D	Diameter	$[m]$
D_H	Hydraulic diameter	$[m]$
E	Total internal energy	$[J]$
$F_{\#}$	SST k-ω turbulence model coefficients	$[-]$
H	Height	$[m]$
H	Total enthalpy	$[J]$
H_x	Measured thrust in x-direction	$[N]$
I	Turbulent intensity	(%)
M	Mach number	$[-]$
Nu	Nusselt number	$[-]$
Nu_x	Local Nusselt number	$[-]$
Pr	Prandtl number	$[-]$
Q	Transport of heat	$[W]$
R	Specific gas constant	$[J/kg \cdot K]$

Roman symbols (continued)

R	Unscaled residual sum	$[-]$
R	Velocity ratio	$[-]$
Re	Reynolds number	$[-]$
Re_l	Reynolds number based on plate length	$[-]$
Re_x	Local Reynolds number	$[-]$
S	Sutherland´s law temperature constant	$[K]$
S_{ij}	Mean rate-of-strain tensor	$[1/s]$
T	Temperature	$[K]$
U	Velocity	$[m/s]$
V	Velocity	$[m/s]$
W	State vector	$[-]$
W	Transport of momentum	$[W]$

Subscripts

∞	Infinity	$[-]$
0	Reference value	$[-]$
7	BPD/Fan station	$[-]$
8	Core station	$[-]$
a	Inlet a	$[-]$
amb	Ambient	$[-]$
b	Inlet b	$[-]$
c	Outlet c	$[-]$
cf	Cross Flow	$[-]$
e	Equiangular cell	$[-]$
f	Fluid	$[-]$
inlet	Computational domain inlet boundary	$[-]$
jet	Jet	$[-]$
m	Material	$[-]$
max	Maximum	$[-]$
outlet	Computational domain outlet boundary	$[-]$
rec	Recovery	$[-]$
ref	Reference	$[-]$
s	Static	$[-]$
solid	Solid geometry	$[-]$
t	Total	$[-]$
top	Top of geometry	$[-]$

Subscripts (continued)

turb	Turbulent	$[-]$
w	Wall	$[-]$
T	Turbulent	$[-]$

Chapter 1 Introduction

In this master thesis the prediction of the wall temperature of a target-type thrust reverser door by means of coupled aero-thermal simulations is investigated. The research project is carried out at Rolls-Royce Deutschland Ltd & Co KG.

The target-type thrust reverser model used in this master thesis is installed on aft-fuselage mounted engines of the Rolls-Royce BR700 series. A picture of a landing Gulfstream G650 with installed Rolls-Royce BR725 engines and deployed thrust reversers can be seen below in Figure 1.1.

Figure 1.1: Landing Gulfstream G650 with installed Rolls-Royce BR725 engines and deployed thrust reversers (Trautvetter, 2012)

Next to the target-type thrust reverser also the cascade and petal-type thrust reversers are used on modern commercial aircraft engines (Vos, 2013). Which of the three types is used depends mainly on the bypass ratio of the engine. The target-type thrust reverser reverses both the bypass and core flow. The cascade and petal type thrust reversers reverse only the bypass flow. The effectiveness of thrust reversers reversing only the bypass flow increases with increasing bypass ratio, this because the core flow thrust is working against the reversed thrust. Therefore engines with relative small bypass ratios use the target-type thrust reverser whether engines with higher bypass ratios (5+ and higher) use the cascade or petal type thrust reverser (Vos, 2013).

Thrust reversers are used to decelerate the aircraft after touch-down. Although thrust reversers are not allowed to be used during the certification of the accelerate-stop or landing distance on a dry runway, almost all aircraft are nowadays equipped with thrust reversers.

The main function of a thrust reverser is to reduce the ground-roll distance during landing or an aborted take-off and thereby adding an extra element of safety during these critical flight phases. Figure 1.2 shows the advantage of using thrust reversers on wet and icy runways. Comparing for instance the ground roll distance on a wet runway with *brakes only* of 850 m to the distance with *target thrust reverser + brakes* of 675 m shows a reduction of 175 m or 21%.

Other benefits of using a thrust reverser are the reduced brake wear and in some cases the ability to taxi backwards from the gate, thereby reducing operating costs (Vos, 2013).

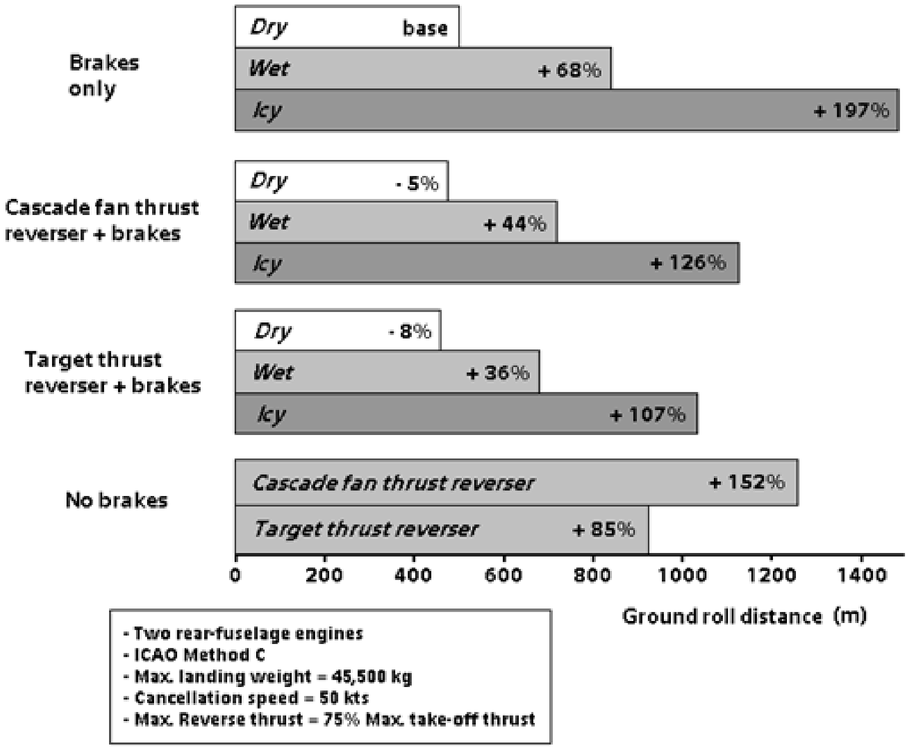

Figure 1.2: Overview of the thrust reverser brake performance on dry, wet and icy runways (Vos, 2013)

The need to accurately predict the temperature distribution on the door of a thrust reverser arises from a material optimisation point of view and influences the exhaust design of the engine. When the temperature distribution is known accurately, the strength and thermal resistance of the door can be optimised. This will eventually lead to a reduction in weight, cost and fuel burn.

Section 1.1 gives some background information on Rolls-Royce Deutschland Ltd & Co KG where this project is carried out. Section 1.2 gives the statement of work followed by the project plan in section 1.3.

1.1 Rolls-Royce Deutschland Ltd Co & KG

This master thesis project is carried out at Rolls-Royce Deutschland (RRD) Ltd & Co KG, location Dahlewitz. Rolls-Royce employs over 55,000 employees worldwide of which 3,500 are working for RRD. At the Dahlewitz location of RRD the design and assembly of the BR700 series engines takes place. In 2013 the 3,000th BR700 series engine was delivered. The series consists out of the BR710, 715 and 725 engines described briefly below (Rolls-Royce Deutschland Ltd and Co KG, 2015).

The BR710 engine powers long range business jets including the Gulfstream V, Bombardier Global Express/Global 5000 and Gulfstream G500/G550. The engine has a bypass ratio of 4, a maximum thrust of 68 kN and a weight of 1850 kg. Interesting fact is that the bypass duct is made out of composite materials.

The BR715 engine is a larger version of the BR710 and powers the Boeing 717-200. The engine has a bypass ratio of 4.6, a maximum thrust of 95 kN and a weight of 2085 kg.

The newest member of the BR700 series is the BR725 engine. The design is based on the BR710 and improved by technologies from the Trent series engines. The engine has a bypass ratio of 4.2, a maximum thrust of 75.2 kN and a weight of 1635 kg. Compared to the BR710 it produces more thrust and less fuel consumption, pollution and noise. With the BR725 engine, Rolls-Royce is the sole engine supplier for the Gulfstream G650.

Figure 1.3 below shows the Bombardier Global 5000, Boeing 717-200 and Gulfstream G650 to get an impression of the aircraft powered by the BR700 series engines.

Figure 1.3: Rolls-Royce powered aircraft. Left: Bombardier Global 5000. Middle: Boeing 717-200. Right: Gulfstream G650 (Bombardier Business Aircraft, 2015; Time for Flight, 2015; E-news, 2015)

Next to the design and assembly of the BR700 series engines, also the final assembly of the IAE V2500 engine is performed in Dahlewitz. The IAE V2500 is developed by the International Aero Engines consortium consisting out of Rolls-Royce, Pratt & Whitney, Japanese Aero Engine Corporation and MTU Aero Engines. The V2500 powers the Airbus A320 family consisting out of the Airbus A319, A320, A321 and the Airbus Corporate Jet.

This research project is carried out at the Installations Aerodynamics group of RRD. The group is responsible for the aerodynamic design of the intake, bypass-duct (BPD), thrust reverser unit (TRU) and exhaust. The research and work performed on the TRU consists out of sizing, CFD based design processes, preparing and post-processing experiments and performance calculations. The results of this research project will help to improve the TRU door design in the future. Both target-type as well as cascade thrust reversers are designed by the group.

1.2 Statement of Work

The two most common used thrust reverser systems are the target-type and cascade thrust reversers. The focus in this master thesis project will be on the target-type thrust reverser. A schematic representation of such a thrust reverser can be seen in Figure 1.4.

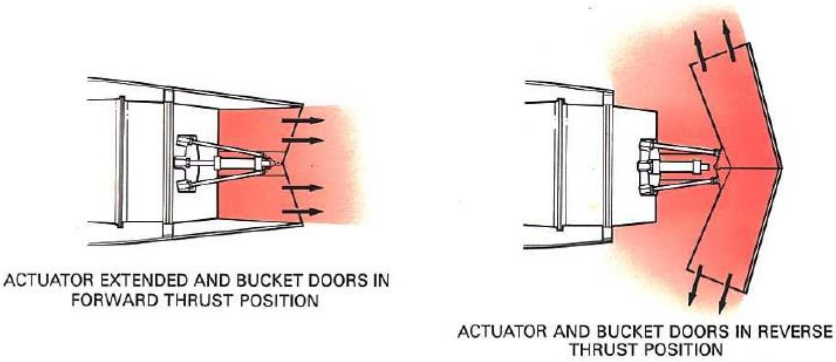

Figure 1.4: Schematic representation of a target-type thrust reverser in stowed (left) and deployed (right) position (Rolls-Royce plc, 1996)

A target-type thrust reverser reverses both the hot core and cold bypass duct flow. The bypass duct flow temperature is equal to the ambient temperature of the air plus a total temperature increase caused by the fan. The temperature of the hot core flow can be as high as 700 K (Rolls-Royce plc, 1996).

The importance of CFD for the design and sizing of the thrust reversers is increasing. Because of the complicated geometry and flow phenomena present for the thrust reverser, the convergence and accuracy of the CFD results are highly dependent on the mesh and computational model applied.

When CFD results were compared with experimental data it was observed that the temperature distribution predicted by the CFD simulations showed a large discrepancy with the measured temperatures on the door. In order to be able to design the TRU door for the high temperatures it is exposed to during deployment, a more accurate prediction of the temperature distribution is required.

To improve the temperature prediction on the door’s surface it is worthwhile to investigate and evaluate the possibilities to perform coupled aero-thermal simulations. The main goal of this research project is therefore,

The prediction of the wall temperature distribution on the door of a target-type thrust reverser by means of coupled aero-thermal simulations

First the flow topology needs to be determined by means of CFD simulations. Focus during this stage of the project will be on the creation of a high quality mesh and applying the most suitable computational model to obtain a satisfactory level of convergence and accuracy. When the flow topology is determined the CFD simulations can be coupled to a thermal solver which takes the door structure into account. Validation test cases will be evaluated to determine the solving strategy. CFD results for the TRU will be compared to available experimental data. The experiments are performed on a 1:5 scaled thrust reverser model.

1.3 Project Set-up

In order for the reader to get familiar with the subject of this thesis project a detailed introduction to the target-type thrust reverser is given in Chapter 2. In this chapter the research field and relevance of the work is shortly evaluated followed by an explanation about the working principles and design considerations of the thrust reverser.

The computational models and background theory which are used during this project are described in Chapter 3.

As indicated in the previous section, the first part of the research project is focused on determining the flow topology around the TRU. The flow topology is determined by making use of the Ansys Fluent (14.0) software (Ansys Inc., 2011a) which is one of the default CFD analysis tools of RRD. The research objective of the first part of the project is formulated as follows,

The research objective of the first part of this project is to determine the flow topology around the TRU with a satisfactory level of convergence and accuracy by creating a high quality mesh and selecting the most suitable computational model by making use of the Ansys Fluent software

In order to help deciding on a meshing strategy and computational model four validation test cases are evaluated which are described in the first part of Chapter 4. The actual determination of the flow topology is described in Chapter 5.

Aim of the second part of this project is to predict the wall temperature distribution on the TRU door by making use of coupled aero-thermal simulations. The research objective connected to this part of the project is formulated as follows,

The research objective of the second part of this project is to perform coupled aero-thermal simulations to determine the wall temperature distribution on the TRU door by selecting a feasible coupling technique and validate this technique with simple test cases

The validation of the coupling techniques is described in the second part of Chapter 4. The set-up and results of the coupled aero-thermal simulations is described in Chapter 6.

Finally Chapter 7 gives the conclusions and recommendations for further work.

Chapter 2 The Target-Type Thrust Reverser

Before the technical part of this research project is evaluated a detailed introduction to the subject of the target-type thrust reverser is given. To place this research project in the research field and point out the relevance of the work a summary of the literature related to target-type thrust reverser research is given in section 2.1. The working principles and design considerations which need to be taken into account during the development of the TRU are explained in section 2.2.

2.1 Relevance of Work

To get an overview of the research performed in the field of thrust reverser aerodynamics a thorough literature study was performed. A small part of the found literature dealt with target-type thrust reverser aerodynamics while the largest part consisted out of cascade type thrust reverser aerodynamics. The relevant literature on target-type thrust reverser aerodynamics is selected and discussed briefly below. According to the number of papers found on this subject one can conclude that not a lot of research is performed on this subject or is not published due to company confidentiality reasons.

The development in CFD methods and computer power can be clearly recognised from the literature found from the early research on thrust reverser aerodynamics. Sarpkaya and Hiriart (1975) describe the inviscid, incompressible 2D flow simulations of the internal flow through a simplified target-type thrust reverser. Discrepancies ranging from 2% to 28% could be found when the reversed-thrust ratios calculated by the CFD simulations were compared to experimental data. The reversed-thrust ratio is the ratio of the actual reversed-jet thrust to the forward jet thrust of the nozzle. These discrepancies were accounted to the Coanda effect (which is not modelled) and the nozzle pressure ratio. Also noted is that the Coanda effect can cause an unstable flowfield and destructive vibrations.

The research documented in the papers by Imlay, et al.(1984) and Imlay (1986) describes the viscous, compressible, 2D flow simulations through thrust reversing nozzles. The compressible RANS equations are used together with a Baldwin-Lomax algebraic eddy viscosity model. Bad convergence observed in the first paper was solved by switching the discretization scheme (factored to unfactored MacCormack implicit method) in the second paper. Large reversed flow areas were not observed in the first paper while a small region of separated flow was observed in the second paper. The nozzle discharge coefficients (ratio of actual and ideal mass flow) are predicted within 1% for all but the lowest nozzle pressure ratio compared to experimental data. Pressure data compare reasonable well with experimental data away from the separated flow areas.

The research by Strash, et al.(2000) is the first paper describing a full 3D CFD simulation on a target-type thrust reverser. The 3D inviscid compressible flow around an entire contemporary business jet with deployed thrust reversers is modelled by solving the Euler equations with a 7-level multigrid calculation procedure. Qualitatively, the exhaust plume trajectory and computed static pressure distributions on the windward side of the thrust reverser door compare well with experimental data.

Quantitatively, the static pressure distributions differ from 10% to 30% between computed and measured data. The computed net braking force and reverser efficiency show good agreement with experimental data with only 2% and 1% differences, respectively. The differences in computed static pressure distributions are accounted to the fact that the geometry is simplified to avoid complicated flow phenomena like flow leakage in small voids around the doors and the inability of the Euler solver to predict vortices which originate from the base of the kickerplate. The solution was considered converged although oscillations in residuals and set lift and drag monitors were observed. The simulations were performed at a freestream Mach number of 0.15. The mesh contained 2 million grid points and a Cray J90 computer was used to find a solution in approximately 18 hours (wall-clock time).

The work performed by Blin, Hadjadj and Vervisch (2003) shows a test case representative for the curved mixing layer which is formed between the TRU flow and freestream flow emanating from the fan ramp. The result of a Large Eddy Simulation (LES) is compared with experimental data and a RANS simulation in which the k-ε model is used for turbulence closure. The Reynolds number based on inlet velocity and duct height is in the order of 10^7. The Mach number varies from 0.5 at the inlet to 1.0 at the nozzle exit. These numbers are comparable to the Reynolds and Mach numbers in this master thesis project.

The TRU geometry is modelled as a curved rectangular channel to eliminate complex flow phenomena like separated flow at the base of the door and curvature effects induced on the flow by the door geometry. The mesh in the region of the mixing layer is refined and near the wall the resolution of the mesh is increased to accurately model the boundary layer. Comparing the results which are shown in Figure 2.1 and Figure 2.2, shows that the velocity field is reasonably well resolved by both models whereas the maximum turbulent kinetic energy is not well resolved by the RANS simulations (80% loss of maximum turbulent kinetic energy compared with LES results).

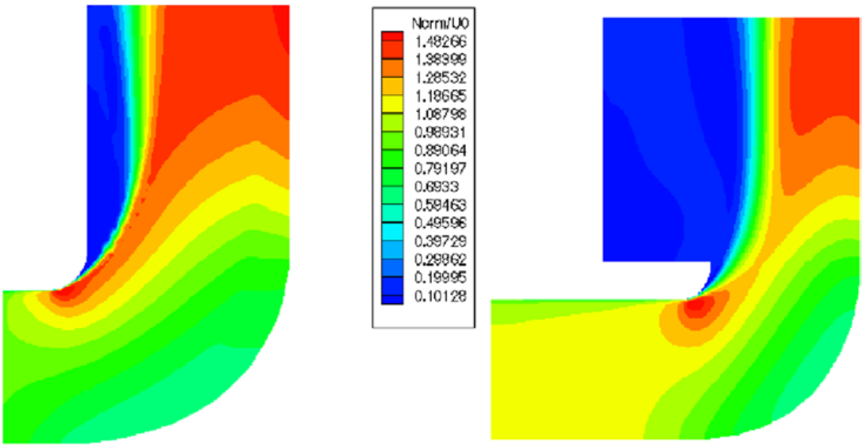

Figure 2.1: Magnitude of the mean velocity. Left: LES results. Right: RANS k-ε results (Blin, Hadjadj and Vervisch, 2003)

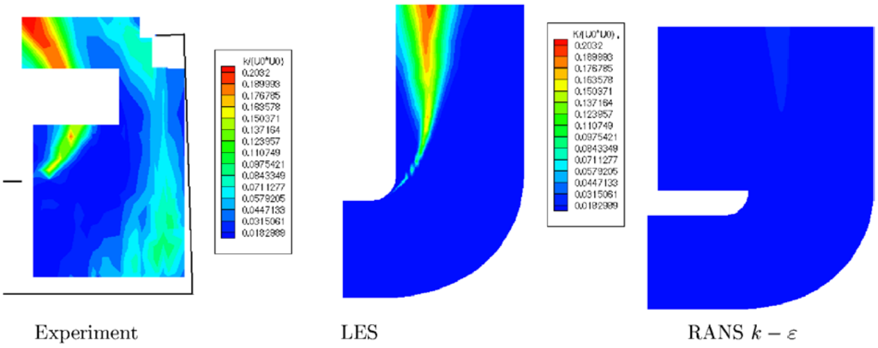

Figure 2.2: Snapshot of the turbulent kinetic energy (Blin, Hadjadj and Vervisch, 2003)

Furthermore, the paper discusses the observed flow physics. From the LES results a Kelvin-Helmholtz instability can be recognized which establishes at the trailing edge of the fan ramp. The 3D iso-vorticity fields at three instances in time can be seen in Figure 2.3. Downstream of the fan ramp fluctuations in turbulence properties are recognized. This observation indicates the existence of unsteady flow phenomena and 3D effects in the flow. Notice that in this paper only one of the many flow phenomena representative for the TRU flow is isolated which indicates the complexity of the full TRU flow field.

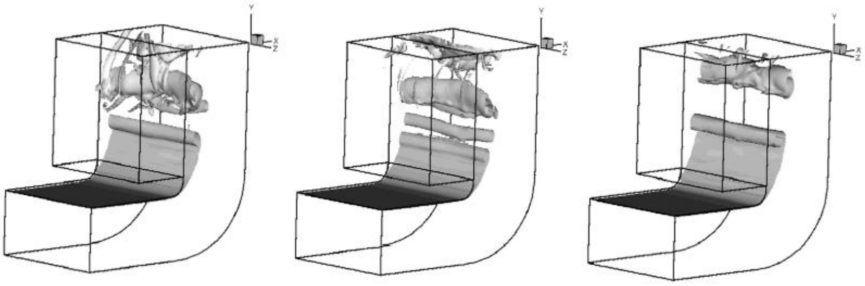

Figure 2.3: Iso-vorticity field at three instances in time (Blin, Hadjadj and Vervisch, 2003)

The simulations were performed on a mesh which contained 4.7 million grid points. The computations were performed on a CRAY-T3E using 175 processors. 105 Hours of CPU time were needed to obtain a converged solution for the LES.

From the literature can be seen that a detailed 3D CFD simulation is not yet performed. An important fact which is mentioned in every paper is the complicated geometry and flow physics. An almost complete overview of the observed flow physics around a thrust reverser is given in the paper of Blin, Hadjadj and Vervisch (2003) and is repeated below in Figure 2.4. Next to the plane mixing layer, backward-facing step and curved channel flow, the jet in a crossflow is added to the observed flow physics by the author of this report. These four test cases represent the following flow phenomena: free shear flow, separating/reattaching flow, streamline curvature and jet entrainment in a cross flow. The test cases are used as validation test cases to test different solving strategies and are described in Chapter 4.

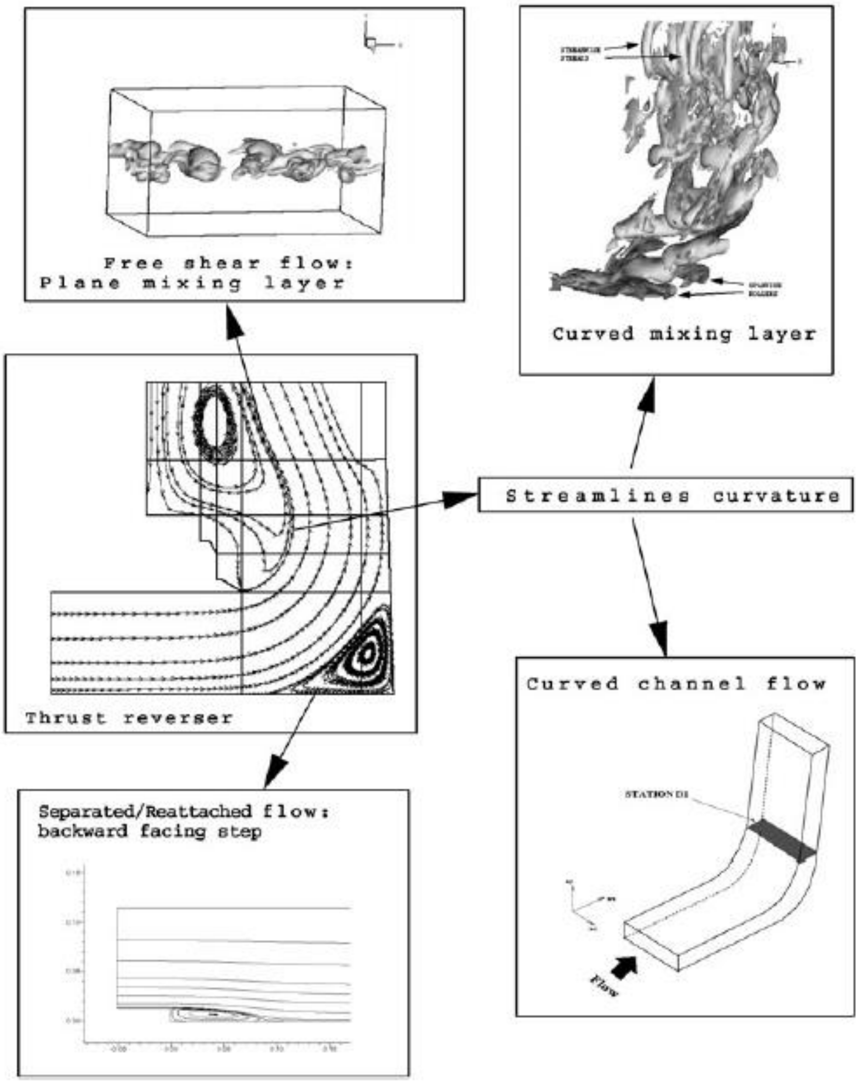

Figure 2.4: Schematic Diagram of the flow physics observed in a thrust reverser (Blin, Hadjadj and Vervisch, 2003)

In order to be able to compare CFD results with experimental data, the geometry cannot be simplified too much and the flow physics have to be modelled correctly. Research in which thermal effects and a fluid-structure coupling for a thrust reverser are investigated could not be found. From this summarised literature review can be concluded that the current research will add new knowledge to the field of thrust reverser aerodynamics and will be a new step in the direction of multidisciplinary design methods for the thrust reverser.

2.2 Working Principles and Design Considerations

The target-type thrust reverser is an integral part of the exhaust system. The reverser is deployed hydraulically after touch-down and full reverse thrust is reached a few seconds later. The aircraft will decelerate causing the reversed flow jet to move forward and possibly causing re-ingestion of the hot reversed flow. Figure 2.5 illustrates the high speed and low speed reversed flow jet trajectories. From the figure the forward movement of the jet at lower speeds can be seen.

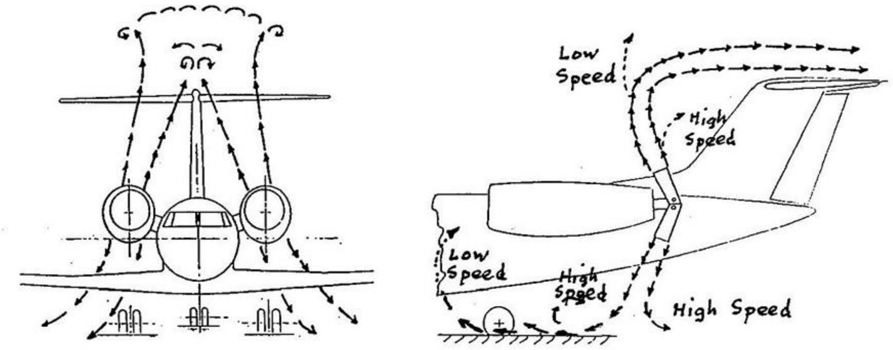

Figure 2.5: Front and side view of aft fuselage mounted engines with deployed thrust reversers illustrating reversed flow jet trajectories (Vos, 2013)

The re-ingested flow can cause foreign object damage (FOD) or disturb the inlet fan/compressor pressure distribution causing surge. Both effects can cause severe fan or compressor blade damage and should therefore be avoided. The so-called cut-off speed is introduced which is the speed at which the thrust reverser is stowed to avoid flow re-ingestion and FOD.

As can be seen from Figure 2.5 the upper reversed flow jet can cause interference effects with the control surfaces causing a decrease or even loss of directional control. The jet should not hit the horizontal tail plane to avoid excessive loading of the plane. Finally, the braking force creates a moment around the CG of the aircraft which causes a lower nose-wheel loading which on its turn makes the brakes less effective (Vos, 2013).

Important factors which need to be taken into account during the design of the thrust reversers, to avoid the above described effects, are the determination of the jet trajectory at different ground-roll speeds and the forces caused by the reversed flow.

Because the target-type thrust reverser is an integral part of the exhaust nozzle, the optimisation of the reverser is a difficult and extensive work with a lot of constrains. Due to the loads the reversers have to withstand they are heavy, expensive and maintenance prone. An accurate prediction of the pressure and temperature loading during deployment will help to optimise the reverser design and thereby saving cost and weight.

For the sizing of the door, the mass flow leaving the engine is an important parameter. When the mass flow drops below a certain limit, fan flutter can occur. This can eventually lead to blade damage. As a rule of thumb, the mass flow in reversed mode should be at least as large as the mass flow in forward mode (Schieffer, 2013).

Chapter 3 The Computational Model

This chapter gives an overview of the background theory and computational models used during this research project. The commercial CFD Ansys Fluent (14.0) software package (Ansys Inc., 2011a) is used to determine the flow topology due to its large number of options and the fact that it is one of the default CFD software packages within RRD. The theory and methods used to determine the flow topology are described in section 3.1. For the coupled aero-thermal simulations two approaches were tested. First the in-house SC03 code (Rolls-Royce plc, 2015) was tested and second the capability of Ansys Fluent was tested to predict the temperature distribution on the TRU door. The theory and methods used for the coupled aero-thermal simulations are described in section 3.2.

3.1 Resolving the Flow Topology

This section deals with the methods and underlying theory of the Ansys Fluent software package. This section is further divided into the governing equations described in subsection 3.1.1. The selected spatial and temporal discretisation techniques are discussed in subsection 3.1.2. The turbulence modelling and mesh quality requirements and techniques are described in subsections 3.1.3 and 3.1.4 respectively. Finally, this section is completed by subsection 3.1.5 which deals with the convergence criteria and monitors.

3.1.1 Governing Equations

The simulations which are performed on the TRU deal with turbulent, compressible flow. To account for the turbulent behaviour of the flow, the Navier-Stokes equations are Reynolds averaged. By applying the Reynolds averaging technique all turbulence is modelled. For compressible flow the constant density assumption is not valid anymore, therefore the flow variables are density weighted averaged in time, also called Favre-averaged. Combining the Reynolds and Favre averaging techniques give the following decompositions for the velocity and scalar (pressure, energy, etc.) variables,

$$\tilde{u}_i = \frac{\overline{\rho u_i}}{\bar{\rho}} \qquad \widetilde{\varphi}_i = \frac{\overline{\rho \varphi_i}}{\bar{\rho}} \tag{3.1}$$

$$u_i = \widetilde{u}_i + u_i'' \tag{3.2}$$

$$\varphi_i = \widetilde{\varphi}_i + \varphi_i'' \tag{3.3}$$

When these expressions are inserted in the instantaneous conservation equations the Favre-Reynolds Averaged Navier-Stokes (F-RANS) equations are derived (Wilcox, 2006).

$$\frac{\partial \bar{\rho}}{\partial t} + \frac{\partial}{\partial x_i}(\bar{\rho}\tilde{u}_i) = 0 \tag{3.4}$$

$$\frac{\partial}{\partial t}(\bar{\rho}\tilde{u}_i) + \frac{\partial}{\partial x_j}(\bar{\rho}\tilde{u}_i\tilde{u}_j) = -\frac{\partial p}{\partial x_i} + \frac{\partial}{\partial x_j}\left[\bar{t}_{ij} + \bar{\rho}\tau_{ij}\right] \tag{3.5}$$

$$\frac{\partial}{\partial t}[\bar{\rho}E] + \frac{\partial}{\partial x_j}[\bar{\rho}\tilde{u}_j H] = \frac{\partial}{\partial x_j}\left[-q_{L_j} - q_{T_j} + \overline{t_{ij}u_i''} - \overline{\rho u_j''\frac{1}{2}u_i''u_i''}\right] + \frac{\partial}{\partial x_j}\left[\tilde{u}_i(\bar{t}_{ij} + \bar{\rho}\tau_{ij})\right] \tag{3.6}$$

$$p = \bar{\rho}R\tilde{T} \tag{3.7}$$

In which equation (3.7) is used because the air is assumed to be an ideal gas. E and H are given by,

$$E = \tilde{e} + \frac{\tilde{u}_i\tilde{u}_i}{2} + k \qquad H = \tilde{h} + \frac{\tilde{u}_i\tilde{u}_i}{2} + k \tag{3.8}$$

With,

$$\tilde{e} = c_v\tilde{T}, \qquad \tilde{h} = c_p\tilde{T} \tag{3.9}$$

The dynamic (or molecular) viscosity, μ, used to calculate the viscous stress tensor, t_{ij}, is assumed to only vary with temperature. With this assumption, Sutherland’s law can be applied to calculate the dynamic viscosity. The viscous stress tensor and Sutherland’s law are defined as follows,

$$\bar{t}_{ij} = \mu\left(\frac{\partial\tilde{u}_i}{\partial x_j} + \frac{\partial\tilde{u}_j}{\partial x_i}\right) - \frac{2}{3}\mu\frac{\partial\tilde{u}_k}{\partial x_k}\delta_{ij} \tag{3.10}$$

$$\mu = \mu_{ref}\left(\frac{\tilde{T}}{T_{ref}}\right)^{3/2}\frac{T_{ref} + S}{\tilde{T} + S} \tag{3.11}$$

In which $\mu_{ref} = 1.716e - 5\ kg/ms$ at $T_{ref} = 273.11\ K$ and $S = 110.56\ K$.

The specific heat, c_p, and thermal conductivity, k, are given by a four and three coefficient polynomial function dependent on the temperature, specified by Rolls-Royce.

In order to be able to solve equations (3.4) to (3.11), closure approximations are required.

The first approximation is the Boussinesq approximation to ensure closure for the Reynolds-stress tensor, τ_{ij}. This approximation is used together with zero, one or two equation turbulence models and is given by,

$$\bar{\rho}\tau_{ij} = -\overline{\rho u_i''u_j''} = 2\mu_t\left(\frac{\partial\tilde{u}_i}{\partial x_j} + \frac{\partial\tilde{u}_j}{\partial x_i}\right) - \frac{2}{3}\left(\bar{\rho}k + \mu_t\frac{\partial\tilde{u}_k}{\partial x_k}\right)\delta_{ij} \tag{3.12}$$

A disadvantage of the Boussinesq approximation (Ansys Inc., 2011b) is the assumption that μ_t is an isotropic scalar quantity. The assumption works in general well for shear flows in which only one of the turbulent shear stresses is dominant such as wall boundary layers, mixing layers and jets. In flows with anisotropic turbulence such as highly swirling and stress-driven secondary flows, the assumption is not valid anymore and models like the Reynolds Stress transport Model (RSM) should be used.

Wilcox (2006) determined the following applications for which models based on the Boussinesq approximation fail due to the above described assumption,

- Flow with sudden changes in mean strain rate
- Flow over curved surfaces
- Flow in ducts with secondary motion
- Flow in rotating fluids
- Three-dimensional flow

The bullet points indicate that the assumption of an isotropic turbulent viscosity is only valid for simple flow problems. The flow phenomena present in the TRU flow field are complicated and compared with the above bullet points, would fail the assumption of an isotropic turbulent viscosity.

Because alternatives (RSM, LES, etc.) to the Boussinesq approximation and the use of turbulence models are not yet feasible due to the lack of computational resources, the ability of the turbulence models to solve these complicated flow phenomena is investigated in this research project. As an indication, the simulation of the flow around a single turbine blade with a Reynolds number of 10^5-10^6 requires a mesh of 10^6 cells for a RANS simulation and 10^9 cells for a LES (Eggenspieler, 2012). The table shown below summarises the different memory and computational requirements for a RANS simulation and LES. Especially the CPU ratio indicates that for this project, methods like a LES are computationally too expensive.

Table 3.1: Comparison of memory and computational requirements for RANS and LES simulations (Eggenspieler, 2012)

Method	Number of cells	Number of time steps	Inner loop per Δt	CPU ratio
RANS	~10^6	~10^2	1	1
LES	~10^9	~10^4	10	10^6

The second approximation is called the Reynolds analogy and is used to ensure closure for the turbulent heat-flux vector, q_{T_j}. The Reynolds analogy gives the relation between the momentum and heat transfer and is given by,

$$q_{T_j} = \overline{\rho u_j'' h''} = -\frac{\mu_T c_p}{Pr_T}\frac{\partial \overline{T}}{\partial x_j} == -\frac{\mu_T}{Pr_T}\frac{\partial \overline{h}}{\partial x_j} \tag{3.13}$$

An often applied assumption is the one of a constant turbulent Prandtl number, Pr_T. This assumption is valid for shock-free flows up to low supersonic speeds if the heat transfer is not too high. For boundary layer flows a value of 0.89-0.9 is common while at the boundary layer edge and throughout shear layers a value of 0.5 is advised. By letting Pr_T vary through the boundary layer, heat transfer predictions can be improved somewhat. During the calibration of the Ansys Fluent software package a value of 0.85 was found to be the most robust for a wide variety of flows. This default value of 0.85 is used in this master thesis project.

The molecular diffusion and turbulent transport of turbulent kinetic energy given by $\overline{t_{ij} u_i''}$ and $\overline{\rho u_j'' \frac{1}{2} u_i'' u_i''}$ are often ignored. This is a valid approximation for flows with Mach numbers up to the supersonic regime. When a closure approximation is needed, the most common approximation is the following,

$$\overline{t_{ij}u_i''} - \overline{\rho u_j'' \frac{1}{2} u_i'' u_i''} = \left(\mu + \frac{\mu_T}{\sigma_k}\right)\frac{\partial k}{\partial x_j} \tag{3.14}$$

3.1.2 Discretisation Techniques

For this research project the assumption is made that the flow is steady. In order to solve the steady F-RANS equations, they need to be discretised in space. The computational domain needs to be divided into physical elements (mesh generation) in which the flow quantities are solved. After the mesh is generated the equations need to be spatially discretised. In order to be able to iteratively determine the steady-state flow variables the governing equations need to be linearized. The spatial discretisation and linearization techniques used in this research project are described below according to the book of Blazek (2001) and the Fluent theory and users guides (Ansys Inc., 2011b and c).

Spatial Discretisation

Fluent uses the finite volume spatial discretisation approach. In this method the computational domain is divided in an arbitrary number of polyhedral control volumes. The mesh needs to be generated in such a way that the flow properties can be captured accurately in the areas of interest. The cell types and sizes used together with the quality of the mesh are important factors which influence the accuracy of the solution. More on this is explained in section 3.1.4.

The surface integrals of the Navier-Stokes equations are approximated by the sum of the fluxes crossing the individual faces of the control volume. A control volume can be defined by a cell-centred or cell-vertex scheme. Fluent uses the cell-centred approach which is shown on the left in Figure 3.1 below.

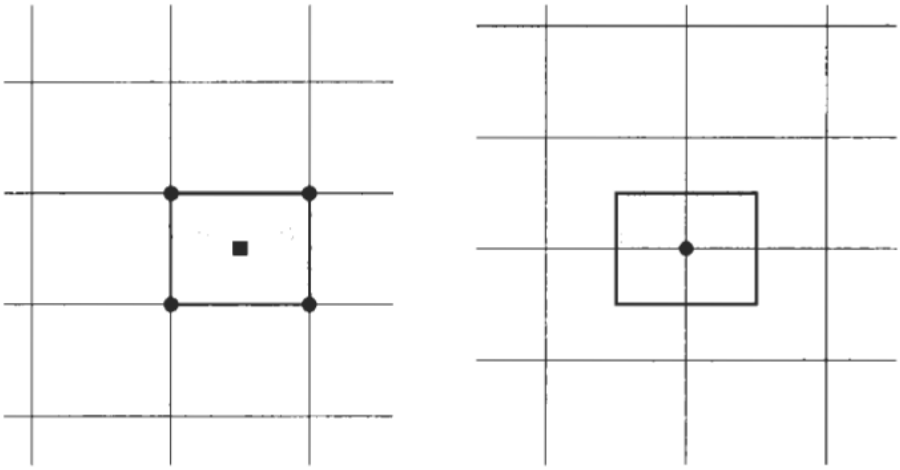

Figure 3.1: Control volume determined by the cell centred (left) and cell vertex (right) scheme (Blazek, 2001)

Now the control volume is known, the actual fluxes can be calculated. This is done by discretising the convective fluxes. In this research project the Roe-Flux Difference Splitting (Roe-FDS) scheme is used as default. This scheme is an upwind scheme which means that it takes the flow direction into account. A Riemann problem is solved at the interface between two control volumes to determine the left and right states. To reduce the numerical effort an approximation of the Riemann solver was developed by Roe. The scheme is widely used due to its ability to model boundary layers accurately and the fact that it can be easily implemented on structured and unstructured grids.

Additionally limiter functions are used to prevent the generation of spurious oscillations near strong discontinuities for second and higher order spatial accuracy. It is known that limiter functions stall the convergence by accidental switching in smooth flows. Small wiggles in the solution must be taken into account and the limiter functions require a high computational effort, especially on unstructured grids.

By default, the flow solutions in this research project are solved second order accurate. Dependent on whether the flow is solved first or second order accurate, one or two upstream data points are taken into account to determine the spatial derivative. Compared to the first order scheme, the second order scheme is known to be less diffusive in regions with high gradients at the cost of its robustness.

To determine gradients which are used in some interpolation schemes, secondary diffusion terms and velocity derivatives, the least squares cell-based gradient evaluation method is used by default. The least squares method computes the cell centre gradient by assuming the gradient is linear. Compared with the two other methods offered by Fluent the least squares method is in general more accurate on skewed and distorted unstructured meshes and is the computationally least expensive method.

By default the numerical scheme used to discretise the viscous fluxes is the central difference scheme.

Linearization of Governing Equations

The discrete, non-linear governing equations are linearized to produce a system of equations for the dependent variables in each computational cell. This linear system of equations is then solved to obtain an updated flow-field solution. This process is repeated until a converged flow solution is found according to the defined convergence criteria described in section 3.1.5.

The method of linearizing the governing equations is called the implicit time integration. By the implicit time integration the unknown value in each cell of a given variable is computed using a relation that includes both existing and unknown values from neighbouring cells. This means that each unknown appears in more than one equation in the system and that the total set of equations needs to be solved simultaneously. In this way the implicit approach solves for all variables in all cells at the same time.

This results in higher memory requirements in comparison with the explicit approach (in which the unknowns are solved one equation at a time). In general the implicit approach is more stable and needs less iterations to reach a steady-state converged solution.

To accelerate the solution convergence, the Convergence Acceleration for Stretched Meshes (CASM) and High Order Term Relaxation (HOTR) functions are used by default. The CASM function calculates the local time step in a cell not from the minimum cell characteristic distance but from the maximum characteristic length of the cell and aspect ratio (AR). This means that the local CFL number of a cell increases with increasing cell AR which accelerates the solution convergence. The HOTR function improves the start-up and the general solution behaviour of flow simulations when higher order spatial discretisations are used. High-order terms can often lead to numerical instabilities which are solved by using the HOTR function.

3.1.3 Turbulence Modelling

The turbulence models which are needed to solve the Boussinesq approximation and used in this research project are described in this subsection. The Spalart-Allmaras, Realizable k-ε and Shear Stress Transport (SST) k-ω turbulence models are selected to be used. The models have their own advantages and disadvantages and are calibrated for different flows. The governing equations and properties of the models are discussed in this subsection. The validation of the theory described below is documented in sections 4.1 to 4.4. The flow near the wall is treated differently than the flow away from walls. The near wall treatment of turbulence models is explained at the end of this subsection.

Spalart-Allmaras Model

The Spalart-Allmaras (SA) turbulence model (Spalart and Allmaras, 1992) is a one-equation turbulence model which models the turbulent viscosity. The Spalart-Allmaras model was specifically designed for aerospace applications, e.g. flow past wings. It is designed for wall-bounded flows and in general gives good results for boundary layers subjected to (moderate) adverse pressure gradients. It is not recommended to use this model when large separated regions are expected. The model also gives reasonable results for mixing layers. One of the limitations of this model is that it is unsuitable for applications involving jet-like free shear regions (plane, radial and round jet flows). The model is known to be robust and in general converges fast to a steady-state solution. The kinematic eddy viscosity and eddy viscosity equation are given by,

$$\nu_T = \tilde{\nu} f_{v_1} \tag{3.15}$$

$$\frac{\partial \tilde{\nu}}{\partial t} + u_i \frac{\partial \tilde{\nu}}{\partial x_i} = c_{b1} \tilde{S} \tilde{\nu} - c_{w1} f_w \left(\frac{\tilde{\nu}}{d}\right)^2 + \frac{1}{\sigma} \frac{\partial}{\partial x_j} \left[(\nu + \tilde{\nu}) \frac{\partial \tilde{\nu}}{\partial x_j} \right] + \frac{c_{b2}}{\sigma} \frac{\partial \tilde{\nu}}{\partial x_j} \frac{\partial \tilde{\nu}}{\partial x_j} \tag{3.16}$$

In equation (3.16) the first term on the right-hand side represents the production of turbulent viscosity. In Fluent by default $\tilde{S}$ is based on the mean rate-of-rotation tensor, Ω_{ij}. This approach avoids unphysical turbulence production in inviscid flow regions like stagnation lines. In vortical flows however this approach overpredicts the production of turbulence and thus overpredicts the eddy viscosity. In order to avoid this, an alternative formulation for $\tilde{S}$ was developed which is based on both the rotation and strain rate tensor.

The second term in equation (3.16) represents the turbulent destruction. Note that this term and its coefficients and relations depend on the distance from its closest surface, d. This means that far from solid boundaries this term tends to zero and therefore is not able to predict decay of the eddy viscosity.

The third and fourth term in equation (3.16) represent the conservative and non-conservative diffusion of turbulence.

Realizable k-ε Model

The realizable k-ε turbulence model (Shih, et al., 1995) is based on the standard k-ε model originally proposed by Launder and Spalding (1972). The realizable model differs from the standard model in that it has an alternative formulation for the turbulent viscosity and a modified transport equation for the dissipation rate, ε. With these modifications the model shows substantial improvements in flows with strong streamline curvature, vortices and rotation. Fluent states that the realizable model shows the best performance over all k-ε models for several validation studies of separated flows and flows with complex secondary flow features.

Compared to the Spalart-Allmaras model the k-ε models are less robust. This is caused by the fact that the damping functions in the turbulence equations lead to equations with stiff source terms. Also the accuracy of the k-ε models degrades for flows with adverse pressure gradients. The models are considered inaccurate for separated flows. The transport equations for the realizable k-ε model can be found below,

$$\mu_t = \rho C_\mu \frac{k^2}{\varepsilon} \tag{3.17}$$

$$\frac{\partial}{\partial t}(\rho k) + \frac{\partial}{\partial x_j}(\rho k u_j) = \frac{\partial}{\partial x_j}\left[\left(\mu + \frac{\mu_t}{\sigma_k}\right)\frac{\partial k}{\partial x_j}\right] + \mu_t S^2 - \rho\varepsilon - 2\rho\epsilon M_t^2 \tag{3.18}$$

$$\frac{\partial}{\partial t}(\rho \varepsilon) + \frac{\partial}{\partial x_j}(\rho \varepsilon u_j) = \frac{\partial}{\partial x_j}\left[\left(\mu + \frac{\mu_t}{\sigma_\varepsilon}\right)\frac{\partial \varepsilon}{\partial x_j}\right] + \rho C_1 S\varepsilon - \rho C_2 \frac{\varepsilon^2}{k + \sqrt{\nu\varepsilon}} \tag{3.19}$$

For the standard and RNG k-ε models the value for C_μ is given a constant value of 0.09 and 0.0845 respectively. For the realizable k-ε model the value for C_μ is a function of the mean strain and rotation rate, the angular velocity of the system rotation and the turbulence fields.

The first term on the right-hand side of equation (3.18) represents the conservative diffusion of turbulent kinetic energy.

The second term represents the production of turbulent kinetic energy due to the mean velocity gradients in which S is in this case the modulus of the mean rate-of-strain tensor, S_{ij}.

The fourth term represents the contribution of the fluctuating dilatation in compressible turbulence to the overall dissipation rate. This term is included to account for the decreased spreading rate with increasing Mach number for compressible mixing and other free shear layers. This term is always included when the compressible form of the ideal gas law is used. For incompressible cases this term is normally neglected.

The first term on the right-hand side of equation (3.19) represents the conservative diffusion of turbulent dissipation.

The second and third terms represent the production and destruction terms of the turbulent dissipation. Note that the production term is again dependent on the modulus of the mean rate-of-strain tensor, S_{ij}. Note here the difference with the Spalart-Allmaras model where the production term is by default dependent on the modulus of the mean rate-of-rotation tensor, Ω_{ij}. Also note that in the above equations no geometric dependency variable is included such as the distance from the closest surface as is the case for the Spalart-Allmaras model.

SST k-ω Model

The SST k-ω model is developed by Menter (1994) and combines the robust and accurate k-ω model in the near-wall region and the free-stream independence of the k-ε model in the far-field. To achieve this, both models are multiplied by a blending function which smoothly blends both models. The SST model incorporates a damped cross-diffusion term in the ω-equation. Finally the expression for the turbulent viscosity from the k-ε model is modified to account for the transport of the turbulent shear stress.

The above modifications and the fact that the SST model uses the blending of the k-ε and k-ω models make the model more accurate and reliable for a wider class of flows than the standard k-ω model. Bardina, Huang and Coakley (1997) describe that the SST model forces the turbulent shear stress to be bounded by a constant times the turbulent kinetic energy inside boundary layers. Because of this modification the prediction of flows with strong adverse pressure gradients and separation is significantly improved compared to the k-ε models. The k-ω model accurately reproduces measured spreading rates for different free shear flows. Also the k-ω models do not need damping functions which leads to a higher numerical stability for the same accuracy compared to the k-ε models. The transport equations for the SST k-ω model can be found below,

$$\mu_t = \frac{\rho k}{\omega} \frac{1}{max\left[\frac{1}{\alpha^*}, \frac{SF_2}{\alpha_1 \omega}\right]} \tag{3.20}$$

$$\frac{\partial}{\partial t}(\rho k) + \frac{\partial}{\partial x_j}\left(\rho k u_j\right) = \frac{\partial}{\partial x_j}\left[\Gamma_k \frac{\partial k}{\partial x_j}\right] + \widetilde{G_k} - \rho \beta^* k \omega \tag{3.21}$$

$$\frac{\partial}{\partial t}(\rho \omega) + \frac{\partial}{\partial x_j}\left(\rho \omega u_j\right) = \frac{\partial}{\partial x_j}\left[\Gamma_\omega \frac{\partial \omega}{\partial x_j}\right] + \frac{\alpha}{\nu_t}\widetilde{G_k} - \rho \beta_i \omega^2 + 2(1 - F_1)\rho \frac{1}{\omega \sigma_{\omega,2}} \frac{\partial k}{\partial x_j} \frac{\partial \omega}{\partial x_j} \tag{3.22}$$

As one can see, the structure of the transport equations is similar to the equations for the realizable k-ε model. In equation (3.21) the first term on the right-hand side represents the diffusion of the turbulent kinetic energy, followed by the production due to the mean velocity gradients and dissipation of the turbulent kinetic energy. The diffusion and production terms make use of the blending between the two models, while the dissipation term does not incorporate blending.

Equation (3.22) shows the same structure. The first three terms on the right-hand side are respectively the diffusion, production and dissipation of the specific dissipation rate, ω. The fourth term is a result of the transformation of the standard k-ε model equations into equations based on k and ω and is called the cross-diffusion term. In this equation all terms on the right-hand side make use of blending between the k-ε and k-ω models.

Near Wall Treatment

To accurately predict boundary layers along walls it is important that the flow variables are resolved accurately in the near-wall region where the gradients are high. Fluent models the flow near the wall by using the Law of the Wall. The Law of the Wall is an empirically determined relation which shows that the streamwise velocity in the near wall region varies logarithmically with distance from the wall. The logarithmic velocity profile can be seen in Figure 3.2.

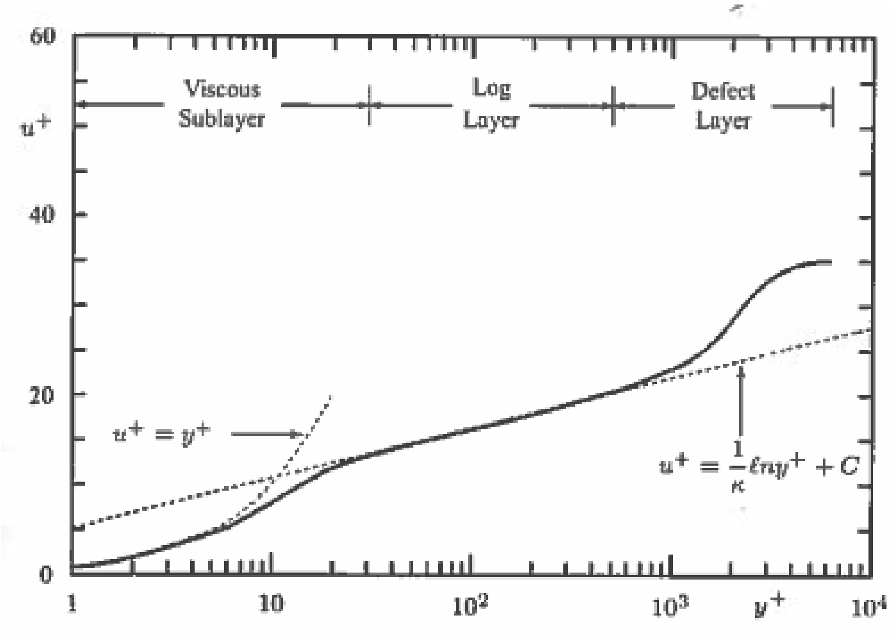

Figure 3.2: Typical non-dimensionalised velocity profile for a turbulent boundary layer (Wilcox, 2006)

Indicated in the top of the figure are the three main layers,

- The viscous sublayer, valid for a y^+ less than 5 where $u^+ = y^+$
- The log layer (turbulent core), valid for a y^+ larger than 30 where $u^+ = \frac{1}{\kappa}\ln y^+ + C^+$
- The defect layer which connects the boundary layer with the freestream flow

The region between the viscous sub- and log layer is called the buffer layer. As can be seen from the figure this region needs a blending function to blend the two expressions for the viscous sub- and log layer. Also a blending function is needed to account for the region between the log layer and freestream flow.

In general to be able to accurately model the boundary layer close to the wall, fine meshes with a y^+ value of one are needed to capture the high velocity gradients in wall normal direction. Ansys Fluent developed the enhanced wall treatment which is a near-wall modelling method that combines a two-layer model (viscous sub- and log layer) with so-called enhanced wall functions. This method does not specify a minimum value for the y^+ value of the first cell adjacent to the wall as is illustrated in Figure 3.3. In this way larger y^+ values can be used in areas of less interest which saves cells and thus computational cost. It is however recommended to give the first cell a y^+ value in the order of one and about 30 prism layers when accurate boundary layer modelling is required, to for instance accurately predict the temperature boundary layer profile.

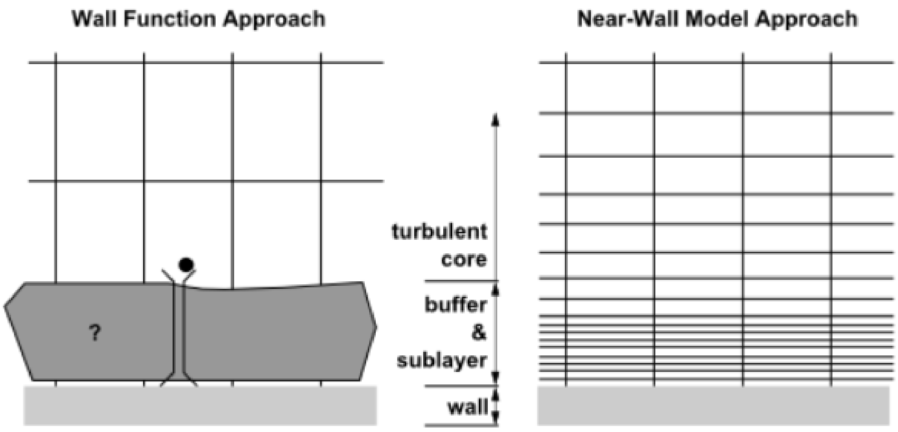

Figure 3.3: Near-wall modelling methods. Left: Enhanced wall function approach. Right: Near-wall model approach (Ansys Inc., 2011b)

3.1.4 Mesh Quality Requirements and Meshing Techniques

As stated in the research objective a high quality mesh is required. A poor mesh quality can cause convergence difficulties, unphysical or diffused solutions. How a high quality mesh is defined is explained in this section. Also the meshing technique has an influence on the solution convergence and accuracy. The advantages and disadvantages of structured and unstructured meshes are given in this subsection according to the found literature. During the evaluation of the test cases both structured and unstructured meshes are tested to show their differences.

Mesh Quality Requirements

The three most important mesh quality parameters found in the literature are the orthogonal quality, skewness and aspect ratio (Ansys Inc., 2011d).

The orthogonal quality of a cell is determined to be the minimum of the following two equations and is computed for each face i,

$$\frac{\vec{A_i} \cdot \vec{f_i}}{|\vec{A_i}| \cdot |\vec{f_i}|} \qquad \frac{\vec{A_i} \cdot \vec{c_i}}{|\vec{A_i}| \cdot |\vec{c_i}|} \tag{3.23}$$

The vectors used in the above equation are shown in Figure 3.4 in the top left. A_i is the face normal vector, f_i the vector from the centroid of the cell to the centroid of the face and c_i the vector from the centroid of the cell to the centroid of the adjacent cell. A cell is considered to have an unacceptable orthogonal quality when its value is below 0.01 according to RRD meshing standards and 0.001 according to the Ansys meshing standards. A cell is considered to have a bad orthogonal quality when its value is between 0.001 and 0.14 according to the Ansys meshing standards.

To determine the skewness of a cell, two methods are available. The first method determines the equilateral volume deviation,

$$skewness = \frac{optimal\ cell\ size - cell\ size}{optimal\ cell\ size} \tag{3.24}$$

This expression only applies to tetrahedrons. The second method is the normalised angle deviation,

$$skewness = \max\left[\frac{\theta_{max} - \theta_e}{180 - \theta_e}, \frac{\theta_e - \theta_{min}}{\theta_e}\right] \tag{3.25}$$

Where θ_e is the equiangular cell angle (60° for tetrahedrons and 90° for hexahedrons). This applies to all cell shapes. The idea behind the two skewness relations is shown in Figure 3.4 in the top middle and right respectively. A cell is considered to have an unacceptable equivolume skewness when its value is above 0.98 according to both the RRD and Ansys meshing standards. A cell is considered to have a bad equivolume skewness when its value is between 0.95 and 0.98.

In the bottom of Figure 3.4 the requirements specified by Ansys for the orthogonal quality and skewness can be seen.

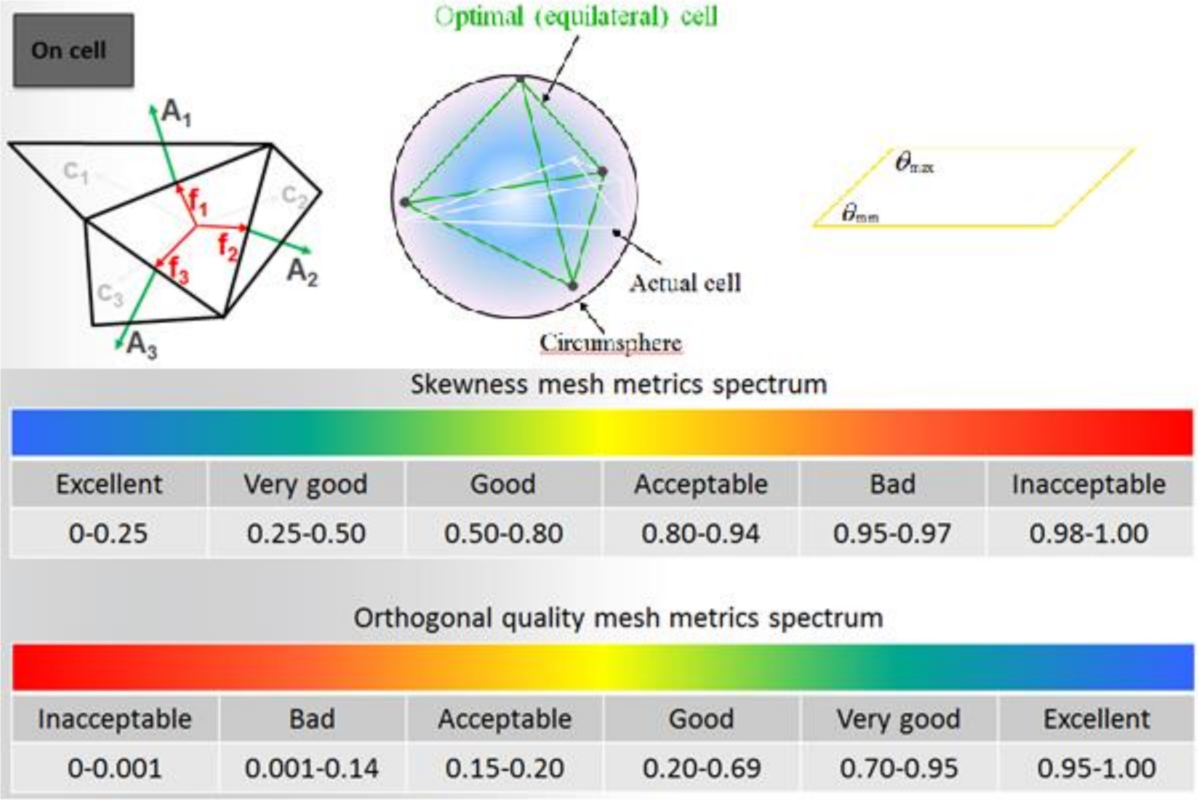

Skewness mesh metrics spectrum

Excellent	Very good	Good	Acceptable	Bad	Inacceptable
0-0.25	0.25-0.50	0.50-0.80	0.80-0.94	0.95-0.97	0.98-1.00

Orthogonal quality mesh metrics spectrum

Inacceptable	Bad	Acceptable	Good	Very good	Excellent
0-0.001	0.001-0.14	0.15-0.20	0.20-0.69	0.70-0.95	0.95-1.00

Figure 3.4: Overview of the mesh quality requirements (Ansys Inc., 2011d)

The aspect ratio is a measure of the stretching of a cell. It is computed as the ratio of the maximum value to the minimum value of any of the following distances: the normal distance between the cell centroid and face centroids, and the distances between the cell centroid and nodes (Ansys Inc., 2011c). Ansys states that the limitation for iterative solvers is between 10 and 100. Larger aspect ratios are accepted in regions where no strong transverse gradients are present such as in boundary layers.

If after mesh generation still bad quality cells are present, the poor mesh numerics option can be activated. This option facilitates solution convergence on meshes of poor quality. By activating this option the solution in the bad cells is locally corrected. The corrected solution can be of 0th, 1st or 2nd order,

- The 0th order scheme determines the solution in the bad cells directly from the surrounding solutions in the better quality cells
- The 1st order scheme applies locally low order discretization methods and neglects some non-orthogonal contributions to the gradients when computing the diffusive fluxes
- The 2nd order scheme only modifies the numerics in the bad cells by assembling the gradient vector for the given solution variable from the gradients in the surrounding better quality cells

The 1st order correction scheme provides a reasonable compromise between accuracy and stability and is therefore the recommended option. If the mesh is of poor quality according to the above requirements, the poor mesh numerics 1st order scheme is used in this research project by default.

Meshing Techniques

Both structured and unstructured (hybrid) meshes are tested on their convergence and accuracy during the evaluation of the test cases. A 3D structured mesh is constructed out of hexahedral elements while an unstructured mesh can be constructed out of hexahedral, tetrahedral, prism and pyramid elements.

The advantage of a structured mesh is that each node is uniquely defined and can be easily accessed by the solver. The disadvantage is that the mesh generation is very difficult for complex geometries. Often a multiblock meshing approach is chosen which is also not optimal because it creates hanging nodes between the meshing blocks.

For complex geometries an unstructured mesh is more suitable. It can better adapt to the geometry boundaries and the meshing process is automated. The disadvantage of unstructured meshes is the necessity to employ sophisticated data structures inside the flow solver. In general also the memory requirements are higher compared to structured meshes.

Salman, et al. (2000) compared the performance of structured and unstructured meshes on the prediction of planar and convoluted shear layers. They concluded for the planar shear layer that a mixed mesh would be the best meshing approach. In the shear layer region a structured mesh block should be placed combined with an unstructured mesh away from the shear layer. A structured mesh gives better accuracy in shear layers because there is less numerical diffusion. This is caused by the fact that the faces of the structured mesh are perpendicular to the mean flow direction. For an unstructured mesh the cell faces are almost never aligned with the mean flow direction which gives a higher numerical diffusion which is larger than the physical diffusion. This causes an increased spreading which results in a lower production of turbulent energy and hence turbulent viscosity. The experiments were performed with a k-ε turbulence model.

Morgut and Nobile (2009) also compared a hexa-structured and hybrid-unstructured meshing approach for the numerical prediction of the flow around marine propellers. Morgut and Nobile state that in general hybrid meshes give less accurate results than structured meshes, but the time and effort to make a hybrid mesh is lower. The flow is evaluated in Ansys CFX and the SST k-ω turbulence model with enhanced wall treatment is used for turbulence closure. Morgut and Nobile conclude that the performance curves (thrust and torque) and velocity profiles for both meshes are in line with experimental data but the structured mesh gives slightly better results. The turbulent velocity fluctuations are however under predicted by the hybrid mesh. The main conclusion is that hybrid meshes can be used for the prediction of the propulsive performance but are not recommended for a detailed investigation of the flow field due to the presence of excessive diffusion in the solution.

3.1.5 Convergence Criteria and Monitors

Convergence of a CFD simulation can in general be checked by examining the residuals, mass-flow rates and additional characteristic parameters.

A first indication of convergence can be the values of the different residuals plotted in Fluent. In this research project the globally scaled residuals are monitored during the CFD simulations. These residuals are defined as follows,

$$\frac{R(W)_{iteration\ N}}{R(W)_{iteration\ 5}} \tag{3.26}$$

In which $R(W)$ is defined as the unscaled residual sum for all the coupled equations,

$$R(W) = \sqrt{\sum \left(\frac{\partial W}{\partial t}\right)^2} \tag{3.27}$$

In which W in equation (3.27) is the state vector. The denominator in equation (3.26) is the largest absolute value of the residual in the first five iterations. Fluent defines that for most problems the default convergence criterion is sufficient and requires the globally scaled residuals to decrease to 10^{-3} and the energy equation to 10^{-6}. Because of the fact that the residuals are scaled, it is possible that the residual values do not decrease to the specified value when a good initial solution is started from.

Additionally to the residuals, also the mass-flow rates can be checked which give an indication of the conservation of mass. When the mass-flow rates are not oscillating anymore this could be an indication that a steady-state solution is reached.

Finally, parameters which are characteristic for the simulation can be set as solution monitors. Such parameters are for instance the forces, pressures or temperatures on a surface. Just like the mass-flow rates these parameters should reach steady-state for the simulation to be fully converged.

Oscillations in residuals or monitors can imply unsteady effects, bad mesh quality or incorrect meshing.

3.2 Coupled Aero-Thermal Simulations

This section deals with the selected methods and underlying theory to perform the coupled aero-thermal simulations. First the background theory and governing equations used to determine the temperature distribution in a solid are described in subsection 3.2.1. The coupling techniques available from the literature and the application of these techniques are described in subsection 3.2.2.

3.2.1 Governing Equations

To understand how a thermal solver works, first some fundamental background theory on heat transfer is given in this subsection. The theory described in this section helps to understand the statements made later in this thesis report. The theory described below is found from Clarkson (2010).

The static temperature of a fluid indicates the level of energy possessed by the substance at the molecular/atomic level, also called its internal energy. Additionally to this, when a fluid is moving it also possesses kinetic energy associated with that movement. When a fluid is brought to rest this kinetic energy is converted into internal energy and the local static temperature rises. This static temperature is called the recovery temperature, T_{rec}, which is for air close to the total temperature, T_0,

$$T_{rec} \approx T_0 = T + \frac{v^2}{2c_p} \qquad (3.28)$$

In general three heat transfer mechanisms exist: Conduction, convection and radiation. In this research project radiation is neglected and only conduction and convection are considered. Conduction is the ability of a solid to transfer heat from so-to-say location A to location B. Convection represents the heat transfer between a solid and a (moving) fluid.

To understand the two heat transfer mechanisms of conduction and convection better, a 1D steady-state problem is considered for both mechanisms illustrated in Figure 3.5. Considering conduction; the heat transferred per unit area, also known as the heat flux, can be expressed mathematically as,

$$\frac{Q}{A} = q = -k\frac{(T_2 - T_1)}{l} \qquad (3.29)$$

The thermal conductivity, k, is a proportionality constant and dependent on the material properties of the solid. The negative sign originates from the convention of defining a positive heat flux in the direction of a negative temperature gradient. Just like for conduction, the heat transferred per unit area can be expressed mathematically for the mechanism of convection as,

$$\frac{Q}{A} = q = h(T_f - T_w) \qquad (3.30)$$

The proportionality constant in equation (3.30) is the heat transfer coefficient (HTC), h, which is dependent on the flow structure and fluid properties.

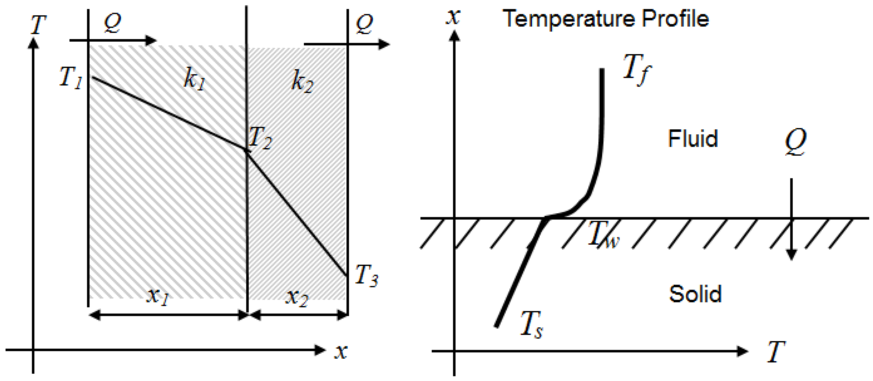

Figure 3.5: 1D steady-state heat transfer problem. Left: Conduction. Right: Convection (Clarkson, 2010)

When the flow is brought to rest at the wall, the kinetic energy is converted into internal energy as explained earlier. This is only valid when the wall is an adiabatic wall which means that the heat flux is zero at the wall. When the heat flux is not zero ('diabatic'), the wall temperature is not equal to the so-called recovery temperature, T_{rec}, but is also dependent on the temperature of the solid (Figure 3.6, left). In Chapter 4 and Chapter 6 it is shown that the difference between the temperature prediction with an adiabatic and coupled wall can be significant.

The energy transfer processes in a well-developed boundary layer are characterised by molecular transport of heat away from the wall, Q, and the molecular transport of momentum towards the wall, W. The ratio of the two is known as the Prandtl number,

$$Pr \propto \frac{W}{Q} = \frac{C_p \mu}{k} \tag{3.31}$$

The energy transfer processes are schematically shown in the centre of Figure 3.6. Finally, for an adiabatic wall the effect the Prandtl number has on the total temperature at the wall can be seen in the right of Figure 3.6.

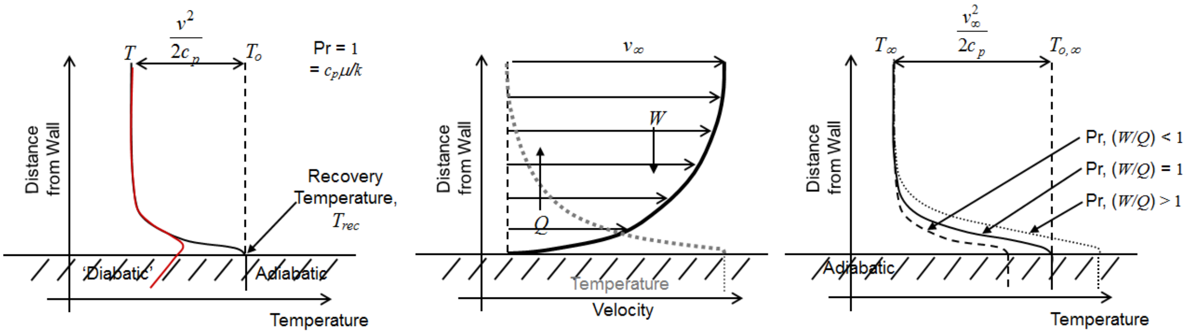

Figure 3.6: Temperature boundary layers. Left: Diabatic vs. adiabatic. Centre: Energy transfer processes. Right: Influence of Prandtl number (Clarkson, 2010)

As explained in the above discussion, the temperature at the wall when an adiabatic wall boundary condition is applied does not take the wall properties and temperature into account and is thus not realistic. Therefore in this research project it is investigated how much the temperature prediction at the wall of the TRU can be improved by performing a coupled simulation.

The 3D convective heat transfer is solved by the fluid solver, in this case Ansys Fluent, by solving the energy equation (See equation (3.6)).

The 3D conductive heat transfer is solved by the thermal solver. The conductive heat transfer is defined by Fourier's law which states that the thermal energy flux in any direction is proportional to the temperature gradient in that direction and is given by,

$$\rho c \frac{\partial T}{\partial t} = \frac{\partial}{\partial x}\left(k \frac{\partial T}{\partial x}\right) + \frac{\partial}{\partial y}\left(k \frac{\partial T}{\partial y}\right) + \frac{\partial}{\partial z}\left(k \frac{\partial T}{\partial z}\right) + q_g \tag{3.32}$$

In which ρc is the specific heat per unit volume, k the thermal conductivity of the solid and q_g the internal heat generation rate per unit volume. This equation can only be solved using a numerical approach and by applying appropriate boundary conditions.

In order to make sure conservation of energy is ensured, the heat flux and temperature at the interface between fluid and solid needs to be continuous. In order to achieve this, a valid coupling technique to couple the CFD with the thermal solver has to be used. This is discussed in the next section.

3.2.2 Coupling Techniques and Application

Now the governing equations for both the fluid and thermal solvers are known, the two solvers need to be coupled. The available coupling techniques are described below followed by the application of the techniques.

Coupling Techniques

In general three aero-thermal coupling techniques exist: conjugate heat transfer analysis and the non-coupled and coupled FE/CFD analysis methods (Chew and Hills, 2007).

In a conjugate heat transfer analysis the dependent variables in the fluid and solid domain are modelled by one code. Disadvantage is that the codes often lack specialist thermal modelling features and deformations and stresses are not taken into account (if one would extend the fluid-structure simulations). Another disadvantage is the fact that the flow time scales are significantly smaller than the solid time scales which stalls the convergence of the simulations. The boundary conditions exchanged at the fluid-solid interface for a conjugate heat transfer analysis can be visualised as follows,

$$q_f = q_s \tag{3.33}$$

$$T_f = T_s \tag{3.34}$$

In a non-coupled FE/CFD analysis the heat flux at the interface is passed from a converged CFD simulation to the FE solver. As the name of the method implies, the temperatures calculated by the FE solver are not fed back to the CFD solver. Therefore, the effect the temperature of the solid has on the fluid is still not taken into account. The boundary conditions exchanged from fluid to solid for a non-coupled FE/CFD analysis can be visualised as follows,

$$q_{f_i} = q_{s_i} \tag{3.35}$$

$$T_{s_i} \neq T_{f_{i+1}} \tag{3.36}$$

In which i stands for the coupling iteration.

To take the effect of the temperature of the solid into account a coupled FE/CFD analysis can be performed. The coupled analysis takes full advantage of the CFD and FE codes and information is exchanged between both solvers during the calculations. First, a converged CFD solution should be found which is used to start the coupling iterations between fluid and thermal solver. The CFD code supplies the thermal solver with heat fluxes at the interface and on its turn the thermal solver supplies the CFD code with temperatures after a converged solution is found. This coupling process is iterated till the temperature distribution at the coupling interface reaches a steady-state solution. The boundary conditions exchanged from fluid to solid for a coupled FE/CFD analysis can be visualised as follows,

$$q_{f_i} = q_{s_i} \tag{3.37}$$

$$T_{s_i} = T_{f_{i+1}} \tag{3.38}$$

Due to the above advantages and disadvantages the coupled FE/CFD analysis method is investigated in this research project. To resolve the flow topology, the Ansys Fluent software package is used. To resolve the temperature distribution in the solid, two codes are tested. The Rolls-Royce in-house SC03 code and the Ansys Fluent software package are tested. The performance of both codes is compared during the evaluation of the two aero-thermal test cases. How the coupling is performed is described below.

Rolls-Royce In-house SC03 Code

The SC03 FE code (Rolls-Royce plc, 2015) can be used to perform structural and thermal analyses. In this research project only the thermal analysis function of the solver is used (Illingworth and Hills, 2004).

The solver is originally designed to solve for the transient temperatures in a solid. A finite element discretisation in space and finite difference discretisation in time is used to solve Fourier’s law for heat (see equation (3.32)). A non-linear implicit system of equations is solved to obtain the temperatures in the solid at the end of each time step. By calculating a time stepping error and comparing it with the set time stepping accuracy, the convergence within a time step is ensured. In the same way a mesh discretisation error is calculated and compared with the set mesh refinement accuracy, to check if a mesh refinement iteration is required. The solid mesh is created by the solver internally by a Delauney algorithm.

To couple the SC03 solver to Fluent the SC89 plugin is used. The plugin extracts heat fluxes from the CFD solver and supplies these as boundary conditions to the FE solver. Subsequently the temperatures from the FE solver are supplied to the CFD solver.

The plugin exchanges the HTC and temperature at the interface. The HTC is determined by running two CFD simulations at the start of every time step. For the first simulation the CFD metal temperatures are taken from the original SC03 results as boundary conditions. For the second simulation the CFD metal temperatures are taken from the original SC03 results as boundary conditions and raised by 20 K. The heat fluxes q_1 and q_2 at the interface resulting from these two simulations are used to calculate the HTC,

$$h = \frac{(q_1 - q_2)}{20} \tag{3.39}$$

With this HTC the fluid temperatures at each CFD node point can now be calculated as follows,

$$T_f = \frac{q_1}{h} + T_m \tag{3.40}$$

The HTC and fluid temperature are supplied to SC03 by the plugin to calculate the heat flux with equation (3.30). Unfortunately, the SC03 solver is designed in such a way that the heat flux has to be calculated by equations (3.39), (3.40) and (3.30) and cannot be supplied directly to SC03. The temperatures at the interface calculated by SC03 can be supplied directly to Fluent by the plugin.

Finally, a maximum wall temperature tolerance needs to be set. This tolerance is used to check at the start of each analysis for a given SC03 iteration, if the metal temperature has changed by more than the user specified tolerance since the last time the CFD wall temperatures were updated. If this temperature tolerance is exceeded, the plugin starts a new CFD analysis to determine new HTC's at the coupled walls.

Figure 3.7 and Figure 3.8 show respectively the iterative coupling process between the SC03 and Fluent solver and the SC89 plugin strategy described above.

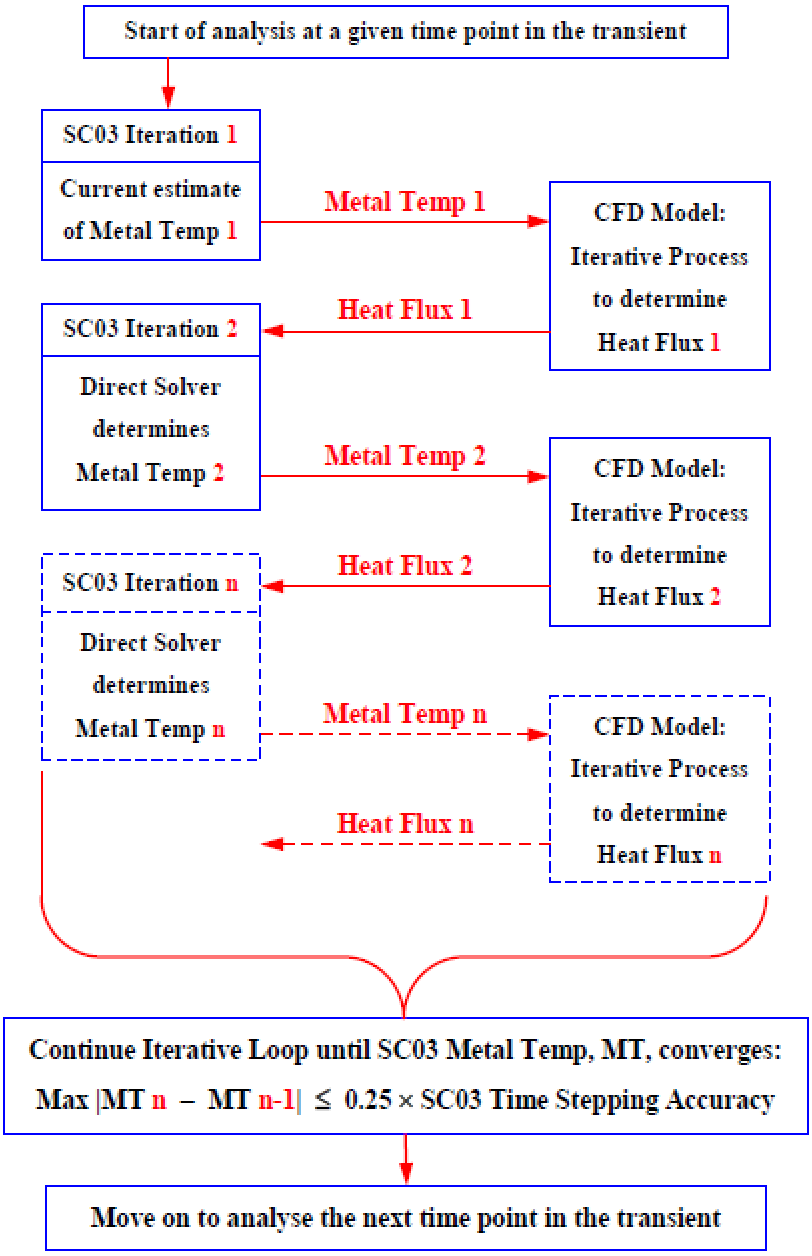

Figure 3.7: Overview of iterative coupling process within a time-step (Illingworth and Hills, 2004)

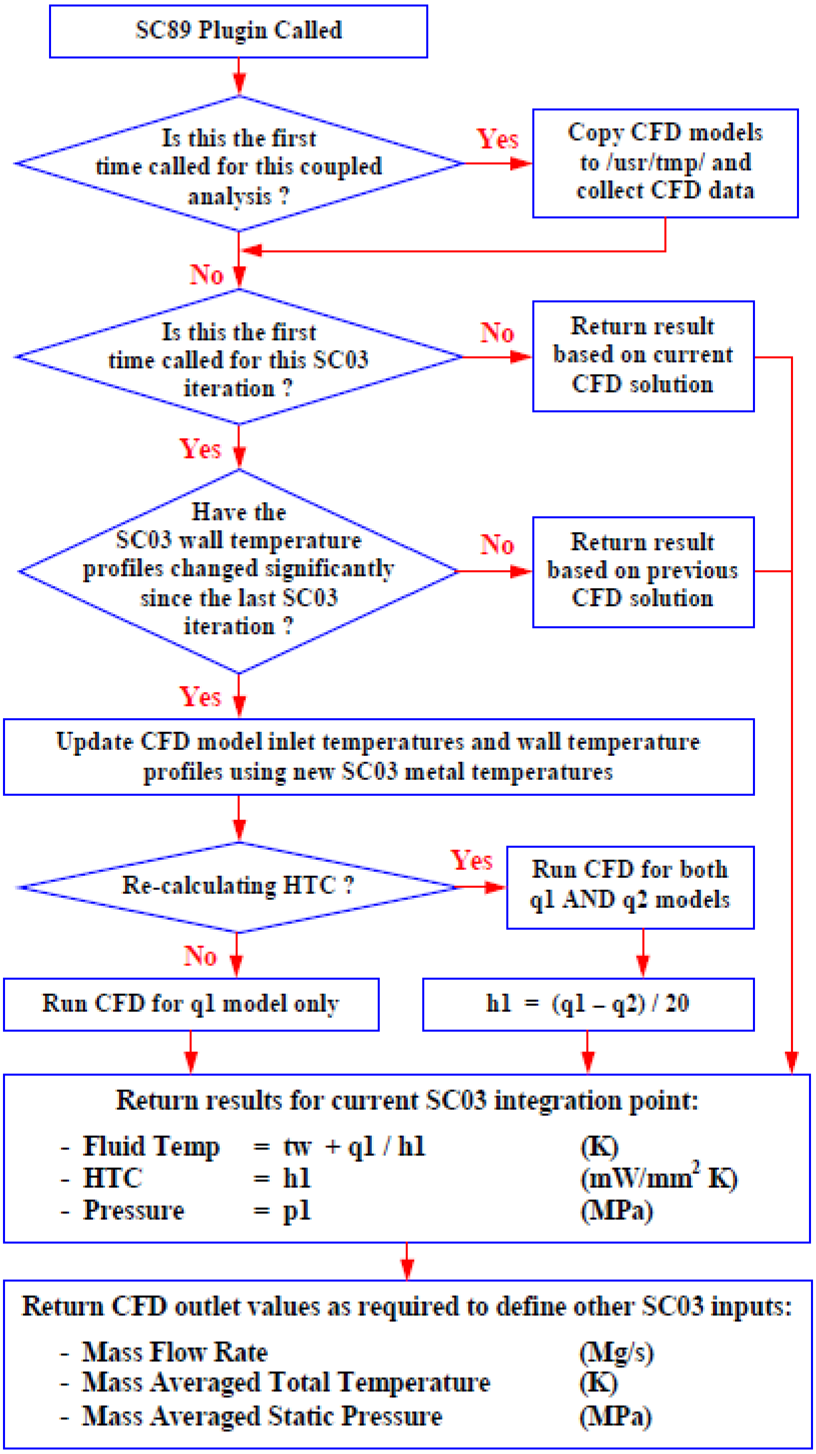

Figure 3.8: Overview of SC89 plugin strategy (Illingworth and Hills, 2004)

The interpolation of data at the interface is illustrated in Figure 3.9 and Figure 3.10.

As can be seen in Figure 3.9 to determine the metal temperature at the location of the CFD node, the two nearest SC03 integration points are determined. The metal temperatures from these two points are then interpolated with respect to distance to determine the temperature at the CFD node. This approach results in a smooth, continuous wall temperature profile which can be read into the CFD model as a wall boundary condition.

As can be seen in Figure 3.10 the interpolation of the heat fluxes from the CFD nodes to the SC03 integration points is performed somewhat different. SC89 assumes that the SC03 integration points will always be more sparsely distributed than the CFD node points. First the nearest SC03 integration point is determined for each CFD node. The CFD nodes determined for each integration point are grouped together. Because each CFD node has a certain cell area and heat flux associated with it, the following relation is used to calculate the heat flux passed to each SC03 integration point,

$$q_{IP} = \frac{\sum q_{node} \cdot A_{node}}{\sum A_{node}} \tag{3.41}$$

In which the subscript IP corresponds to the SC03 integration point.

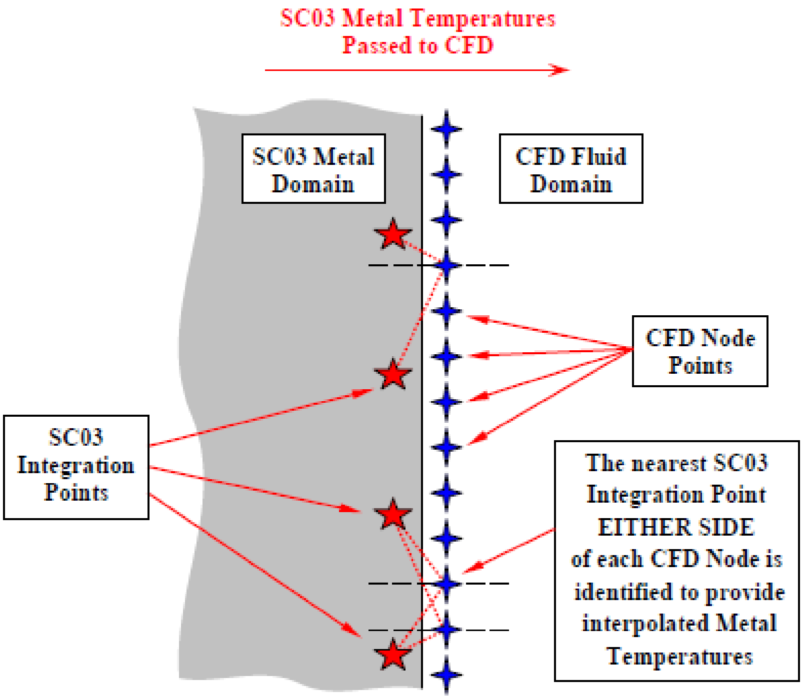

Figure 3.9: Interpolation of SC03 temperatures at a coupled wall boundary (Illingworth and Hills, 2004)

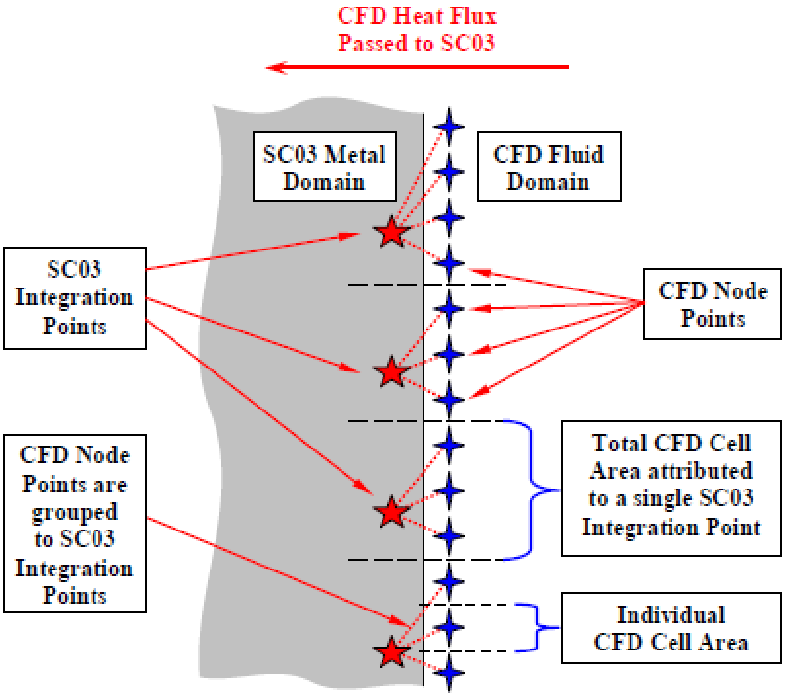

Figure 3.10: Interpolation of CFD heat flux at a coupled wall boundary (Illingworth and Hills, 2004)

Ansys Fluent Code

The Ansys Fluent solver can also be used to determine the temperature distribution in a solid. The computational domain needs to be defined as a solid and the solid density, specific heat and thermal conductivity need to be specified. Just like for the SC03 solver a temperature or heat flux boundary condition can be specified for a solid wall.

As described in section 3.1 the Roe-Flux-Difference Splitting scheme is used for spatial discretisation. Fourier's law for heat (See equation (3.32)) is solved first-order accurate in space. Fourier's law is linearized into its implicit form to solve for the dependent variables iteratively. Just like for the fluid simulations the gradients are calculated by the least squares cell based method. No corrections or convergence accelerators are used.

The coupling between fluid and solid simulations is done by writing a so-called journal-file. In a journal-file the consecutive commands needed to perform the coupling iterations are stored.

The calculations performed by the SC89 plugin are not needed and the temperatures and heat fluxes at the interface can be exchanged directly. Just like for the SC03-coupling the solid is supplied by the heat flux distribution and the fluid by the temperature distribution at the interface. This is done by writing out boundary-profiles. While reading the boundary-profiles into the simulation set-up the data is interpolated automatically. A zeroth-order interpolation is used to assign the profile point values to the nearest cell faces at the boundary (Nearest Neighbour Interpolation).

Comparison of Both Solvers

Advantages of the SC03 solver are its robustness and the fact that no licences are needed (Rolls-Royce in-house tool).

A disadvantage is the fact that the requirements on the geometry CAD-file are different and higher than for the Centaur mesher (CentaurSoft, 2012) which is used to make a mesh suitable to be used in Fluent.

Another disadvantage is that SC03 and Fluent are opened and closed during the coupling iterations which means that Fluent licences can be lost during the simulations which results in a crashed simulation. When using only Fluent the solver is not closed during coupling iterations.

Finally, later in the research project was found out that SC03 was not available on the Rolls-Royce calculation clusters. The size of the simulations is such that the simulations cannot be performed on a local computer which means an alternative to SC03 needed to be found. This brought the author of this report to the idea of using Fluent as a thermal solver.

Chapter 4 Validation Test Cases

In the first part of this chapter, the solver capabilities of the Ansys Fluent (14.0) software package (Ansys Inc., 2011a) will be validated to model the four most important flow phenomena representative for the TRU flow. In the second part, the Ansys Fluent and SC03 (Rolls-Royce plc, 2015) aero-thermal coupling capabilities will be validated.

The four most important flow phenomena observed in a thrust reverser simulation are found from the literature study described in section 2.1 and shown in Figure 2.4. Experiments performed to investigate these flow phenomena were found from the literature and used as validation test cases in this research project. The selected test cases are the jet in a cross flow, plane mixing layer, backward-facing step and curved channel flow which are discussed in sections 4.1 to 4.4.

From the literature dealing with coupled aero-thermal simulations, two test cases were selected which serve as validation test cases to validate the two selected coupling techniques. Sections 4.5 and 4.6 describe the coupled simulations of the flow over a semi-infinite flat plate and the flow through a convergent-divergent nozzle, respectively. The turbulence model used for the coupled aero-thermal simulations is the Realizable k-ε model.

If not stated otherwise, the solver settings used for the evaluation of the test cases are given below in Table 4.1.

Table 4.1: Summary of solver settings for the evaluation of the validation test cases

Solver Setting	**Chosen Approach**
Solver Type	Density-based solver
Time	Steady
Energy-equation	On
Density properties, ρ $[kg/m^3]$	Ideal gas
Specific heat, c_p $[J/kgK]$	RRD defined polynomial function
Thermal conductivity, k $[W/mK]$	RRD defined polynomial function
Viscosity, μ $[kg/ms]$	Sutherland's law
Linearization method	Implicit
Flux Type	Roe-FDS
Gradients	Least squares cell based
Flow accuracy	Second-order upwind
Turbulence accuracy	First-order upwind

4.1 Jet in a Cross Flow

The jet in a cross flow (JICF) test case is based on the experimental results by Dennis, Tso and Margason (1993) and the numerical results by Chiu, et al.(1993). The JICF is selected due to its similarity in flow topology with the reversed flow jet in the TRU simulations. The pressure coefficients around the jet exit orifice obtained from the experiments are used to validate different turbulence models and mesh densities.

Figure 4.1 below shows the four most important vortical structures for this test case. Fric and Roshko (1994) showed that the jet shear layer and wake vortices are intrinsically unsteady while the horseshoe vortex and counter-rotating vortex pair have mean flow definition.

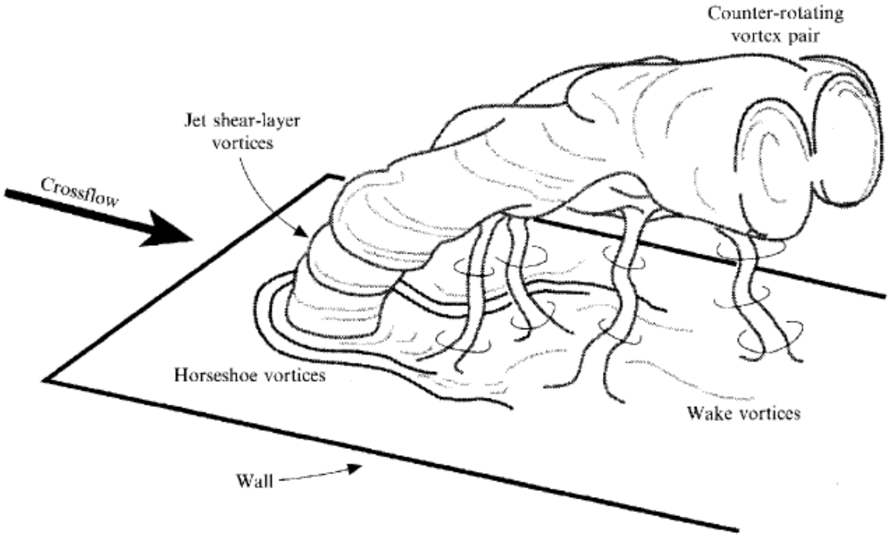

Figure 4.1: Sketch of the JICF flow topology (Fric and Roshko, 1994)

The boundary conditions, computational domain and validation data used for the simulations can be found from Appendix A.1. A number of meshes were investigated with an increasing amount of refinement. The results of the two most refined meshes are shown in this section. A summary of the mesh characteristics for these two meshes is given below in Table 4.2. The quality criteria used in the table are described in section 3.1.4.

Refinement of mesh 1 resulted in mesh 2. From the table can be seen that this refinement did not lead to a clear improvement in mesh quality. By refining the mesh around the jet exit orifice the y^+ value range improved somewhat.

Figure 4.2 shows the pressure coefficient in flow direction at the leading edge/stagnation point of the jet exit orifice for mesh 1. All three turbulence models give a fairly good agreement to the validation data, except for the small region where the flow accelerates (between r/D = 1-2).

Table 4.2: Summary of the mesh characteristics for the JICF test case

Variable	**Mesh 1**	**Mesh 2**
Mesh generator	Centaur	Centaur
Meshing strategy	Hybrid	Hybrid
Mesh size [-]	9,334,968	12,976,779
Prism layers [-]	30	30
Worst ortho. quality [-]	0.041	0.023
No. unacc. cells, Ansys [-]	0	0
No. unacc. cells, RRD [-]	0	0
No. bad cells, Ansys [-]	2,452	9,992
Worst equi. skew [-]	0.944	0.946
No. unacc. cells [-]	0	0
No. bad cells [-]	0	0
Aspect ratio [-]	3,186	3,558
y^+ value range [-]	0-1.8	0-0.7

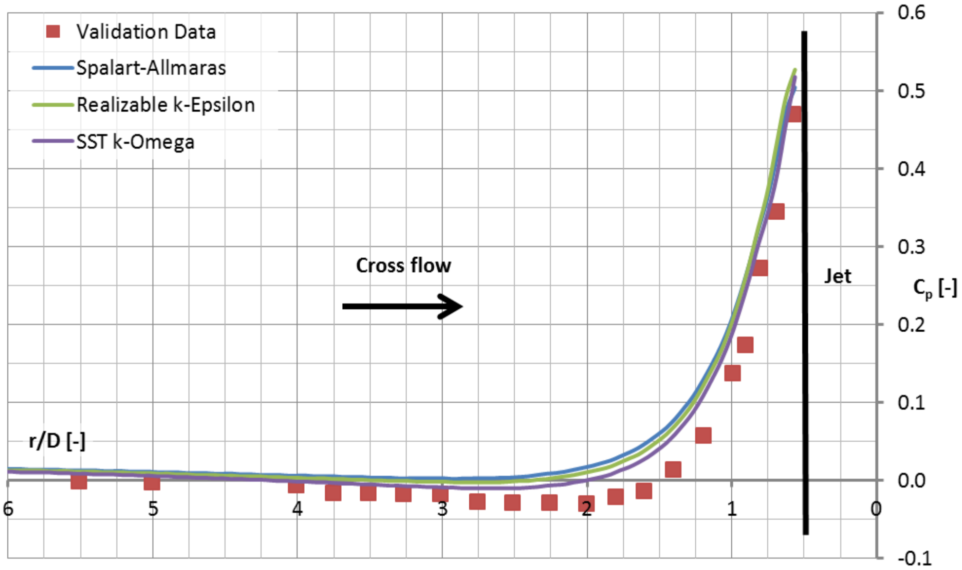

Figure 4.2: C_p distributions along the 0° azimuthal line on mesh 1 for the SA, Realizable k-ε and SST k-ω turbulence models

Figure 4.3 shows the pressure coefficient in flow direction at the trailing edge of the jet exit orifice for mesh 1. Both the Spalart-Allmaras and SST k-ω model give a fairly good agreement to the validation data with a maximum error of 13% and 8% respectively. The realizable k-ε model clearly predicts a less negative pressure coefficient, resulting in a maximum error of 32%.

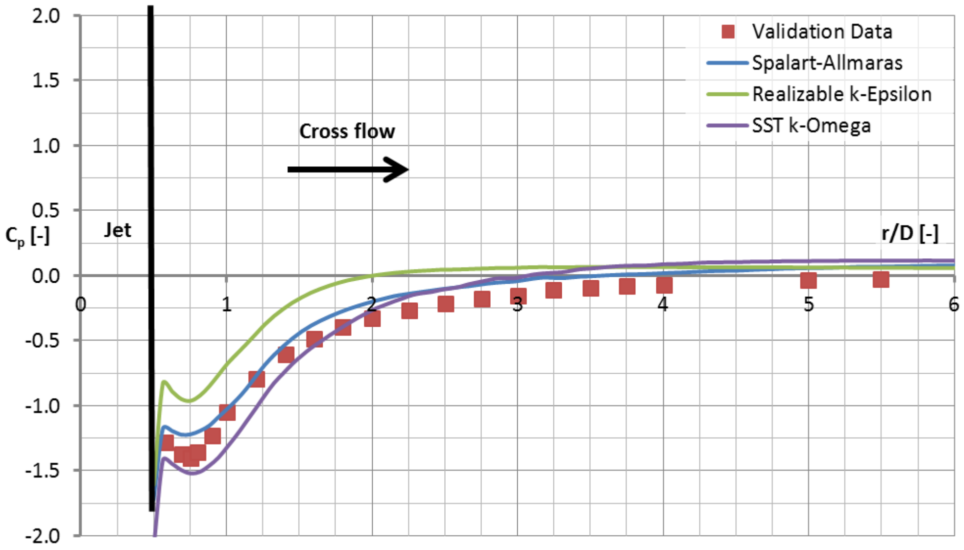

Figure 4.3: C_p distributions along the 180° azimuthal line on mesh 1 for the SA, Realizable k-ε and SST k-ω turbulence models

Figure 4.4 shows the pressure coefficient distribution around the jet exit orifice for mesh 1, according to the azimuthal angles shown in Appendix A.1. A first observation shows a large asymmetry in the results for all three turbulence models. The asymmetry is most pronounced in the regions were an adverse pressure gradient is present ($90° \leq \theta \leq 270°$). In these regions it is known that the isotropic turbulence assumption is not valid, see section 3.1.1. Also the performance of the turbulence models in adverse pressure gradient and separated flow regions is doubtful, see section 3.1.3. The maximum errors for the Spalart-Allmaras, Realizable k-ε and SST k-ω models are respectively 76%, 117% and 61%.

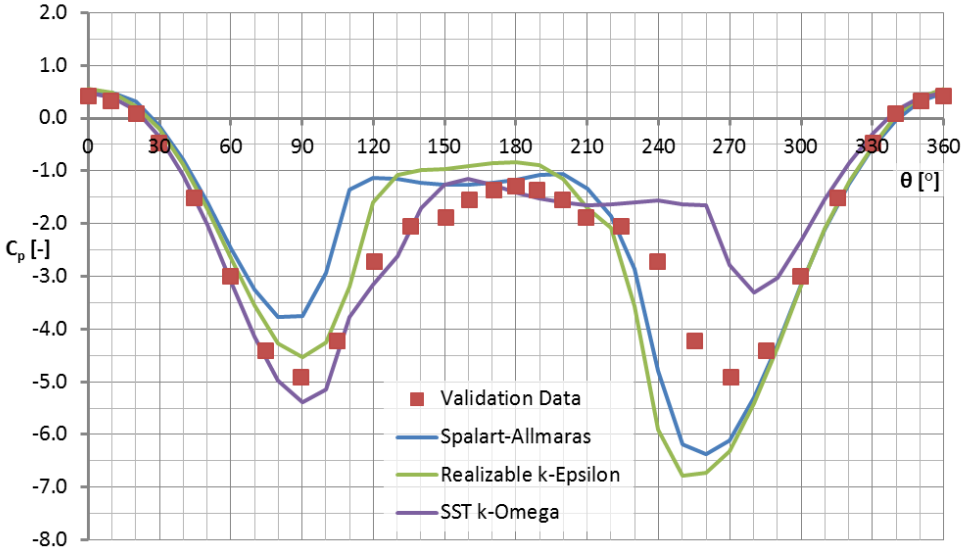

Figure 4.4: C_p distributions near the jet exit orifice at r/D = 0.58 on mesh 1 for the SA, Realizable k-ε and SST k-ω turbulence models

As shown in Figure 4.1, four vortical structures are present in the JICF problem. A mesh study was performed to see which influence the mesh density has on the modelling of these structures. From Figure 4.5 can be seen that by refining the mesh in the area upstream of the jet, the SST k-ω model is the only turbulence model which is able to model the horseshoe vortex.

The counter-rotating vortex pair could be recognised, and is modelled similarly for all three models and investigated mesh densities. The unsteady jet shear layer and wake vortices could not be recognised for all three models and investigated mesh densities.

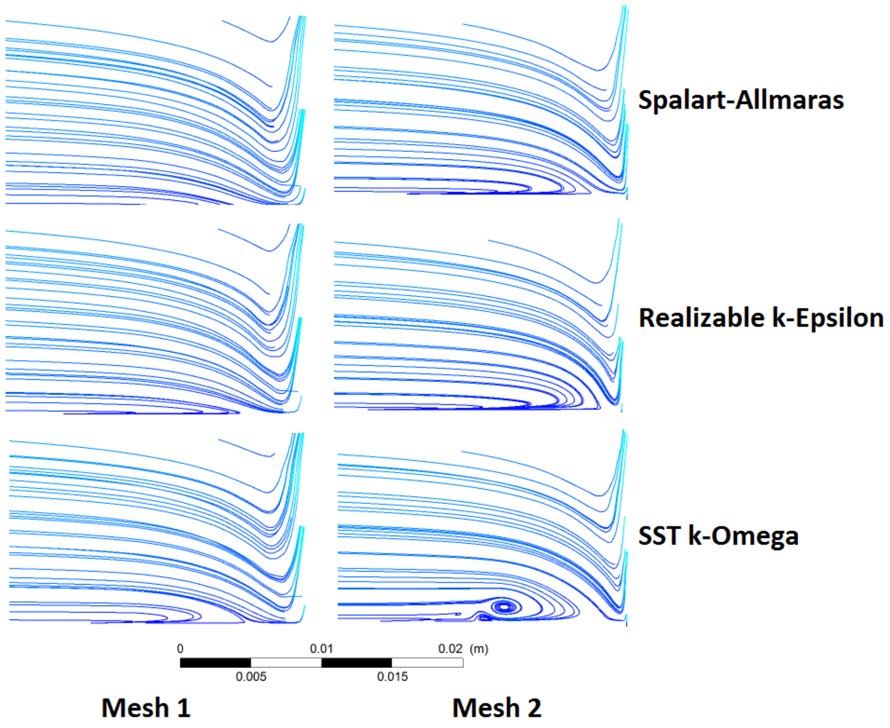

Figure 4.5: 2D streamline plot of the flow region along the 0° azimuthal line to visualise the horseshoe vortex

4.2 Plane Mixing Layer

The plane mixing layer test case is based on the experimental results by Delville, et al.(1999) and Druault, Delville and Bonnet (2005). Components of the Reynolds stress tensor and velocity profiles in the mixing layer were measured with hot wire anemometers. Some of these Reynolds stress and velocity profiles are used to compare simulation results for different turbulence models and meshing strategies. A schematic representation of the windtunnel with installed splitter plate can be seen below in Figure 4.6.

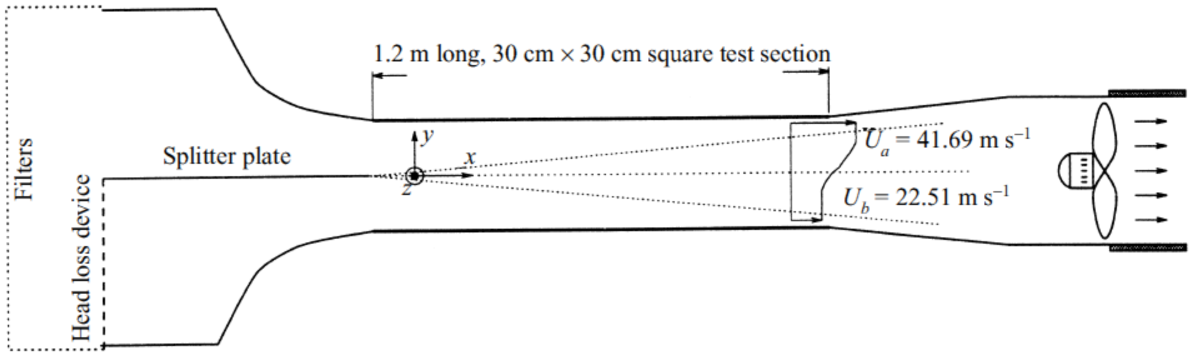

Figure 4.6: Schematic representation of the windtunnel with installed splitter plate (Delville, et al., 1999)

Several researchers like Bell and Mehta (1990), Rogers and Moser (1994) and Olsen and Dutton (2002), showed that there is a clear difference in flow topology in the near- and far-field of the mixing layer. In the near-field the unsteady Kelvin-Helmholtz instability is present while in the far-field the non-dimensionalised velocity profiles and Reynolds stresses show self-similar behaviour and are independent of downstream position. The experimental data used in this section is obtained in the self-similar region of the mixing layer.

The boundary conditions, computational domain and validation data used for the simulations can be found from Appendix A.2. In total 6 different meshes were tested for this test case. The difference between the meshes is the way in which the mixing region is meshed. The different approaches tested are: a block of structured hexagonal cells, unstructured (refined) tetrahedral cells, a wake block, a combination of these options or a fully structured mesh constructed with the Ansys ICEM CFD mesh generator (SAS IP, Inc., 2011). A wake block is an extension of the prism layer cells behind the splitter plate into the mixing region. A summary of the mesh characteristics for these meshes is given below in Table 4.3.

From Table 4.3 some important relations can be recognised relating to the mesh quality,

- The decrease in number of prism layers together with an increase of initial layer thickness increases the y^+ value but on the other hand,
    - Improves the orthogonal quality
    - Improves the equivolume skewness
    - Reduces the aspect ratio which implies that large aspect ratio values are caused by the first prism layer cells and their thickness (how smaller y^+, how larger the aspect ratio)
- A structured mesh (mesh 6) saves a considerable amount of cells while maintaining good quality characteristics and a reasonable y^+ value.

Figure 4.7 shows the Reynolds normal- and shear-stress distribution over a 2D cross-section of the mixing layer in streamwise direction. The Reynolds normal- and shear-stress distribution is a measure of the ability of the turbulence models to model velocity fluctuations in the mixing layer. The Reynolds stresses are modelled by the turbulence models which rely on the Boussinesq approximation given by Equation (3.12).

Table 4.3: Summary of the mesh characteristics for the plane mixing layer test case

Variable	**Mesh 1**	**Mesh 2**	**Mesh 3**	**Mesh 4**	**Mesh 5**	**Mesh 6**
Mesh generator	Centaur	Centaur	Centaur	Centaur	Centaur	ICEM CFD
Meshing strategy	Hybrid	Hybrid	Hybrid	Hybrid	Hybrid	Structure
Structured mesh block	Yes	-	-	Yes	-	-
Refined mesh block	-	Yes	-	-	Yes	-
Wake block	-	-	Yes	Yes	Yes	-
Mesh size [-]	3,534,378	2,912,914	2,978,945	3,498,274	4,073,997	968,843
Prism layers [-]	30	30	15	15	15	30
Worst ortho. quality	0.026	0.049	0.058	0.038	0.093	0.099
No. unacc. cells, Ansys	0	0	0	0	0	0
No. unacc. cells, RRD	0	0	0	0	0	0
No. bad cells, Ansys [-]	17,696	14,643	3	8	8	341
Worst equi. skew [-]	0.977	0.993	0.998	0.987	0.976	0.162
No. unacc. cells [-]	0	7	4	2	0	0
No. bad cells [-]	1	535	3	9	8	0
Aspect ratio [-]	9,724	5,061	72	112	46	5,553
y^+ value range [-]	0-0.23	0-0.45	0-85.0	0-82.0	0-82.0	0-2.72

Most interesting result of Figure 4.7 is the fact that the Spalart-Allmaras model is not able to model the Reynolds normal stress. As is described in section 3.1.3, the turbulent kinetic energy is not modelled by the Spalart-Allmaras model. The turbulent kinetic energy forms a large component of the Reynolds normal stress as is confirmed by the figure. The best approximation is given by the SST k-ω model which is now used as the reference model for this test case.

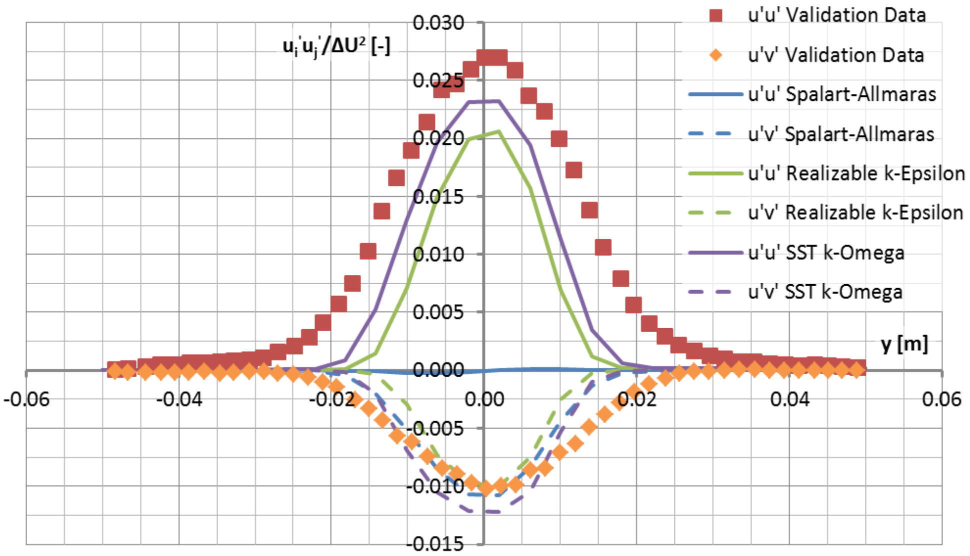

Figure 4.7: Comparison of Reynolds stresses for the three turbulence models on mesh 1 at station 500 mm

Comparing the streamwise development of the Reynolds normal stresses for the six different meshes, shown in Figure 4.8, it can be concluded that a structured mesh shows clearly the best results. Mesh 1 has a structured mesh block at stations 200, 400 and 600 mm. Its maximum Reynolds normal stress value has an error of 4%, 12% and 14% compared to the validation data at these locations. Mesh 4 has a structured mesh block at stations 800 and 1000 mm and shows errors of 13% and 11% at these locations. Finally mesh 6, which is a structured mesh, shows the most consistent results over all downstream locations with an average error of about 17%.

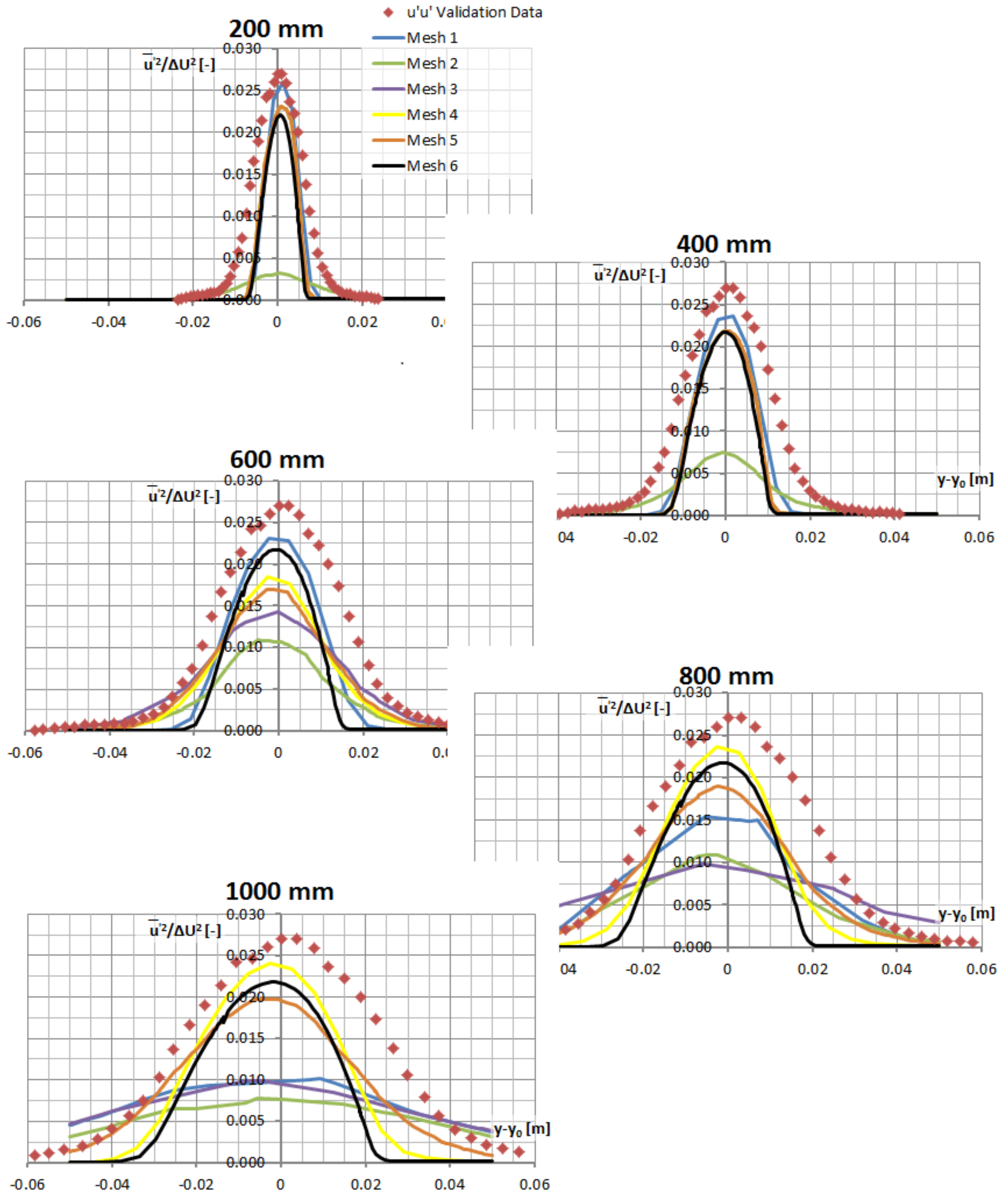

Figure 4.8: Development of streamwise Reynolds normal stresses at different locations in the mixing region for the SST k-ω model and the six different meshes

Figure 4.9 shows the normalised mean streamwise velocity profile for the six different meshes. The results are shown for the SST k-ω model but similar results were obtained with the Spalart-Allmaras and Realizable k-ε turbulence models. From the figure can be seen that the modelling of the velocity is less sensitive to the meshing strategy. This is in line with the information found from the literature about different meshing strategies described in section 3.1.4. In the transition regions from mixing layer to freestream, the discrepancies are highest with errors of up to 10% for mesh 6. These discrepancies are most likely caused by the velocity gradient (between mixing layer and freestream) which is not accurately captured in these two areas. Mesh 6 gives the largest error probably because its mesh density is not as fine as the other meshes in these two areas.

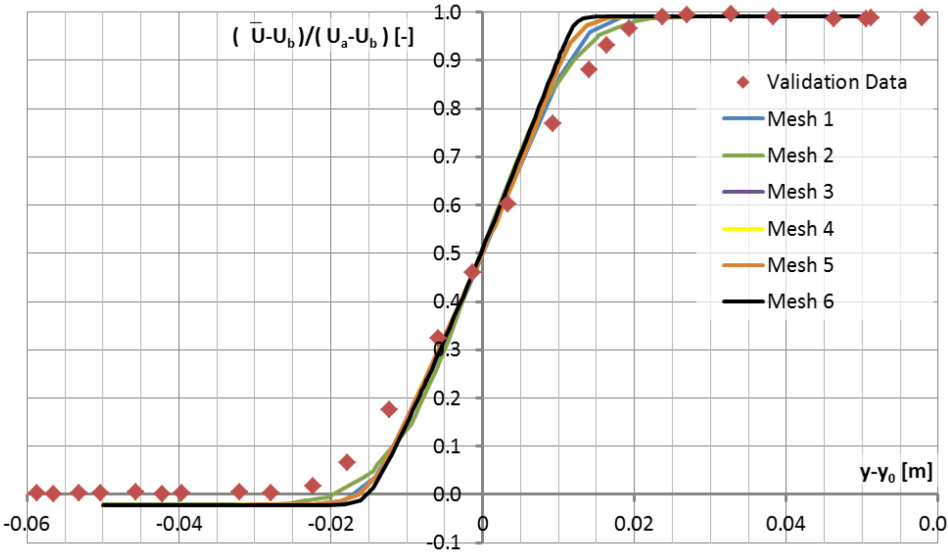

Figure 4.9: Normalised mean streamwise velocity profile for the SST k-ω model and the six different meshes at station 500 mm

4.3 Backward-Facing Step

The backward-facing step test case is based on the experimental results by Jovic and Driver (1994) and the DNS results by Le, Moin and Kim (1997). An LDV instrument was used to measure mean velocity components and components of the Reynolds stress tensor. Besides this, also surface pressure and skin-friction coefficients were measured. The surface pressure and skin-friction coefficients together with the experimental data of the velocity profiles are used to validate the simulation results for different turbulence models and meshing strategies.

The focus during the evaluation of this test case is on the area downstream of the step were the flow is separated and later reattaches to the downstream surface again. In the separated region, two recirculation areas can be recognised as can be seen from Figure 4.10 below.

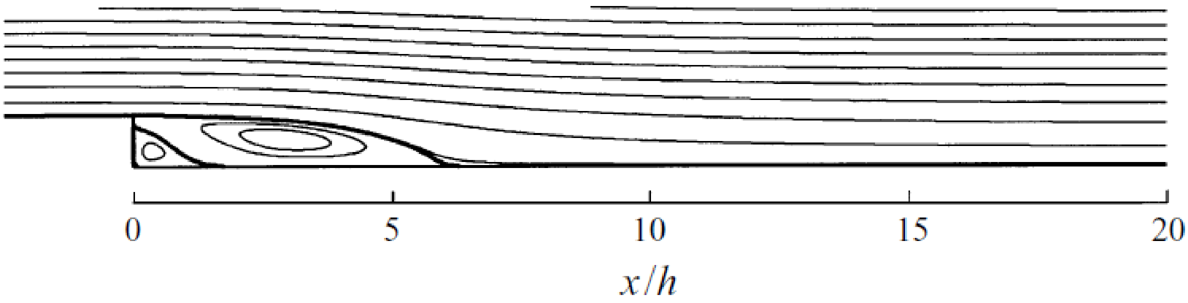

Figure 4.10: Contours of mean stream function ψ. Reattachment length $X_r = 6.28h$ (Le, Moin and Kim, 1997)

The boundary conditions, computational domain and validation data used for the simulations can be found from Appendix A.3. The results for a hybrid and structured mesh are shown in this section. The most important mesh characteristics for these two meshes are given below in Table 4.4.

Table 4.4: Summary of the mesh characteristics for the backward-facing step test case

Variable	Mesh 1	Mesh 2
Mesh generator	Centaur	ICEM CFD
Meshing strategy	Hybrid	Structured
Mesh size [-]	4,851,930	1,286,734
Prism layers [-]	30	30
Worst ortho. quality [-]	0.019	0.566
No. unacc. cells, Ansys [-]	0	0
No. unacc. cells, RRD [-]	0	0
No. bad cells, Ansys [-]	30,126	0
Worst equi. skew [-]	0.993	0.249
No. unacc. cells [-]	22	0
No. bad cells [-]	2,177	0
Aspect ratio [-]	2,293	617
y^+ value range [-]	0-0.87	0-4.66

The statements made in the previous section about the differences in mesh quality between a hybrid and a structured mesh are confirmed when the mesh characteristics in Table 4.4 are considered. The worst values for the orthogonal quality as well as equivolume skewness are considerably better for the structured mesh. No cells of unacceptable or bad quality are present for the structured mesh and besides this, also the aspect ratio is lower.

Figure 4.11 shows the skin friction coefficient at the wall downstream of the step. The normalised x position coincides with the positions shown in Figure 4.10. From the figure can be seen that the results are not that dependent on the meshing strategy (hybrid or structured mesh) as the Reynolds stresses were in the previous section. The differences between the turbulence models are however more pronounced.

Both the Spalart-Allmaras and Realizable k-ε models overestimate the magnitude (19% and 25% error respectively) and underestimate the position (17% and 34% error respectively) of the minimum skin friction coefficient. The reattachment zone indicated in the figure is the zone in which the reattachment point oscillated during the experiments. The Spalart-Allmaras model is able to predict the reattachment point accurately. The Realizable k-ε model is able to predict the reattachment point accurately on mesh 1 but underpredicts the position of the point by about 10% for mesh 2.

The SST k-ω model shows a good agreement with the validation and DNS data in the recirculation area. The position of the reattachment point is however overpredicted by about 25% for mesh 1 and 17% for mesh 2.

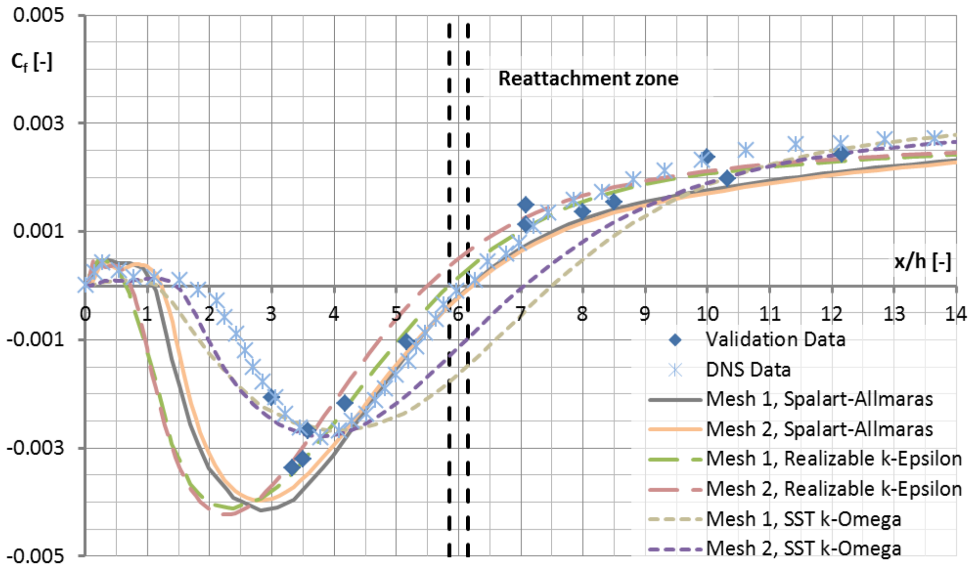

Figure 4.11: Skin friction coefficient for the three turbulence models on mesh 1 and 2

Figure 4.12 shows the pressure coefficient at the wall downstream of the step. As can be seen from the figure the SST k-ω model gives a good agreement with the validation data. The offset in pressure coefficient in the recovery region further downstream from the step, $x/h \geq 10$, is probably caused by a difference in boundary conditions for the experiments and simulations. The error for the Spalart-Allmaras and Realizable k-ε models in the reattachment zone is about 33%.

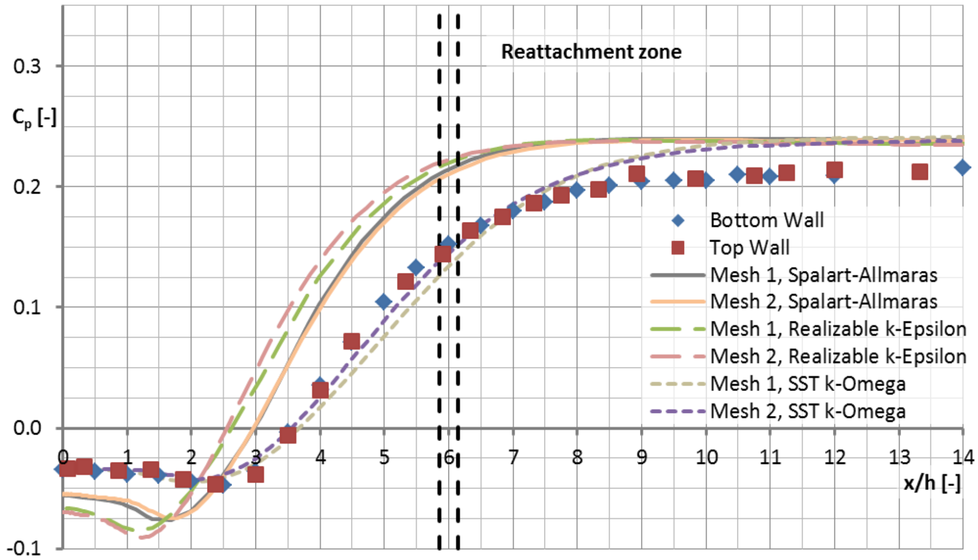

Figure 4.12: Pressure coefficient for the three turbulence models on mesh 1 and 2

Finally the normalised velocity profiles at four different x/h positions are shown in Figure 4.13 for the three turbulence models. All turbulence models have a fuller velocity profile upstream of the step ($x/h = -3.12$). This is probably caused by a mismatch in turbulence boundary conditions. The effect of this fuller profile can be seen in the profiles downstream of the step which are fuller at a height of $x/h = 1.5$ compared to the validation data.

Comparison of the results of the different turbulence models shows that the SST k-ω model gives the most accurate results in the recirculation area. At $x/h = 6$ the SST k-ω model still shows some reversed flow. It would be worthwhile to investigate if the prediction of the reattachment point (C_f) would improve for the SST k-ω model with different turbulent boundary conditions. The results for the Spalart-Allmaras and Realizable k-ε models are similar. The models do predict some reversed flow close to the wall but underpredict the amount of reversed flow and thereby the size of the vortex shown in Figure 4.10.

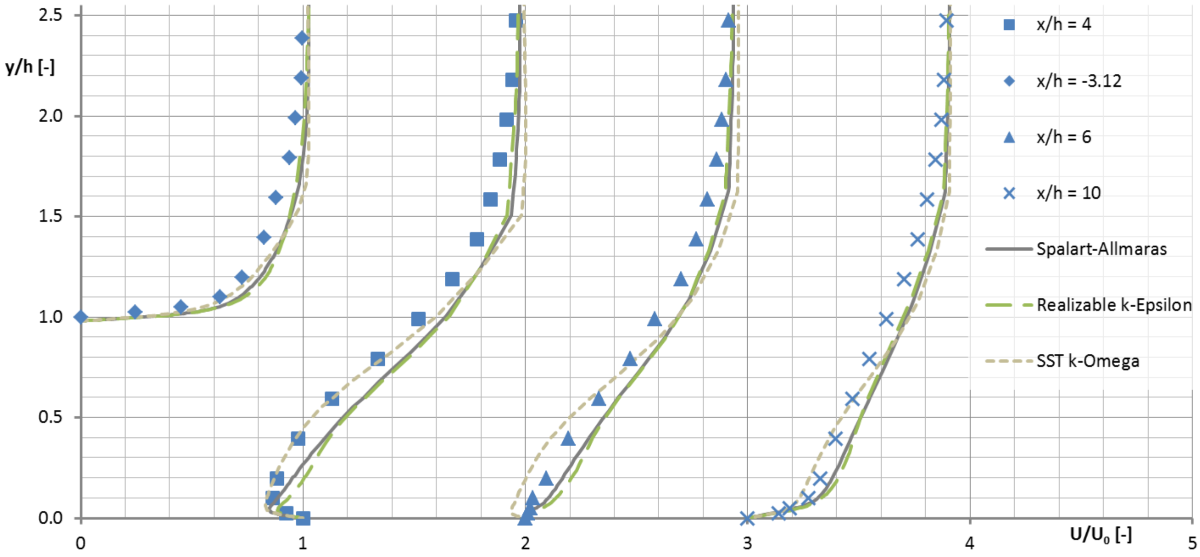

Figure 4.13: Normalised velocity profiles for the three turbulence models on mesh 1

4.4 Curved Channel Flow

The curved channel flow test case is based on the experimental data by Kim and Patel (1994). The experiments serve as validation data for computational methods which incorporate a Curvature Correction (CC).

The CC was developed and validated by Spalart and Shur (Spalart and Shur, 1997; Shur, et al., 1998 & 2000) and first applied to the production term of the Spalart-Allmaras turbulence model, described in section 3.1.3. The CC was later modified by Smirnov and Menter (2009) such that it could be applied to two equation turbulence models like the SST k-ω and Realizable k-ε models. This CC showed superior results over the original turbulence models without influencing the robustness and computational efficiency of the models. The CC is incorporated in the Ansys Fluent software package and therefore validated with this test case.

The skin friction coefficients were measured at several cross-sections of the curved channel. The locations of the cross-sections can be seen below in Figure 4.14.

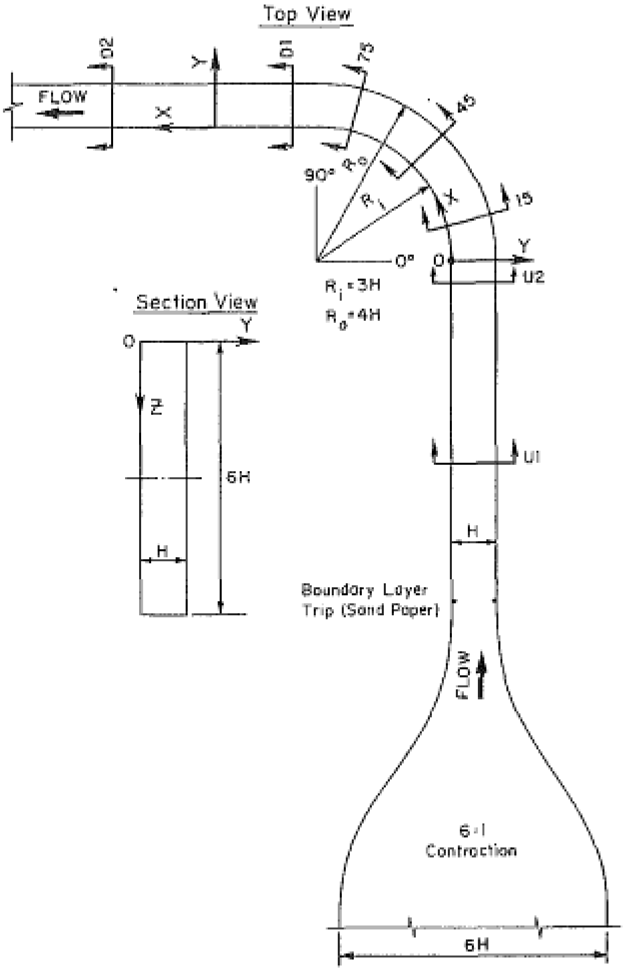

Figure 4.14: Curved channel wind tunnel. Measurement cross-sections, U2, 15°, 45°, 75°, D1 and D2, included (Kim and Patel, 1994)

Kim and Patel (1994) state that convex curvature has a stabilizing effect on the flow while concave curvature has a destabilizing effect on the flow. Due to the curvature, two vortices develop in the two corners on the inner wall of the duct. The appearance of these vortices can be recognised from the measured skin friction coefficients. The modelling of these two developing vortices for the different turbulence models and meshing strategies is validated in this test case.

The boundary conditions, computational domain and validation data used for the simulations can be found from Appendix A.4. The results for a hybrid and structured mesh are shown in this section. The most important mesh characteristics for these two meshes are given below in Table 4.5.

The differences in mesh quality between the hybrid and structured mesh are less pronounced for this test case. The cause for this is the curvature of the channel which decreases the orthogonal quality for the hybrid but also for the structured mesh. As can be seen from the table, the equivolume skewness and aspect ratio are both better for the structured mesh.

Table 4.5: Summary of the mesh characteristics for the curved channel flow test case

Variable	**Mesh 1**	**Mesh 2**
Mesh generator	Centaur	ICEM CFD
Meshing strategy	Hybrid	Structured
Mesh size [-]	2,346,012	2,311,200
Prism layers [-]	30	30
Worst ortho. quality [-]	0.012	0.016
No. unacc. cells, Ansys [-]	0	0
No. unacc. cells, RRD [-]	0	0
No. bad cells, Ansys [-]	76,909	10,044
Worst equi. skew [-]	0.977	0.740
No. unacc. cells [-]	0	0
No. bad cells [-]	252	0
Aspect ratio [-]	2,959	599
y^+ value range [-]	0-2.65	0-6.41

As can be seen from Figure 4.14 and the validation data in Appendix A.4, 6 measurement locations are given in which the skin friction coefficient around the half perimeter of the cross-section is measured (starting at the middle of the convex inside wall and ending at the middle of the concave outside wall).

The results of the simulations were compared to the validation data at all measurement locations for the two meshes and three turbulence models. The results for the D1 measurement location are included in this report and can be seen in Figure 4.15, Figure 4.16 and Figure 4.17. Results for the other measurement locations were similar. The validation data of Shur, et al.(2000) are used to compare the results of the performed simulations with. This because the experimental results of Kim and Patel (1994) seem to be inaccurate in the corners of the duct cross-section at $s/H = 3$ and 4 compared to the data of Shur, et al.(2000).

The vortex which is formed in the corner on the convex inside wall of the duct can be recognised by the decrease and increase of the skin friction coefficient between $s/H = 1$ and 3. On the side-wall of the duct the vortex can be recognised by the parabolic shape of the skin friction coefficient whether on the concave outside wall the influence of the vortex is less pronounced.

From the figures can be seen that by using the CC the results for the skin friction coefficient are improved for all three turbulence models and both meshes. In general the results for mesh 2 are better, especially in the area where the vortex is present.

On the convex inside wall the Spalart-Allmaras model gives the worst result. The vortex is best modelled by the SST k-ω model with CC.

On the side wall no difference can be seen between the simulations with and without CC. From the three turbulence models the Spalart-Allmaras model gives the best results.

On the concave outside wall the SST k-ω model gives the worst results. The best results are produced by the Spalart-Allmaras model. An improvement of the results on mesh 2 with and without CC can be seen for the Realizable k-ε model.

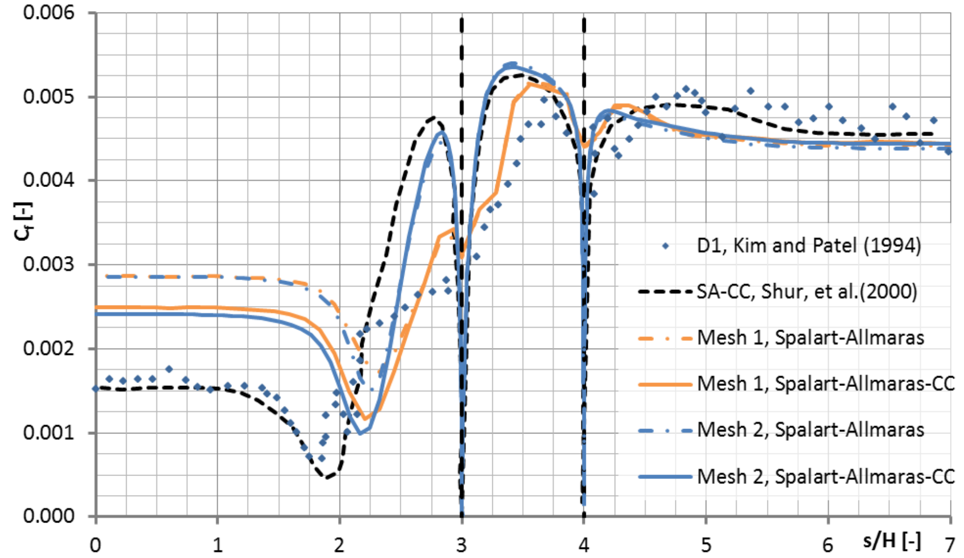

Figure 4.15: Skin friction coefficient at location D1 for the Spalart-Allmaras model with and without CC on mesh 1 and 2

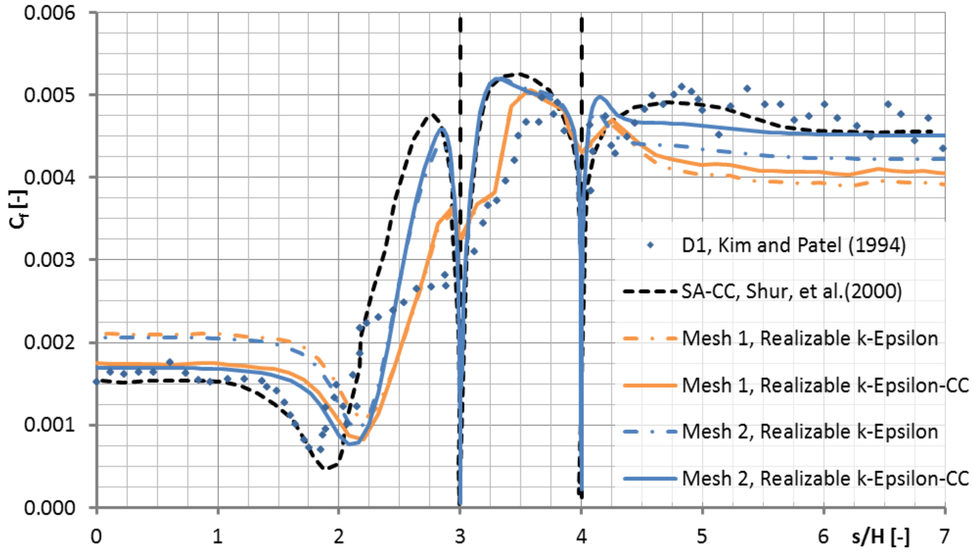

Figure 4.16: Skin friction coefficient at location D1 for the Realizable k-ε model with and without CC on mesh 1 and 2

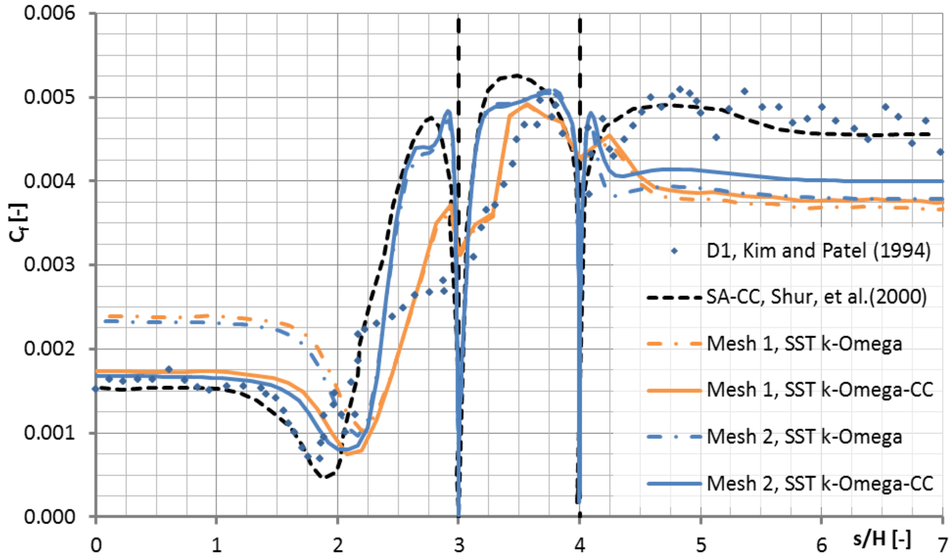

Figure 4.17: Skin friction coefficient at location D1 for the SST k-ω model with and without CC on mesh 1 and 2

The fact that the Spalart-Allmaras model gives the best results on two of the three inspected walls can be caused by the fact that the CC was originally developed for the Spalart-Allmaras model. Nonetheless the use of the CC improves the results for all three turbulence models.

4.5 Semi-Infinite Flat Plate

This test case and the following one are used to validate the coupled aero-thermal simulation capabilities of the Ansys Fluent software package and the SC03 thermal solver.

The semi-infinite flat plate test case is based on the paper by Kao and Liou (1997). The paper describes a method that computes the conjugate heat transfer problem using a hybrid overset grid system. The influence of the mesh density at the coupling interface between fluid and structure is investigated during the evaluation of this test case. The results for the Ansys Fluent solver are compared with the results of the SC03 solver.

The test case set-up can be seen below in Figure 4.18.

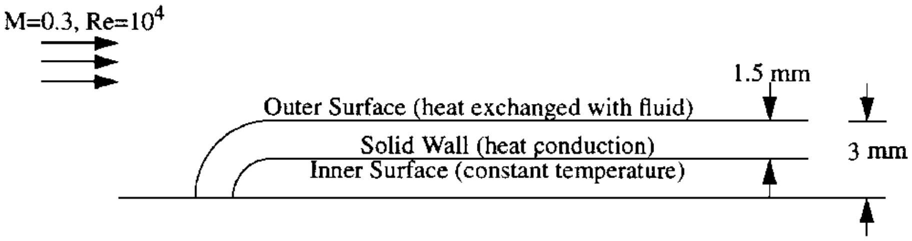

Figure 4.18: Schematic representation of the test case set-up (Kao and Liou, 1997)

The boundary conditions, computational domains and validation data used for the simulations can be found from Appendix A.5.

As indicated in the introduction of this chapter, both the Ansys Fluent(Fluid)-Ansys Fluent(Solid) and Ansys Fluent(Fluid)-SC03(Solid) coupling methods are tested. Three fluid and solid meshes were constructed for use in the Ansys Fluent solver. The most important mesh characteristics for these six meshes are given below in Table 4.6 and Table 4.7.

Table 4.6: Summary of the fluid mesh characteristics for the semi-infinite flat plate test case for use in Ansys Fluent

Variable	**Fluid Mesh 1**	**Fluid Mesh 2**	**Fluid Mesh 3**
Mesh generator	Centaur	Centaur	Centaur
Meshing strategy	Hybrid	Hybrid	Hybrid
Mesh size [-]	624,466	535,686	542,013
Prism layers [-]	30	25	25
Worst ortho. quality [-]	0.141	0.170	0.237
No. unacc. cells, Ansys [-]	0	0	0
No. unacc. cells, RRD [-]	0	0	0
No. bad cells, Ansys [-]	0	0	0
Worst equi. skew [-]	0.950	0.989	0.950
No. unacc. cells [-]	0	3	0
No. bad cells [-]	0	4	0
Aspect ratio [-]	1,643	292	36
y^+ value range [-]	0-1.48	0-7.74	0-74.0
Surface cell l_{edge} $[mm]$	5	5	5

Table 4.7: Summary of the solid mesh characteristics for the semi-infinite flat plate test case for use in Ansys Fluent

Variable	**Solid Mesh 1**	**Solid Mesh 2**	**Solid Mesh 3**
Mesh generator	Centaur	Centaur	Centaur
Meshing strategy	Tetrahedral	Tetrahedral	Tetrahedral
Mesh size [-]	53,457	6,622	897
Worst ortho. quality [-]	0.136	0.247	0.267
No. unacc. cells, Ansys [-]	0	0	0
No. unacc. cells, RRD [-]	0	0	0
No. bad cells, Ansys [-]	1	0	0
Worst equi. skew [-]	0.999	0.949	0.947
No. unacc. cells [-]	4	0	0
No. bad cells [-]	9	0	0
Aspect ratio [-]	27	18	18
Surface cell l_{edge} $[mm]$	6.25	12.5	50

Because the mesh generation for the SC03 solver is performed internally the quality characteristics of these meshes cannot be checked. The information obtained for the three constructed SC03 meshes is shown below in Table 4.8.

Table 4.8: Summary of the solid mesh characteristics for the semi-infinite flat plate test case for use in SC03

Variable	**Solid Mesh 4**	**Solid Mesh 5**	**Solid Mesh 6**
Mesh generator	SC03	SC03	SC03
Meshing strategy	Tetrahedral	Tetrahedral	Tetrahedral
Mesh size [-]	16,753	1,734	184
Surface cell l_{edge} $[mm]$	6.25	25	50

As can be seen from Table 4.6, Table 4.7 and Table 4.8 three different meshes are created from a fine to coarse y^+ value for the fluid meshes, and fine to coarse mesh density for the solid meshes. All possible combinations of fluid and solid meshes are evaluated.

Again here it can be seen from the tables that by coarsening the mesh, and especially increasing the initial layer thickness, an improvement in mesh quality is obtained at the cost of the y^+ value.

A first observation made while analysing the results for this test case is that the fluid mesh determines the accuracy of the solution. In Figure 4.19 it can be seen that changing the solid mesh from fine to coarse does not have any effect on the local Nusselt number distribution along the plate in the case of the Ansys Fluent-SC03 coupling (lines on top of each other). Changing the fluid mesh from fine to coarse does have an effect on the local Nusselt number distribution along the plate. The fine fluid mesh shows an error of 1% while the coarse fluid mesh shows an error of 10% at the end of the plate. The error for the coarse fluid mesh also develops over the distance of the plate which could imply that the (temperature) boundary layer development is not modelled correctly due to the large y^+ value. The same observations were made for the Ansys Fluent-Ansys Fluent coupling.

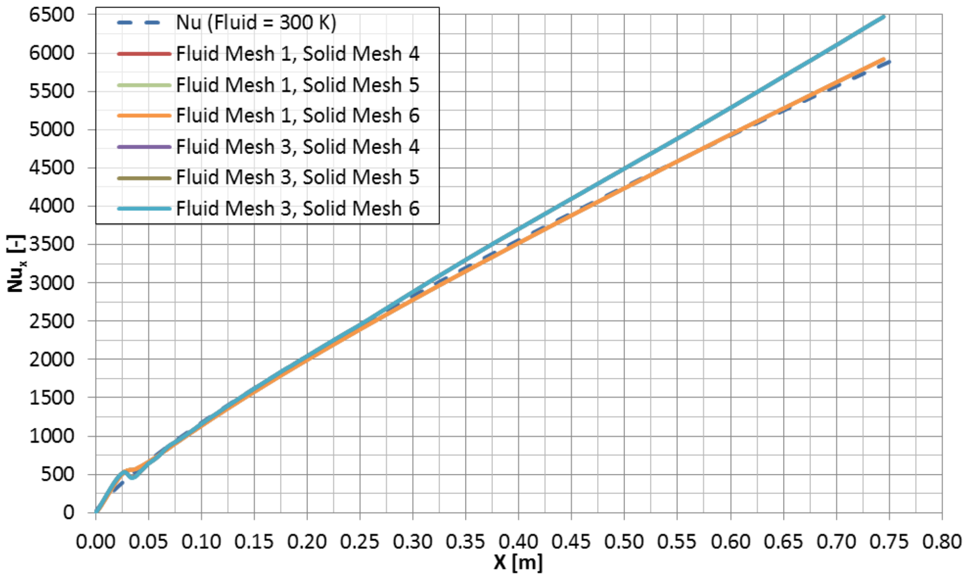

Figure 4.19: Comparison of Nusselt number distribution using different fluid and solid meshes for the Ansys Fluent-SC03 aero-thermal coupling

Figure 4.20 and Figure 4.21 show the local Nusselt number distribution along the plate for the Ansys Fluent-Ansys Fluent and Ansys Fluent-SC03 aero-thermal coupling, respectively. Due to the independency of the Nusselt number distribution on the solid mesh only the fine solid meshes are included in the plots.

As can be seen from the figures for one of the cases the fluid temperature was increased from $300\ K$ to $500\ K$ and for another case the solid temperature was increased from $280\ K$ to $500\ K$.

The increase in fluid temperature directly translates in a change in Prandtl and Reynolds number (equation (4.2)) and according to equation (4.1) a change in the empirical Nusselt number. Comparison of the empirical and simulated Nusselt number shows a fairly good comparison with an error of about 7%.

The increase in solid temperature does not translate in a change in empirical Nusselt number. As one can see the calculated Nusselt number shows an error of about 23% with the empirical Nusselt number based on a fluid temperature of $300\ K$.

While the solid temperature is so much higher than the fluid temperature the air is heated considerably close to the plate's surface. This changes the HTC between fluid and solid which is normally incorporated in the definition of the Nusselt number (simulated value, equation (4.3)), but unfortunately is not incorporated in the empirical relation for the Nusselt number, see equation (4.1), causing the large error.

These two cases with elevated temperatures were included in the evaluation of this test case to get a better understanding and feeling for the coupled heat transfer process.

$$Nu_{tur} = 0.0296\sqrt[3]{Pr}Re_x^{4/5} \tag{4.1}$$

$$Pr = \frac{C_p\mu}{k} \qquad Re = \frac{\rho u l}{\mu} \tag{4.2}$$

$$Nu = \frac{hD}{k} \tag{4.3}$$

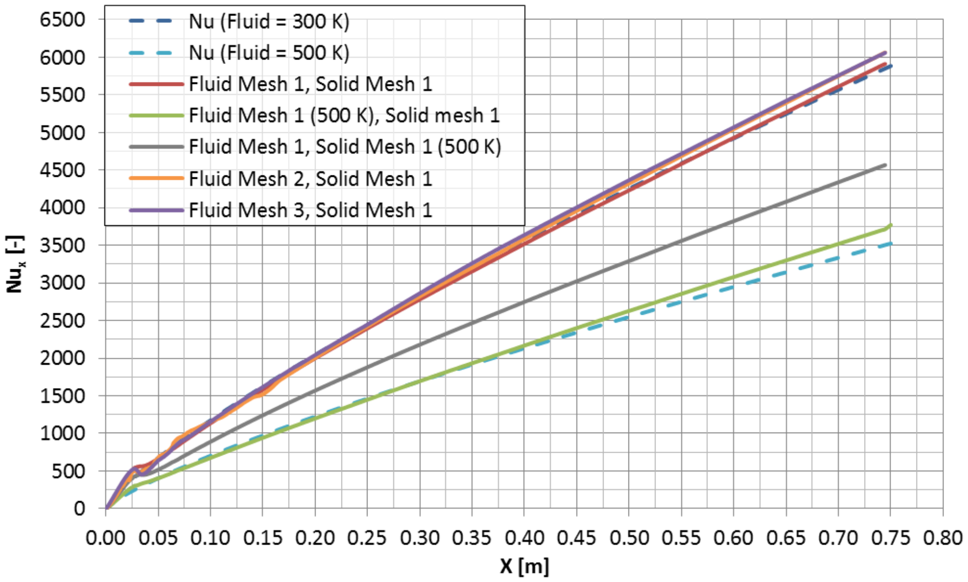

Figure 4.20: Local Nusselt number distribution along the flat plate for the Ansys Fluent-Ansys Fluent aero-thermal coupling

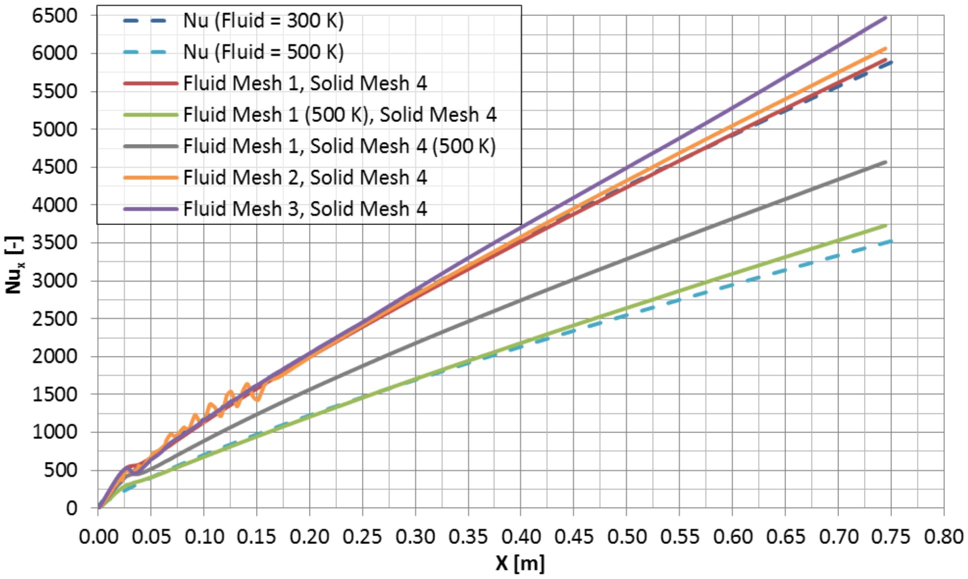

Figure 4.21: Local Nusselt number distribution along the flat plate for the Ansys Fluent-SC03 aero-thermal coupling

Finally, comparing the two coupling methods it can be observed that the coarse fluid mesh for the Ansys Fluent-SC03 coupling method (8%) is considerably more off than the coarse fluid mesh for the Ansys Fluent-Ansys Fluent coupling method (3%). It is not caused by the differences in solid mesh because solid meshes 4, 5 and 6 gave the same result in combination with fluid mesh 3. It can therefore only be caused by the solving algorithm of the SC03 solver or the communication of boundary conditions between fluid and solid meshes by the SC89 plug-in.

The results for the other combinations of meshes and boundary conditions are identical between both coupling methods.

4.6 Convergent-Divergent Nozzle

The convergent-divergent nozzle test case is based on the experimental results by Back, Massier and Gier (1964) and the coupled CFD/FE simulation results by Liu, Luke and Cinnella (2005).

The temperature at the coupling interface between fluid and structure is determined by making use of thermocouples in the experiments described in the paper by Back, Massier and Gier (1964). The results are used to validate a newly developed coupling technique in the paper by Liu, Luke and Cinnella (2005). Also in this test case the influence of the mesh density at the coupling interface between fluid and structure is investigated. The results for both the Ansys Fluent solver and SC03 solver are compared with each other.

A schematic representation of the nozzle geometry can be seen below in Figure 4.22.

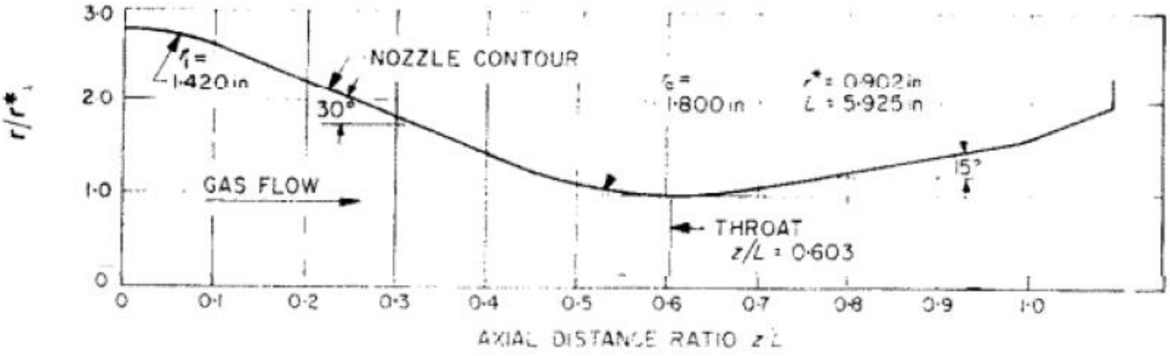

Figure 4.22: Schematic representation of the nozzle geometry (Back, Massier and Gier, 1964)

The boundary conditions, computational domains and validation data used for the simulations can be found from Appendix A.6.

The most important mesh characteristics for the three constructed fluid and solid meshes for the Ansys Fluent-Ansys Fluent coupling can be found below in Table 4.9 and Table 4.10.

As explained in section 3.2.2, later in the research project was found out that SC03 is not available on the Rolls-Royce calculation clusters. Therefore for this last aero-thermal validation test case more attention was paid on the Ansys Fluent-Ansys Fluent coupling. Only one solid mesh was tested for the Ansys Fluent-SC03 coupling. The characteristics of this mesh are summarised in Table 4.11 below.

Table 4.9: Summary of the fluid mesh characteristics for the conv-div nozzle test case for use in Ansys Fluent

Variable	**Fld Mesh 1**	**Fld Mesh 2**	**Fld Mesh 3**	**Fld Mesh 4**	**Fld Mesh 5**
Mesh generator	Centaur	Centaur	Centaur	Centaur	Centaur
Meshing strategy	Hybrid	Hybrid	Hybrid	Hybrid	Hybrid
Mesh size [-]	1,168,964	2,304,498	1,106,251	1,039,787	668,770
Prism layers [-]	40	36	36	33	30
Worst ortho. quality [-]	3.07e-4	0.001	0.002	0.003	0.012
No. unacc. cells, Ansys [-]	170	0	0	0	0
No. unacc. cells, RRD [-]	10,240	1,135	1,088	198	0
No. bad cells, Ansys [-]	54,270	28,035	26,737	16,179	10,249
Worst equi. skew [-]	0.950	0.950	0.950	0.950	0.950
No. unacc. cells [-]	0	0	0	0	0
No. bad cells [-]	0	0	0	0	0
Aspect ratio [-]	161,113	31,733	33,027	16,938	6,836
y^+ value range [-]	0-0.06	0-0.27	0-0.28	0-0.57	0-0.75
Surface cell l_{edge} $[mm]$	5	2.5	5	5	5

Table 4.10: Summary of the solid mesh characteristics for the conv-div nozzle test case for use in Ansys Fluent

Variable	**Solid Mesh 1**	**Solid Mesh 2**	**Solid Mesh 3**
Mesh generator	Centaur	Centaur	Centaur
Meshing strategy	Tetrahedral	Tetrahedral	Tetrahedral
Mesh size [-]	322,635	19,474	14,732
Worst ortho. quality [-]	0.124	0.123	0.235
No. unacc. cells, Ansys [-]	0	0	0
No. unacc. cells, RRD [-]	0	0	0
No. bad cells, Ansys [-]	5	1	0
Worst equi. skew [-]	0.996	0.970	0.950
No. unacc. cells [-]	6	0	0
No. bad cells [-]	46	9	0
Aspect ratio [-]	39	37	23
Surface cell l_{edge} $[mm]$	5	10	25

Table 4.11: Summary of the solid mesh characteristics for the conv-div nozzle test case for use in SC03

Variable	**Solid Mesh 4**
Mesh generator	SC03
Meshing strategy	Tetrahedral
Mesh size [-]	21,660
Surface cell l_{edge} $[mm]$	4

From Table 4.9 can be seen that just like for the semi-infinite flat plate test case the meshes range from a fine to a coarse y^+ value range. As seen also for other test cases a smaller y^+ value results in a worse orthogonal quality and aspect ratio. Next to the influence of the y^+ value on the accuracy of the solution, also the surface cell edge length size is investigated by refining the surface size of the cells from mesh 3 which resulted in mesh 2.

By changing the surface cells edge length size for the solid meshes three solid meshes with changing mesh density were created for use in the Ansys Fluent solver. One solid mesh was created for use in the SC03 solver which has a smaller surface cell edge length size compared to the Centaur meshes.

Similar as for the semi-infinite flat plate test case, a comparison of different combinations of fluid and solid meshes is shown in Figure 4.23 (Coupled (316) represents the simulation results by Liu, Luke and Cinnella (2005)). Also here the fluid mesh determines the accuracy of the solution. Changing the solid mesh from fine to coarse only has minor effects. It can be seen that the coarser fluid mesh 5 shows worse results than the fluid mesh 3 compared to the validation data.

The nozzle coordinates are the coordinates extracted from Figure 4.22 to construct the nozzle geometry. The scaling on the vertical axis on the right is the nozzle radius normalised by the throat radius. This ratio should be 1.0 in the throat of the nozzle but as can be seen from Figure 4.23 the ratio is slightly smaller than 1.0. This is caused by the fact that the extraction of the nozzle coordinates from Figure 4.22 was hard.

Also, comparing the locations of maximum temperature of the simulation results with the validation data, it is observed that the simulation results are offset slightly to the right. From the nozzle coordinate plot it can be seen that the location of the throat coincides with the maximum temperature location of the simulations. Therefore the offset to the right of the simulation results is most probably caused by an offset in geometry. Also offsets in temperatures in the throat area could be caused by the smaller throat radius.

Due to time constrains, these problems were not solved which resulted in a geometry (fluid computational domain) that is slightly different from the experiments and thus validation data.

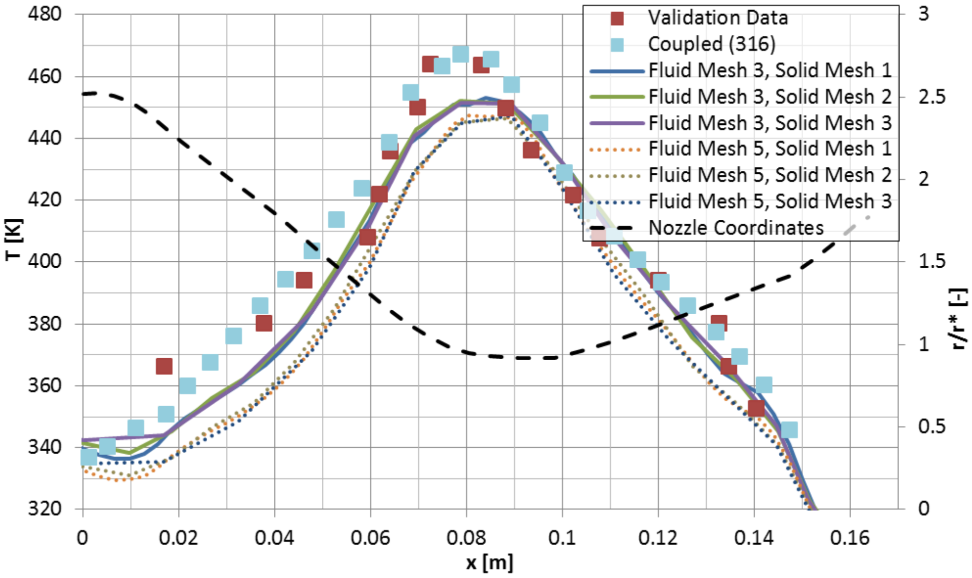

Figure 4.23: Comparison of temperature distribution using different fluid and solid meshes for the Ansys Fluent-Ansys Fluent aero-thermal coupling

Figure 4.24 shows the temperature distribution at the interface between fluid and solid domain for the Ansys Fluent-Ansys Fluent coupling. The data is extracted from the 90° intersection plane shown in Figure A.12. Fluid meshes 1 to 5, from fine to coarse are plotted in combination with solid mesh 2. It can be seen that just like for the semi-infinite flat plate a finer y^+ value gives a better agreement with the validation data. The error in maximum temperature prediction, compared to the validation data in the throat area of the nozzle, is 2% for fluid mesh 1 and 4% for fluid mesh 5. The offset to the right of the simulation results compared to the validation data can be seen in this figure.

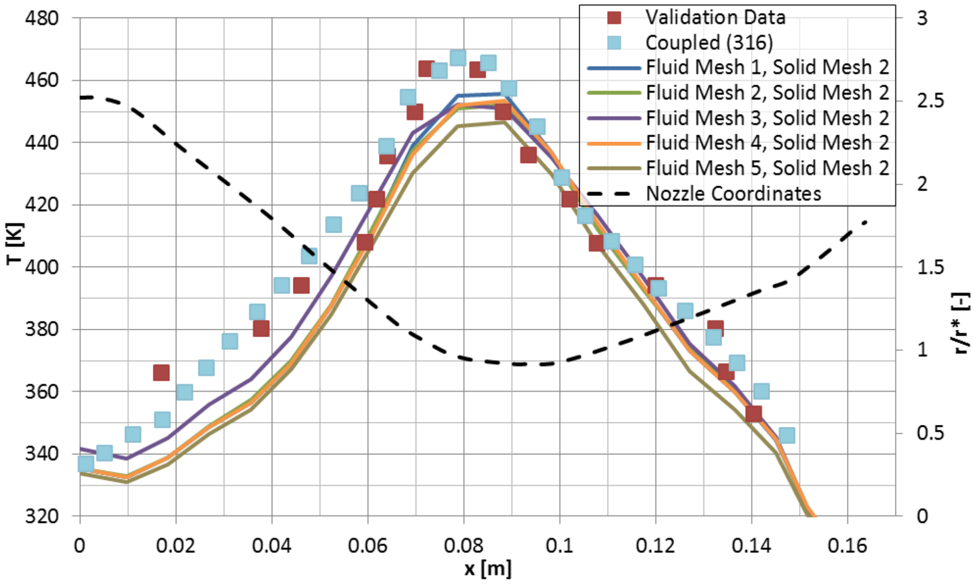

Figure 4.24: Temperature distribution along the conv-div nozzle for the Ansys Fluent-Ansys Fluent aero-thermal coupling

Figure 4.25 shows the temperature distribution for the Ansys Fluent-SC03 coupling. Fluid mesh 4 and 5 give similar results as for the Ansys Fluent-Ansys Fluent coupling, but the results for fluid mesh 3 are considerably better. The error in maximum temperature prediction for fluid mesh 3 is 1%. The offset to the right of the simulation results can also in this figure be seen.

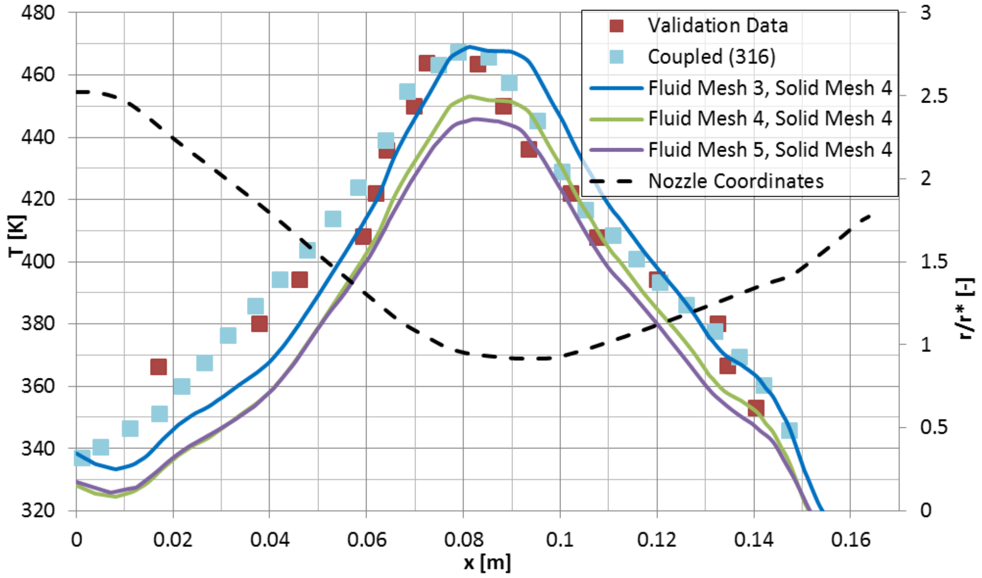

Figure 4.25: Temperature distribution along the conv-div nozzle for the Ansys Fluent-SC03 aero-thermal coupling

Figure 4.26 shows the HTC distribution at the interface between the fluid and solid domain for the Ansys Fluent-Ansys Fluent coupling. Just like for the temperature distribution, fluid mesh 1 gives the most accurate solution and only differs from the reference calculated validation data in the throat area. The error in maximum HTC prediction is however 20% compared to the experimental validation data for fluid mesh 1 and 30% for fluid mesh 5. A higher mesh density or a better modelling of the geometry in the throat area could possibly give more accurate results.

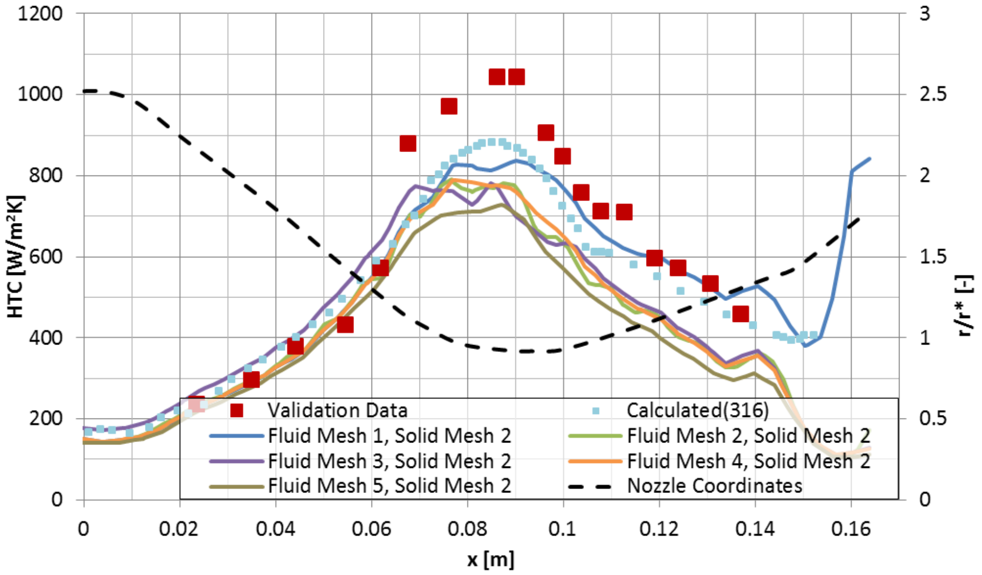

Figure 4.26: HTC distribution along the conv-div nozzle for the Ansys Fluent-Ansys Fluent aero-thermal coupling

4.7 Conclusions

The aim of this chapter was to validate the Ansys Fluent solver capabilities and Ansys Fluent and SC03 coupling capabilities by evaluating representative test cases. The conclusions of this validation study are given in this section. The conclusions presented in this section are used when possible during the case set-up for the determination of the TRU flow topology and TRU temperature prediction described in Chapter 5 and Chapter 6 respectively.

From the above results the SST k-ω model is the preferred model to use for the TRU simulations as expected from the literature. Skin friction coefficients, pressure coefficients and velocity profiles especially in areas with separated, mixing or vortical flows were modelled in general more accurately than for the Spalart-Allmaras and Realizable k-ε turbulence models. The mismatch in reattachment point location for the backward-facing step should however be kept in mind.

In general maximum errors with the validation data for the SST k-ω model vary from about 8% (JICF, C_p) to 25% (Backward-facing step, $C_f = 0$ location). The Spalart-Allmaras and Realizable k-ε models show similar results but can differ from the SST k-ω model considerably with errors of up to 30-40% in skin friction and pressure coefficient prediction. The use of the CC improves the accuracy of the simulation results for all three turbulence models.

The errors of the turbulence models with the validation data found in this chapter should be kept in mind during the evaluation of the TRU simulation results in the upcoming chapters.

Structured meshes are shown to be numerically less dissipative than hybrid meshes especially in areas where the variations in velocity directions are high like mixing and vortical flows (Plane mixing layer and curved channel flow). This observation confirms the information found from the literature described in section 3.1.4. If possible structured mesh blocks should be used in these areas.

During mesh generation a compromise should be found between the accuracy of the solution (y^+ value) and the mesh quality (convergence of solution, see section 3.1.5). Especially for the aero-thermal test cases was shown that a smaller y^+ value resulted in more accurate results.

As seen from for instance the JICF and aero-thermal test cases, the fluid mesh density can be of influence on the accuracy of the solution or modelling of particular flow phenomena. A surface size edge length of 5 mm is used for the aero-thermal test cases. This will probably be to fine for the TRU simulations and will cause the mesh to become too large. Therefore a surface size edge length of 10 mm is started with. If time permits smaller surface sizes should be tested.

As seen from the aero-thermal test cases, the mesh density of the solid mesh has no large influence on the accuracy of the solution. Therefore in this master thesis project no mesh refinement study is planned for the solid mesh. A surface size edge length of 25 mm was selected for the solid mesh.

Chapter 5 Determination of TRU Flow Topology

Now the solving capabilities of the Ansys Fluent (14.0) software package (Ansys Inc., 2011a) are validated and a solving strategy is determined, the flow topology of the TRU can be determined. First, the TRU geometry is shown and explained in section 5.1. The mesh features and case set-up are described in sections 5.2 and 5.3. The results of the simulations are compared with experimental data. How these experimental data are acquired is described in section 5.4. The modelled flow physics are shown in section 5.5. Finally, the results of the simulations and conclusions and recommendations of this chapter are given in sections 5.6 and 5.7.

5.1 Geometry

As can be seen for instance from Figure 1.1, Figure 1.4 and Figure 2.5, the target-type thrust reverser consists out of two doors and is therefore symmetric in the centre-plane of the engine. Because of this symmetry a 180° model of the thrust reverser is considered during this project which saves a lot of cells during meshing and therefore computational resources and time. Figure 5.1 shows the far-field geometry of the computational domain. Later in the thesis project was found out that the mixer is not symmetric in the 180° symmetry plane which is discussed in section 5.5.

The far-field inlet and outlet are respectively located 10 and 18.3 door lengths upstream and downstream of the TRU geometry. The far-field half-cylinder has a radius of 12.5 door lengths. The half cylinder placed in front of the TRU geometry, which connects the TRU geometry with the far-field inlet, is called the nacelle-extension. The far-field dimensions were specified by Rolls-Royce and have proven to be sufficiently far away from the TRU geometry to avoid solution interference.

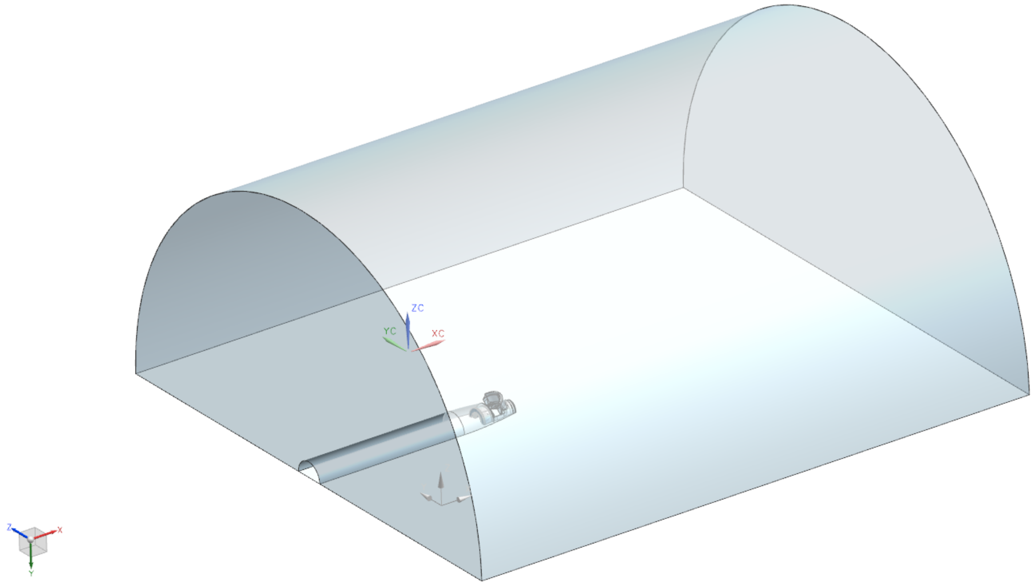

Figure 5.1: Geometry of the 180° TRU model computational domain

To understand the nomenclature used for the different surfaces of the TRU geometry throughout the remainder of this report Figure 5.2 and Table 5.1 can be used. Note also the small void under the door which serves as a flow leakage channel to alleviate the forces on the door-actuator.

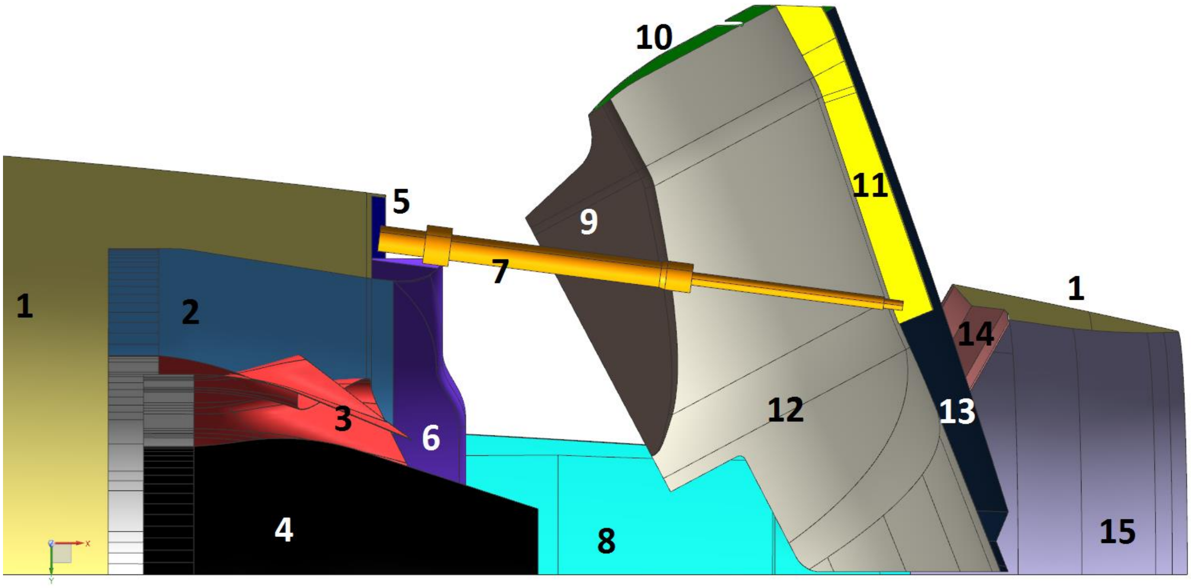

Figure 5.2: 90° sliced model of the deployed TRU with coloured surfaces

Table 5.1: Legend to Figure 5.2

No.: Colour	Surface name	No.: Colour	Surface name
1: Yellow, Lemon	Outer-nacelle	9: Brown	Door-side-flange
2: Blue, Light Sky	Bypass-duct	10: Green	Kicker-plate
3: Red, Crimson	Mixer	11: Yellow	Door-actuator-void
4: Black	Bullet	12: Grey	Door-inner-surface
5: Blue, Dark Sky	Nacelle-fan-ramp con.*	13: Blue-Midnight	Door-outer-surface
6: Purple	Fan-ramp	14: Red, Salmon	Door-fitting
7: Orange	Door-actuator	15: Purple, Lavender	Nozzle
8: Cyan	Inner-nacelle	*connection	

The TRU geometry is a complex geometry with many thin edges, sharp corners and small voids, which makes the mesh generation difficult. Simplifying and modifying the geometry in such a way that the mesh generation becomes easier without changing the flow physics too much, is therefore desirable. Due to the lack of resources at the time of this project this could not be done by a specialist. Therefore the author of this report did his best to make some simplifications to the geometry himself.

The original geometry can be seen below in Figure 5.3. The door-actuator, door-actuator-void and the two voids between fan-ramp and inner-nacelle can be recognised from the figure. The door-actuator is removed from the geometry. The door-actuator and fan-ramp-nacelle voids are both closed to simplify the geometry. The gap in the kicker-plate on the top of the door is thereby also closed.

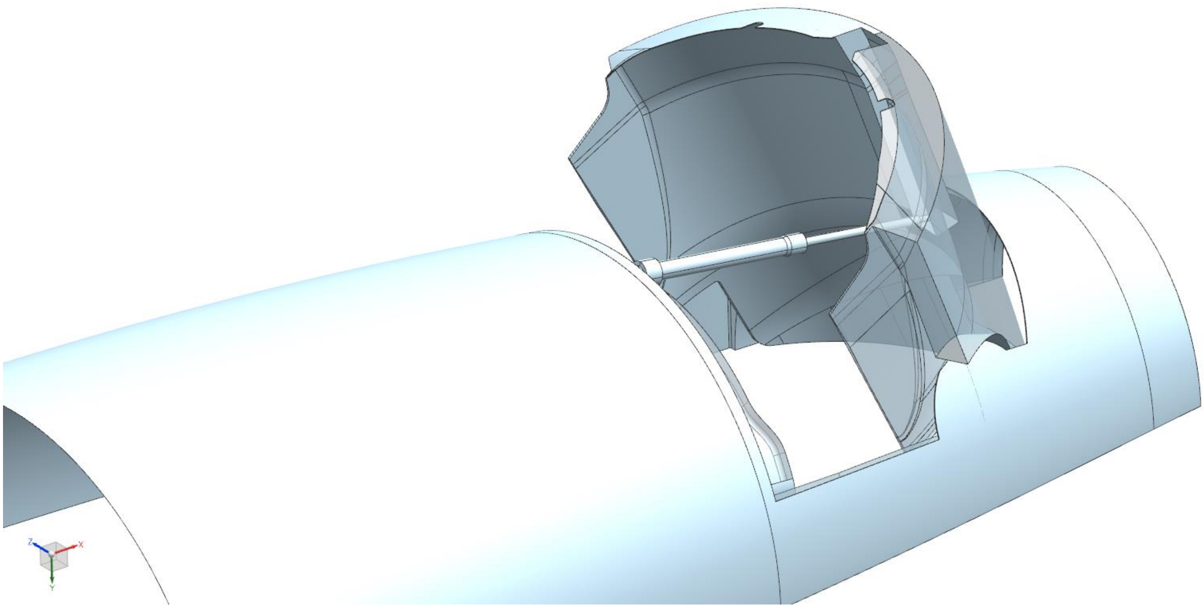

Figure 5.3: Original 180° model of the deployed TRU

5.2 Mesh

For the simulations performed in this chapter three different meshes are used. Goal during the mesh generation is to create a mesh, which is able to model the flow physics accurately compared to the experimental data and has an acceptable level of mesh quality according to the criteria described in sections 3.1.3 and 3.1.4.

As found from the test cases it would be desirable to use structured mesh blocks in areas with mixing and vortical flows. During mesh generation, problems were encountered when structured mesh blocks were inserted in the computational domain. Because of this, structured mesh blocks were not used.

Two of the three meshes used in this chapter are created by the author of this report by making use of the Centaur hybrid mesh generator (CentaurSoft, 2012). The third mesh was created by Gero Schieffer of RRD and is used due to the fact that it is a semi-structured mesh.

With semi-structured is meant that the mesh consists out of octahedral volumes and a body-fitted prism layer. This results for the largest part of the computational domain in a structured mesh. At the intersection of prism layer and structured mesh, the mesh needs to be connected and is not structured. The mesh is created in the Boxer mesh generator (Cambridge Flow Solutions Ltd., 2014).

The main differences between the meshes created by the two mesh generators are,

- Centaur creates a hybrid mesh while Boxer creates a semi-structured mesh.
- The Boxer mesh has a larger y^+ value and 10 prism layers which causes a less accurate boundary layer modelling but a better mesh quality.

- The Centaur mesh has a smaller y^+ value and 25 prism layers which causes a more accurate boundary layer modelling but a worse mesh quality.
- The trade-off between accuracy and mesh quality discussed in the previous chapter can be recognised from the different meshing approaches.

Which of the two meshing strategies produces a better simulation result in terms of convergence levels and accuracy of the solution is evaluated in section 5.6. Although structured mesh blocks could not be inserted in the Centaur meshes, the performance of a structured mesh can now still be investigated by including mesh 3.

Difficulties were experienced as expected during the mesh generation. Either the mesh generation crashed or the CFD simulation diverged on the first constructed meshes. This was caused by bad mesh quality, small volume cells or a too large jump in cell volumes. As described in section 4.7 the SST k-ω turbulence model is the preferred model. During the iterative process of constructing a mesh and performing a CFD simulation both the SST k-ω and Spalart-Allmaras models did not give any solution. Due to time constraints and previous bad experiences of RRD with these two turbulence models it was not further investigated why these models did not give any solution.

Finally, two meshes resulted from this mesh study. The Realizable k-ε turbulence model is, due to the above described circumstances, used as default turbulence model. Mesh 2 is equal to Mesh 1 with the reversed flow jet and nozzle area refined.

Table 5.2 summarises the main characteristics of the meshes used in this research project. The reference mesh created by the Centaur mesh generator and used before by RRD is included in the table to point out the improvements in mesh quality for the meshes used in this master thesis project.

Table 5.2: Summary of reference and used mesh characteristics

Variable	**Reference Mesh**	**Mesh 1**	**Mesh 2**	**Mesh 3**
Mesh generator	Centaur	Centaur	Centaur	Boxer
Mesh size [-]	37,932,522	47,305,209	50,498,680	32,271,465
Prism layers [-]	30	25	25	10
Worst ortho. quality [-]	0.00019	0.00077	0.00057	0.00774
No. unacc. cells, Ansys [-]	n.a.	1	1	0
No. unacc. cells, RRD [-]	55,305	1,379	1,361	1
No. bad cells, Ansys [-]	n.a.	440,939	440,125	12,720
Worst equi. skew [-]	1.00000	1.00000	1.00000	0.99987
No. unacc. cells [-]	29,588	5,481	3,147	1,370
No. bad cells [-]	n.a.	87,909	94,542	11,966
Aspect ratio [-]	197,166	10,729	10,729	665
AVG y^+ door-inner [-]	n.a.	0.48	0.47	12.2

From Table 5.2 one can again clearly see the compromises needed to create a mesh which has an acceptable quality, a sufficiently small y^+ value and a sufficient number of prism layers to accurately model the boundary layer.

Several approaches were used to improve the mesh quality compared to the reference mesh. The following methods were used to establish a better mesh quality,

- The surface size for all thin edges, i.e. the edges of the door-side-flanges and nozzle, is controlled in such a way that these surfaces contain at least 2-3 cells over its width.
- The stretching of the prism layer is reduced at these thin edges to improve the equivolume skewness of the first tetrahedral cells connected to the prism layer. See Figure 5.4, top left.
- At the convex corners of these thin edges the convex area treatment function of Centaur was enabled which places an extra cell between the two corner prism cells to improve the orthogonal quality at these convex corners. See Figure 5.4, top right.
- For all other surfaces, the surface size and prism layer stretching is controlled in such a way that the first tetrahedral cell connected to the last prism layer cell is of equal size as the prism layer cell. In this way the equivolume skewness quality criteria is satisfied for the first tetrahedral cells connected to the prism layer normally giving the bad quality cells. See Figure 5.4, middle left.
- If the surface size, prism layer stretching or convex area treatment measures described above do not work, manually applied volume sources need to be specified around these edges. These sources do not specify a uniform surface size but specify the surface size variation from small to large around an edge and control the stretching of the prism layer. See Figure 5.4, middle right. From this figure the reduced prism layer stretching in these difficult corners and edges can be recognized.
- In voids, i.e. between the door-outer-surface and door-fitting, the surface size and stretching of the prims layer is reduced as much as possible such that the prism layers on both sides of the void do not interfere with each other. See Figure 5.4, bottom left.
- Chopping of the prism layer is almost everywhere disabled and instead the prism layer stretching is reduced in these areas. Chopping of the prism layer was observed to have a negative effect on the equivolume skewness.
- The y^+ value of the mesh is kept constant over all surfaces to avoid jumps in first prism layer thicknesses which cause bad orthogonal quality cells. Only the y^+ value on the nacelle-extension is increased to save cells.
- To ensure a better equivolume skewness, make sure the mesh generator does not crash or apply a mesh refinement, the tetrahedral size needs to be controlled with a volume source. See Figure 5.4, bottom right.
- In the areas of interest, inside the TRU geometry, large jumps in cell volumes were avoided by controlling the cell sizes and thereby controlling the cell aspect ratios. See Figure 5.4, bottom right.
- The overall surface and tetrahedral edge length sizes are taken from the conclusions from the validation test cases and set to 10 mm, see section 4.7.
- Due to the mesh size in combination with the computational resources available and limited time of this research project not all mesh features investigated in Chapter 4 could be

incorporated. As explained before, because of these reasons also no solutions were found for the Spalart-Allmaras and SST k-ω turbulence models.

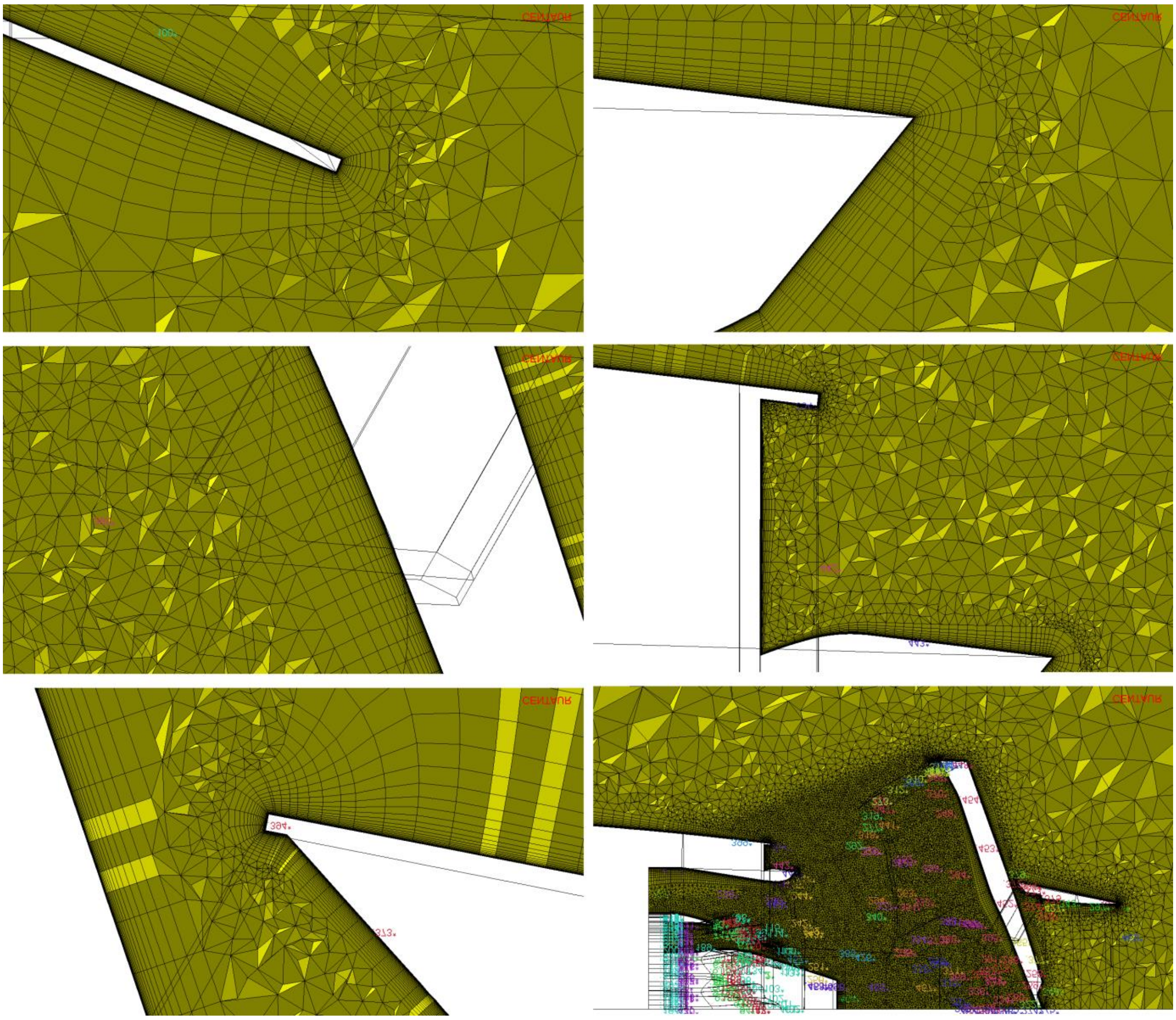

Figure 5.4: Screenshots of specific meshing applications. Top left: Reduced stretching at edges. Top right: Convex area treatment. Middle left: Surface size-prism layer stretching. Middle right: Variable surface size and prism layer stretching. Bottom left: Meshing in voids. Bottom right: Tetrahedral refinement

The marked unacceptable orthogonal quality (RRD standards) and equivolume skewness cells can be seen below in Figure 5.5.

It can be seen that a large part of the unacceptable quality cells for mesh 1 and 2 are located at the nacelle-fan-ramp-connection. The mesh at this location can be seen in the middle right of Figure 5.4. Because of the sharp concave corner between fan-ramp and nacelle-fan-ramp-connection the orthogonal quality became unacceptable. By reducing the stretching of the prism layer the orthogonal quality of these cells was improved but the solution diverged, probably because of the very small volumes of the prism layer cells. A compromise was found which solved the solution divergence problems but unfortunately reduced the orthogonal quality of the cells as can be seen in Figure 5.5.

For both meshes can be seen that the area between inner-nacelle and door-outer-surface give the most unacceptable quality cells. In these problem areas, the prism layer has to be squeezed into voids and fitted to sharp corners, which cause both unacceptable orthogonal quality and equivolume skewness cells. Closing the voids would change the flow physics considerably. A better idea in these areas is to apply fillets at sharp corners and investigate the reduction of the number of prism layers or chopping of these layers. Due to the lack of design support resources and time these options could not be investigated during this research project.

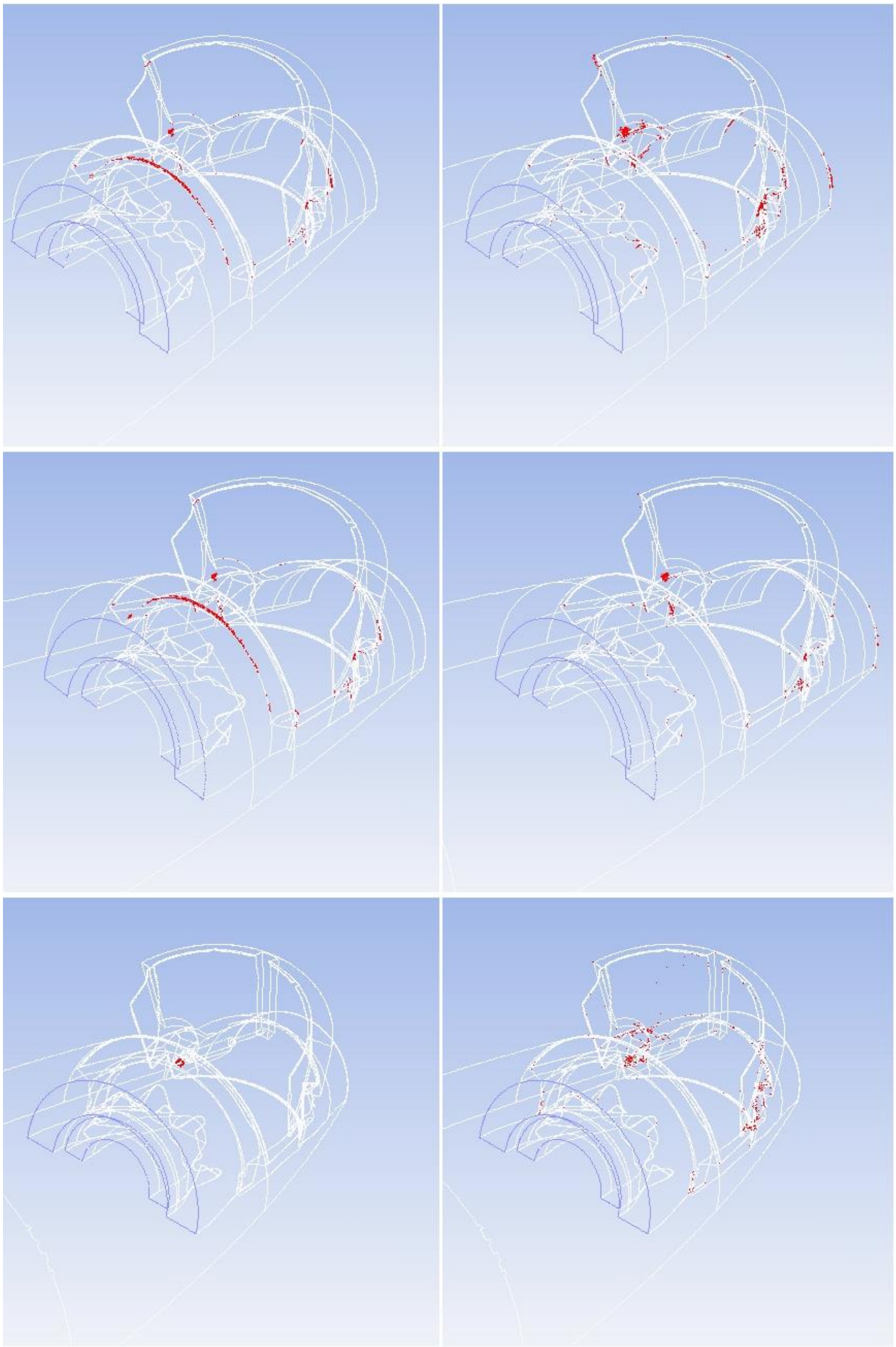

Figure 5.5: Screenshots of the marked unacceptable orthogonal quality (left) and equivolume skewness cells (right) for mesh 1 (top), mesh 2 (middle) and mesh 3 (bottom)

As a comparison the far-field mesh and mesh around the TRU geometry for meshes 1 to 3 can be seen below in Figure 5.6. From the figures the difference between the Centaur and Boxer meshing approaches can be clearly seen. The far-field geometry for the Boxer mesh has different dimensions and as can be seen is smaller than for the two Centaur meshes. Next to this it can be seen that the only difference between meshes 1 and 2 is the addition of a tetrahedral refinement in the reversed flow jet and nozzle area.

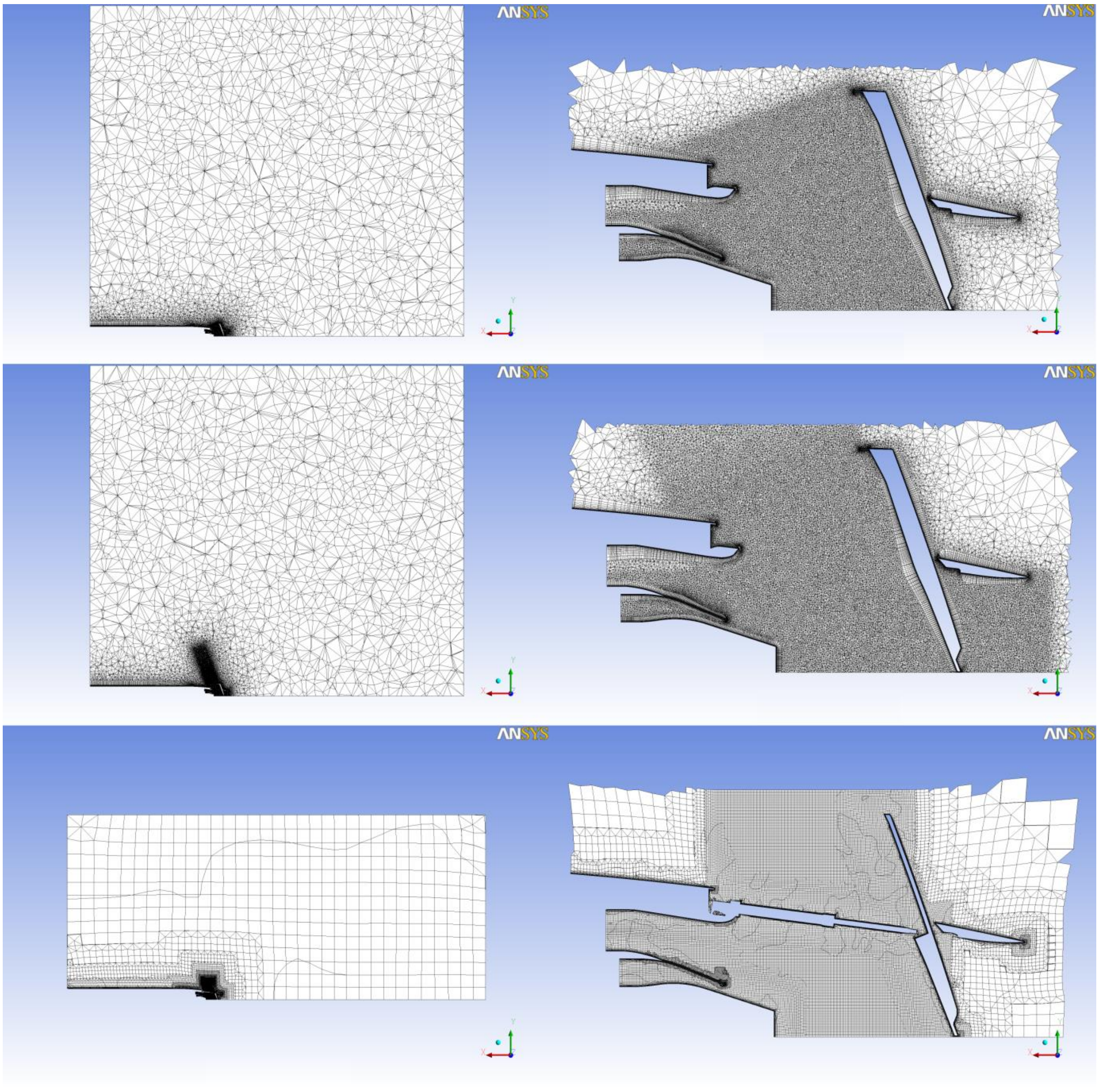

Figure 5.6: Screenshots of the far-field mesh (left) and mesh in the area of interest (right) for mesh 1 (top), mesh 2 (middle) and mesh 3 (bottom)

5.3 Case Set-up

The starting point of the coupled aero-thermal simulations is a converged CFD simulation in which according to subsection 3.1.5 the residuals, mass-flow rates and additional characteristic parameters should reach a steady-state solution.

The level of convergence of the TRU-CFD simulations in general is known to be a problem within RRD. Due to the complexity of the geometry and involved flow physics, the cause for the convergence problems is not yet determined. The results of the simulations are however used and given a larger contingency during the design process while the simulations are not fully converged.

In this first part of the research project, the possible causes for the convergence problems are investigated with the purpose to find a steady-state solution which can be used for the coupled aero-thermal simulations. Next to this, the accuracy of the solutions are checked in section 5.6 by comparing them to experimental data.

The solver settings are kept the same for all performed simulations and are summarised below in Table 5.3 and explained into more detail in Chapter 3.

Table 5.3: Summary of solver settings

Solver Setting	**Chosen Approach**
Solver Type	Density-based solver
Time	Steady
Energy-equation	On
Turbulence model	Realizable k-ε model
Near-wall treatment	Enhanced wall treatment
Density properties, ρ $[kg/m^3]$	Ideal gas
Specific heat, c_p $[J/kgK]$	RRD defined polynomial function
Thermal conductivity, k $[W/mK]$	RRD defined polynomial function
Viscosity, μ $[kg/ms]$	Sutherland's law
Linearization method	Implicit
Flux Type	Roe-FDS
Gradients	Least squares cell based
Flow accuracy	Second-order upwind
Turbulence accuracy	First-order upwind
Applied corrections	• Curvature correction • HOTR • CASM • Poor mesh numerics

The boundary condition types are summarised below in Table 5.4.

Table 5.4: Summary of boundary condition types

Surface	BC Type
Far-field inlet	Pressure-far-field
Far-field outlet	Pressure-outlet
Far-field half-cylinder	Pressure-far-field
Far-field symmetry	Symmetry
Nacelle-extension	Inviscid wall
Bypass-duct inlet	Pressure-inlet
Core inlet	Pressure-inlet
Solid surfaces	Viscous wall

Two sets of boundary conditions are used for the simulations in this report, matched to two test-runs described in the test report of the experiments (Pipkin, Long and McDonald, 2007). The Fan Nozzle Pressure Ratio (FNPR), Pressure Split (PS), Fan Nozzle Temperature Ratio (FNTR) and Temperature Split (TS) describe the non-dimensionalised boundary conditions,

$$FNPR = \frac{p_{t_{fan}}}{p_{amb}} = \frac{p_{t_7}}{p_{amb}} \tag{5.1}$$

$$PS = \frac{p_{t_{fan}}}{p_{t_{core}}} = \frac{p_{t_7}}{p_{t_8}} \tag{5.2}$$

$$FNTR = \frac{T_{amb}}{T_{t_{fan}}} = \frac{T_{amb}}{T_{t_7}} \tag{5.3}$$

$$TS = \frac{T_{t_{core}}}{T_{t_{fan}}} = \frac{T_{t_8}}{T_{t_7}} \tag{5.4}$$

The boundary conditions set for the simulations, which are based on test-runs 1 and 2, are summarised below in Table 5.5.

Table 5.5: Summary of boundary conditions

Test-run	$\boldsymbol{M_\infty}[-]$	$\boldsymbol{FNPR}[-]$	$\boldsymbol{PS}[-]$	$\boldsymbol{FNTR}[-]$	$\boldsymbol{TS}[-]$
1	0.05	1.52	1.06	1.00	2.15
2	0.05	1.32	1.05	1.00	2.16

The difference between the test-runs 1 and 2 is mainly the reduction in $FNPR$ as can be seen from Table 5.5.

To conclude this section the test-matrix including all simulations evaluated in this chapter is given in Table 5.6. From the test-matrix can be easily seen which geometry and mesh is used and which boundary conditions are applied to each case.

Table 5.6: Test-matrix of performed simulations

Simulation #	Geometry	Mesh	BC's	# of Iterations	p & T monitors
1.1	1:5 Scaled	Mesh 2	Test 1	14,800	-
1.2	1:5 Scaled	Mesh 2	Test 1	14,800-20,800	Yes
2.1	Unscaled	Mesh 1	Test 1	14,800	-
2.2	Unscaled	Mesh 1	Test 1	14,800-20,800	Yes
3.1	1:5 Scaled	Mesh 2	Test 2	19,300	-
3.2	1:5 Scaled	Mesh 2	Test 2	14,800-17,800	yes
4.1	1:5 Scaled	Mesh 3	Test 1	14,800	-
4.2	1:5 Scaled	Mesh 3	Test 1	14,800-20,800	yes

For three cases 6,000 additional iterations were performed to monitor pressure and temperature points which coincide with measurement locations on the TRU door. For simulation 3.2 only 3,000 additional iterations were performed. Due to time constraints at the end of the master thesis project the additional 6,000 iterations could not be performed in time. Why this is done is explained in section 5.6.

For the ease of the reader, the numbered simulations can also be recognised by the short descriptions listed below used later in this report,

- Simulation 1: Base simulation
- Simulation 2: Unscaled geometry simulation
- Simulation 3: Different BC´s simulation
- Simulation 4: Boxer mesh simulation

5.4 Experimental Data

The results of the simulations are compared with experimental data (Pipkin, Long and McDonald, 2007). The experiments are performed on a 1:5 scaled model of the TRU geometry. During the experiments 29 pressure taps and 30 thermocouples were installed on the surface of the door. Besides these measurements also the nozzle (reversed) thrust is measured which is used to calculate the reversed thrust coefficient in x-direction defined as,

$$C_{T_x} = \frac{H_x}{\dot{m}_7 v_{i_7} + \dot{m}_8 v_{i_8}} \tag{5.5}$$

The BPD and core effective areas ($C_D A$) are calculated and given in the test report. These effective areas can also be compared to the effective areas of the simulation results.

The experiments are performed in a dual-flow static thrust stand which is used to determine the performance of exhaust nozzles in both forward and reverse mode. The core (primary) and bypass (fan) flow exhaust nozzles are separated which makes it possible to vary the exhaust temperatures and velocities of both flows. The nozzle thrust is measured with a 3-component strain-gage force balance.

H_x in equation 5.5 is measured by this 3 component strain-gage force balance. To determine the force the flow exerts on the door for the flow simulations, the following relation is used,

$$H_x = \int_{BPD+Core} (p - p_{amb}) \cdot n_x dA + \int_{BPD+Core} \rho v_x^2 \cdot n_x dA - \int_{Solid\,Walls} (\tau \cdot n_x) dA \tag{5.6}$$

The core and bypass flows are obtained by a 500 psi, or about 3.45 MPa, dry air storage system. The core and bypass flows are both throttled and metered through a long-radius ASME nozzle, ducted to the bypass and core exhaust nozzles and finally exhausted to atmosphere. The temperature of the core flow is obtained by heating the flow upstream of the long-radius ASME nozzle (air heater) and mixing it with the cold (bypass) flow to achieve the desired flow temperature.

A schematic representation of the test facility can be seen below in Figure 5.7.

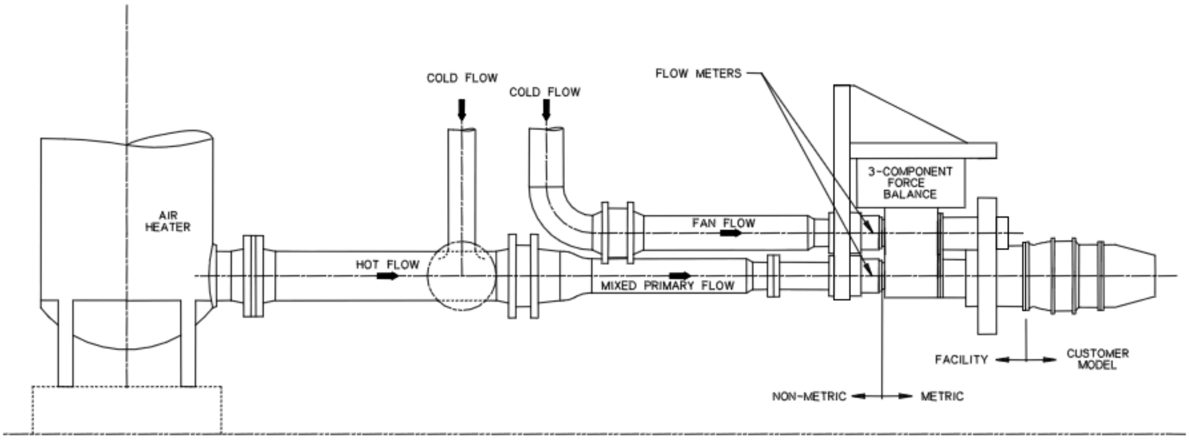

Figure 5.7: Schematic representation of test facility (Pipkin, Long and McDonald, 2007)

A schematic representation of the 1:5 scaled TRU test model, which represents the "customer model" in Figure 5.7, can be seen below in Figure 5.8.

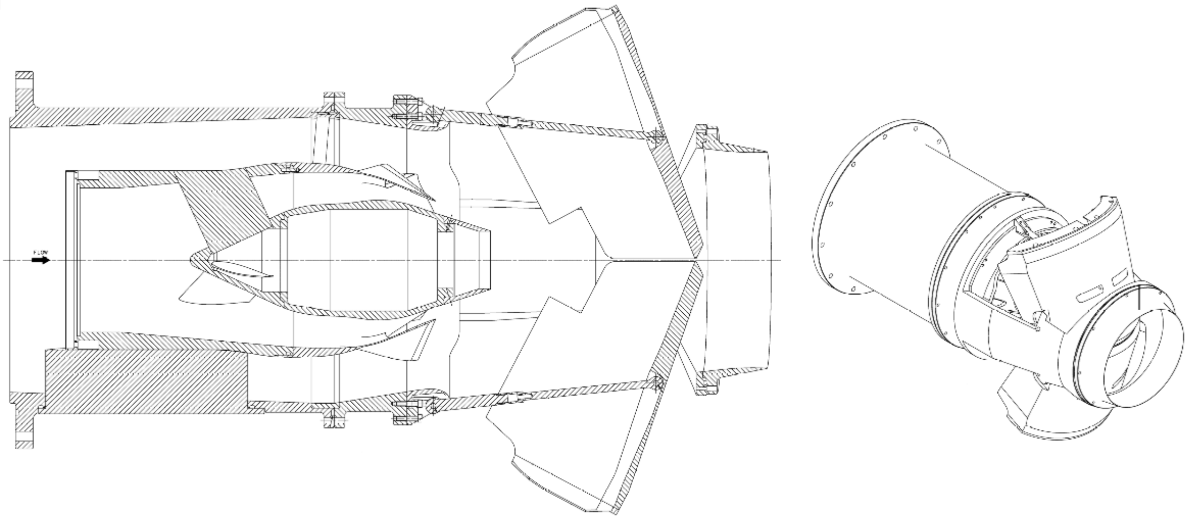

Figure 5.8: Schematic representation of the 1:5 scaled TRU test model (Pipkin, Long and McDonald, 2007)

In total three lines with respectively 15, 5 and 9 pressure taps are installed on the (upper) TRU door surface. The lines of pressure taps are distributed as follows,

- 15 pressure taps in flow direction offset from the centre of the door (P501 to P515)
- 5 pressure taps in flow direction at the centre of the door (P516 to P520)
- 9 pressure taps in cross-flow direction at the top of the door (P521 to P529)

Also three lines with respectively 15, 5 and 10 thermocouples are installed on the (lower) TRU door surface. The lines of thermocouples are distributed as follows,

- 15 thermocouples in flow direction offset from the centre of the door (T501 to T515)
- 5 thermocouples in flow direction at the centre of the door (T516 to T520)
- 10 thermocouples in cross-flow direction at the bottom of the door (T521 to T530)

Figure 5.9 shows the locations of the pressure taps and thermocouples on the door with on the left- and right-side the upper and lower door respectively. The kicker-plate and symmetry-plane of the simulations are indicated in the figure to better understand the flow direction.

The locations of the pressure taps and thermocouples on the 180° computational model are shown in Figure 5.10. For clarity the pressure taps are shown on the left side of the door while the thermocouples are shown on the right side of the door. In reality the pressure taps and thermocouples are also located on the other sides of the door to check if the pressure and temperature distributions are symmetric for the simulations.

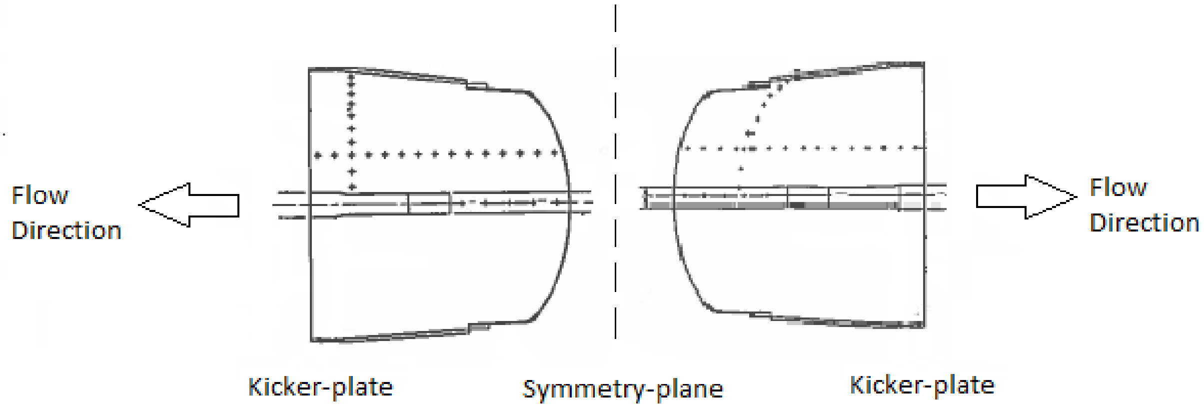

Figure 5.9: Locations of pressure taps on the upper door (left) and thermocouples on the lower door (right) (Pipkin, Long and McDonald, 2007)

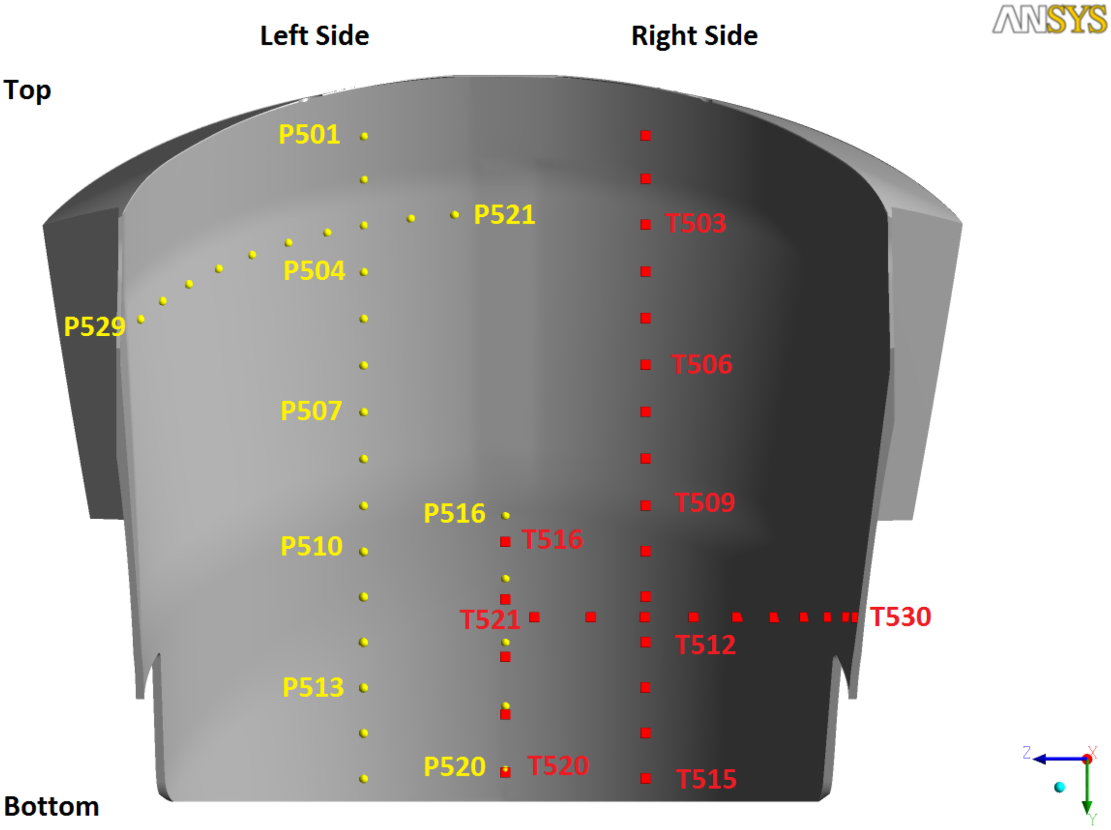

Figure 5.10: Locations of pressure taps and thermocouples on TRU 180° computational model

After analysing the test-report some remarks can be made about the performed experiments,

- From Figure 5.8 can be seen that the core and bypass-duct exhaust nozzles are supported by frames. Total pressure and temperature losses (which are measured before the frames) are not taken into account.
- The total pressure and temperature BC's of the experiments are matched with the full-scale engine model. The experiments are however performed on a 1:5 scaled model which results in different Reynolds numbers between the full-scale and scaled model. The effect of using

the same BC’s but using different scaled models is investigated by comparing the results of the unscaled with scaled geometries simulation results in section 5.6.2.

- In the test-report no information is given on how the measurements are sampled, what the time intervals between the measurement points are and the accuracy of the measurement devices. Unsteady effects can therefore not be determined from the experimental data.
- As can be seen from Figure 5.9 the measurements for both the pressure and temperatures are only performed on one side of the door. Because of this, asymmetries in the flow field cannot be detected from the experimental data.
- During the analysis of the test report some remarks on the accuracy of the experiments were observed. From a picture of the test set-up (which could not be published due to confidentiality reasons) could be seen that the walls of the room in which the test was performed were close to the test model. This could cause interference effects with the flow field inside the TRU geometry, by blocking the reversed flow jet.
- Next to this, the cabling connected to the pressure taps and thermocouples were bundled together and guided back along the test model to the connecting measurement hardware. The author of this report believes that the cables can have an intrusive effect on the flow which leaves the model between the fan-ramp and door-side-flanges and could cause an upstream effect.
- From a picture of the test set-up could be seen that the thermocouples were emerged into the boundary layer and therefore measure a different boundary layer temperature as seen from Figure 3.6. The thermocouples are actually blocking the flow and thereby creating a stagnation point which could also negatively affect the correctness of the measured temperatures. What effect this observation has on the measured data is hard to determine without a reference experiment with non-intrusive thermocouples.
  However, the fact that the thermocouples are emerged in the boundary layer shows that the measured temperature is dominated by the flow topology. It would be better if the surface temperature of the door could be measured with for instance thermal paint or infrared measurement techniques.

5.5 Modelled Flow Physics

Due to the complex TRU geometry shown in Figure 5.3 a lot of different flow phenomena are present in the simulations. The test cases have shown that these isolated flow phenomena can be solved by the tested RANS turbulence models to a sufficient level of accuracy.

To give the reader an idea and understanding of the flow field created by the geometry and boundary conditions some contour and 2D/3D streamline plots are shown in this section. The results shown in this section are taken from the base simulation (see Table 5.6) and are comparable to the results of the other simulations in terms of flow physics.

In Figure 5.11 six numbered 3D streamline plots can be seen. The plots are explained below according to their numbering,

- Plot 1 shows the 3D streamlines of the two large vortices in front of the TRU door. The vortices are created by the curvature of the door and rotate from the outside to the inside of the door. The cores of the vortices can be clearly seen while they leave the TRU geometry.

- Plot 2 shows the 3D streamlines developing from a plane at the nozzle exit. Only a very few of these streamlines originate from the bypass-duct inlet. All other streamlines originate from outside the TRU geometry (far-field). This means that a large part of the nozzle flow is not leaving the nozzle but entering the nozzle causing reverse flow in the nozzle.
- Plot 3 shows the 3D streamlines leaving the nozzle geometry between the fan-ramp and left-door-side-flange. Most flow originates from the far-field-inlet and is then mixed and deflected by the reversed flow jet. It can also be seen that a large area of separated recirculating flow is present behind the door created by this “leakage” flow.
- Plot 4 shows the 3D streamlines tangential to the outer-nacelle. Part of these streamlines “stick” to the surface and create a vortex in front of the nacelle-fan-ramp connection. This sticking to the surface effect is also known as the Coanda effect. One part of the flow is mixed and deflected by the reversed flow jet. The other part separates from the nozzle and creates an area of recirculating flow behind the door.
- Plot 5 shows the 3D streamlines originating from the bypass-duct and core inlet planes. The two flows are mixed by the mixer and the two large vortices shown in plot 1, before leaving the TRU geometry on the sides (leakage flow) and top. A small part of this high energy flow is captured in the recirculation area behind the door.
- Plot 6 finally shows again the 3D streamlines originating from the bypass-duct and core inlet planes but now seen from the far-field-outlet plane. From this plot can be seen that the reversed flow jet is not symmetric. The left and right leakage flows join behind the TRU geometry and then tend to the right of the middle when flowing more downstream. A small part of the left leakage flow is entrained in the main reversed flow jet and thereby creating a roll-up of the jet from the inside-out. A similar result was observed during the evaluation of the JICF test case.

The streamlines in Figure 5.11 are coloured by the (global) velocity magnitude.

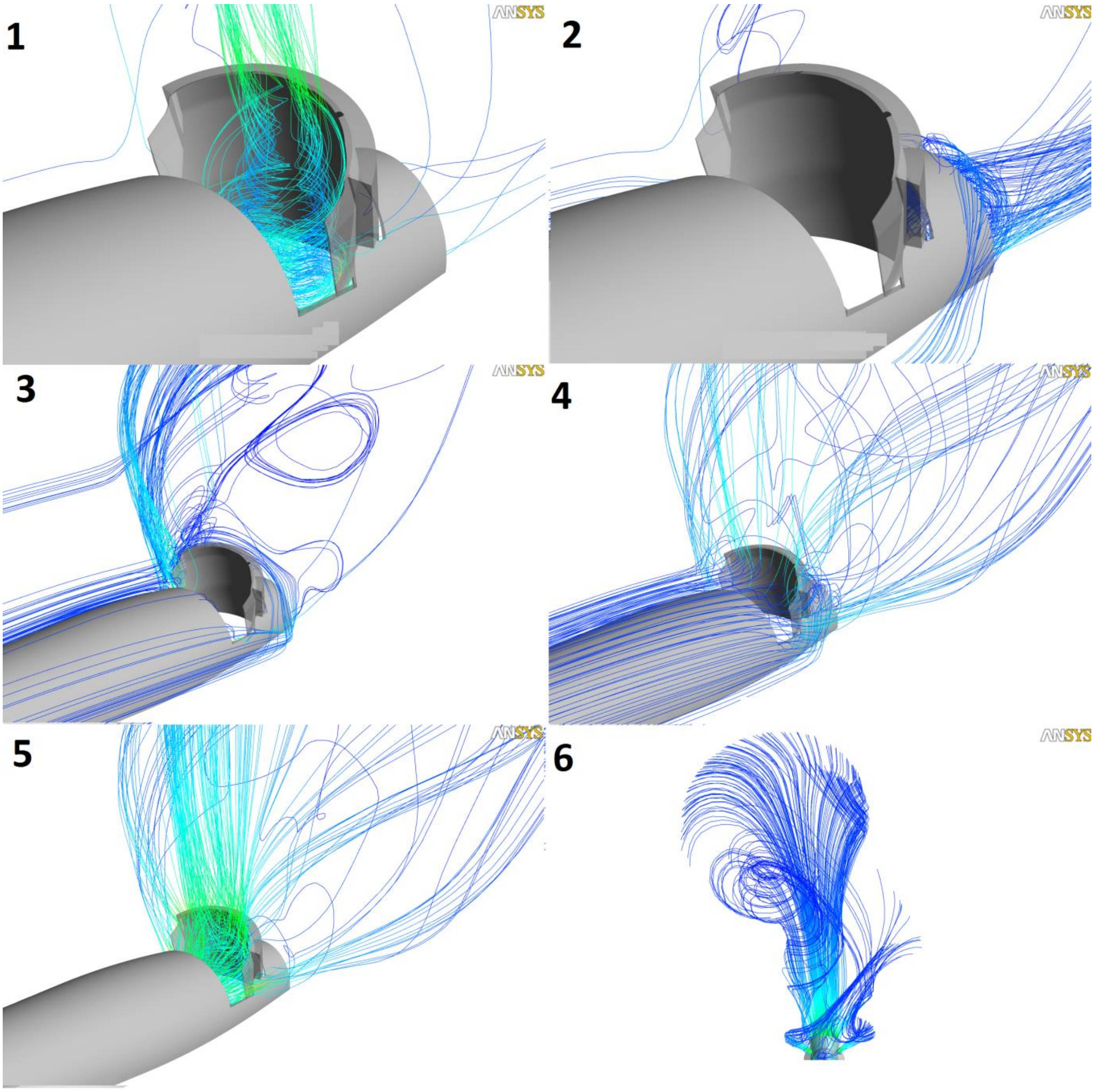

Figure 5.11: 3D streamline plots to visualise different flow phenomena

To further clarify the flow phenomena described above and visualised with the 3D streamline plots, 2D contour and streamline plots are shown in Figure 5.13. Figure 5.12 shows the locations of the reference planes for contour plots 1 to 9. Contour plots 10 to 15 represent planes between reference plane 9 and the TRU door surface to visualise the development of the mixing flow. The 3D contour plots 17 and 18 represent the pressure and temperature distribution on the TRU door geometry. The plots are explained below according to their numbering,

- Velocity contour and streamline plots 1 to 3,
    - The velocity difference between the high velocity reversed jet flow and low velocity freestream flow can be clearly seen as well as the mixing layer formed between these two flows
    - In contour plot 2 the different flow directions caused by the mixer can be seen.
    - The high velocity area at the fan ramp can be recognised from the plots as well as the vortex created in front of the nacelle-fan-ramp connection.

    - From streamline plots 1 and 2 can be seen that most of the bypass-duct and core inlet flow is entrained in the two large vortices whether most of the flow for plot 3 directly impinges on the door's surface.
    - The reversed jet is considerably smaller in plot 3 which is caused by the fact that part of the reversed flow is leaking away between the fan-ramp and door-side-flange.
    - Finally the recirculation area behind the door and reversed flow in the nozzle can be clearly recognised from the plots.
- Pressure contour and streamline plots 4 to 6 and 16,
    - The two large vortices in front of the door can be seen from the streamline plots.
    - The vortex created in front of the nacelle-fan-ramp connection can be seen in plot 4.
    - As can be seen from these plots the two large vortices in front of the door rotate from the outside to the inside of the door. This confirms the observation made that the inlet flow for plots 1 and 2 are entrained in the vortices while the flow for plot 3 impinges or flows alongside the door before being entrained in the vortices.
    - The leakage-flow between fan-ramp and door-side-flanges can be clearly recognised. From plot 5 a recirculation area between the leakage-flow and door-outer-surface can be seen.
    - The two vortices created in the nozzle area can be seen from the streamline plots. From contour plot 16, which is identical to plot 6 but with a smaller data range (Colouring everything outside the data range blue or red), the adverse pressure gradient can be seen.
    - From the plots can be seen that the geometry is not symmetric, as was initially expected. The nozzle geometry on the left and right (in flow direction) have a different angle with respect to the freestream flow causing an asymmetric flow-field in the freestream and nozzle areas. This can also be seen in the pressure distribution of contour plot 16.
- Temperature contour and streamline plots 7 to 9,
    - From plots 7 to 9 the hot core and cold bypass-duct flow can be seen.
    - The plots show that the mixer creates two mixing patterns in which one of the patterns (Boxed patterns in plot 9) has a hotter core area than the other (neighbouring) pattern. These two patterns together form a mixing pair.
    - From these plots it can also be seen that the first mixing patterns on the left and right side next to the centre/symmetry plane are not the same. Although at first sight it was thought that the geometry and thus flow-field was symmetric in the engine centre-plane, this is not the case.
- Temperature contour plots 10 to 15 and 18,
    - From the development of the mixer flow one can see that the top two mixing pairs are entrained in the two large vortices and are fully mixed, i.e. no temperature differences can be recognised anymore as from plot 13 on.
    - The other two mixing pairs on the left and right side next to the engine centre-plane determine for a large part the door-inner-surface temperature distribution shown in plot 18. This because as explained before, the two large vortices rotate from the outside to the inside of the door so the flow at the outside of the door is flowing along the door's surface before it is entrained in the vortices.

  - The two boxed patterns in plot 9 have a hotter core compared to the neighbouring mixing pattern. If these two mixing patterns are followed from plot 10 to 15 it can be seen that the right hot pattern is closer to the door and thus impinges first on the right door-side-flange (plot 10). The left hot pattern is further away from the door and impinges later on the left door-side-flange (plot 12).
  - Furthermore the asymmetric mixing patterns cause a colder flow area on the left-bottom part and a hotter flow area on the right-bottom part of the door as can be seen from plot 18.
- Pressure contour plot 17,
  - The pressure contour plot of the TRU door geometry shows less asymmetry than the temperature contour plot.
  - One reason could be the fact that the PS is way smaller than the TS making the asymmetry less visible in a contour plot.
  - Another reason could be that the pressure distribution is mainly caused by the two large vortices which are symmetric while the temperature distribution on the door, as explained before, is mainly caused by the asymmetric mixing patterns.
  - Next to this, the high pressure stagnation region between the two vortices in the centre of the bottom of the door can be recognised.
  - Also the two low pressure regions on the top left and right of the door can be seen. Here the flow is speeded up by a combination of the rotational speed of the vortex, the inclined door-inner-surface and kicker-plate.

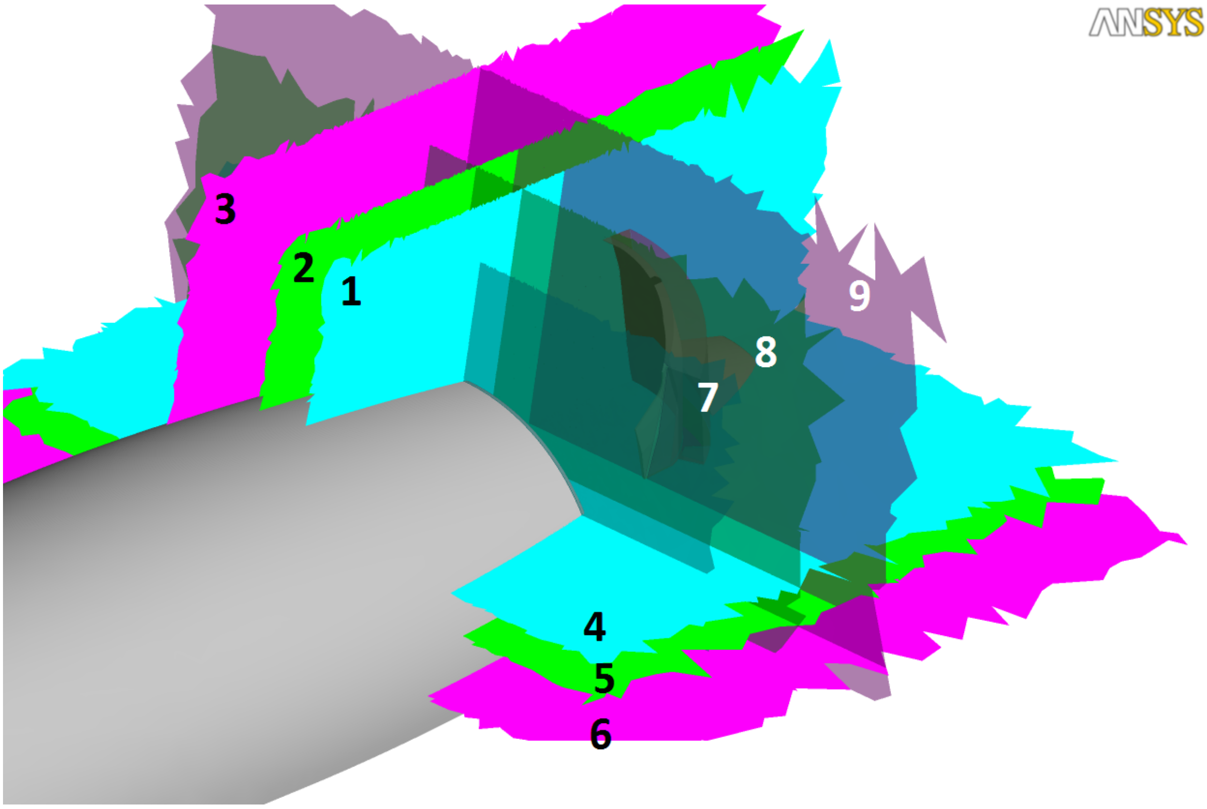

Figure 5.12: Contour plot reference planes indicated in Figure 5.13

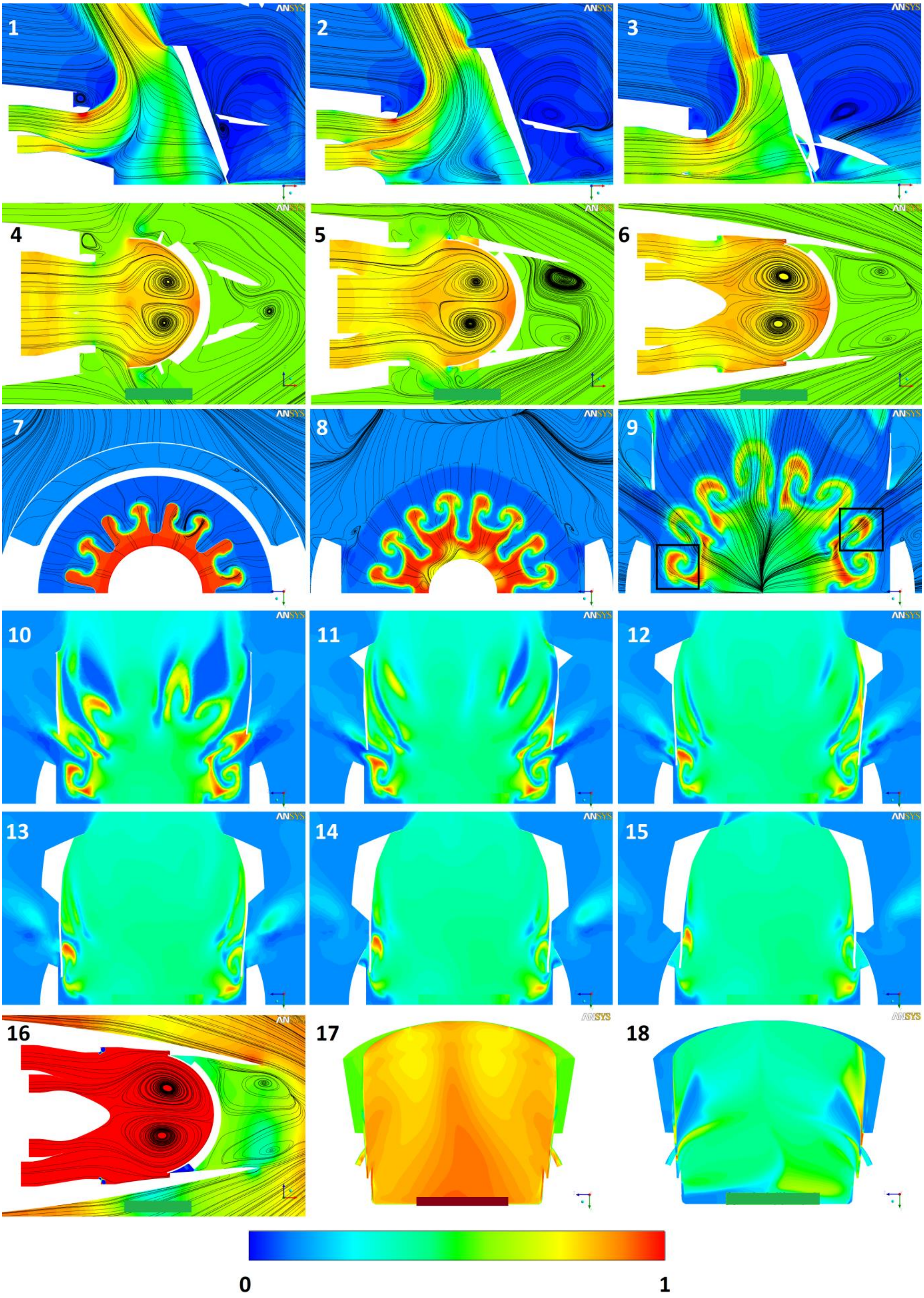

Figure 5.13: Velocity contour plots (1-3), pressure contour plots (4-6), temperature contour plots (7-15), nozzle adverse pressure gradient (16), door pressure distribution (17), and door temperature distribution (18)

5.6 Results

In this section the results of the performed simulations summarised in Table 5.6 are described. The results are evaluated on their convergence and accuracy. The level of convergence is evaluated on the different monitored inlet mass flow rates, pressures and temperatures on the door. The accuracy is evaluated by comparing the pressures and temperatures on the inner-door-surface and door-side-flanges with experimental data. Also the resultant reversed thrust coefficient and effective nozzle areas are compared to experimental data.

In section 5.6.1 the results of the base simulation are shown. Sections 5.6.2 to 5.6.4 evaluate into more detail the results and comparisons of the different simulations to investigate how the scaling of the geometry, boundary conditions and meshing strategy and quality influence the convergence and accuracy of the simulations compared to this base simulation.

5.6.1 Base Simulation Results

The aim of this chapter is to obtain a converged CFD simulation as a starting point for the coupled aero-thermal simulations. The base simulation of this research project was simulation 1.1. The results of simulation 1.1 are shown in this section. According to these results, the different simulations summarised in Table 5.6 were performed to investigate if the results of the base simulation could be improved in terms of convergence and accuracy.

One of the measures to check the convergence of the simulations is the monitoring of the mass flow rates at the bypass duct and core inlets. Figure 5.14 shows the mass flow rate monitor plots for the BPD and core inlets plotted as deviation from its mean value. The figure shows the irregular oscillations of the mass flow rate and clearly the mass flow rates do not converge to a steady-state value.

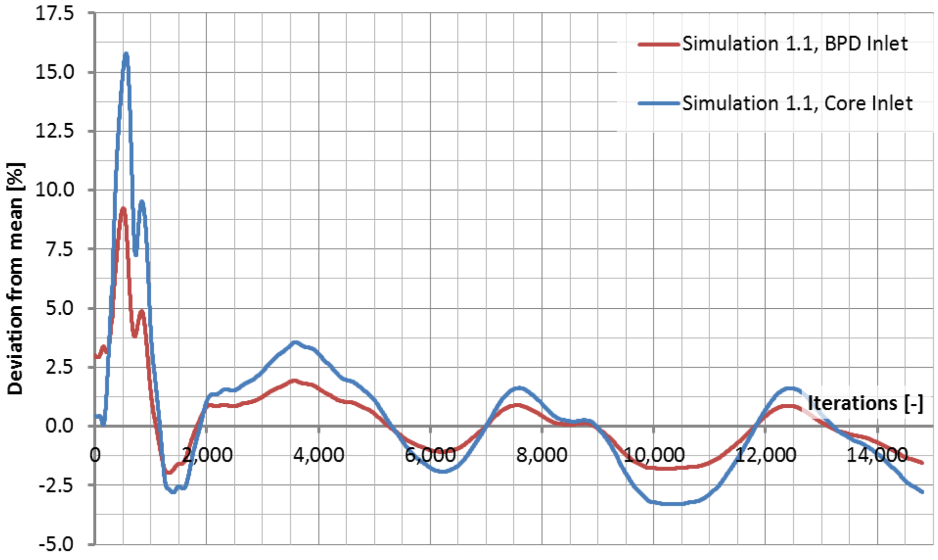

Figure 5.14: Mass flow rate monitor for the base simulation given as deviation from its mean value

Another measure for convergence is the pressure force on solid walls of the TRU geometry. Figure 5.15 shows the pressure force monitor on the door-inner-surface as deviation from the mean. The irregular oscillations seen in Figure 5.14 can be seen in this figure as well. Obviously there is a relation between the oscillations in mass flow rates at the BPD and core inlets and the pressure force on the door-inner-surface. The question here remains by what phenomena these oscillations are caused.

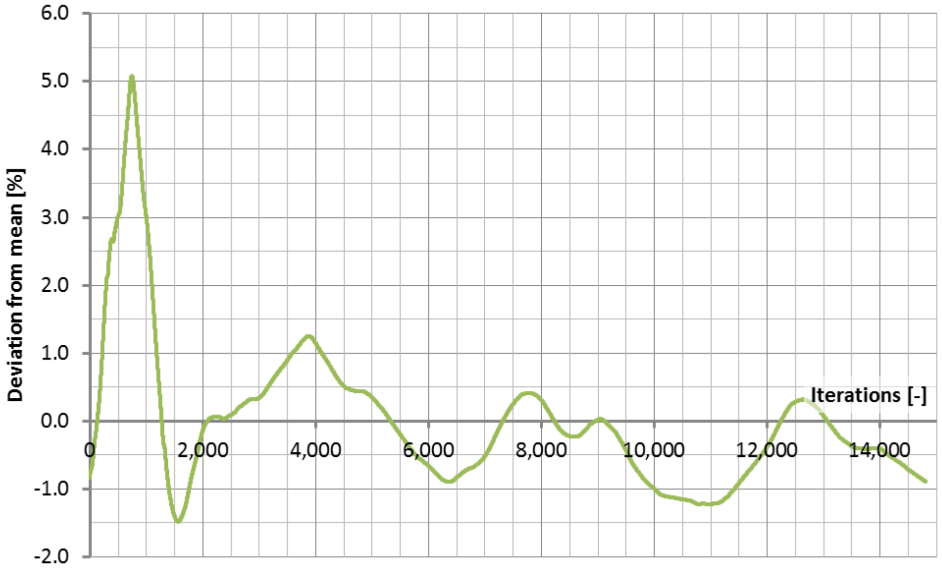

Figure 5.15: Pressure force monitor on the door-inner-surface of the base simulation given as deviation from the mean

During the simulations the solution was checked intermediately. The comparison of these simulation results with experimental data for pressure taps P501 to P515 (shown in Figure 5.10) is shown below in Figure 5.16. The simulation was checked after 11,800; 13,300 and 14,800 iterations respectively. From the figure can be seen that the pressure values on the left and right side of the door after 11,800 iterations are asymmetric with an offset of up to 7%. After 14,800 iterations the pressure values on the left and right side of the door seem to become more symmetric.

The trend of the simulation results compare fairly well with the experimental data. Nonetheless the simulation results still show a deviation from the experimental data of 8%, 2% and 6% after 11,800, 13,300 and 14,800 iterations for the P501 pressure tap on the left side of the door. The deviations are larger at the top than at the bottom part of the door. The oscillations of the pressure force seen in Figure 5.15 are also recognised in the deviating pressure values shown in Figure 5.16.

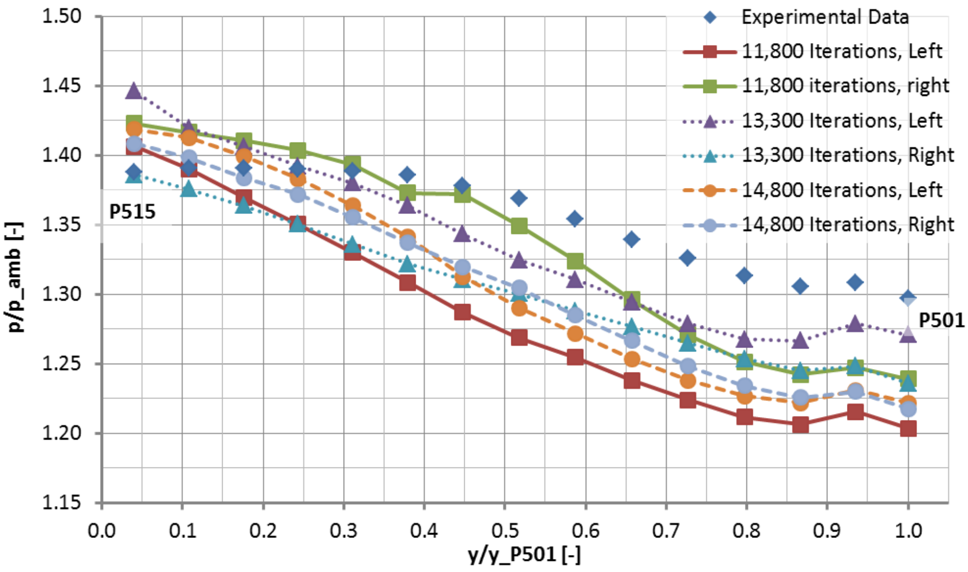

Figure 5.16: Comparison of normalised pressure values with experimental data for the base simulation (P501 to P515)

The comparison of the intermediate simulation results with experimental data for thermocouples T501 to T515 is shown below in Figure 5.17. From this figure no trend can be recognised at all and large deviations in normalised temperature values can be seen. The temperature values on the left and right side of the door at the particular number of iterations do not compare with each other which indicate that the temperature distribution at the door is not symmetric as was already discussed in the previous section.

The error with the experimental data for the T515 thermocouple on the right side of the door is for instance 1%, 42% and 40% after 11,800, 13,300 and 14,800 iterations respectively. The errors for the T515 thermocouple on the left side of the door are however smaller and have values of 5%, 10% and 4% after 11,800, 13,300 and 14,800 iterations respectively. In comparison with the pressure values the temperature values are highly oscillating and show larger deviations from the experimental data.

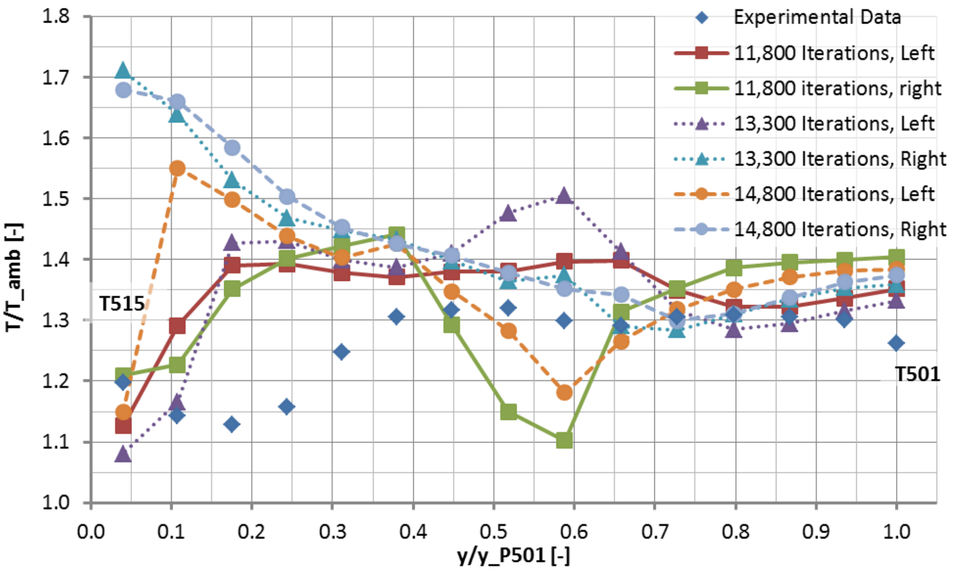

Figure 5.17: Comparison of normalised temperature values with experimental data for the base simulation (T501 to T515)

As can be seen from the oscillating results described above, the simulation is not converged to a steady-state solution. The solution also shows deviations from the experimental results. The pressure values are oscillating but the trend of the results compares fairly well with the experimental data with errors up to 7%. The temperature values however show strong oscillations and deviations from the experimental data with errors of up to 42%.

To get a better understanding of the oscillating behaviour of the simulations and to be able to compare different simulations with each other independent of when the simulation is stopped and post-processed, pressure and temperature values are monitored for 6,000 additional iterations. Due to the high memory demand of these monitors not all 29x2 and 30x2 pressure and thermocouple locations could be monitored. Pressure taps P501, P504, P507, P510, P513 and thermocouples T503, T506, T509, T512 and T515 on the left and right side of the door are monitored, respectively. The monitored pressure taps and thermocouples are indicated in Figure 5.10. The monitor-results are averaged and the maximum and minimum deviation is shown.

After analysing the results of the base simulation, a list with possible causes for the oscillations and deviations of the simulation results was created. To improve the convergence and accuracy of the base simulation, some of these possible causes were investigated in this master thesis project. Other possible causes could not be investigated due to the lack of time or computational resources. The determined possible causes are as follows,

- Scaling of the geometry, described in section 5.6.2. As explained in section 5.4, the boundary conditions of the experiments are taken from the full scale engine model while the experimental model is a 1:5 scaled model. To investigate if the results of the simulations are influenced by this scaling, simulation 2 is performed which makes use of a full scale geometry.
- Boundary conditions, described in section 5.6.3. Due to the relation between the oscillations in inlet mass flow rates and the pressure distribution on the inner-door-surface, a simulation with a lower FNPR is investigated (simulation 3).
- Meshing strategy and quality, described in section 5.6.4. As explained in section 3.1.5 oscillations in simulation results can be caused by a bad mesh quality or incorrect meshing. To investigate this fact, simulation 4 is performed.
- Coupled aero-thermal simulations, described in Chapter 6. The above three measures are mainly focussed on improving the accuracy and reducing the oscillations of the pressure values on the inner-door-surface. To reduce the strong oscillations and large deviations in temperature values, coupled aero-thermal simulations are performed.
- Asymmetric mixer. As explained in section 5.5, the mixer is not symmetric and causes an asymmetric temperature distribution on the inner-door-surface and side-flanges. Simulating a 360° TRU geometry could improve the accuracy of the simulations because the mixing is not constraint at the symmetry plane. Due to the lack of time and computational resources this was not investigated.
- Unsteady flow physics. As also seen for the test cases, unsteady effects are present in the flow and can cause for instance asymmetric solutions, see Figure 4.4. As explained in section 3.1.5 unsteady effects can cause oscillations in the simulation results. Performing an U-RANS simulation or LES could therefore improve the results. This was outside the scope of

this research project due to the lack of time and computational resources as for instance already indicated in Table 3.1.

- Computational model. As shown in Chapter 4 the SST k-ω turbulence model is the preferred model to use. During the project, the only turbulence model which did not diverge was the Realizable k-ε model. Due to time constraints it could not be determined why both the SST k-ω and Spalart-Allmaras turbulence models did not give any solution.
- Experimental data. As explained in section 5.4 there is some doubt on the accuracy of the performed experiments due to the lack of measurement uncertainties and installation of for instance the thermocouples. The measurement uncertainties could not be traced back by the author of this report.

5.6.2 Influence of Scaling of the Geometry

As discussed before in section 5.4, the same boundary conditions are used for the 1:5 scaled geometry used in the experiments as for the full scale engine model. Important to know for the design of the full scale engine is if this scaling factor of five has an influence on the accuracy of the solution.

The mesh is created in Centaur and is then imported and scaled by Fluent. This means the mesh cell edge lengths, faces and volumes are a factor 5, 5^2 and 5^3 smaller for the scaled geometry simulations. Interesting here is to see how the results on both the scaled and unscaled meshes differ.

The Reynolds number is the ratio of the inertial forces over the viscous forces of the fluid and can be used to compare different flows with each other. The Reynolds number indicates the level of turbulence of the fluid. A higher Reynolds number therefore means a more turbulent flow and thereby smaller length and time scales (Wilcox, 2006). A different Reynolds number can therefore be of influence on the flow structure and thus modelling of the turbulent flow.

Coupling the thoughts about the mesh to the turbulent length scales shows a contradiction:

- The Reynolds number is a factor of five higher for the unscaled geometry and therefore has smaller turbulent length and time scales
- The mesh length scales are a factor of five higher compared to the scaled geometry

This means that the turbulent length and time scales are decreased whether the mesh length scales are increased by using the unscaled geometry.

The Reynolds numbers based on the radius of the BPD and core inlets are given below in Table 5.7 for simulations 1 (base simulation) and 2 (unscaled geometry simulation).

Table 5.7: Reynolds numbers for BPD and core inlets for simulations 1 and 2

Simulation 1		**Simulation 2**	
Re_{BPD} [−]	$3.7 \cdot 10^6$	Re_{BPD} [−]	$19.0 \cdot 10^6$
Re_{Core} [−]	$7.5 \cdot 10^5$	Re_{Core} [−]	$3.9 \cdot 10^6$

Figure 5.18 shows the mass flow rate monitor plots of the BPD inlet for simulation 1 and 2 as deviation from the mean. Both simulations show a regular oscillation. For the scaled geometry (simulation 1) four oscillations can be recognised while for the unscaled geometry (simulation 2) five oscillations can be recognised. This could be an indication in differences in the Reynolds number and thus turbulent time scales. This would imply the oscillations are caused by unsteady effects of the flow.

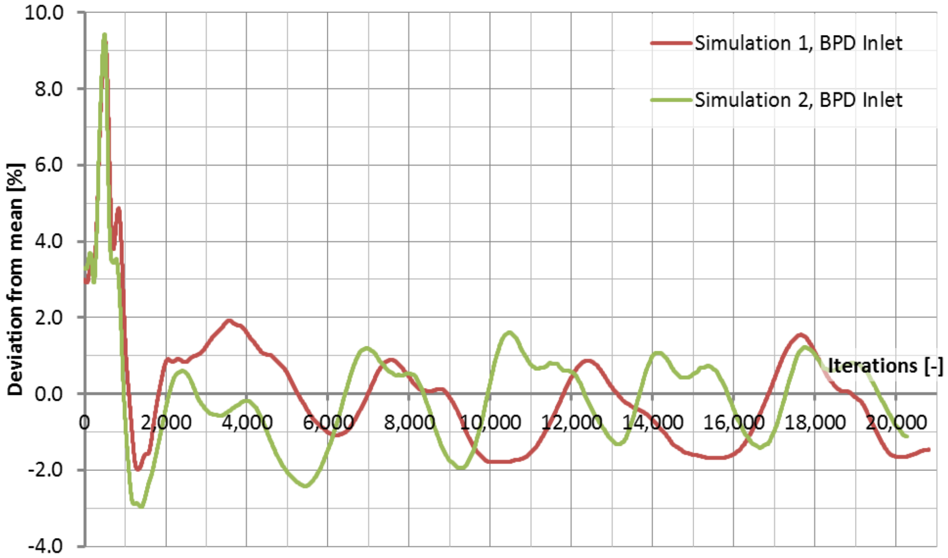

Figure 5.18: Mass flow rate monitor for simulations 1 (base) and 2 (unscaled geometry) for the BPD inlet given as deviation from the mean

For the comparison of the scaled and unscaled geometry simulation results, the monitored pressure tap and thermocouple data is used as explained in the previous section.

Figure 5.19 shows the averaged monitored pressure values together with the maximum and minimum deviation from this value. It can be seen that the range of pressure values, so the deviation from the mean value over these 6,000 monitored iterations, is more or less equal for both simulations. A clear difference can be seen in the averaged pressures of the two simulations. The maximum errors in pressure values for simulations 1.2 and 2.2 are 8% (P504) and 5% (P504, P507 and P510) respectively, as indicated by the boxes.

Although the results for the unscaled geometry are closer to the experimental data, it cannot be determined if this is an improvement while the Reynolds number is different. The offset between the lower and higher Reynolds number simulations could be caused by the different turbulent length scales for the two simulations in combination with the different length scales of the meshes. The combination of these two factors causes a different modelling of the two large vortices in front of the door which determine the pressure distribution on the door, as discussed in section 5.5.

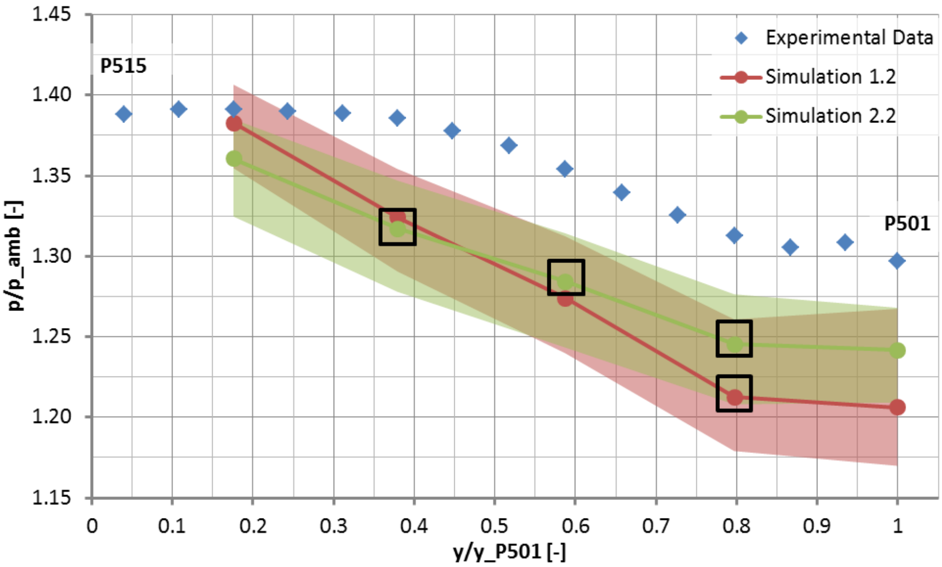

Figure 5.19: Comparison of monitored pressure values with experimental data for simulations 1.2 (base) and 2.2 (unscaled geometry)

Figure 5.20 shows the averaged monitored temperature values together with the maximum and minimum deviation from this value. Just as for the pressure distribution, the higher Reynolds number simulations shows results closer to the experimental data in the "problem" area of the door. The maximum errors in temperature values for simulations 1.2 and 2.2 are 32% (T515) and 21% (T512) respectively.

Due to the difference in Reynolds number, it can again not be determined if this is an improvement. The "problem" area is the bottom of the door on which the BPD and core mixing flow impinges as discussed in section 5.5. Just like for the pressure values, it is believed that the different (turbulent) length scales of the flow and mesh cause a different modelling of the BPD and core mixing flow, which results in a different temperature distribution on the door.

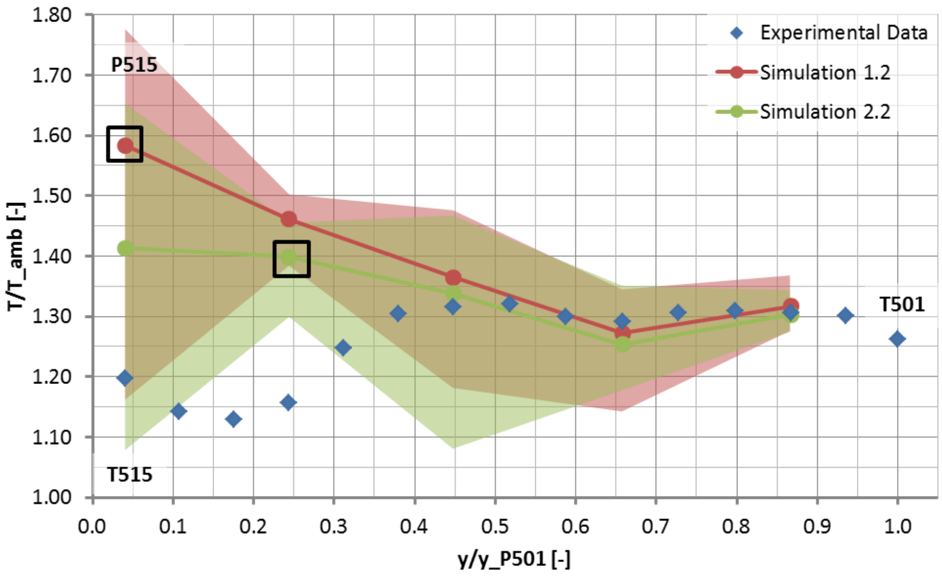

Figure 5.20: Comparison of monitored temperature values with experimental data for simulations 1.2 (base) and 2.2 (unscaled geometry)

The plots used to calculate the averaged pressure and temperature values are shown in Appendix B. Comparing the plots for simulation 1.2 and 2.2 shows that the pressure and temperature is still oscillating for both simulations and do not seem to converge to a steady-state solution. More iterations would probably not improve the convergence of the simulations.

Table 5.8 shows the reversed thrust coefficient and BPD and core effective nozzle areas. In general, the results of simulation 2 compare well with the experimental data. Again, these results cannot be trusted because it is not known what effect the different Reynolds number has on the solution. The reversed thrust coefficient of simulation 1 with the same Reynolds number as the experiments is considerably of.

Table 5.8: Performance parameters for simulation 1 (base) and 2 (unscaled geometry)

Variable	**Simulation 1**	**Error [%]**	**Simulation 2**	**Error [%]**	**Experimental Data**
$C_{T_x}[-]$	-0.24806	13	-0.2867	0.8	-0.2845
$C_{D_7}A_7\ [in^2]$	32.99	0.7	33.65	1.3	33.22
$C_{D_8}A_8\ [in^2]$	12.34	4.9	12.74	1.8	12.98

5.6.3 Influence of Boundary Conditions

Due to the observed relation between the oscillations in the mass flow rates and the pressure distribution on the inner-door-surface the influence of a lower $FNPR$ is investigated. In the set of available experimental data a test-run with a $FNPR$ of 1.32 was found which is considerably lower than the value of 1.52 for the base simulation.

Due to the use of two sets of boundary conditions the results will also be compared with two sets of experimental data as can be seen in Figure 5.22 and Figure 5.23.

Because of time constraints at the end of this master thesis project the pressure and temperature values were only monitored for 3,000 iterations instead of 6,000 iterations which needs to be kept in mind.

Figure 5.21 shows the mass flow rate monitor plots of the BPD inlet for simulations 1 and 3 as deviation from the mean. From this figure can be seen that the oscillations for simulation 3 seem to damp out with increasing iterations. This could be an indication that the simulation is developing towards a steady-state solution and that the lower $FNPR$ is of influence on the solution.

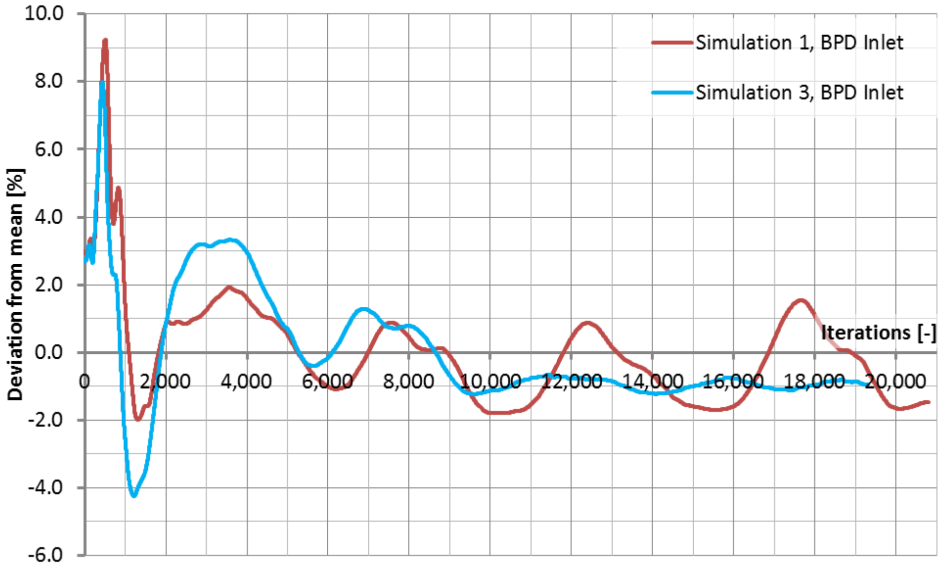

Figure 5.21: Mass flow rate monitor for simulations 1 (base) and 3 (Different BC´s) for the BPD inlet given as deviation from the mean

Figure 5.22 shows the averaged monitored pressure values together with the maximum and minimum deviation from this value. From the figure can be seen that the oscillations in the results with the lower $FNPR$ are considerably lower. This is in line with the observation made for the mass flow rate monitor plot shown in Figure 5.21.

The maximum errors in pressure values for simulations 1.2 and 3.2 are 8% (P504) and 3% (P507) respectively. The fact that the results are both more accurate and show less oscillations, implies that the flow physics can be better modelled by the CFD solver with a lower $FNPR$. Possible explanations for this could be that,

- The two large vortices in front of the door are more stable when the $FNPR$ is lower
- The pressure difference between the TRU flow and freestream is lower causing a better prediction of this mixing flow and separation areas around the door geometry (level of unsteady separation decreases with lower $FNPR$)

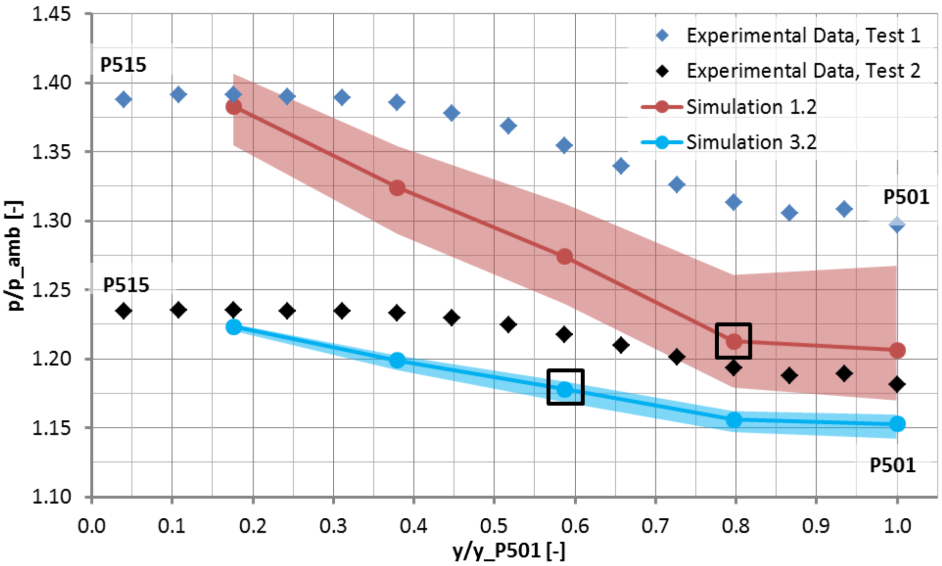

Figure 5.22: Comparison of monitored pressure values with experimental data for simulations 1.2 (base) and 3.2 (different BC´s)

As can be seen from Figure 5.23 the experimental data for the temperature values are almost identical as expected. This because the $FNTR$ and TS are identical as can be seen from Table 5.5. The reduction in oscillations observed for the mass flow rate and pressure values can also be seen for the temperature values with the lower $FNPR$.

The results are comparable for all thermocouples except thermocouple T515. This thermocouple located at the bottom of the door shows a better result for simulation 3.2. This could be caused by the fact that the two large vortices in front of the door and the mixing layer between core and fan flow is modelled better. The maximum errors in temperature values for simulation 1.2 and 3.2 are 32% (T515) and 25% (T512) respectively.

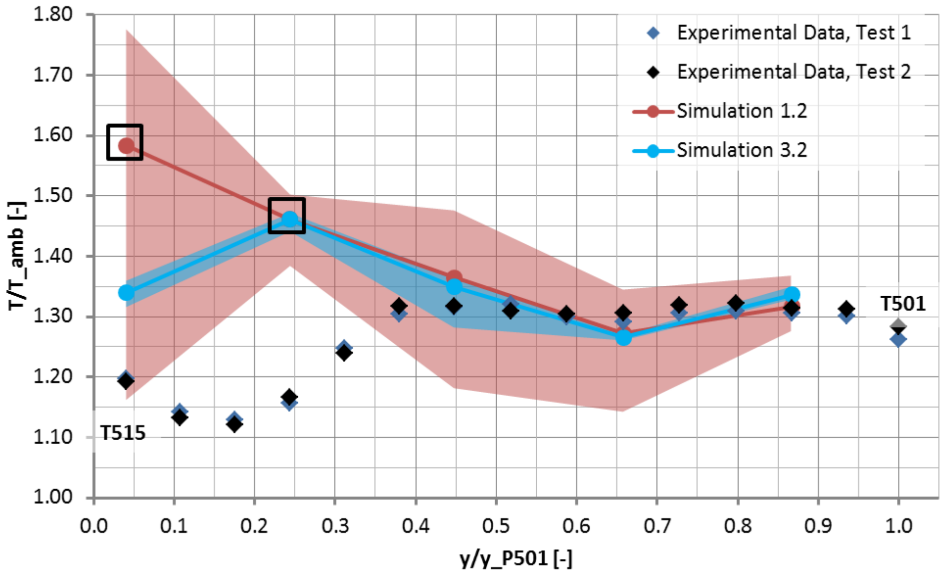

Figure 5.23: Comparison of monitored temperature values with experimental data for simulations 1.2 (base) and 3.2 (different BC´s)

Unfortunately due to the previously mentioned time constraints at the end of this master thesis project the reversed thrust coefficient and BPD and core effective nozzle areas could not be calculated for simulation 3.2

5.6.4 Influence of Meshing Strategy and Quality

In section 3.1.4 is described that the use of a structured mesh can improve the simulation results. During the evaluation of the test cases was shown that a structured mesh is numerically less dissipative than a hybrid mesh, especially in areas where variations in velocity directions are high, like mixing and vortical flows. As can be seen from Table 5.2, the mesh quality of mesh 3 is better than mesh 2. The influence of the meshing strategy and quality are investigated in this section. Simulation 1 makes use of a hybrid mesh (mesh 2) while simulation 4 makes use of a semi-structured mesh (mesh 3).

Figure 5.24 shows the mass flow rate monitor plots of the BPD inlet for simulations 1 and 4 as deviation from the mean. From this figure can be seen that the oscillations for simulation 4 seem to damp out with increasing iterations. This could be an indication that the simulation is developing towards a steady-state solution.

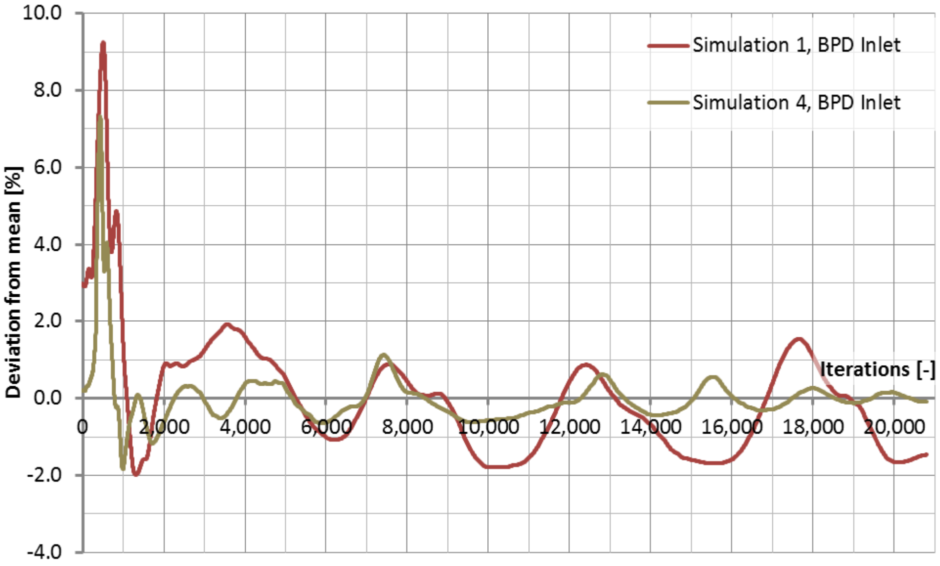

Figure 5.24: Mass flow rate monitor for simulations 1 (base) and 4 (Boxer mesh) for the BPD inlet given as deviation from the mean

Figure 5.25 shows the averaged monitored pressure values together with the maximum and minimum deviation from this value. The most important observation from these results is that the oscillations for simulation 4.2 are much smaller than the oscillations in results for simulation 1.2. This confirms the suspicion that the solution is converging to a steady-state solution.

From the figure can also be seen that the results of simulation 4.2 are somewhat closer to the experimental data at the bottom of the door. A reason for this could be that as described in section 3.1.4 a structured mesh is less dissipative than an unstructured hybrid mesh. Therefore, the two large vortices in front of the door are modelled better which causes the pressure distribution on the door to be more accurate. At the top of the door where the highest deviation from the experimental data can be seen the two simulations give almost identical results. The maximum errors in pressure values for simulations 1.2 and 4.2 are 8% (P504) and 7% (P501 and P504) respectively.

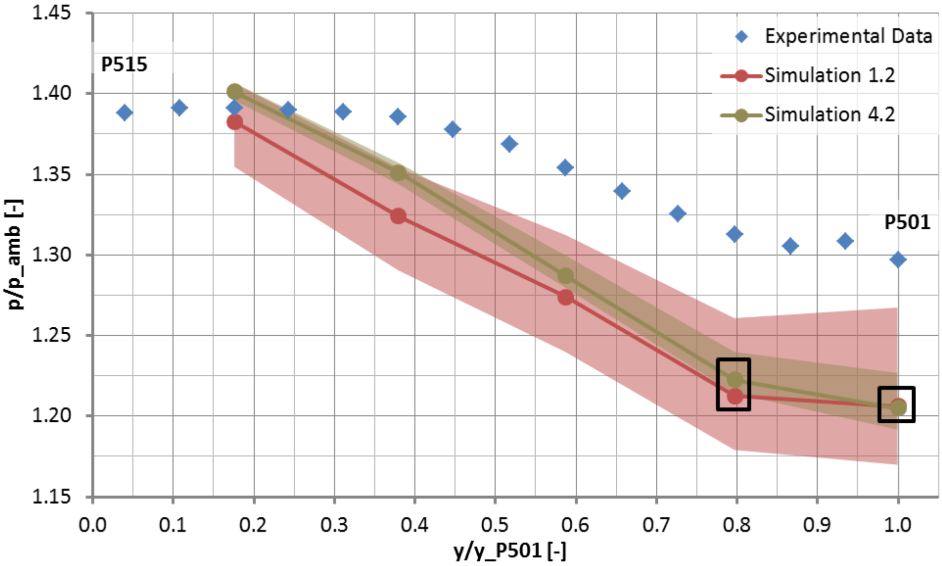

Figure 5.25: Comparison of monitored pressure values with experimental data for simulations 1.2 (base) and 4.2 (Boxer mesh)

Also for the monitored temperatures, shown in Figure 5.26 a decrease in oscillating temperatures can be seen for simulation 4.2. The maximum error of 32% for simulation 1.2 is located at thermocouple T515, while the maximum error of 22% for simulation 4.2 is located at thermocouple T512. This shows that the maximum error in temperature prediction is not only lower, but also changes location for the simulations on a structured mesh. The change in maximum error and location of this error, is believed to be caused by a different (less dissipative) modelling of the BPD and core mixing flow. From the plane mixing layer test case can be seen that a large deviation in mixing layer modelling is observed for different meshing strategies.

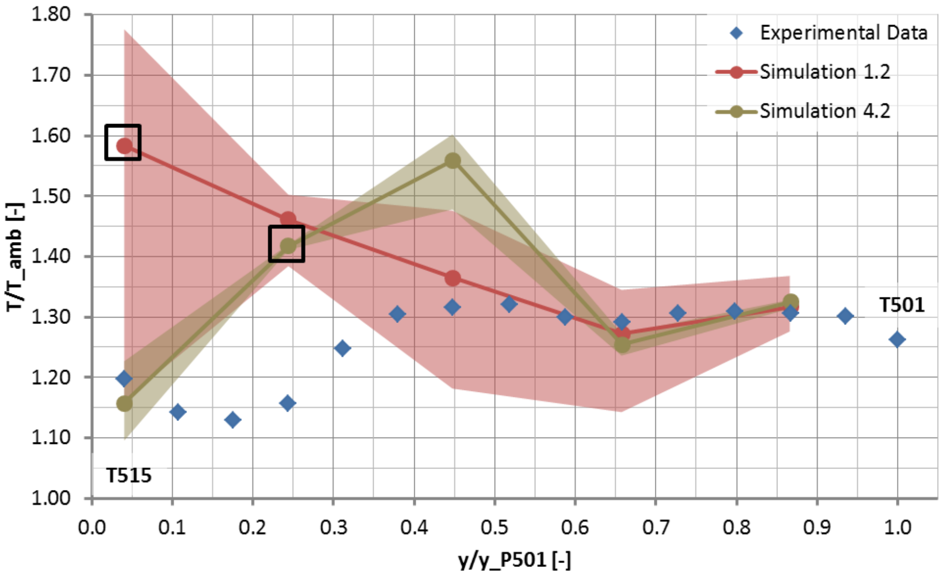

Figure 5.26: Comparison of monitored temperature values with experimental data for simulations 1.2 (base) and 4.2 (Boxer mesh)

The pressure and monitor plots shown in Appendix B for simulation 4.2 show that the oscillations are slowly damped, which implies that if additional iterations would have been performed, a steady-state solution would most probably be reached. Due to time constraints this was not possible. Most interesting is the temperature plot, which in contrast with the unstructured mesh results shows no large oscillations and thermocouples T503, T506 and T512 develop towards a steady-state value. Thermocouples T509 and T515, which are still oscillating also seem to converge towards a steady-state value.

From Table 5.9 below can be seen that the change in mesh does not improve the prediction of the performance parameters. The error of the reversed thrust coefficient and BPD effective nozzle area increased slightly while the error of the core effective nozzle area decreased.

For the calculation of the reversed thrust coefficient the pressure and viscous forces are evaluated on the TRU geometry. Because mesh 3 has a larger y^+ value, it could be that the viscous forces are not modelled accurately which could be an explanation for the larger error in reversed thrust coefficient for simulation 4.

Table 5.9: Performance parameters for simulation 1 (base) and 4 (Boxer mesh)

Variable	Simulation 1	Error [%]	Simulation 4	Error [%]	Experimental Data
$C_{T_x}[-]$	-0.24806	13	-0.2442	14.2	-0.2845
$C_{D_7}A_7\ [in^2]$	32.99	0.7	33.50	0.8	33.22
$C_{D_8}A_8\ [in^2]$	12.34	4.9	12.67	2.4	12.98

5.7 Conclusions & Recommendations

The aim of this chapter was to determine the flow topology of the TRU flow with a satisfactory level of convergence and accuracy, and use this solution to start the coupled aero-thermal simulations. As indicated in section 3.1.5, a solution is converged when the mass flow rates and set monitors are not oscillating anymore. A base CFD simulation was performed, which did not give a satisfactory level of convergence and also comparison with experimental results showed deviations in pressure and temperature values of up to 8% and 32% respectively. By investigating an unscaled geometry, different boundary conditions and a different mesh, a better solution was tried to be found. Some conclusions from this investigation can be summarised below.

It can be concluded that the convergence level of the base simulation is improved by using a lower $FNPR$ and structured mesh. The accuracy was also improved for both simulations. The maximum error in pressure values was reduced to 3% (different BC's) and 7% (different mesh) while the maximum error in temperature values was reduced to 25% (different BC's) and 22% (different mesh).

For further design work scaling of the geometry in comparison with the experimental data should be taken into account. Comparison of the base simulation with the unscaled geometry simulation showed that the results can differ considerably.

From section 5.5 can be seen that the mixing BPD and core flows cause an asymmetric temperature distribution on the door's surface. In the experiments the thermocouples are located on the left side of the door. Unfortunately, the monitored temperatures in this project are located on the right side of the door. Comparison of the temperature values on the left and right side of the door from Figure 5.17 showed a clear difference in maximum error from 42% to 10% for the left and right T515 thermocouple. A strong recommendation for further work is therefore to match the locations of the thermocouples from the experiments and monitored temperatures in the simulations. It is believed that the maximum errors for the monitored temperatures in this section are therefore only an indication of the differences between the performed simulations and not of the errors with the experimental data.

Because the pressure distribution is symmetric, the fact that the monitored pressure values are on the left side of the door and the pressure taps in the experiments on the right side of the door should be of less influence. Therefore, the maximum error of 8% with the experimental data is a valid indication of the accuracy of the simulations.

The fact that simulation 4 is almost fully converged but still shows an error with the experimental data implies that the inaccuracies are not caused by non-convergence of the simulations. The recommendations for further work already given in section 5.6.1 include,

- Performing a 360° computational model simulation.
- Performing a U-RANS simulation to capture unsteady effects.
- Test the SST k-ω model. The model has shown to produce better results for the tested validation test cases discussed in Chapter 4.
- Re-evaluate the validity and techniques used in the experiments, especially for the temperature measurements.

Additional recommendations from the simulations described in sections 5.6.2 to 5.6.4 are,

- A mesh refinement study should be performed for simulation 4.
- More pressure and temperature monitors should be inserted in the simulations to get a better understanding of the oscillations still present in the solution.
- An improvement of the temperature prediction by the use of coupled aero-thermal simulations is investigated in the next chapter.

Because the investigation described above was performed in parallel with the coupled aero-thermal simulations several simulations were used to start the coupled simulations. Simulation 4 was performed at the end of the research phase of this master thesis project and could therefore unfortunately not be used anymore to start the coupled simulations, although it gave the best results.

Chapter 6 TRU Temperature Prediction

As discussed in the previous chapter, the flow topology determined for two different sets of boundary conditions is used in this chapter to start the coupled aero-thermal simulations. The door geometry used to perform the coupled aero-thermal simulations is shown in section 6.1. The mesh features and case set-up are described in sections 6.2 and 6.3. The results of the coupled aero-thermal simulations are compared with the non-coupled simulation results and experimental data in section 6.4. Finally, the conclusions and recommendations based on the results are given in section 6.5.

6.1 Geometry

The door geometry, which is used for the coupled aero-thermal simulations can be seen below in Figure 6.1. The geometry is identical to the door geometry used to determine the flow topology. The surfaces which are coloured red in Figure 6.1 were originally connected to the inner-nacelle surfaces. While extracting the door geometry these surfaces were closed to ensure a waterproof geometry.

To understand the nomenclature used for the different surfaces of the door geometry throughout the remainder of this report, Figure 6.1 and Table 6.1 can be used.

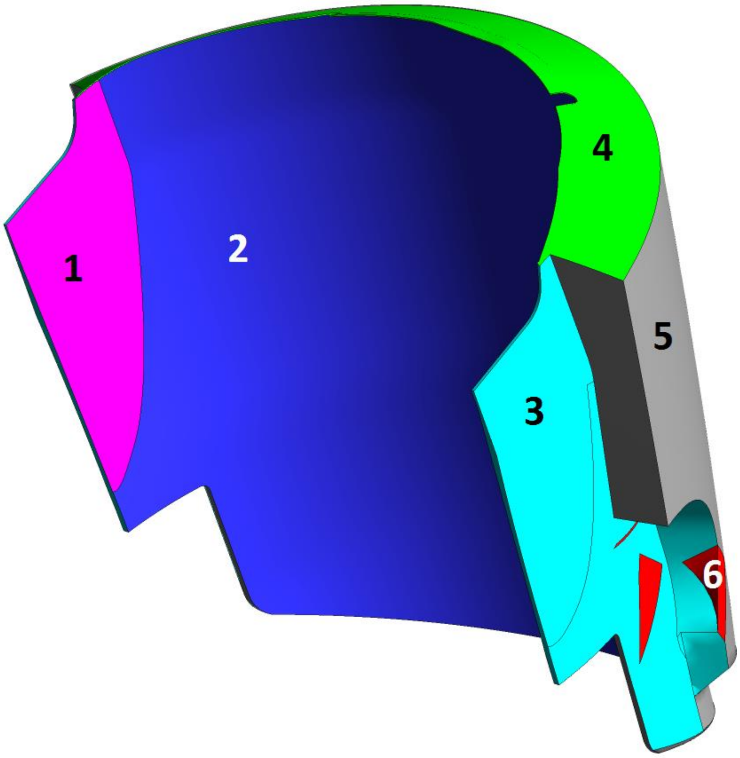

Figure 6.1: Geometry of the isolated TRU door for the coupled aero-thermal simulations

Table 6.1: Legend to Figure 6.1

No.: Colour	Surface Name
1: Pink	Door-inner-side-flange
2: Blue	Door-inner-surface
3: Cyan	Door-outer-side-flange
4: Green	Kicker-plate
5: Grey	Door-outer-surface
6: Red	Nacelle-door-connection

6.2 Mesh

The mesh for the TRU door geometry is made with the Centaur mesh generator (CentaurSoft, 2012). The mesh is fully constructed out of tetrahedral elements. One mesh was made to perform all coupled aero-thermal simulations. Different meshes for the door geometry were not made because from the aero-thermal test-cases, described in sections 4.5 and 4.6, it could already be seen that the influence of the mesh of the solid geometry does not have a large influence on the predicted temperature distribution.

The mesh characteristics are summarised below in Table 6.2. From the table it can be seen that the orthogonal quality criteria are met, which is as expected due to the lack of prism layers. Some unacceptable and bad equivolume skewness cells are present in the mesh. These cells could not be improved without excessively refining the mesh locally. A better surface definition (merging small surfaces into one large surface) in the CAD file could be a fix for this problem, but was out of the scope of this research project. A surface cell edge length of 25 mm was used as described in the conclusions of Chapter 4. This surface size should not influence the accuracy of the solution, as seen in sections 4.5 and 4.6, but the mesh size is kept small which saves computational resources.

The surface mesh and a cut through the symmetry-plane of the door are shown below in Figure 6.2. The cluster of cells on the door-inner-surface is caused by the thin surface of the nacelle-door-connection and could not be avoided.

Table 6.2: Summary of TRU door mesh characteristics

Variable	**TRU Door Mesh**
Mesh generator	Centaur
Mesh size [-]	155,427
Worst ortho. quality [-]	0.132
No. unacc. cells, Ansys [-]	0
No. unacc. cells, RRD [-]	0
No. bad cells, Ansys [-]	0
Worst equi. skew [-]	0.993
No. unacc. cells [-]	13
No. bad cells [-]	61
Aspect ratio [-]	63.5
Surface cell l_{edge} $[mm]$	25

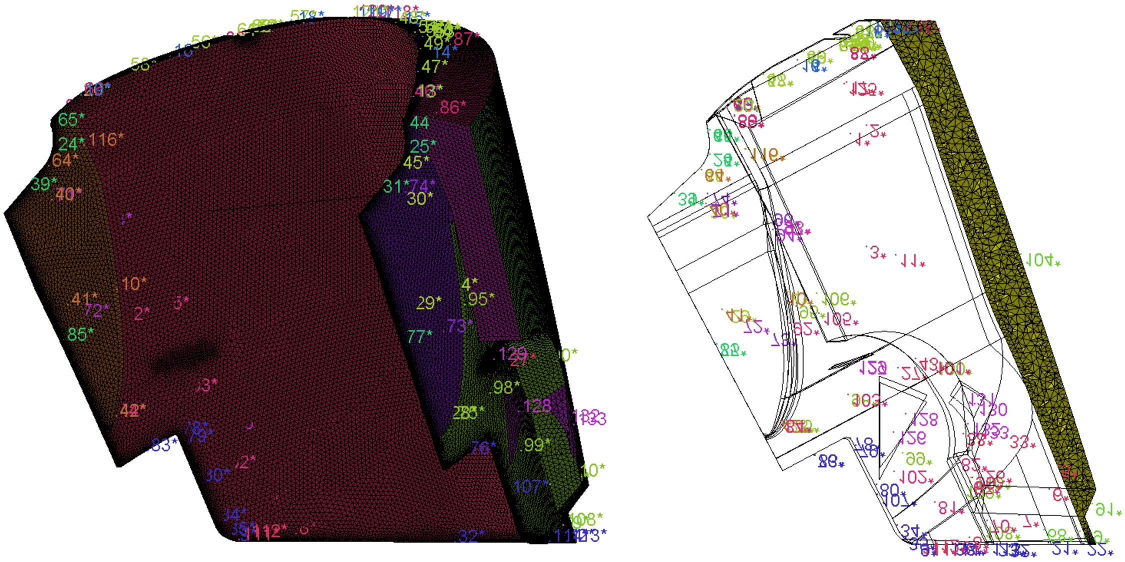

Figure 6.2: Surface mesh and symmetry-plane mesh of the TRU door geometry

6.3 Case Set-up

As discussed in section 3.2.2, due to unforeseen reasons the Ansys Fluent (Ansys Inc., 2011a) software package is used as a thermal solver. The material of the TRU door which is used in the experiments is 416 stainless steel. The material properties were found from Matweb (2015) and confirmed by two other independent sources, AZO Materials (2015) and Elgin Fastener Group (2015).

The solver settings are kept the same for all performed coupled simulations and are summarised below in Table 6.3 and explained into more detail in Chapter 3.

Table 6.3: Summary of solver settings for coupled aero-thermal simulations

Solver Setting	Chosen Approach
Solver Type	Density-based solver
Time	Steady
Energy-equation	On
Density, ρ $[kg/m^3]$	7,800
Specific heat, c_p $[J/kgK]$	460 @ 0-100$°C$
Thermal conductivity, k $[W/mK]$	24.9 @ 100$°C$
Linearization method	Implicit
Flux Type	Roe-FDS
Gradients	Least squares cell based
Energy Equation accuracy	First-order upwind

The boundary condition types are summarised below in Table 6.4.

Table 6.4: Summary of boundary condition types for coupled aero-thermal simulations

Surface	BC Type
Door-inner-side-flanges	Specified heat flux, coupled
Door-inner-surface	Specified heat flux, coupled
Door-outer-side-flanges	Specified temperature
Kicker-plate	Specified temperature
Door-outer-surface	Specified temperature
Nacelle-door-connection	Adiabatic wall, $q = 0\ W/m^2$

The door-inner-side-flanges and door-inner-surface are coupled to the CFD simulations and, as explained in section 3.2.2, are given the heat flux distribution extracted from the CFD simulations as boundary condition. The other surfaces shown in Figure 6.1 are not coupled to the CFD simulations. The possibility of coupling all surfaces to the CFD simulations was investigated shortly, but due to time constraints at the end of the research project this investigation could not be finished successfully.

A thermal boundary condition needs to be specified for the non-coupled surfaces. It was found that if the surfaces, connected to the coupled walls, were modelled as an adiabatic wall, the simulations diverged. This is caused by the fact that the heat flux specified at the coupled walls has a certain value whether the heat flux at the connecting surfaces has a value of zero. This causes a jump in heat flux at the connection of these surfaces, which on its turn causes the simulation to diverge. Therefore, a temperature needs to be specified as boundary condition for the surfaces connected to the coupled walls. During the project, the following two temperature boundary conditions were tested for the non-coupled surfaces,

- A constant temperature equal to the freestream flow ambient temperature.
- The temperature distribution at these surfaces taken from the CFD simulation at the start of the coupled simulations (temperature profiles). This approach is similar to a non-coupled FE/CFD analysis described in section 3.2.2.

During the determination of the flow topology, the boundary conditions for the simulations were matched with the boundary conditions obtained from the test report of the experimental data (Pipkin, Long and McDonald, 2007). The ambient temperature given in the test report had a value considerably higher than the standard used ambient temperature value. At that point it was decided to give the freestream an ambient temperature equal to the BPD temperature as is common practice within RRD.

During the evaluation of the coupled aero-thermal simulations a mismatch in temperatures was observed which is shown later in this chapter. This could be caused by the use of a wrong ambient temperature, as this temperature now has an influence on the temperature prediction due to the coupling. Therefore simulation 1.1 was restarted with an elevated $FNTR$. The boundary conditions for this additional simulation can be seen below in Table 6.5. Test-run 1-1 is the original run used in the previous chapter, whether test-run 1-2 is the run with the corrected $FNTR$. The CFD simulation based on test-run 1-2 is called simulation 1.3. Due to time constraints the corrected $FNTR$ could not be tested for the other CFD simulations.

Table 6.5: Summary of corrected boundary conditions

Test-run	$\boldsymbol{M_\infty}[-]$	$\boldsymbol{FNPR}[-]$	$\boldsymbol{PS}[-]$	$\boldsymbol{FNTR}[-]$	$\boldsymbol{TS}[-]$
1-1	0.05	1.52	1.06	1.00	2.15
1-2	0.05	1.52	1.06	1.07	2.15

Table 6.6 shows the test-matrix including the performed coupled aero-thermal simulations. From the table it can be easily seen which simulations are used as starting point for the coupled simulations, described in Chapter 5, and which boundary conditions are used for the non-coupled surfaces of the thermal model.

Table 6.6: Test-matrix of performed coupled aero-thermal simulations

Simulation #	**Geometry**	**Mesh**	**BC's**	**# of Coupling It.**	**Non-coupled BC's**
5	1:5 Scaled	Mesh 2	1-1	30	Ambient Temp.
6	1:5 Scaled	Mesh 2	1-1	30	Temp. Profile
7	1:5 Scaled	Mesh 2	1-2	30	Temp. Profile
8	1:5 Scaled	Mesh 2	2	30	Temp. Profile

Simulation 5 and 6 are started from CFD simulation 1.1 (base). Simulation 7 is started from simulation 1.3 (base+ correct T_{amb}) and simulation 8 is started from simulation 3.1 (different BC´s).

For the ease of the reader the numbered simulations can also be recognised by the short descriptions listed below,

- Simulation 5: T_{amb}
- Simulation 6: $T_{profile}$
- Simulation 7: Correct T_{amb} + $T_{profile}$
- Simulation 8: Different BC´s + $T_{profile}$

The exchange of boundary conditions is performed 30 times. The CFD simulation performs 100 iterations between two subsequent couplings and the thermal solver performs 2000 iterations in which the thermal solution fully converges.

6.4 Results

In this section the results for the performed coupled aero-thermal simulations summarised in Table 6.6 are described. As was seen in Chapter 5 the five monitored thermocouples showed large oscillations for meshes 1 and 2 but almost converged for mesh 3. The errors of the CFD simulation results compared to the experimental data were however still considerable with errors up to 32% for simulation 1.2 on the bottom side of the door where the mixing flow impinges on the door.

The aim of this chapter is to improve the temperature prediction on the door’s surface. It is investigated if by including the door structure into the simulations a more realistic temperature prediction is found. For instance, the hot air impinging on the side-flanges of the door should, compared with the experiments, not be there (see Figure 6.7 on the left). By including the door structure it is investigated if the temperature prediction in these regions of the door can be improved.

Convergence of the coupling iterations is in this case also important. The coupling is considered to be converged when the averaged door heat flux, temperature and maximum temperature reach a steady-state value. The averaged door heat flux is obtained from the flow simulations while the averaged and maximum temperatures are obtained from the thermal simulations.

6.4.1 Base Simulation Results

Figure 6.3 below shows the results of the coupled simulation 5 in comparison with the non-coupled simulation 1.2 and experimental data for thermocouples T501 to T515. The results of the 15 thermocouples on both the left and right side of the door are included.

As can be seen from the figure there is a large deviation in coupled and non-coupled simulations. The temperature value of thermocouple T515 is for instance reduced by 36% by performing the coupled simulation. The temperature values on the bottom side of the door are closer to the experimental data whether the values on the top side of the door deviate more from the experimental data compared to the non-coupled simulation.

Comparing the coupled and non-coupled simulation results shown in Figure 5.17 shows that the large irregularities seen in the non-coupled results are not present anymore. Also the asymmetry in the left and right side temperature values is not present. This implies that by coupling the simulations the large temperature variations, caused by the hot and cold streams originating from the mixing flow, are decreased resulting in a smoother temperature distribution on the door's surface. The maximum errors in temperature values for the non-coupled and coupled simulations are 32% (T515) and 18% (T508, right) respectively.

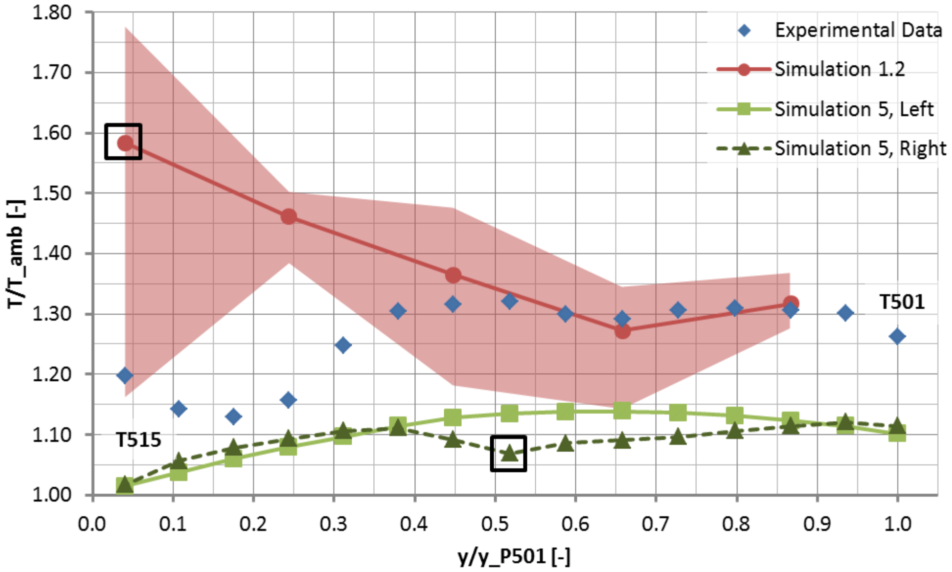

Figure 6.3: Comparison of non-coupled and coupled temperatures with experimental data for simulation 1.2 (base) and 5 (T_{amb}) for thermocouples T501 to T515

The monitor plots for all simulations can be seen below.

Figure 6.4 shows the averaged door heat flux taken from the CFD simulations. At the start of the coupled simulations, the heat flux shows a large overshoot but gradually the overshoots at the start of every coupling iteration decrease. Simulation 5 starts from simulation 1.1. As discussed in the previous chapter, the simulation results of simulation 1.1 showed oscillations which can also be recognised in the averaged heat flux monitor on the door. The averaged heat flux shows an oscillation in the order of 10% for simulation 5.

Figure 6.5 shows the averaged door temperature taken from the thermal solver. Also here the jumps in averaged door temperature decrease with increasing number of coupling iterations. A clear connection can be seen between the oscillations in heat flux values and oscillations in temperature values. Because in the previous chapter was already shown that oscillations are present in the CFD simulation results, it can be concluded that the oscillations in the thermal simulation results are caused by the CFD simulation. The average temperature shows an oscillation in the order of 1% from its mean value.

Figure 6.6 shows the maximum temperature on the door taken from the thermal solver. The values of simulation 5 are shown on the right axis whether the values for the other simulations are shown on the left axis. The jumps in maximum temperature are larger, but as can be seen, converge between two coupling iterations. The difference between the maximum and minimum value shown in the figure for simulation 5 is in the order of 6%.

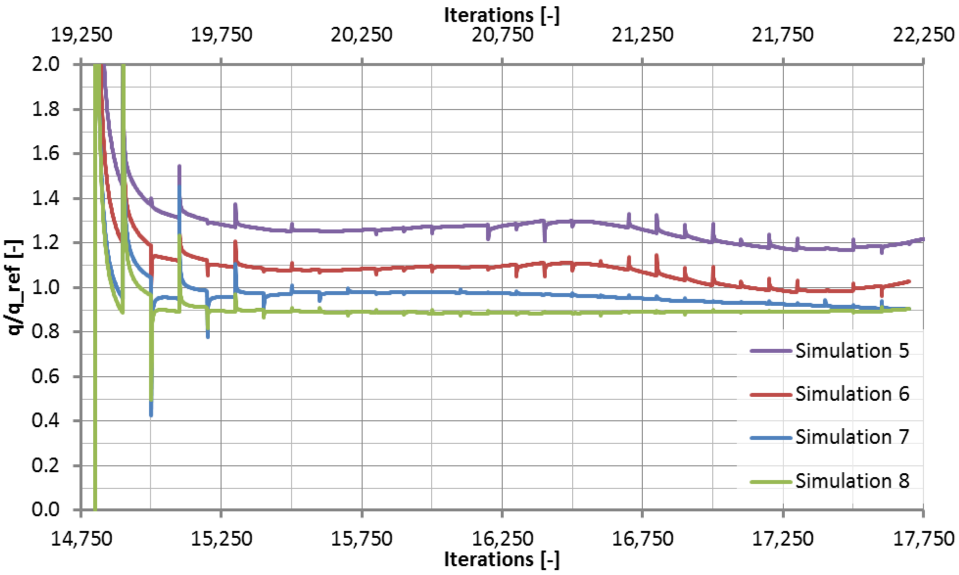

Figure 6.4: Averaged normalised door heat flux for all performed coupled simulations (CFD Simulation)

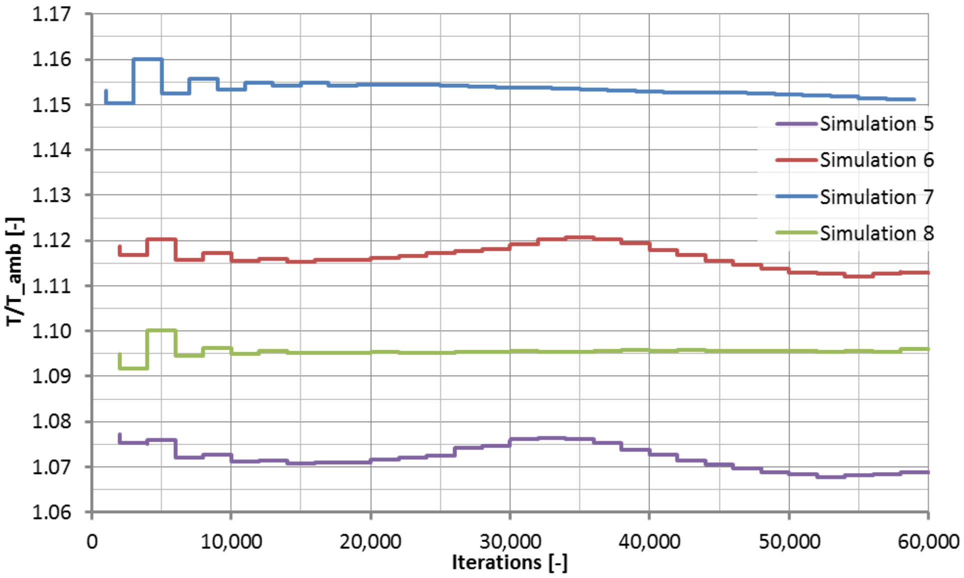

Figure 6.5: Averaged normalised door temperature for all performed coupled simulations (Thermal solver)

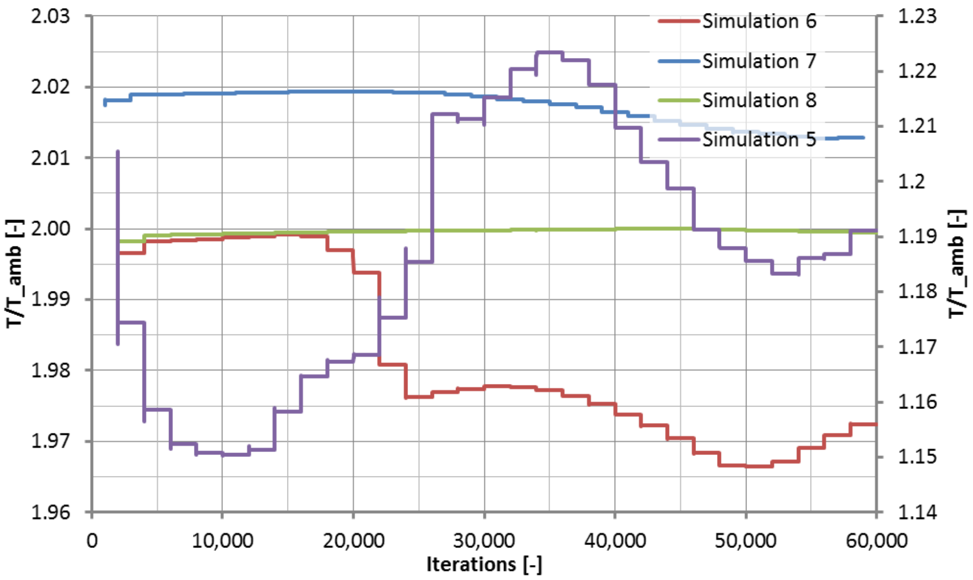

Figure 6.6: Maximum normalised door temperature for all performed coupled simulations (Thermal solver)

From this base simulation can be seen that the coupling iterations converge to a certain level, but due to the oscillations still present in the CFD simulation, full convergence is not reached. The large irregularities and oscillations in temperature values seen for the non-coupled iterations are improved considerably. The accuracy of the results however still needs to be improved. To improve the accuracy of the base simulation a list of possible improvements was again established. Some of these suggested improvements are discussed in the following sections, others could not be investigated, mainly due to time constraints. The determined possible improvements are as follows,

- Using a temperature profile for the non-coupled walls instead of a constant temperature set equal to the ambient temperature. This improvement is discussed in section 6.4.2.
- The influence of the corrected ambient temperature boundary condition is investigated in section 6.4.3
- Next to this, a coupled simulation is performed not by starting from simulation 1.1 but from simulation 3.1, which showed a better convergence as was shown in the previous chapter. This is discussed in section 6.4.4.
- Coupling all walls of the solid to the CFD simulation is desired. This was investigated shortly but a converged solution could not be found. Due to time constraints this option could not be investigated further.
- A mesh study for the solid door geometry could probably improve the results in some parts of the door. Due to time constraints this could not be investigated.

6.4.2 Influence of Non-Coupled Walls Boundary Conditions

In the base simulation, the non-coupled walls were given a constant temperature boundary condition equal to the ambient temperature. For the door-outer-surface this is a realistic boundary condition, while the temperatures here are equal to the ambient temperature.

On the door-outer-side-flanges however this boundary condition is not realistic. Mixed flow from the mixer flows along the door-outer-side-flanges when it “leakes” to the freestream and thereby exposes the door to temperatures considerably higher than the ambient temperature.

As discussed before, coupling of these walls with the CFD simulations did not work, therefore the temperature profile at the start of the coupling iterations is prescribed as boundary condition to all non-coupled surfaces except the nacelle-door-connection surfaces (because these surfaces were not exposed to the flow).

Figure 6.7 below shows six contour plots of the temperature distribution on the door. The left two contour plots show the temperature prediction results of simulation 1.1. The two contour plots in the centre represent the results of simulation 5, while the plots on the right show the results of simulation 6.

The hot streams on the door-side-flanges for simulation 1.1 can be recognised in the plots as discussed before. By applying a constant ambient temperature boundary condition, these "hot-spots" vanish almost completely as shown in the centre of Figure 6.7. Finally, applying temperature profile boundary conditions show an increase in maximum temperature in the door-side-flange regions again.

This figure already qualitatively shows the large influence, which the prescribed non-coupled walls boundary conditions have on the coupled walls temperature prediction. The following discussion evaluates quantitatively the differences of the used boundary conditions.

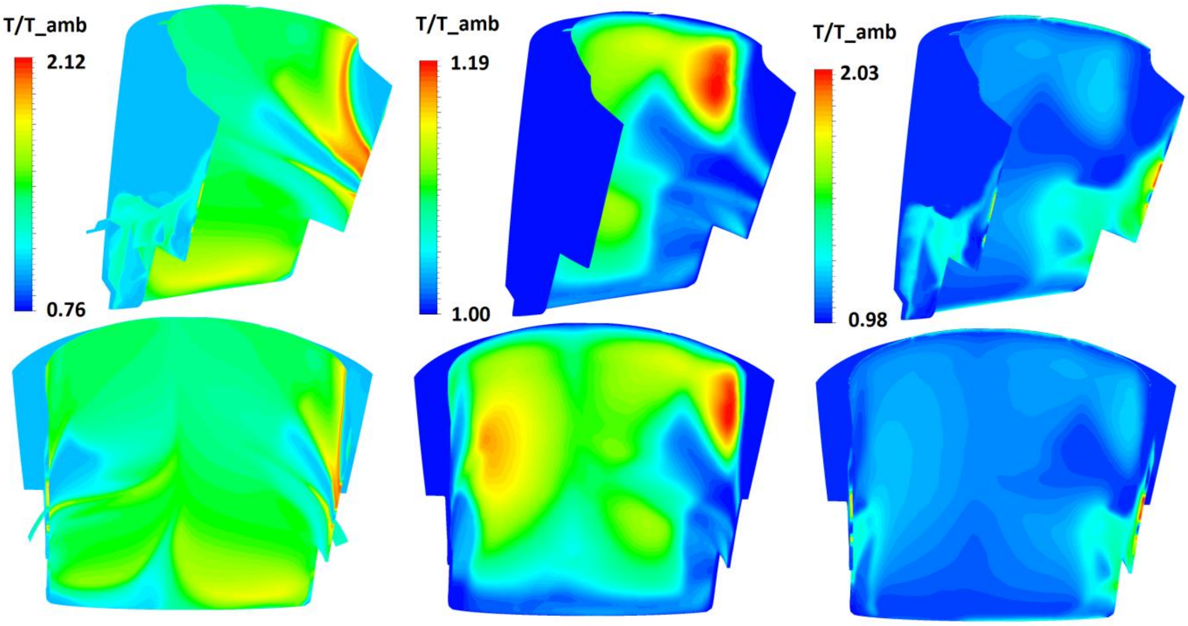

Figure 6.7: Contour plots of the temperature distribution for simulation 1.1 (base) (left), simulation 5 (T_{amb}) (centre) and simulation 6 ($T_{profile}$) (right)

Figure 6.8 shows the results of the coupled simulations 5 and 6 in comparison with the non-coupled simulation 1.2 and experimental data for thermocouples T501 to T515. By using the temperature profile boundary conditions no improvement is obtained in this region of the door. This is as expected, because the door-outer-surface boundary condition has the largest influence on the solution in this region of the door. The ambient temperature boundary condition is here valid and therefore the solution is not improved by applying the temperature profile boundary condition. The maximum errors for simulation 5 and 6 are 18% (T508, right) and 19% (T508, right) respectively, compared to the maximum error for the non-coupled simulations of 32% (T515).

As explained above, applying the temperature profile boundary condition has the most effect in regions where the CFD predicted door temperatures deviate from the ambient temperature. This is the case in the door-side-flanges-region. Figure 6.9 shows the results of the coupled simulations in comparison with the non-coupled simulation 1.1 and experimental data for thermocouples T521 to T530 located in cross-flow direction (see Figure 5.10). Note that the non-coupled simulation 1.1 results are the temperature values of the CFD simulation at the start of the coupling. Unfortunately, these are not averaged temperature values.

From the figure it can be seen that by performing the coupled simulation the temperature prediction is improved considerably. The maximum errors for simulation 5 and 6 are 24% (T529, left) and 11% (T525, left) respectively, compared to the maximum error for the non-coupled simulations of 32% (T521, right). Interesting to note is the difference in results between simulation 5 and 6 in the door-side-flange-region. Simulation 5 shows an error of 24% for the T529 thermocouple on the right side of the door whether simulation 6 shows an error of 2%. This illustrates the importance of prescribing the right thermal boundary conditions for the non-coupled walls as also shown in Figure 6.7.

The edges of the door-side-flanges are not coupled and therefore have the same high temperature as the CFD simulation results (see Figure 6.7). This especially has an influence on the prediction of the T530 thermocouple as can be seen from Figure 6.9 (which is not taken into account while calculating the maximum errors). Coupling these edges would probably give a more accurate prediction and is definitely a recommendation for further work. This shows that prescribing the right boundary conditions for the non-coupled walls can be of great influence on the simulation results.

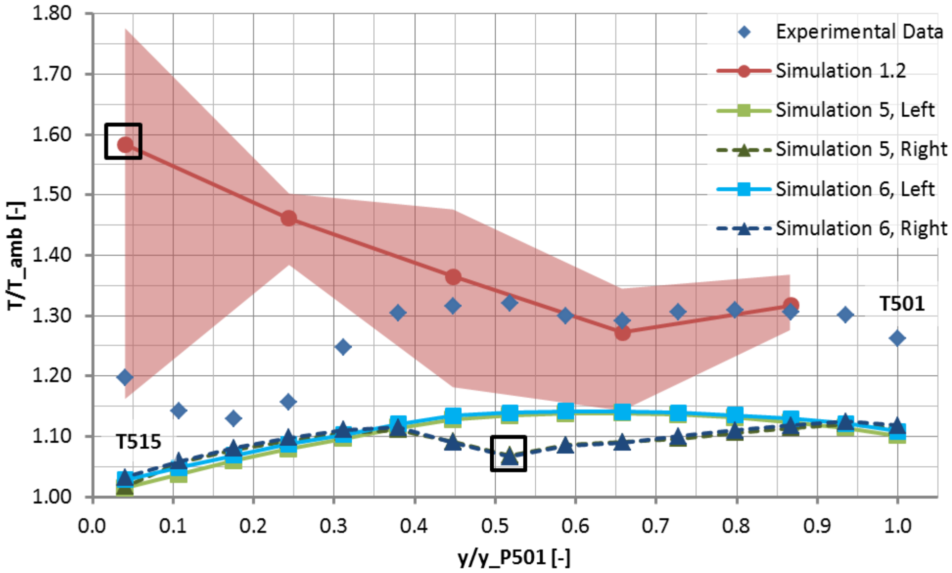

Figure 6.8: Comparison of non-coupled and coupled temperatures with experimental data for simulations 1.2 (base), 5 (T_{amb}) and 6 ($T_{profile}$) for thermocouples T501 to T515

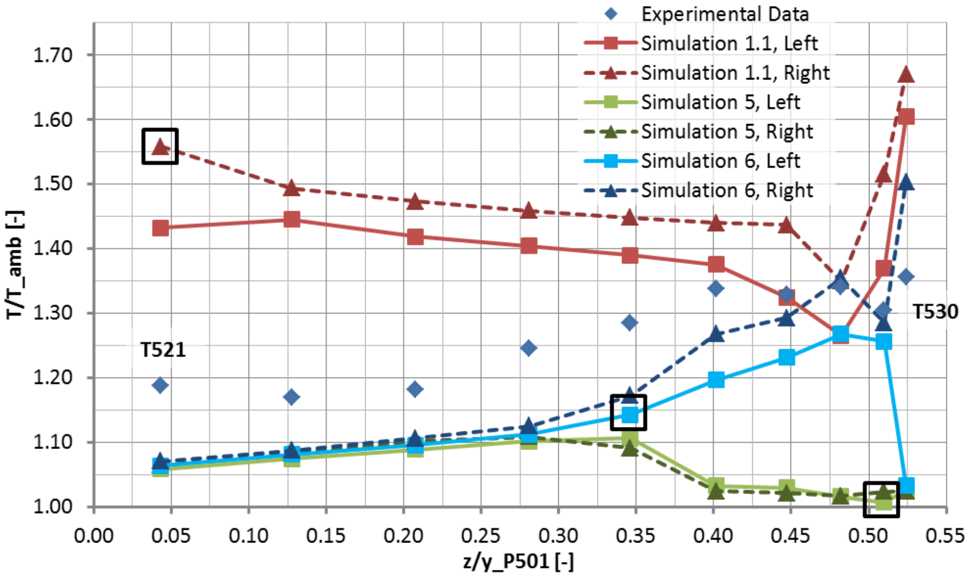

Figure 6.9: Comparison of non-coupled and coupled temperatures with experimental data for simulations 1.1 (base), 5 (T_{amb}) and 6 ($T_{profile}$) for thermocouples T521 to T530

As can be seen from Figure 6.4 to Figure 6.6 no clear difference can be seen in the convergence behaviour of both coupled simulations. The only observed difference is that the maximum temperature is higher for simulation 6 because of a better prediction in the inner-door-side-flange region.

6.4.3 Influence of Corrected Ambient Temperature

As discussed before, the wrong ambient temperature was used during the simulations performed in Chapter 5. Unfortunately, due to the lack of computational resources and time not all simulations could be restarted with the corrected ambient temperature. Simulation 1.1 could however be restarted and is used in this section to investigate how the coupled simulations are influenced by this higher ambient temperature. The non-coupled simulation with corrected ambient temperature is called simulation 1.3.

Figure 6.10 to Figure 6.12 show the results of the coupled simulations 5 and 7 in comparison with the non-coupled simulation 1.3 and experimental data for thermocouples T501 to T515, T516 to T520 and T521 to T530 respectively. From all three figures can be clearly seen that the corrected ambient temperature shifts the results up by about 6% which is also the shift in ambient temperature.

From Figure 6.10 can be seen that still a considerable deviation between simulation 7 and the experimental data is present. The largest errors are found on the top part of the door. The maximum errors in temperature values for simulations 5 and 7 are 18% (T508, right) and 15% (T509, left) respectively. The same deviation can be seen from Figure 6.11 which represents the temperatures of the thermocouples in the bottom centre of the door. The maximum errors observed in Figure 6.11 are 18% (T520) and 13% (T520) for simulations 5 and 7 respectively.

As described in section 5.1 the door-actuator and door-actuator-void are removed from the geometry. The door-actuator, which is normally located above thermocouple T516, blocks the flow coming from the bottom of the door and thereby stagnates the flow, which possibly explains the higher measured temperatures for thermocouples T516 to T520. The door-actuator-void normally located above the door-actuator causes the flow to slow down because it provides a volume increase. This possibly explains the higher measured temperatures for thermocouples T501 to T511.

Comparing the coupled simulation results for simulations 6 and 7, which are shown in Figure 6.9 and Figure 6.12, shows that the temperature prediction for thermocouples T521 to T525 is improved by the corrected ambient temperature. For thermocouples T526 to T530 the temperature prediction of simulation 7 is worse than it is for simulation 6. This is explained by the fact that the temperature profile used at the start of the coupled simulation 7 is different than for simulation 6, because the two starting CFD simulations are different.

Using a temperature profile improves the solution considerably as seen in the previous section. In the door-side-flange-regions the door is thin compared to the other parts of the door and is therefore more sensitive to the prescribed outer-surface boundary conditions.

The results of the current and previous section show that the influence of the outer-surface boundary conditions mainly determine the accuracy of the results. For further work it is therefore recommended to investigate the possibility to also couple the outside walls to the CFD simulation.

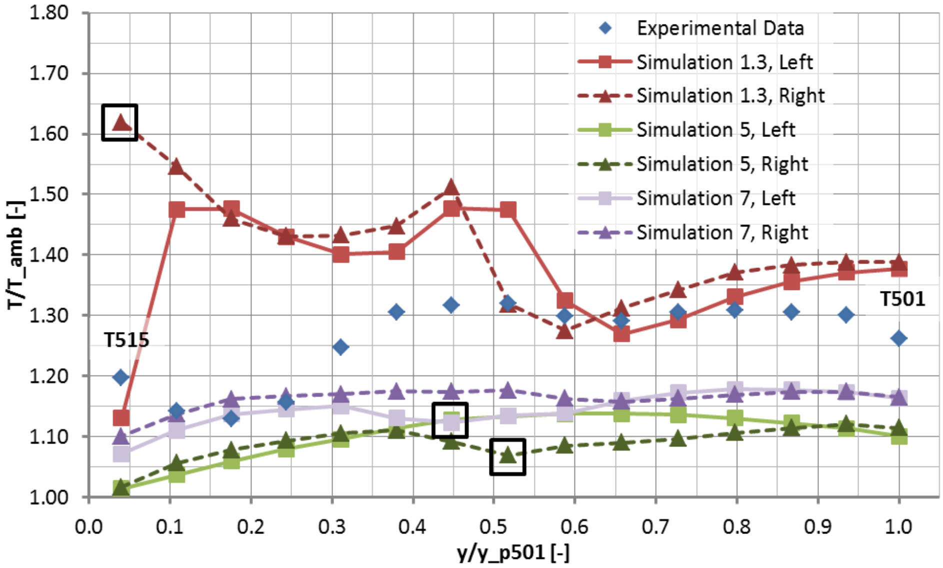

Figure 6.10: Comparison of non-coupled and coupled temperatures with experimental data for simulations 1.3 (base + correct T_{amb}), 5 (T_{amb}) and 7 (correct T_{amb} + $T_{profile}$) for thermocouples T501 to T515

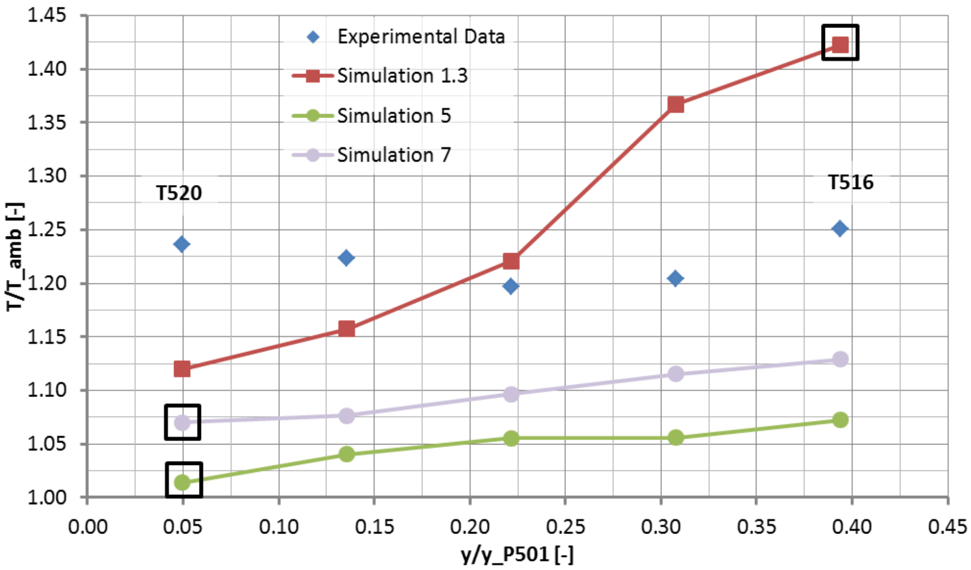

Figure 6.11: Comparison of non-coupled and coupled temperatures with experimental data for simulations 1.3 (base + correct T_{amb}), 5 (T_{amb}) and 7 (correct T_{amb} + $T_{profile}$) for thermocouples T516 to T520

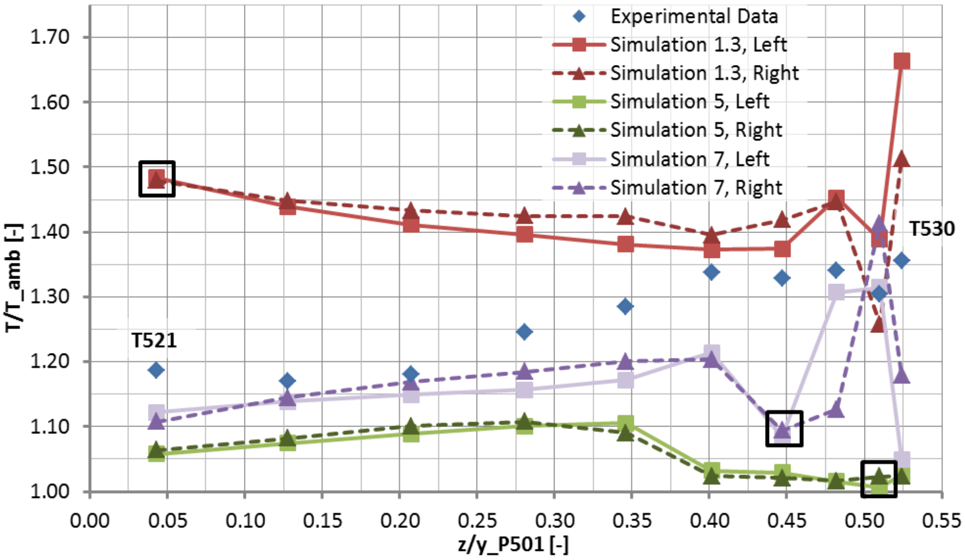

Figure 6.12: Comparison of non-coupled and coupled temperatures with experimental data for simulations 1.3 (base + correct T_{amb}), 5 (T_{amb}) and 7 (correct T_{amb} + $T_{profile}$) for thermocouples T521 to T530

From the averaged heat flux and temperature plots it can be seen that the oscillations are less pronounced than for simulation 5 and 6. Also the jumps in maximum temperature are smaller than for simulation 5 and 6. As can be seen from Figure 6.13 the convergence of the BPD mass flow rate for simulation 1.3 is not much better than for simulation 1.1. Therefore, the increased corrected ambient temperature did not improve the convergence of the CFD simulations, but made the coupled simulations more stable resulting in fewer oscillations in the averaged heat flux and temperature plots.

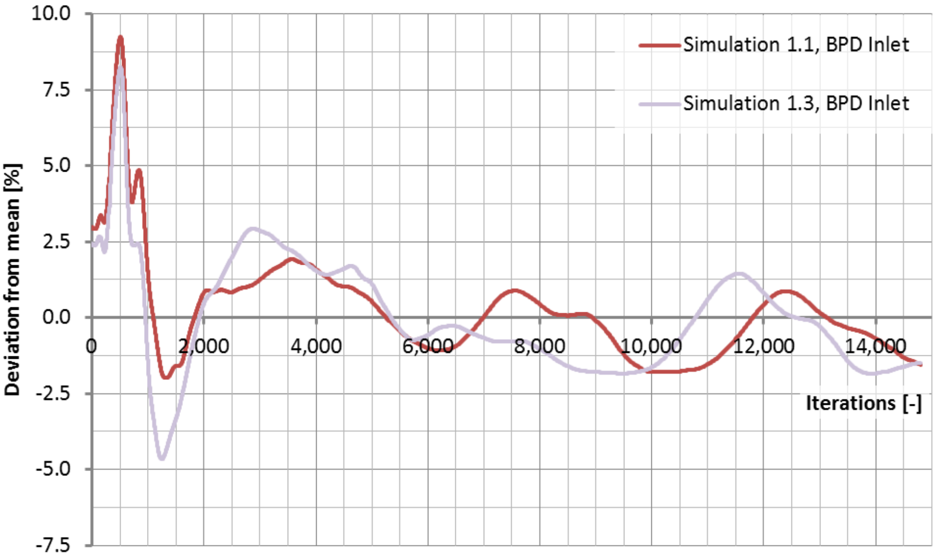

Figure 6.13: Mass flow rate monitor for simulations 1.1 (base) and 1.3 (base + correct T_{amb}) for the BPD inlet given as deviation from the mean

6.4.4 Influence of Convergence Level of the CFD Simulation

As was seen in section 5.6.3 by using a lower $FNPR$ the convergence level of the CFD simulation was improved. As was seen in sections 6.4.1 and 6.4.2, the coupling iterations did not fully converge and some oscillations can still be seen in the averaged heat flux and temperature plots shown in Figure 6.4 and Figure 6.5. Cause for this could be the oscillations still present in the results of CFD simulation 1.1 which is used to start the coupling simulations. By starting from CFD simulation 3.1 it is investigated if the convergence of the coupling simulations can be improved and if this results in a more accurate temperature prediction.

Figure 6.14 shows the results of the coupled simulations 5 and 8 in comparison with the non-coupled simulations 1.2 and 3.2 and experimental data for thermocouples T501 to T515. From the figure can be seen that the experimental data for test-run 1 and 2 are almost identical. Because of this, the two coupled simulations can be compared with each other. From the results can be seen that using different boundary conditions does not improve the accuracy of the solution although the convergence of the coupled iterations is improved. Plots for thermocouples T516 o T520 and T521 to T530 show similar results.

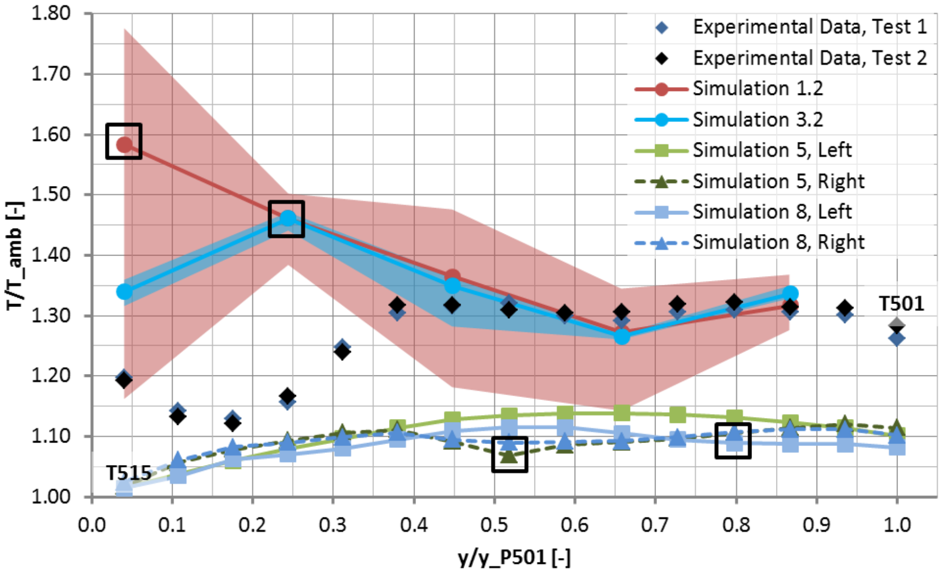

Figure 6.14: Comparison of non-coupled and coupled temperatures with experimental data for simulations 1.2 (base), 3.2 (different BC´s), 5 (T_{amb}) and 8 (different BC´s + $T_{profile}$) for thermocouples T501 to T515

6.5 Conclusions & Recommendations

The aim of this chapter was to improve the temperature prediction on the TRU door-inner-surface and door-side-flanges by performing a coupled aero-thermal simulation. As was seen in Chapter 5 the maximum errors in the temperature distribution prediction could be as high as 32%. Also in this chapter a base coupled simulation is performed which reduced the maximum error in temperature prediction from 32% to 18%. Additional simulations were performed to test possible improvements to the base simulation. The following conclusions can be drawn from the simulations performed in this chapter.

Using temperature profiles taken at the start of the coupled simulations from the CFD results improves the temperature prediction in regions where the ambient temperature boundary condition is not valid. This change in boundary conditions decreased the error in predicted temperatures from 24% to 2% in the door-side-flange regions.

An increase in ambient temperature of 6% directly translates into an increase in predicted temperatures. The maximum error of 18% for thermocouple T508 of simulation 5 is further decreased to 15%. The error of 11% for thermocouple T521 of simulation 5/6 is decreased to 6% by the higher ambient temperature. This shows that the prescribed boundary conditions for the non-coupled walls are of large influence on the accuracy of the coupled simulations.

As is seen from the convergence plots of the simulations the convergence of the coupled simulations is determined by the convergence level of the CFD simulations.

The use of temperature profiles and a correct ambient temperature both improved the results as discussed above. To further improve the results of the coupled simulations some recommendations for further work can be made,

- Including the door-actuator and door-actuator-void could improve the coupled simulation results in the centre and top parts of the door as discussed in section 6.4.3.

- Coupling all door-walls or at least the outer-door-side-flanges walls to the CFD simulation will probably improve the coupled simulation results.
- A coupled simulation starting from CFD simulation 4.2 is highly recommended.
- Temperature monitors at the locations of the thermocouples are recommended to get a better understanding of the oscillatory behaviour of the modelled temperatures for the coupled simulations.
- Although with the aero-thermal test cases is shown that the solid mesh has no influence on the accuracy of the solution, a mesh refinement study should be performed to confirm that the solution is (solid) mesh independent.

Chapter 7 Conclusions & Recommendations

In this chapter, the main conclusions and recommendations based on the previous described research are given. The conclusions are given in section 7.1 followed by the recommendations in section 7.2.

7.1 Conclusions

The main goal of this master thesis project as described in the introduction of this report was as follows,

The prediction of the wall temperature distribution on the door of a target-type thrust reverser by means of coupled aero-thermal simulations

By the validation of the solver capabilities a strategy was determined to solve for the TRU flow topology. The evaluation of the existing coupling techniques and validation of the coupled CFD/FE analysis technique resulted in a successful coupled aero-thermal simulation. The results of the coupled aero-thermal simulations show deviations with the experimental data but the maximum error is reduced from 32% to 15% compared to the non-coupled CFD simulation results.

This report serves as a good foundation in order to further develop the coupled aero-thermal simulations such that the method can be used for design purposes. Recommendations for further work are given in section 7.2.

As described in the project set-up this master thesis project was divided into two main parts. Both parts have their own research objective. The conclusions based on these two research objectives are discussed below.

The research objective of the first part of the project was formulated as follows,

The research objective of the first part of this project is to determine the flow topology around the TRU with a satisfactory level of convergence and accuracy by creating a high quality mesh and selecting the most suitable computational model by making use of the Ansys Fluent software

From the validation test cases was concluded that the SST k-ω model is the preferred model to use for the TRU simulations. Unfortunately, the Realizable k-ε model was the only model with which a flow simulation was found. Therefore, this turbulence model was used for the remainder of this master thesis project.

From the validation test cases was also shown that structured meshes were less dissipative in areas where variations in velocity directions are high like mixing and vortical flows. Incorporating structured mesh blocks in the hybrid mesh used for the TRU simulations was not feasible, therefore a semi-structured mesh supplied by RRD was also tested in this project.

A compromise was found between the y^+ value of the first boundary layer cell, number of prism layers and mesh quality. The y^+ value on the door-inner-surface was on average 0.5 and 25 prism layers were used while the mesh quality was considerably improved in comparison with a reference mesh previously used by RRD.

From the different simulations performed to determine the flow topology it was concluded that both the $FNPR$ and meshing strategy and quality influence the solution convergence. A $FNPR$ of 1.3 gave a converged solution whether a value of 1.5 showed oscillations in the mass flow rate, pressure and temperature monitor plots. The simulations performed on the semi-structured mesh with a $FNPR$ of 1.5 also gave a converged solution which implies that the meshing strategy and quality also have an influence on the solution convergence.

The maximum error in pressure values of 8% in comparison with the experimental data could be improved by the use of a lower $FNPR$ and semi-structured mesh to 3% and 7% respectively. The maximum error in temperature values of 32% in comparison with the experimental data was decreased to 22% by making use of the semi-structured mesh.

From the research can be concluded that an almost converged solution was found for the simulations performed on the semi-structured mesh and with a lower $FNPR$. The accuracy of the simulation on a semi structured mesh is reasonable with a maximum error in modelled pressure and temperature values of 7% and 22% respectively.

The research objective of the second part of the project was formulated as follows,

The research objective of the second part of this project is to perform coupled aero-thermal simulations to determine the wall temperature distribution on the TRU door by selecting a feasible coupling technique and validate this technique with simple test cases

The coupling technique used in this master thesis project makes use of a CFD and thermal solver and is called the coupled CFD/FE analysis technique. Boundary conditions at the interface between fluid and solid are exchanged till a converged temperature distribution at the interface is found.

From the aero-thermal validation test cases it was concluded that the solid mesh has no large influence on the solution accuracy. The y^+ value of the fluid mesh however has shown to have an influence on the solution accuracy. A finer y^+ value gave a more accurate temperature prediction.

The influence of several factors on the accuracy of the temperature prediction on the TRU door was investigated. Conclusions from this investigation are that the ambient temperature used in the CFD simulations has an influence on the temperature prediction. The use of temperature profiles (extracted from the CFD simulation at the start of the coupled simulations) as boundary conditions for the non-coupled walls has shown to have a large influence on the temperature prediction in the door-side-flange regions.

By correcting the ambient temperature and using temperature profiles as boundary conditions, the maximum error in temperature values for the non-coupled simulations of 32% was reduced to 15% for the coupled simulations. Using temperature profiles instead of a constant temperature as boundary condition for the non-coupled walls, reduced the error in temperature prediction from 24% to 2% in the door-side-flange regions.

The convergence of the coupled simulations is dominated by the convergence of the initial CFD simulation. If oscillations in mass flow rate, pressure or temperature monitors are still present in the CFD simulation at the start of the coupled simulations, these will translate into oscillations of the temperature prediction on the door.

From the above conclusions can be seen that the research objectives of this master thesis are to a large extent satisfied. The accuracy of both the non-coupled and coupled simulations can still be improved in terms of pressure and temperature values. Convergence of the non-coupled simulations is achieved with the right boundary conditions and meshing strategy. The convergence of the coupled simulations is mainly influenced by the convergence level of the initial CFD simulation.

7.2 Recommendations

The research described in this master thesis report serves as a good foundation for further research in the field of coupled aero-thermal simulations to predict the temperature distribution on a target-type thrust reverser door.

From the results presented in this thesis report the author of this report came up with recommendations for further work. These recommendations are divided in recommendations to improve the accuracy of the non-coupled simulations and coupled simulations.

The recommendations to improve the accuracy of the non-coupled simulations are as follows,

- The influence of the simplifications to the geometry should be determined to ensure the absence of the door-actuator and door-actuator-void do not cause the inaccuracies in simulation results.
- A simulation with a 360° TRU geometry should be performed. This, because as explained in section 5.5, the flow from the mixer is asymmetric. It is believed that the symmetry plane constraints the mixing flow and thereby possibly incorrectly models the developing mixing flow, which determines to a large extent the temperature distribution on the TRU door.
- A simulation with the SST k-ω should be performed. This because the SST k-ω turbulence model has shown to give more accurate results than the Realizable k-ε model during the evaluation of the test cases.
- A U-RANS simulation can be performed to make sure the oscillations seen in the monitor plots for the simulations performed on a hybrid mesh are not caused by unsteady effects.
- Once a converged solution is found, for instance for the simulations with a lower $FNPR$ or on a structured mesh, a mesh refinement study should be performed to ensure the mesh independent solution is found.
- More pressure and temperature monitors should be inserted in the simulations to get a better understanding of the oscillations still present in the solutions for the unstructured meshes.
- The validity of the experiments should be re-evaluated. From analysing the pictures shown in the experimental test report was observed that the thermocouples are emerged in the flow and therefore to a lesser extend measure the door surface temperatures. Other measurement techniques like thermal paint or infrared measurement techniques could also be considered.

The recommendations to improve the accuracy of the coupled simulations are as follows,

- Coupling of all surfaces of the TRU door to the CFD simulation should be investigated. From the performed research could already be seen that the boundary conditions are of large influence on the temperature prediction. Therefore, coupling all surfaces is believed to give a further improvement in accuracy.
- Due to time constraints a coupled simulation initialised by the converged solution of the semi-structured mesh could not be performed. Using this CFD simulation as a starting point of the coupled simulations could improve the coupled simulation results.
- When a converged solution is found also here a mesh refinement study for the solid mesh should be performed to ensure a mesh independent solution is found.

Chapter 8 Bibliography

Ansys Inc., 2011a. Ansys Fluent (14.0). [Computer Program] Ansys Inc. Available at: http://www.ansys.com/Products/Simulation+Technology/Fluid+Dynamics/Fluid+Dynamics+Products/ANSYS+Fluent [Accessed 22 April 2014].

Ansys Inc., 2011b. Ansys Fluent Theory Guide (14.0). [pdf] Canonsburg, PA, USA: Ansys Inc. Available at: http://cdlab2.fluid.tuwien.ac.at/LEHRE/TURB/Fluent.Inc/v140/flu_th.pdf [Accessed 11 May 2014].

Ansys Inc., 2011c. Ansys Fluent Users Guide (14.0). [pdf] Canonsburg, PA, USA: Ansys Inc. Available at: http://cdlab2.fluid.tuwien.ac.at/LEHRE/TURB/Fluent.Inc/v140/flu_ug.pdf [Accessed 23 April 2014].

Ansys Inc., 2011d. Introduction to ANSYS Meshing, Lecture 7: Mesh Quality [Powerpoint Presentation]. Canonsburg, PA, USA: Ansys Inc.

AZO Materials, 2015. 416 Stainless Steel Material Properties. [online] Available at: http://www.azom.com/article.aspx?ArticleID=971 [Accessed 17 March 2015]

Back, L.H., Massier, P.F., Gier, H.L., 1964. Convective Heat Transfer in a Convergent-Divergent Nozzle. *International Journal of Heat and Mass Transfer*, Volume 7, Article 5, pp. 549-568.

Bardina, J.E., Huang, P.G., Coakley, T.J., 1997. Turbulence Modeling Validation, Testing and Development. *NASA Technical Memorandum 110446.*

Bell, J.H., Mehta, R.D., 1990. Development of a Two-Stream Mixing Layer from Tripped and Untripped Boundary Layers. *AIAA Journal,* Volume 28, Article 12, pp. 2034-2042.

Blazek, J., 2001. *Computational Fluid Dynamics: Principles and Applications*. 1st Edition. Amsterdam: Elsevier Science Ltd.

Blin, L., Hadjadj, A., Vervisch, L., 2003. Large Eddy Simulation of Turbulent Flows in Reversing Systems. *Journal of Turbulence*, Volume 4, Article 1.

Bombardier Business Aircraft, 2015. Bombardier Inc. [online] Available at: http://businessaircraft.bombardier.com/en/aircraft/global/global5000.html [Accessed 04 March 2015]

Cambridge Flow Solutions Ltd., 2014. Boxer (3.6.0). [Computer Program] Cambridge Flow Solutions Ltd. Available at: http://www.cambridgeflowsolutions.com/en/products/boxer-mesh/ [Accessed 8 April 2014]

CentaurSoft, 2012. Centaur Plus (9.7). [Computer Program] CentaurSoft. Available at: https://www.centaursoft.com/products [Accessed 24 October 2014].

Chew, J.W., Hills, N.J., 2007. CFD for Turbomachinery Internal Air Systems. *Philosophical Transactions of the Royal Society A: Mathematical, Physical and Engineering Sciences*, Volume 365, pp. 2587-2611.

Chiu, S., Roth, K.R., Margason, R.J., Tso, J., 1993. A Numerical Investigation of a Subsonic Jet in a Crossflow. In: *AIAA 31st Aerospace Sciences Meeting and Exhibit*, Reno, USA, January 11-14, 1993.

Clarkson, R., 2010. Thermal Analysis, Heat Transfer Fundamentals. [Powerpoint Presentation]. Rolls Royce plc, London.

Delville, J., Ukeiley, L., Cardier, L., Bonnet, J.P., Glauser, M., 1999. Examination of Large-Scale Structures in a Turbulent Plane Mixing Layer. Part 1. Proper Orthogonal Decomposition. *Journal of Fluid Mechanics*, Volume 391, pp. 91-122.

Druault, P., Delville, J., Bonnet, J.P., 2005. Experimental 3D Analysis of the Large Scale Behaviour of a Plane Turbulent Mixing Layer. *Flow, Turbulence and Combustion,* Volume 74, Article 2, pp. 207-233.

Dennis, R.F., Tso, J., Margason, R.J., 1993. Induced Surface Pressure Distribution of a Subsonic Jet in a Crossflow. In: AIAA Meeting Papers, *AIAA Powered Lift Conference*. Santa Clara, USA, December 1-3, 1993.

Eckert, E., Weisse, W., 1941. Die Temperatur Unbeheizter Koerper in einem Gasstrom hoher Geschwindigkeit. *Forschung auf dem Gebiet des Ingenieurswesens A,* Volume 12, Article 1, pp. 40-50.

Eggenspieler, G., 2012. Turbulence Modeling. [Powerpoint Presentation]. Ansys Inc., Canonsburg, PA, USA.

Elgin Fastener Group, 2015. 416 Stainless Steel Material Properties. [online] Available at: http://elginfasteners.com/resources/raw-material-technical-data-specifications/stainless-steel-416-material-property-data-sheet/ [Accessed 17 March 2015]

E-news. [online] Available at: http://www.e-news.com.bd/2014/11/26/gulfstream-manufactures-100th-g650 [Accessed 04 March 2015]

Fric, T.F., Roshko, A., 1994. Vortical Structure in the Wake of a Transverse Jet. *Journal of Fluid Mechanics*, Volume 279, pp. 1-47.

Illingworth, J., Hills, N.J., 2004. *CFD-SC03 Coupling*. University of Sussex.

Imlay, S.T., 1986. Numerical Solution of 2-D Thrust Reversing and Thrust Vectoring Nozzle Flowfields. In: AIAA Meeting Papers, *AIAA 24th Aerospace Sciences Meeting and Exhibit*. Reno, USA, January 6-9, 1986.

Imlay, S.T., Kao, T.J., McMaster, D.L., MacCormack, R.W., 1984. Solution of the Navier-Stokes Equations for Flow within a 2-D Thrust Reversing Nozzle. In: AIAA Meeting Papers, *AIAA 22nd Aerospace Sciences Meeting and Exhibit*. Reno, USA, January 9-12, 1984.

Jovic, S., Driver, D.M., 1994. Backward-facing Step Measurements at Low Reynolds Number, Re_h = 5000. *NASA Technical Memorandum 108807.*

Kao, K.H., Liou, M.S., 1997. Application of Chimera/Unstructured Hybrid Grids for Conjugate Heat Transfer. *AIAA Journal*, Volume 35, Article 9, pp. 1472-1478.

Kim, W.J., Patel, V.C., 1994. Origin and Decay of Longitudinal Vortices in Developing Flow in a Curved Rectangular Duct. *Journal of Engineering,* Volume 116, Article 1, pp. 45-52.

Launder, B.E., Spalding, D.B., 1972. Lectures in Mathematical Models of Turbulence. *Academic Press*, London, England.

Le, H., Moin, P. Kim, J., 1997. Direct Numerical Simulation of Turbulent Flow over a Backward-facing Step. *Journal of Fluid Mechanics,* Volume 330, pp. 349-374.

Liu, Q.Y., Luke, E.A., Cinnella, P., 2005. Coupling Heat Transfer and Fluid Flow Solvers for Multidisciplinary Simulations. *Journal of Thermophysics and Heat Transfer*, Volume 19, Article 4, pp. 417-427.

Matweb, 2015. 416 Stainless Steel Material Properties. [online] Available at: http://www.matweb.com/search/DataSheet.aspx?MatGUID=87084f2733d84828a72052812ac4311b&ckck=1 [Accessed 17 March 2015]

Menter, F.R., 1994. Two-Equation Eddy-Viscosity Turbulence Models for Engineering Applications. *AIAA Journal*, Volume 32, Article 8, pp. 1598-1605.

Morgut, M., Nobile, E., 2009. Comparison of Hexa-Structured and Hybrid-Unstructured Meshing Approaches for Numerical Prediction of the Flow around Marine Propellers. *Ocean Engineering*, Volume 42, pp. 26-34.

Olsen, M.G., Dutton, J.C., 2002. Stochastic Estimation of Large Structures in an Incompressible Mixing Layer. AIAA Journal, Volume 40, Article 12, pp. 2431-2438.

Pipkin, J.M., Long, D.F., McDonald, T.J., 2007. Rolls Royce Confidential Test Report.

Rogers, M.M., Moser, R.D., 1994. Direct Simulation of a Self-Similar Turbulent Mixing Layer. Physics of Fluids, Volume 6, Article 2, pp. 903-923.

Rolls-Royce Deutschland Ltd and Co KG, 2015. Rolls-Royce in Deutschland. [online] Available at: http://www.rolls-royce.com/country-sites/deutschland.aspx [Accessed 04 March 2015]

Rolls-Royce plc, 2015. SC03 (15D0). [Computer Program] Rolls-Royce In-house Tool.

Rolls-Royce plc, 1996. *The Jet Engine*. 5th Edition. Birmingham: Renault Printing Co Ltd.

Salman, H., McGuirk, J.J., Page, G.J., Moinier, P., 2000. Influence of Unstructured Mesh Type on the Prediction of Convoluted Shear Layers. *Technical Report*, Report No. 00/08, University of Oxford.

Sarpkaya, T., Hiriart, G., 1975. Analysis of Curved-Target Type Thrust Reversers. *AIAA Journal*, Volume 13, Article 2, pp. 185-192.

SAS IP, Inc., 2011. Ansys ICEM CFD (14.0). [Computer Program] SAS IP, Available at: http://www.ansys.com/Products/Other+Products/ANSYS+ICEM+CFD/ [Accessed 16 October 2014]

Schieffer, G., 2013. Schubumkehrsysteme für Strahlantriebe, Auslegung und mögliche Entwicklungen. [Powerpoint Presentation].

Shih, T.H., Liou, W.W., Shabbir, A., Yang, Z., Zhu, J., 1995. A new k-ε Eddy-Viscosity Model for High Reynolds Number Turbulent Flows – Model Development and Validation. *Computer Fluids*, Volume 24, Article 3, pp. 227-238.

Shur, M.L., Strelets, M.K., Travin, A.K., Spalart, P.R., 1998. Two Numerical Studies of Trailing Vortices. In: AIAA Meeting Papers, *AIAA 36th Aerospace Sciences Meeting and Exhibit.* Reno, USA, January 12-15, 1998.

Shur, M.L., Strelets, M.K., Travin, A.K., Spalart, P.R., 2000. Turbulence Modeling in Rotating and Curved Channels: Assessing the Spalart-Shur Correction. *AIAA Journal*, Volume 38, Article 5, pp. 784-792.

Smirnov, P.E., Menter, F.R., 2009. Sensitization of the SST Turbulence Model to Rotation and Curvature by Applying the Spalart-Shur Correction Term. *Journal of Turbomachinery,* Volume 131, Article 4.

Spalart, P.R., Allmaras, S.R., 1992. A one-equation Turbulence Model for Aerodynamic Flows. In: *AIAA 30th Aerospace Sciences Meeting and Exhibit*. Reno, USA, January 6-9, 1992.

Spalart, P.R., Shur, M.L., 1997. On the Sensitization of Turbulence Models to Rotation and Curvature. *Aerospace Science and Technology,* Volume 1, Article 5, pp. 297-302.

Strash, D.J., Summa, J.M., Frank, J.H., Standish, R., 2000. Aerodynamic Analysis of an Installed Thrust Reverser. *AIAA Journal of Propulsion and Power*, Volume 16, Article 1, pp. 10-15.

Time for Flight. [online] Available at: http://timeforflight.tripod.com/717.html [Accessed 04 March 2015]

Trautvetter, C., 2012. Gulfstream G650 Crosses the Certification Finish Line. AIN Online. [online] Available at: http://www.ainonline.com/aviation-news/business-aviation/2012-09-07/gulfstream-g650-crosses-certification-finish-line [Accessed 04 March 2015]

Vos, R., 2013. Engine Intakes, Exhausts and Reversers, *AE4-240*. [Powerpoint Presentation]. Technical University Delft, Delft.

Wilcox, D.C., 2006. *Turbulence Modeling for CFD.* 3rd Edition. La Cañada: DCW Industries, Inc.

Appendix A Validation Test Cases

In this appendix the boundary conditions, computational domains and validation data for the simulations of the test cases are given.

A.1 Jet in a Cross Flow

By combining the information given in the papers of Dennis, Tso and Margason (1993) and Chiu, et al.(1993) the boundary conditions for the JICF test case are derived.

The experiment is performed in the unpressurised, closed return, closed throat windtunnel at the NASA/Ames Research Center. This implies that the total pressure, temperature and density are at ISA ambient conditions at ground level. The total temperature of the jet was approximately equal to the freestream value and temperature variations are caused by isentropic expansion. In the paper by Dennis, Tso and Margason (1993) isentropic relations are used together with the velocity ratio to calculate important flow variables. All known variables are summarised in Table A.1 below.

Table A.1: Table with all known variables for the JICF test case

Parameter	Value
$p_{t,cf}$ $[Pa]$	101,325
$T_{t,cf}$ $[K]$	288
$\rho_{t,cf}$ $[kg/m^3]$	1.225
M_{cf} $[-]$	0.13
M_{jet} $[-]$	0.78
R $[-]$	6
d_{jet} $[cm]$	5.08

With the isentropic relations the static conditions can be calculated in the cross flow based on the total conditions and Mach number,

$$p_{s,cf} = p_{t,cf}\left(1+\frac{\gamma-1}{2}M_{cf}^2\right)^{\frac{-\gamma}{\gamma-1}} = 101{,}325\left(1+\frac{1.4-1}{2}0.13^2\right)^{\frac{-1.4}{1.4-1}} = 100{,}135\ Pa \tag{A.1}$$

$$T_{s,cf} = T_{t,cf}\left(1+\frac{\gamma-1}{2}M_{cf}^2\right)^{-1} = 288\left(1+\frac{1.4-1}{2}0.13^2\right)^{-1} = 287\ K \tag{A.2}$$

$$\rho_{s,cf} = \rho_{t,cf}\left(1+\frac{\gamma-1}{2}M_{cf}^2\right)^{\frac{-1}{\gamma-1}} = 1.225\left(1+\frac{1.4-1}{2}0.13^2\right)^{\frac{-1}{1.4-1}} = 1.215 kg/m^3 \tag{A.3}$$

From the fact that the total temperature of the jet is approximately equal to the freestream value the jet static temperature can be calculated,

$$T_{s,jet} = T_{t,jet}\left(1 + \frac{\gamma - 1}{2}M_{jet}^2\right)^{-1} = 288\left(1 + \frac{1.4 - 1}{2}0.78^2\right)^{-1} = 257\,K \tag{A.4}$$

With this static jet temperature the jet velocity can be calculated by making use of the relation for the Mach number,

$$M_{jet} = \frac{V_{jet}}{\sqrt{\gamma R T_{s,jet}}} \xrightarrow{yields} V_{jet} = M_{jet}\sqrt{\gamma R T_{s,jet}} = 0.78\sqrt{1.4 \cdot 287 \cdot 257} = 250\,m/s \tag{A.5}$$

The same is done to calculate the cross flow velocity,

$$M_{cf} = \frac{V_{cf}}{\sqrt{\gamma R T_{s,cf}}} \xrightarrow{yields} V_{cf} = M_{cf}\sqrt{\gamma R T_{s,cf}} = 0.13\sqrt{1.4 \cdot 287 \cdot 287} = 44\,m/s \tag{A.6}$$

Now with the velocity ratio the static jet density can be calculated followed by the static jet pressure from the ideal gas law. Again with the isentropic relations the total jet pressure can be calculated.

$$R = \frac{V_{jet}}{V_{cf}}\sqrt{\frac{\rho_{s,jet}}{\rho_{s,cf}}} \xrightarrow{yields} \rho_{s,jet} = \rho_{s,cf}\left(\frac{R \cdot V_{cf}}{V_{jet}}\right)^2 = 1.215\left(\frac{6 \cdot 44}{250}\right)^2 = 1.361\,kg/m^3 \tag{A.7}$$

$$p_{s,jet} = \rho_{s,jet} R T_{s,jet} = 1.316 \cdot 287 \cdot 287 = 100{,}386\,Pa \tag{A.8}$$

$$p_{t,jet} = p_{s,jet}\left(1 + \frac{\gamma - 1}{2}M_{jet}^2\right)^{\frac{\gamma}{\gamma-1}} = 100{,}386\left(1 + \frac{1.4 - 1}{2}0.78^2\right)^{\frac{1.4}{1.4-1}} = 150{,}043\,Pa \tag{A.9}$$

The Mach numbers in the cross flow and jet are known as well as the velocity ratio. The viscosity in the cross flow and jet can be calculated with the assumption that the viscosity is dependent only on the temperature. With this assumption Sutherland's law can be used to calculate the viscosity. The reference viscosity, temperature and Sutherland´s temperature are $1.716 \cdot 10^{-5}\,kg/ms$, $273.15\,K$ and $110.4\,K$ respectively.

$$\mu_{cf} = \mu_{ref}\left(\frac{T_{s,cf}}{T_{ref}}\right)^{\frac{3}{2}}\frac{T_{ref} + S}{T_{s,cf} + S} = 1.716 \cdot 10^{-5}\left(\frac{287}{273.15}\right)^{\frac{3}{2}}\frac{273.15 + 110.4}{287 + 110.4} = 1.784 \cdot 10^{-5}\,kg/ms \tag{A.10}$$

$$\mu_{jet} = \mu_{ref}\left(\frac{T_{s,jet}}{T_{ref}}\right)^{3/2}\frac{T_{ref} + S}{T_{s,jet} + S} = 1.716 \cdot 10^{-5}\left(\frac{257}{273.15}\right)^{\frac{3}{2}}\frac{273.15 + 110.4}{257 + 110.4} = 1.635 \cdot 10^{-5}\,kg/ms \tag{A.11}$$

The Reynolds numbers for the cross flow and jet can now be calculated to be,

$$Re_{cf} = \frac{\rho_{s,cf} \cdot V_{cf} \cdot l}{\mu_{cf}} = \frac{1.215 \cdot 44 \cdot 1}{1.784 \cdot 10^{-5}} = 3.0 \cdot 10^6 \tag{A.12}$$

$$Re_{jet} = \frac{\rho_{s,jet} \cdot V_{jet} \cdot l}{\mu_{jet}} = \frac{1.361 \cdot 250 \cdot 0.0508}{1.635 \cdot 10^{-5}} = 1.1 \cdot 10^6 \tag{A.13}$$

The turbulent boundary conditions are calculated with the turbulence relations given below and found from the Ansys Fluent Theory Guide (Ansys Inc., 2011b).

$$I = 0.16Re^{-1/8} \tag{A.14}$$

$$k = 1.5(I \cdot u)^2 \tag{A.15}$$

$$\varepsilon = C_\mu \frac{k^2}{100 \cdot \mu} \tag{A.16}$$

$$l_{turb} = C_\mu^{3/4} \frac{k^{3/2}}{\varepsilon} \tag{A.17}$$

$$\omega = C_\mu^{-1/4} \frac{\sqrt{k}}{l_{turb}} \tag{A.18}$$

In which the turbulent viscosity ratio is used for the Spalart-Allmaras model and k, ε and ω for the Realizable k-ε and SST k-ω turbulence models respectively.

Table A.2 shows the summarised boundary conditions used for the simulations.

Table A.2: Summary of boundary conditions for the JICF test case

Parameter	**Value**
$p_{t,cf}$ $[Pa]$	101,325
$p_{s,cf} [Pa]$	100,135
$T_{t,cf}$ $[K]$	288
$p_{t,jet}$ $[Pa]$	150,043
$p_{s,jet}$ $[Pa]$	100,386
$T_{t,jet}$ $[K]$	288
$p_{s,outlet}$ $[Pa]$	100,135
$T_{t,outlet}$ $[K]$	288
μ_{turb}/μ $[-]$	10
k_{cf} $[J/kg]$	1.815
k_{jet} $[J/kg]$	128.34
ε_{cf} $[J/kgs]$	166.2
ε_{jet} $[J/kgs]$	906,669
ω_{cf} $[1/s]$	1210
ω_{jet} $[1/s]$	85,562

The computational domain for the simulations is shown below in Figure A.1. The pressure inlet is located about 30 jet diameters upstream of the jet exit orifice and has an area of 60x30 jet diameters. The pressure outlet is located 90 jet diameters downstream of the jet exit orifice. The walls of the pipe are modelled as a viscous wall to ensure fully developed pipe flow at the jet exit orifice. The plate is modelled as a viscous wall. The side-walls and top-wall of the domain are given the symmetry boundary condition.

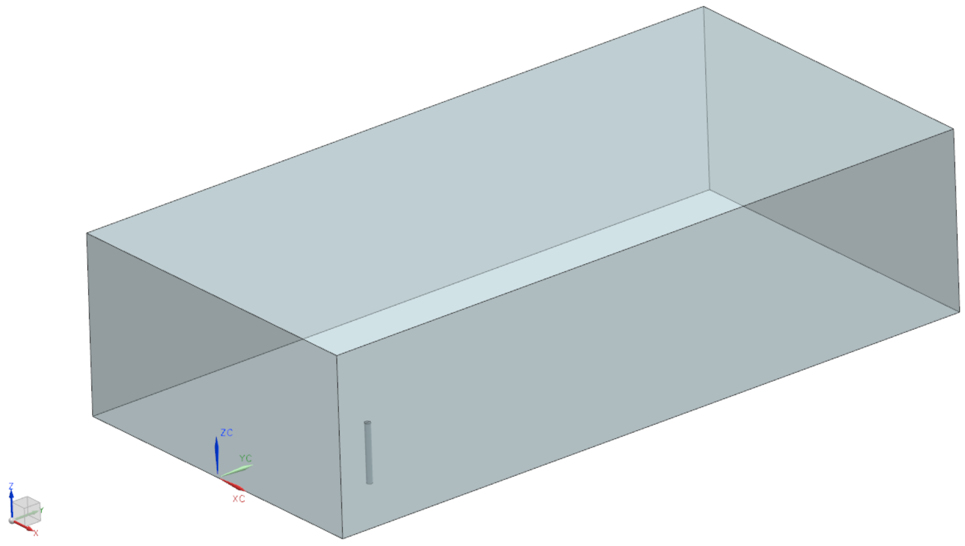

Figure A.1: Geometry of the computational domain for the JICF test case

The numbering convention for the azimuthal angles is shown in Figure A.2. Figure A.3 shows the validation data used for this test case.

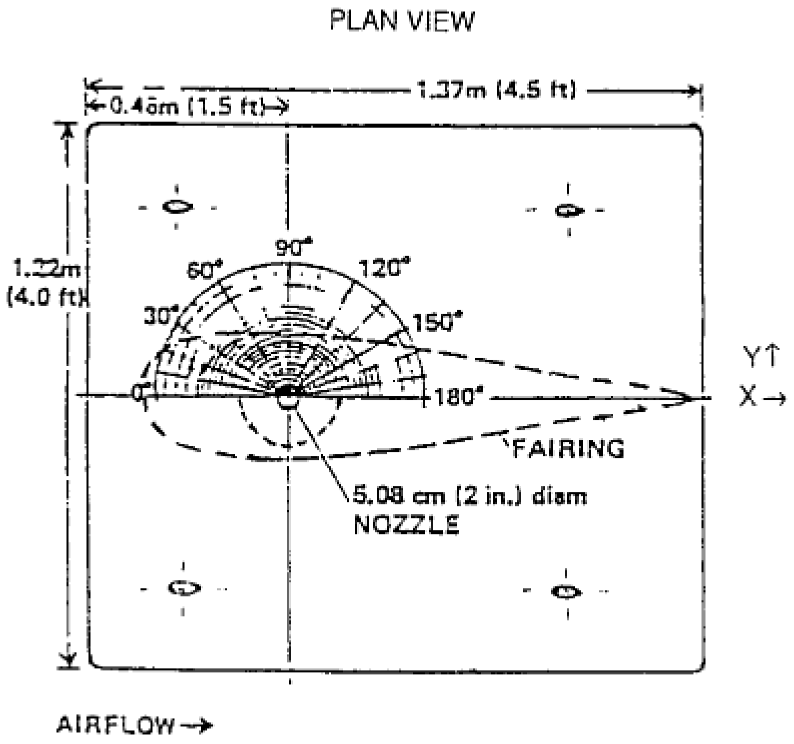

Figure A.2: Azimuthal angles numbering convention (Dennis, Tso and Margason, 1993)

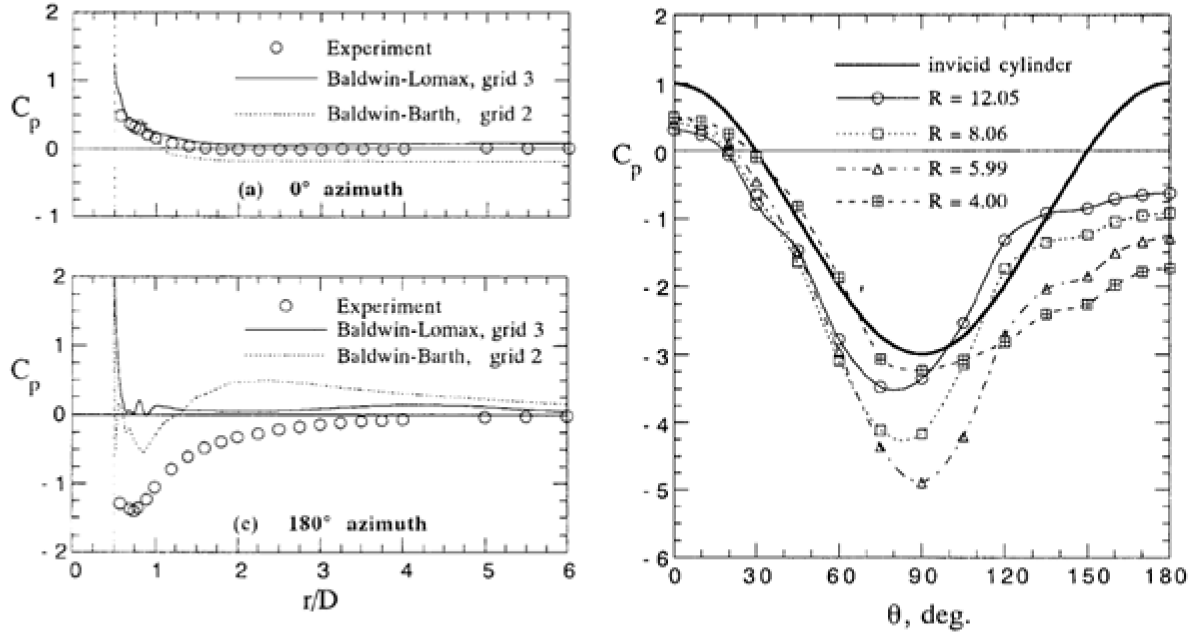

Figure A.3: Comparison of measured radial C_p distribution with CFD solutions (Chiu, et al., 1993) at $R = 6.0$, $M_j = 0.74$. Right: C_p near jet exit ($r/D = 0.58$) at $M_j = 0.74$ for various velocity ratios compared with 2D-cylinder theoretical inviscid flow C_p (Dennis, Tso and Margason, 1993)

A.2 Plane Mixing Layer

From the papers by Druault, Delville and Bonnet (2005) and Delville, et al.(1999) the boundary conditions for the mixing layer test case can be determined.

The experiments are performed in a standard open loop windtunnel. The flow is considered to be incompressible. Isentropic expansion through the convergent part of the windtunnel is assumed. The total pressure in the test section is assumed to be equal to the ambient pressure at ISA ground level conditions. The reference velocities taken for this derivation of the boundary conditions are $U_a = 41.7\ m/s$ and $U_b = 22.5\ m/s$.

With the incompressible Bernoulli equation the static pressure at the two inlets of the test section can be determined,

$$p_{t,inlet,a} = p_{s,inlet,a} + \frac{1}{2}\rho U_a^2 \rightarrow p_{s,inlet,a} = 101{,}325 - \frac{1}{2} \cdot 1.225 \cdot 41.7^2 = 100{,}260\ Pa \tag{A.19}$$

$$p_{t,inlet,b} = p_{s,inlet,b} + \frac{1}{2}\rho U_b^2 \rightarrow p_{s,inlet,b} = 101{,}325 - \frac{1}{2} \cdot 1.225 \cdot 22.5^2 = 101{,}015\ Pa \tag{A.20}$$

Because of the small difference in velocity between the two flows, the temperature is assumed to be constant at both inlets and outlet and has a value of 288 K.

The outlet velocity is calculated to be the so-called convection velocity of the mixing layer,

$$U_c = \frac{U_a + U_b}{2} = 32.1\ m/s \tag{A.21}$$

The static pressure at the outlet now becomes,

$$p_{t,outlet} = p_{s,outlet} + \frac{1}{2}\rho U_c^2 \rightarrow p_{s,outlet} = 101{,}325 - \frac{1}{2} \cdot 1.225 \cdot 32.1^2 = 100{,}694\ Pa \tag{A.22}$$

Because pressure far-field inlet boundary conditions are used in Ansys Fluent, the inlet Mach numbers need to be known,

$$M_a = \frac{U_a}{\sqrt{\gamma RT}} = \frac{41.7}{\sqrt{1.4 \cdot 287 \cdot 288}} = \frac{41.7}{340.2} = 0.123 \tag{A.23}$$

$$M_b = \frac{U_b}{\sqrt{\gamma RT}} = \frac{22.5}{\sqrt{1.4 \cdot 287 \cdot 288}} = \frac{22.5}{340.2} = 0.066 \tag{A.24}$$

In the paper by Druault, Delville and Bonnet (2005) the boundary layer thicknesses at the trailing edge of the splitter plate are given to be 1.8 and 2.6 mm. This is however for the experiments with the two streams having respectively a velocity of $U_a = 25\ m/s$ and $U_b = 11\ m/s$. To match the splitter plate length of the simulations with the experiments an estimation is made based on the experiments with the lower inlet velocities. The boundary layer thickness over a turbulent flat plate can be estimated by,

$$\frac{\delta}{x} = \frac{0.385}{Re^{0.2}} \tag{A.25}$$

Using the above given velocities and boundary layer thicknesses for the experiments and assuming ISA ground level conditions x was determined to be $3.3\ cm$. This way of determining the length of the splitter plate is valid while the same splitter plate/windtunnel is used for both experiments.

The turbulent intensity level in the freestream is given to be 0.6%. A second turbulence boundary condition should be specified. Therefore the hydraulic diameter is used which is $0.15\ m$ at the inlets and $0.3\ m$ at the outlet.

Table A.3 shows the summarised boundary conditions used for the simulations.

Table A.3: Summary of boundary conditions for the plane mixing layer test case

Parameter	**Value**
$p_{s,inlet,a}\ [Pa]$	100,260
$M_a\ [-]$	0.123
$p_{s,inlet,b}\ [Pa]$	101,015
$M_b\ [-]$	0.066
$p_{s,outlet}\ [Pa]$	100,694
$T\ [K]$	288
$I\ [\%]$	0.6
$D_{H,inlets}\ [m]$	0.15
$D_{H,outlet}\ [m]$	0.3

The computational domain for the simulations is shown below in Figure A.4. The splitter plate is $1{,}20\ m$ just like the mixing region behind the splitter plate (just like the windtunnel dimensions). As described above, $3.3\ cm$ of the splitter plate is modelled as a viscous plate. The inlets are defined as pressure far-field inlets. The sides, top and bottom of the domain are given a symmetry boundary condition. The outlet is specified to be a pressure outlet. The cross-sectional area of the domain is $30x30\ cm$.

The validation data selected for this test case is shown in Figure A.5. Note that the x-axis' in section 4.2 are given by y and $y - y_0$. Because the vorticity thickness could not be determined from the simulations but was given in the bottom right graph of Figure A.5, the scaling of data from simulations and validation data could be matched. Unfortunately y_0 could not be determined from the simulations, therefore the results scaled by $y - y_0$ have a small offset between simulations and validation data. This offset is probably equal to y_0.

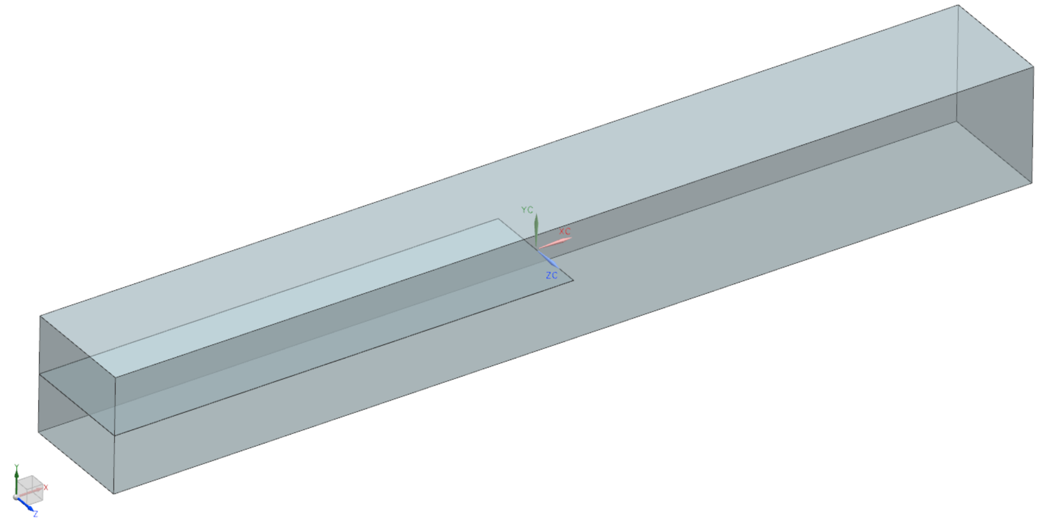

Figure A.4: Geometry of the computational domain for the plane mixing layer test case

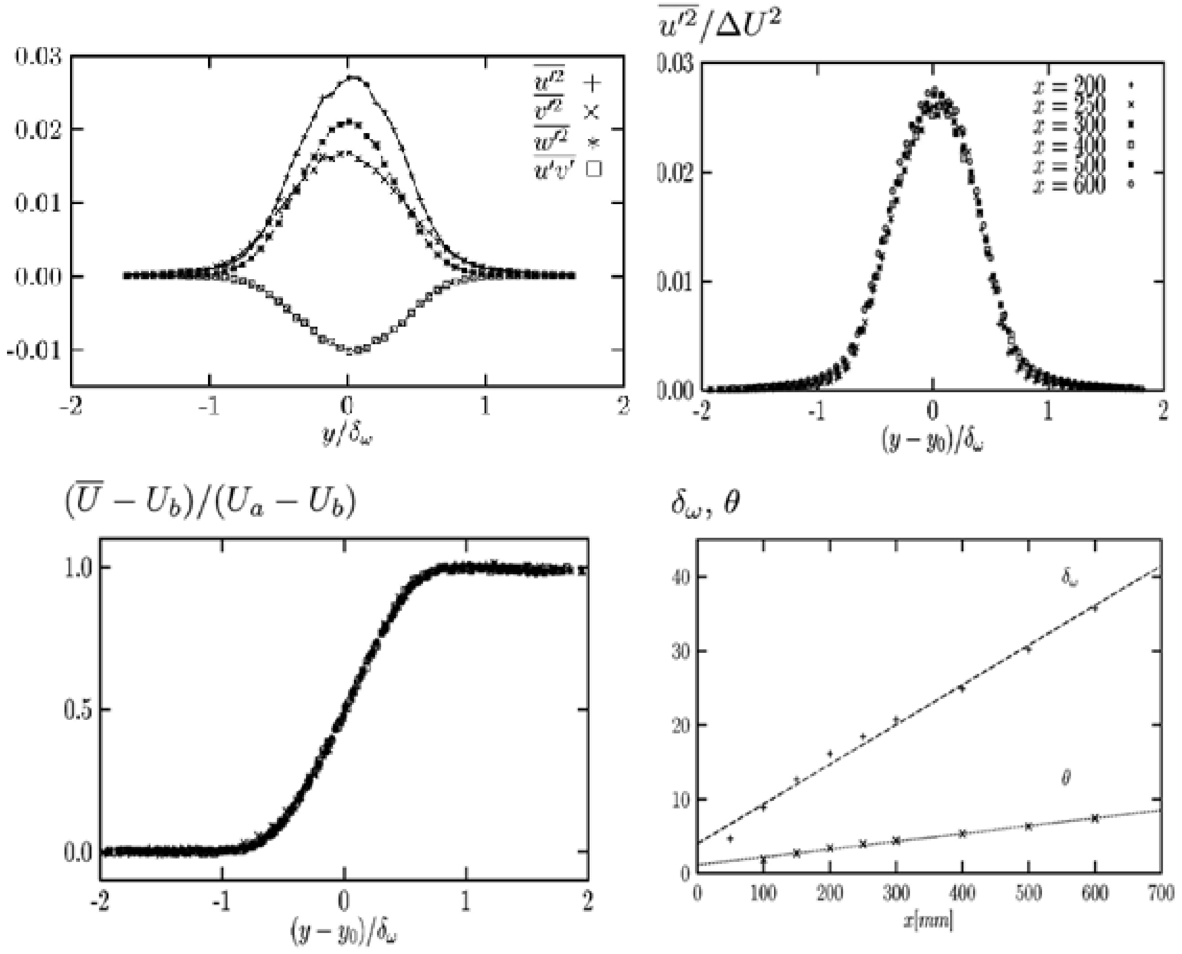

Figure A.5: Top Left: Reynolds stresses normalised with ΔU^2 and obtained in the self-similar region of a plane turbulent mixing layer at $x_0 = 500\ mm$ downstream of the splitter plate. Top Right: Streamwise Reynolds stress tensor component. Bottom Left: Streamwise mean velocity profile obtained at several streamwise positions. Bottom Right: Streamwise evolution of the vorticity and momentum thickness (Druault, Delville and Bonnet, 2005)

A.3 Backward-Facing Step

From the papers by Jovic and Driver (1994) and Le, Moin and Kim (1997) the boundary conditions for the backward-facing step test case can be determined.

The experiment is performed in the suction-driven open-return windtunnel of the NASA/Ames Research Center. Because the windtunnel is of the open-return type, it is assumed that the air at the inlet of the tunnel is at ambient total conditions. Also isentropic expansion through the convergent part of the windtunnel is assumed. The total pressure in the test section is assumed to be equal to the ambient pressure at ISA ground level conditions. The reference velocity for this experiment is given to be $U_0 = 7.72\ m/s$, this implies incompressible flow and therefore density variations are neglected.

With the incompressible Bernoulli equation the static pressure at the inlet of the test section can now be determined,

$$p_{t,inlet} = p_{s,inlet} + \frac{1}{2}\rho U_0^2 \rightarrow p_{s,inlet} = 101{,}325 - \frac{1}{2} \cdot 1.225 \cdot 7.72^2 = 101{,}289\ Pa \tag{A.26}$$

The outlet velocity can be calculated by the mass flow conservation for an incompressible flow and with an expansion ratio (ER) of 1.2 to be,

$$(\rho A U)_{inlet} = (\rho A U)_{outlet} \rightarrow U_{outlet} = U_{inlet}\frac{A_{inlet}}{A_{outlet}} = U_{inlet}\frac{1}{ER} = 7.72\frac{1}{1.2} = 6.43\ m/s \tag{A.27}$$

The static pressure at the outlet can now be determined to be,

$$p_{t,outlet} = p_{s,outlet} + \frac{1}{2}\rho U_0^2 \rightarrow p_{s,outlet} = 101{,}325 - \frac{1}{2} \cdot 1.225 \cdot 6.43^2 = 101{,}300\ Pa \tag{A.28}$$

Because the pressure far-field inlet boundary condition is used in Ansys Fluent, the inlet Mach number needs to be known,

$$M_a = \frac{U_a}{\sqrt{\gamma R T}} = \frac{7.72}{\sqrt{1.4 \cdot 287 \cdot 288}} = \frac{7.72}{340.2} = 0.023 \tag{A.29}$$

The temperature is assumed to be $288\ K$ throughout the computational domain.

Just like for the plane mixing layer test case the boundary layer thicknesses between simulations and experiments need to be matched. The boundary layer thickness in the experiments is given to be $1.15\ cm$ at $x = 3.05h$ with the step height, $h = 0.98\ cm$. The upstream length before the step is determined by using equation (A.25) to be $x = 36.5\ cm$ to match the boundary layer thickness.

The turbulent intensity level in the freestream is given to be 1.0%. The second turbulence boundary condition used for this test case is the turbulent length scale which was set equal to the step height.

Table A.4 shows the summarised boundary conditions used for the simulations.

Table A.4: Summary of the boundary conditions for the backward-facing step test case

Parameter	Value
$p_{s,inlet}$ $[Pa]$	101,289
M_{inlet} $[-]$	0.022
$p_{s,outlet}$ $[Pa]$	101,300
T $[K]$	288
I $[\%]$	1
l_{turb} $[cm]$	0.98

The computational domain for the simulations is shown below in Figure A.6. The pressure far-field inlet is located 36.5 cm upstream of the step as explained earlier. The pressure outlet is located 135 cm downstream of the step. The domain is 30.5 cm wide and 4.8 cm high upstream of the step similar to the windtunnel dimensions. The bottom walls are modelled as a viscous wall just like the step wall. The side and top walls are specified as a symmetry boundary condition.

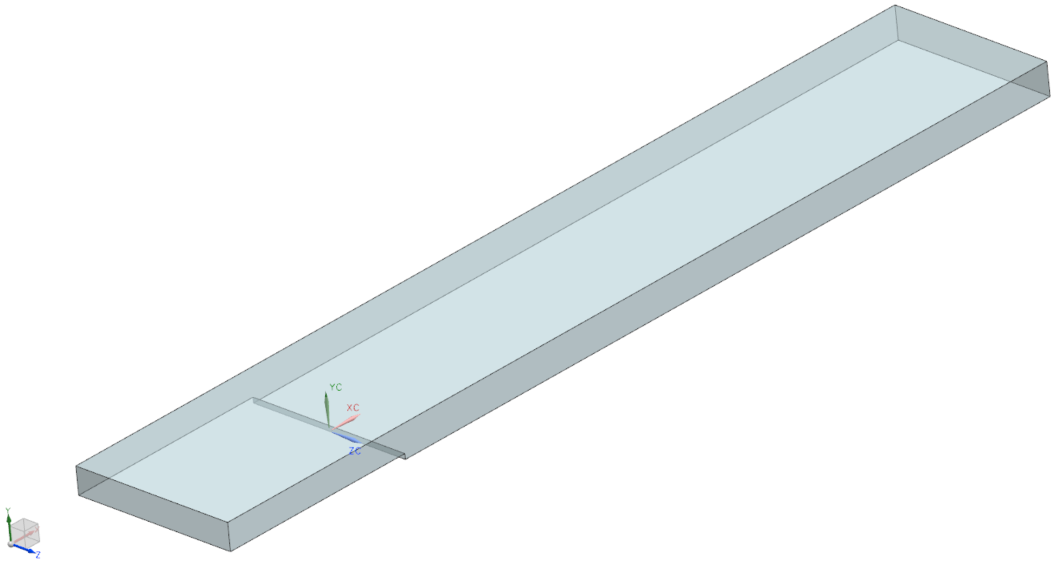

Figure A.6: Geometry of the computational domain for the backward-facing step test case

The used validation data used for this test case can be seen in Figure A.7. The mean streamwise velocity profile for $x/h = -3.12$ is given in a table in the appendix of the paper by Jovic and Driver (1994).

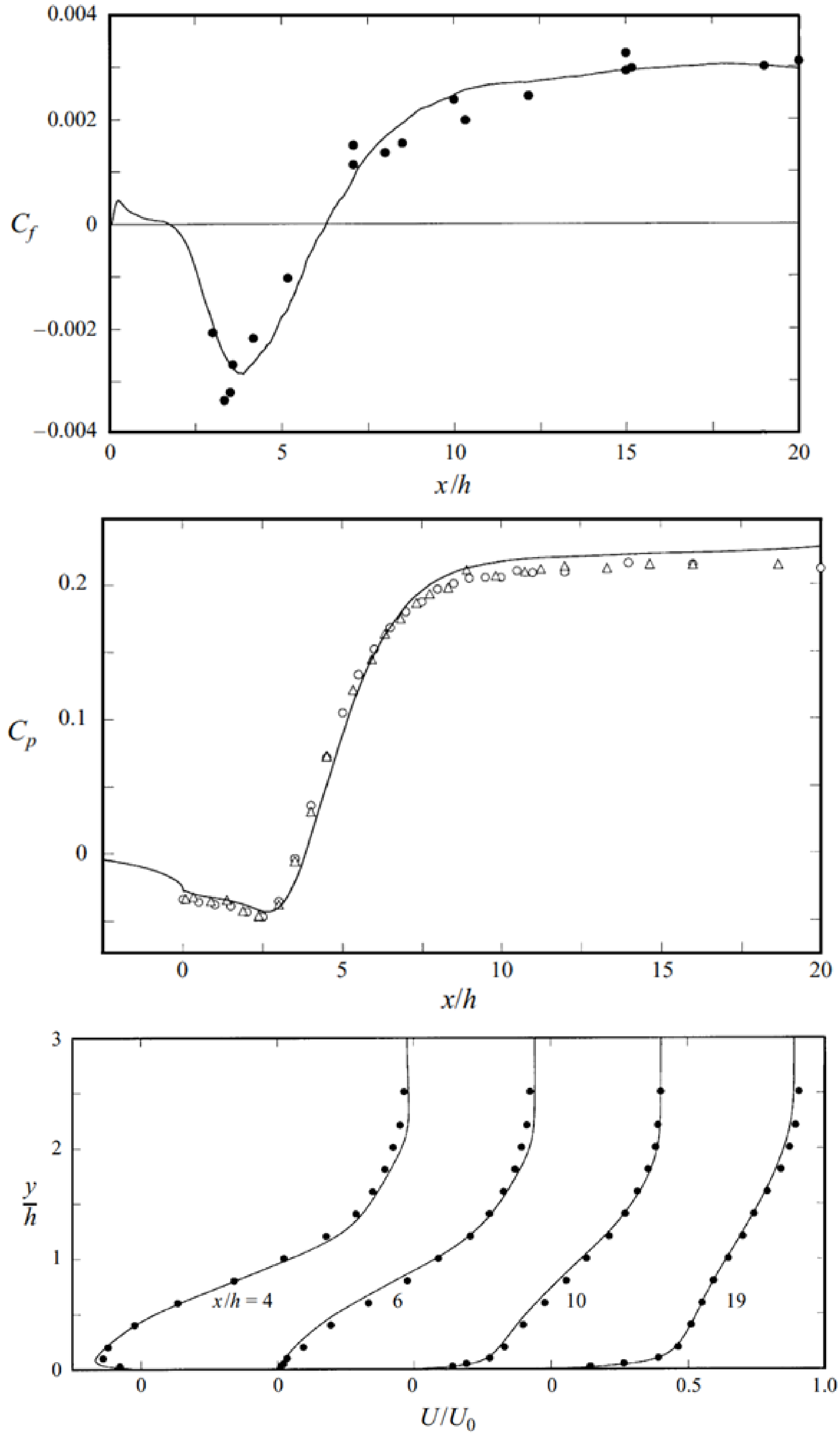

Figure A.7: Comparison of C_f, C_p and mean streamwise velocity profiles between computations (solid lines)(Le, Moin and Kim, 1997) and experiments (dots)(Jovic and Driver, 1994)

A.4 Curved Channel Flow

From the paper by Kim and Patel (1994) the boundary conditions for the curved channel flow test case can be determined.

The experiments are performed in an open-return, suction-driven windtunnel. Because the windtunnel is of the open-return type it is assumed that the air at the inlet of the tunnel is at ambient total conditions. Isentropic expansion through the convergent part of the windtunnel is assumed, such that the total pressure in the test section is equal to the ambient total pressure at ISA ground level conditions. The freestream velocity for this experiment is given to be $16\,m/s$, this implies incompressible flow and therefore density variations are neglected.

With the incompressible Bernoulli equation the static pressure at the inlet of the test section can now be determined,

$$p_{t,inlet} = p_{s,inlet} + \frac{1}{2}\rho U_0^2 \rightarrow p_{s,inlet} = 101{,}325 - \frac{1}{2} \cdot 1.225 \cdot 16^2 = 101{,}168\,Pa \tag{A.30}$$

The temperature is then given by the ideal gas law,

$$p_{s,inlet} = \rho R T_{s,inlet} \rightarrow T_{s,inlet} = \frac{p_{s,inlet}}{\rho R} = \frac{101{,}289}{1.225 \cdot 287} = 288\,K \tag{A.31}$$

Fully developed duct flow is considered in this test case. The outlet static pressure and temperature are assumed to have the same value as at the inlet of the windtunnel.

Because the pressure far-field inlet boundary condition is used in Ansys Fluent, the inlet Mach number needs to be known,

$$M_a = \frac{U_a}{\sqrt{\gamma R T}} = \frac{16}{\sqrt{1.4 \cdot 287 \cdot 288}} = \frac{16}{340.2} = 0.047 \tag{A.32}$$

The freestream turbulent intensity is given to be 1%. The second turbulence boundary condition used for this test case is the turbulent length scale which is set equal to the duct height, H.

Table A.5 shows the summarised boundary conditions used for the simulations.

Table A.5: Summary of the boundary conditions for the curved channel flow test case

Parameter	**Value**
$p_{s,inlet}\ [Pa]$	101,168
$M_{inlet}\ [-]$	0.047
$p_{s,outlet}\ [Pa]$	101,168
$T\ [K]$	288
$I\ [\%]$	1
$l_{turb}[cm]$	20.3

The computational domain for the simulations is shown below in Figure A.8. As explained before, the pressure far-field inlet boundary is located $7.5H$ upstream of the bend. The pressure outlet is located $25.5H$ downstream of the bend. The cross-section of the duct is $6H$ wide and H high. The walls of the duct are modelled as viscous walls.

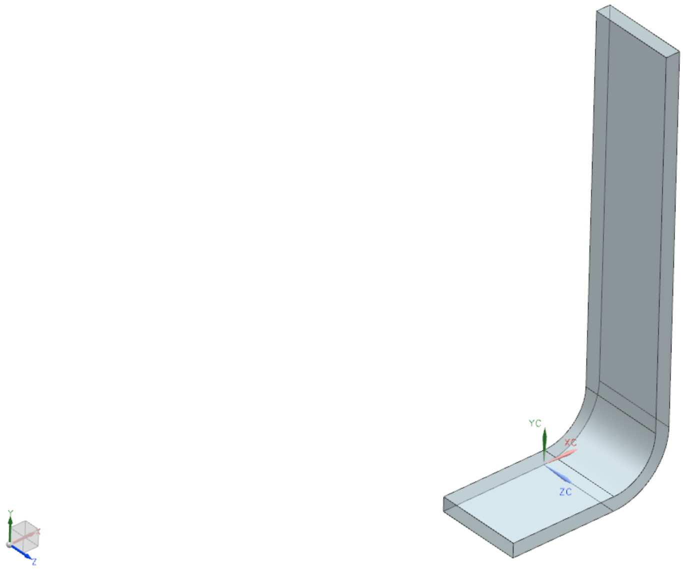

Figure A.8: Geometry of the computational domain for the curved channel flow test case

The used validation data for this test case can be seen in Figure A.9. In the bottom of the figure the normalised ($l = s/H$) numbering convention for the x-axis of the data can be seen.

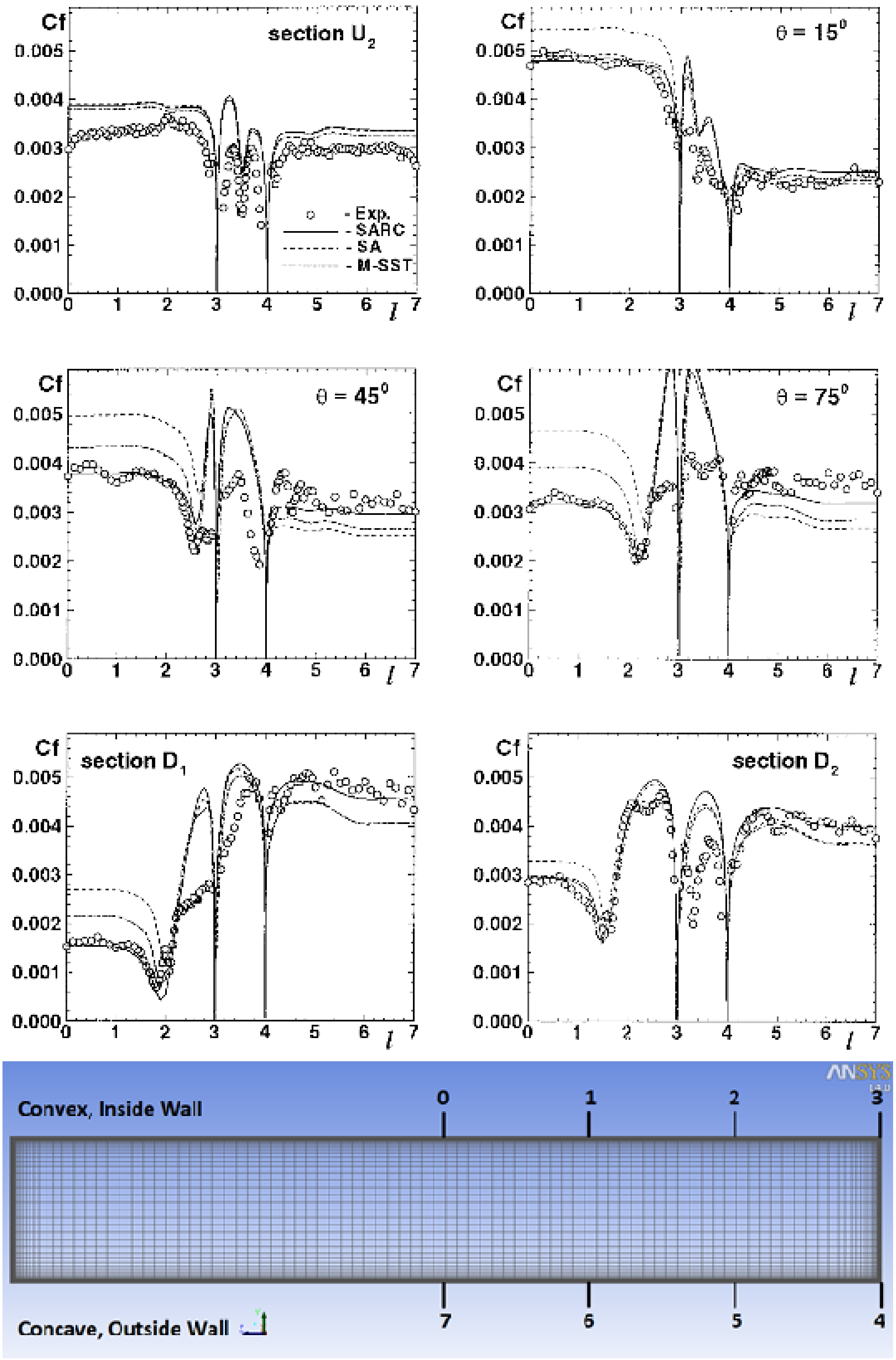

Figure A.9: Computed (solid lines)(Shur, et al., 2000) and measured (dots)(Kim and Patel, 1994) streamwise evolution of the skin friction coefficient distribution along the perimeter of the cross-section of the rectangular duct with 90° bend (shown in the bottom figure)

A.5 Semi-Infinite Flat Plate

From the paper by Kao and Liou (1997) the boundary conditions for this test case can be determined. The Mach number of the incoming flow is 0.3. With the temperature of $300\,K$ given, the velocity can be determined,

$$M = \frac{u}{\sqrt{\gamma RT}} \xrightarrow{yields} u = M \cdot \sqrt{\gamma RT} = 0.3 \cdot \sqrt{1.4 \cdot 287 \cdot 300} = 104\,m/s \tag{A.33}$$

The dynamic viscosity can now be calculated with Sutherland's law, by using the following constants: $\mu_0 = 1.716 \cdot 10^{-5}\,kg/ms,$, $273.15\,K$ and $S = 110.4\,K$.

$$\begin{aligned}\mu_{cf} = \mu_{ref}\left(\frac{T_s}{T_{ref}}\right)^{\frac{3}{2}}\frac{T_{ref}+S}{T_s+S} &= 1.716 \cdot 10^{-5}\left(\frac{300}{273.15}\right)^{\frac{3}{2}}\frac{273.15+110.4}{300+110.4} \\ &= 1.846 \cdot 10^{-5}\,kg/ms\end{aligned} \tag{A.34}$$

With a Re_l of 10^4 and the dynamic viscosity determined above, the density can be calculated to be,

$$Re_l = \frac{\rho ul}{\mu} \xrightarrow{yields} \rho = \frac{Re_l \mu}{ul} = \frac{10^4 \cdot 1.846 \cdot 10^{-5}}{104 \cdot 1} = 0.00178\,kg/m^3 \tag{A.35}$$

This seems like a very low value for the density. The simulation results are compared with analytical data determined by an expression of Eckert and Weisse (1941) for a laminar flow and a constant temperature flat plate given by,

$$Nu = 0.333\sqrt[3]{Pr}\sqrt{Re_x}\left(\frac{l}{x}\right) \tag{A.36}$$

This expression seems wrong to the author of this report. The paper by Eckert and Weisse (1941) was checked but this equation could not be verified. Some further research was done to find an analytical expression for the Nusselt number for a turbulent flow and a constant temperature flat plate. An analytical expression was found from Berman, et al.(2011),

$$Nu_{tur} = 0.0296\sqrt[3]{Pr}Re_x^{4/5} \tag{A.37}$$

The expression is valid for a Prandtl number between 0.6 and 60 for turbulent flow. Furthermore Bergman, et al.(2011) determined the transition Reynolds number for a flat plate to be $Re_x = 5 \cdot 10^5$.

The idea behind the test case is still based on the paper by Kao and Liou (1997) but the validation data used and boundary conditions are changed. The new boundary conditions are as follows:

- The static density is $1.172\,kg/m^3$ based on a total density of $1.225\,kg/m^3$ at $M = 0.3$
- Due to practical reasons during the evaluation of the test case the plate length, $l = 0.75\,m$
- The Reynolds number at the end of the plate is $Re_l = 5.0 \cdot 10^6$ (turbulent)
- The inlet static and total pressure and total temperature are determined to be,

$$p_s = \rho_s RT_s = 1.172 \cdot 287 \cdot 300 = 100{,}909\,Pa \tag{A.38}$$

$$p_t = p_s\left(1+\frac{\gamma-1}{2}M^2\right)^{\frac{\gamma}{\gamma-1}} = 100{,}909\left(1+\frac{1.4-1}{2}0.3^2\right)^{3.5} = 107{,}411\,Pa \tag{A.39}$$

$$T_t = T_s\left(1+\frac{\gamma-1}{2}M^2\right) = 300\left(1+\frac{1.4-1}{2}0.3^2\right) = 305.4\,K \tag{A.40}$$

A turbulent Intensity of 0.1% and a turbulent viscosity ratio of 10 are used as turbulent boundary conditions.

Table A.6 shows the summarised boundary conditions used for the simulations.

Table A.6: Summary of the boundary conditions for the semi-infinite flat plate test case

Parameter	**Value**
$p_{s,inlet}\ [Pa]$	100,909
$M_{inlet}\ [-]$	0.3
$p_{s,outlet}\ [Pa]$	100,909
$T\ [K]$	300
$I\ [\%]$	0.1
$\mu_{turb}/\mu\ [-]$	10

The flat plate is made out of aluminium. The used material properties are shown below in Table A.7.

Table A.7: Physical and thermal properties of aluminium (Kao and Liou, 1997)

Parameter	**Value**
Material	Aluminium
$\rho\ [kg/m^3]$	2700
$C_p\ [J/kgK]$	900
$k\ [W/mK]$	211

The fluid and solid computational domain are shown below in Figure A.10.

The pressure far-field inlet is located $0.3\ m$ upstream of the leading edge of the plate. The bottom wall upstream of the plate is modelled as an inviscid wall. The plate has a length of $0.75\ m$. The sides of the computational domain are given a symmetry boundary condition and are $0.1\ m$ apart from each other. The top wall is defined as a pressure far-field inlet. The plate wall is modelled as a solid wall and forms the interface with the solid computational domain. As discussed in section 3.2.2 the temperature distribution at the wall is defined by the solution of the solid domain.

The bottom of the solid domain is given a constant temperature of $280\ K$. The thermal boundary condition at the top/interface wall is the heat flux which is obtained from the fluid domain solution. The side walls of the solid domain are defined as adiabatic walls ($q = 0$). Due to difficulties during the meshing of the solid it was decided to increase the plate thickness from $1.5\ mm$ to $15\ mm$.

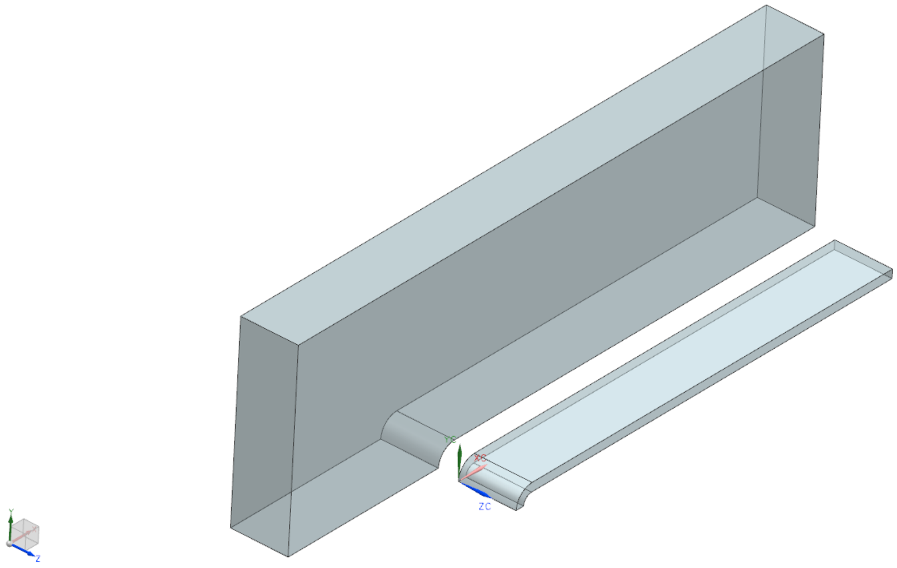

Figure A.10: Geometry of the computational domain for the semi-infinite flat plate test case

A.6 Convergent-Divergent Nozzle

From the paper by Liu, Luke and Cinnella (2005) the boundary conditions for this test case can be determined. The boundary conditions summarised in Table A.8 and Table A.9 below are already given in the paper.

Table A.8: Given boundary conditions (Liu, Luke and Cinnella, 2005)

Parameter	**Value**
$p_{t,inlet}$ $[Pa]$	517,100
$T_{t,inlet}$ $[K]$	843
$\rho_{t,inlet}$ $[kg/m^3]$	2.1306
$T_{solid,top}$ $[K]$	See Figure A.11
$T_{solid,inlet}$ $[K]$	299
$T_{solid,outlet}$ $[K]$	283

Table A.9: Physical and thermal properties of AISI stainless steel at $400\ K$ (Liu, Luke and Cinnella, 2005)

Parameter	**Value**
Material	AISI 316
ρ $[kg/m^3]$	8238
C_p $[J/kgK]$	504
k $[W/mK]$	15.2

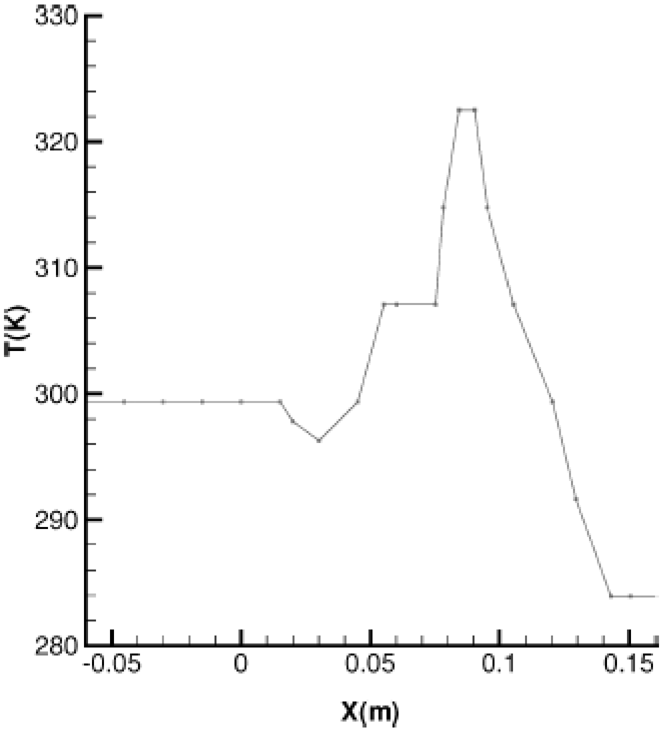

Figure A.11: Nozzle top wall temperature profile (Liu, Luke and Cinnella, 2005)

The flow is assumed to be isentropic through the nozzle. With the contour plot of the Mach number, shown in , the Mach number at the inlet and outlet of the nozzle can be approximated. With these Mach numbers the static pressures at the inlet and outlet can be determined as follows,

$$p_{s,inlet} = p_{t,inlet}\left(1+\frac{\gamma-1}{2}M_{inlet}^2\right)^{\frac{-\gamma}{\gamma-1}} = 517{,}100\left(1+\frac{1.4-1}{2}0.08^2\right)^{-3.5} = 514{,}790\ Pa \qquad \text{(A.41)}$$

$$p_{s,outlet} = p_{t,outlet}\left(1+\frac{\gamma-1}{2}M_{outlet}^2\right)^{\frac{-\gamma}{\gamma-1}} = 517{,}100\left(1+\frac{1.4-1}{2}2.5^2\right)^{-3.5} = 30{,}265\ Pa \qquad \text{(A.42)}$$

A turbulent Intensity of 6% and a turbulent viscosity ratio of 10 are used as turbulent boundary conditions.

Table A.10 shows the summarised boundary conditions used for the simulations.

Table A.10: Summary of the boundary conditions for the convergent-divergent nozzle test case

Parameter	**Value**
$p_{s,inlet}\ [Pa]$	514,790
$p_{t,inlet}\ [Pa]$	517,100
$p_{s,outlet}\ [Pa]$	30,265
$T\ [K]$	843
$I\ [\%]$	6
$\mu_{turb}/\mu\ [-]$	10

The fluid and solid computational domain are shown below in Figure A.12.

As can be seen from the figure a 180° model of the nozzle is tested. The pressure inlet is located $0.6\ m$ upstream of the convergent part of the nozzle according to the information from the paper by Back, Massier and Gier (1964). The contours of the nozzle were determined as accurately as possible from Figure 4.22. The pressure outlet is located $0.164\ m$ downstream of the convergent part of the nozzle. The bottom plane is given a symmetry boundary condition. The walls of the nozzle are modelled as a solid wall and form the interface with the solid computational domain. The temperature distribution at the wall is defined by the solution of the solid domain. The 90° angle surface in Figure A.12 is a surface for extracting data and is not a part of the computational domain.

As already defined in Table A.8 the inlet, outlet and top walls thermal boundary conditions of the solid domain were already specified in the paper by Liu, Luke and Cinnella (2005). The thermal boundary condition at the bottom/interface wall is the heat flux which is obtained from the fluid domain solution.

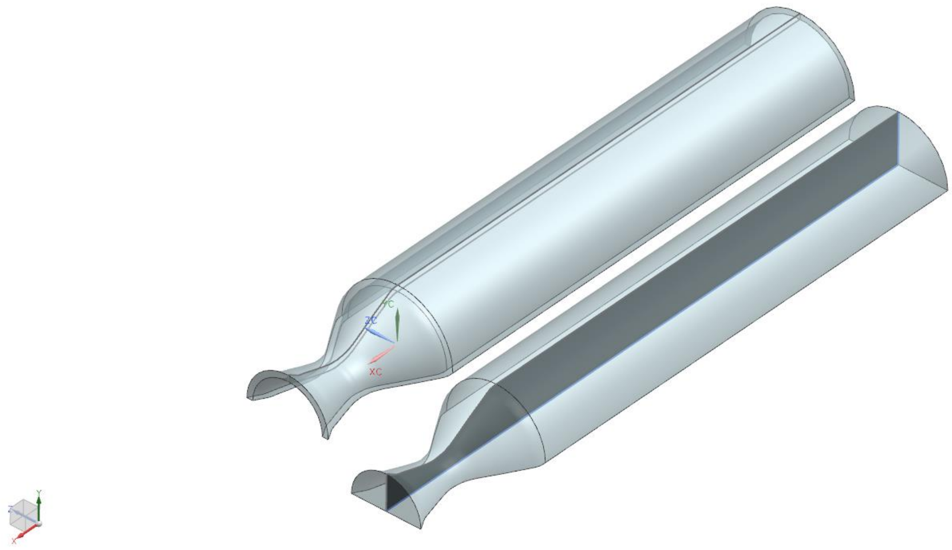

Figure A.12: Geometry of the computational domain for the convergent-divergent nozzle test case

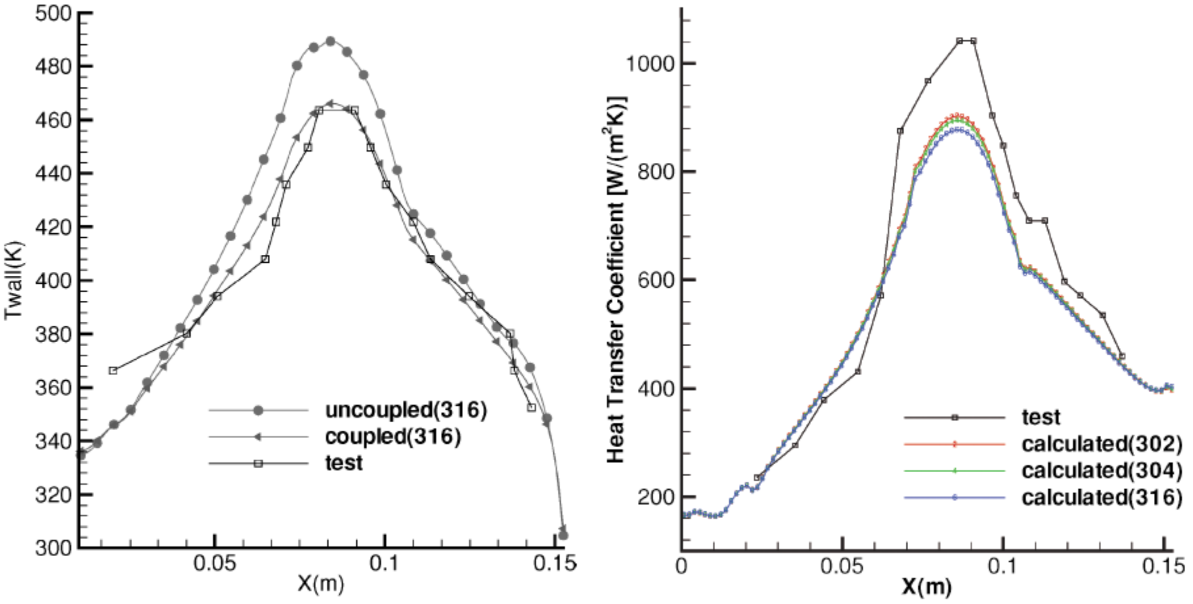

Figure A.13: Plots of the interface wall temperature and HTC (Liu, Luke and Cinnella, 2005)

Appendix B Monitored Pressure and Temperature Plots

In this appendix the monitored pressure and temperature plots are displayed which are used in Chapter 5 to determine the average pressure and temperature values and their maximum and minimum deviations from this average value. The following sections give the plots for simulations 1.2, 2.2, 3.2, and 4.2 respectively.

B.1 Simulation 1.2 (base)

Below the monitored pressure and temperature plots can be seen for pressure taps P501, P504, P507, P510 and P513, and thermocouples T503, T506, T509, T512 and T515 for simulation 1.2.

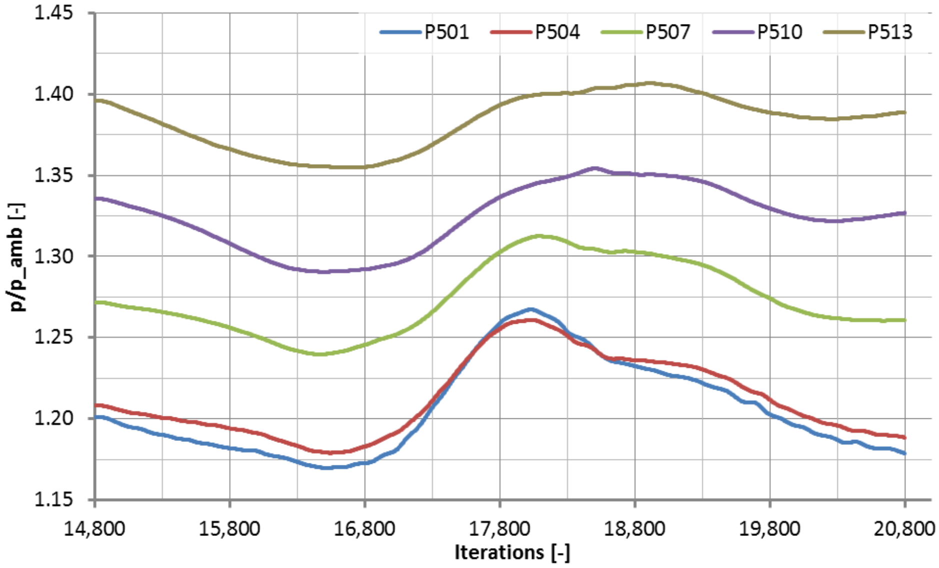

Figure B.1: Monitored pressure plot for simulation 1.2 (base) and pressure taps P501, P504, P507, P510 and P513

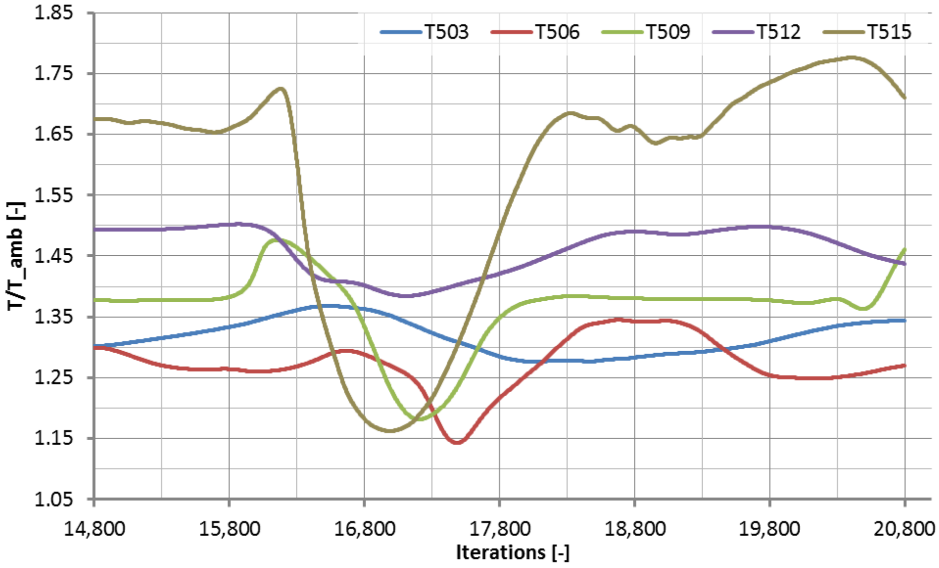

Figure B.2: Monitored temperature plot for simulation 1.2 (base) and thermocouples T503, T506, T509, T512 and T515

B.2 Simulation 2.2 (unscaled geometry)

Below the monitored pressure and temperature plots can be seen for pressure taps P501, P504, P507, P510 and P513, and thermocouples T503, T506, T509, T512 and T515 for simulation 2.2.

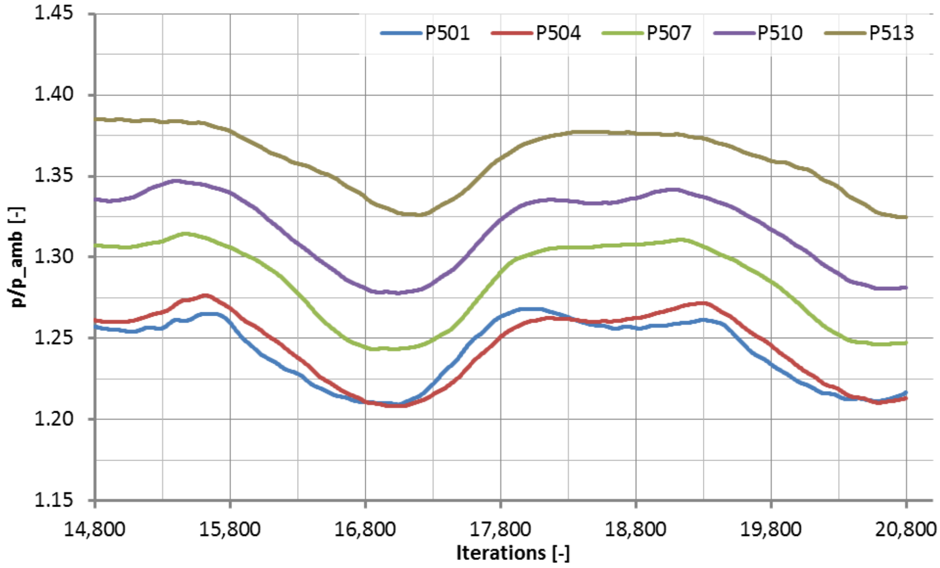

Figure B.3: Monitored pressure plot for simulation 2.2 (unscaled geometry) and pressure taps P501, P504, P507, P510 and P513

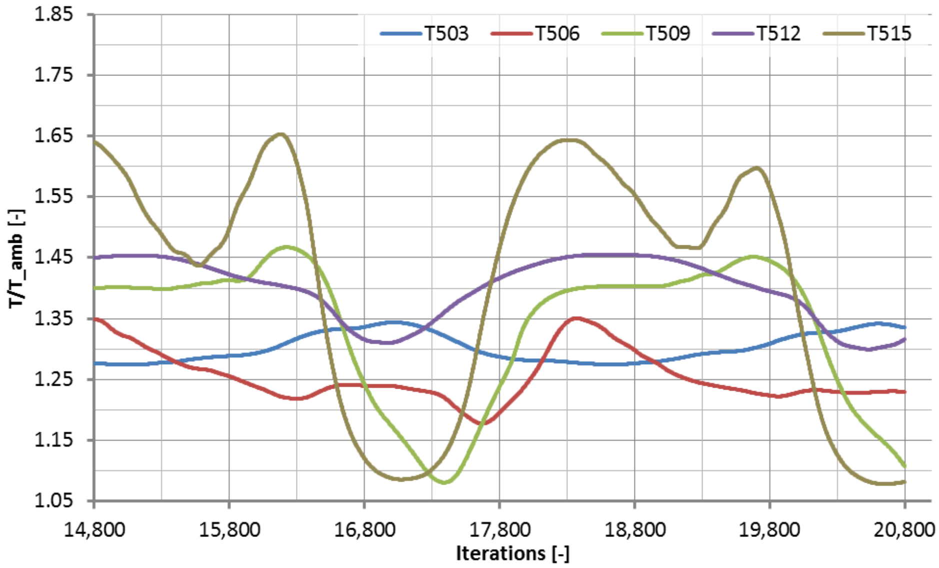

Figure B.4: Monitored temperature plot for simulation 2.2 (unscaled geometry) and thermocouples T503, T506, T509, T512 and T515

B.3 Simulation 3.2 (different BC´s)

Below the monitored pressure and temperature plots can be seen for pressure taps P501, P504, P507, P510 and P513, and thermocouples T503, T506, T509, T512 and T515 for simulation 3.2.

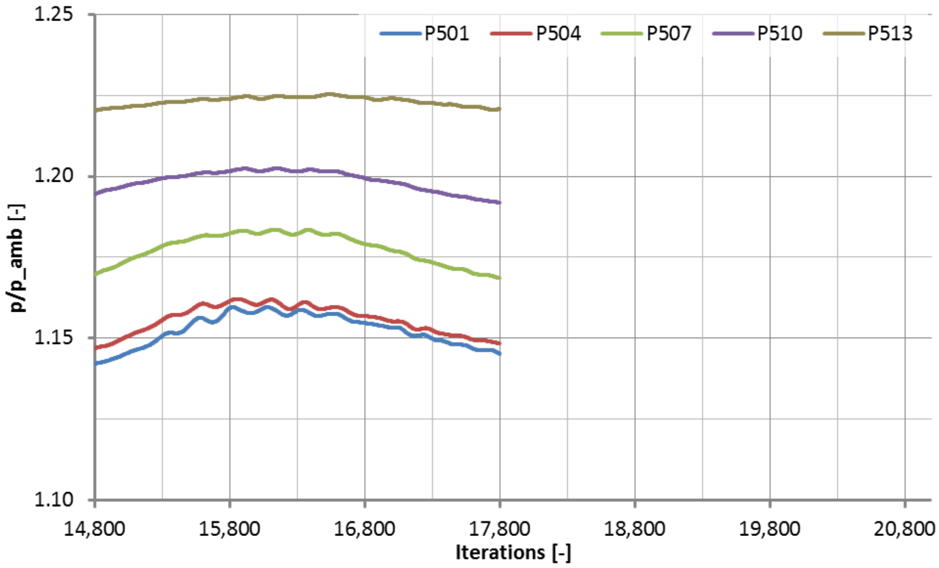

Figure B.5: Monitored pressure plot for simulation 3.2 (different BC´s) and pressure taps P501, P504, P507, P510 and P513

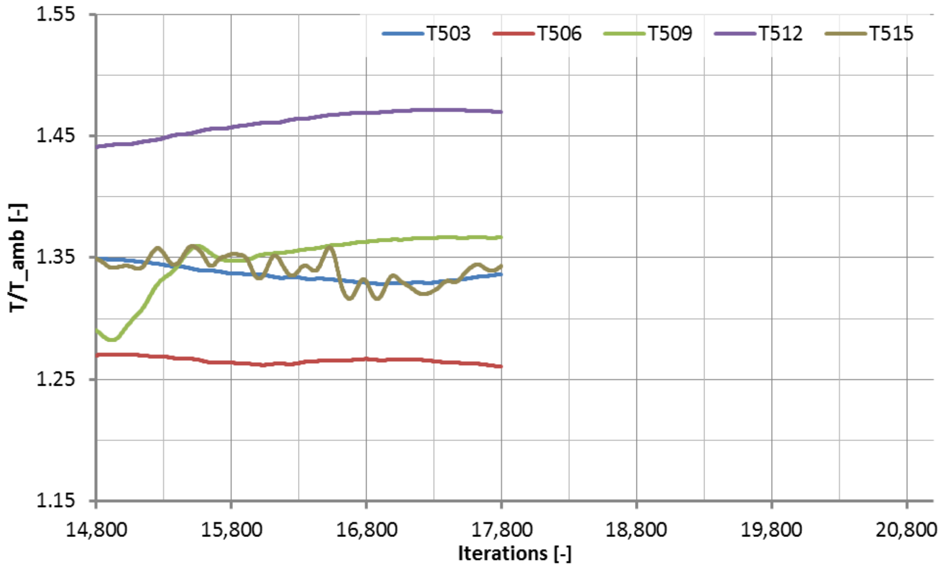

Figure B.6: Monitored temperature plot for simulation 3.2 (different BC´s) and thermocouples T503, T506, T509, T512 and T515

B.4 Simulation 4.2 (Boxer mesh)

Below the monitored pressure and temperature plots can be seen for pressure taps P501, P504, P507, P510 and P513, and thermocouples T503, T506, T509, T512 and T515 for simulation 4.2.

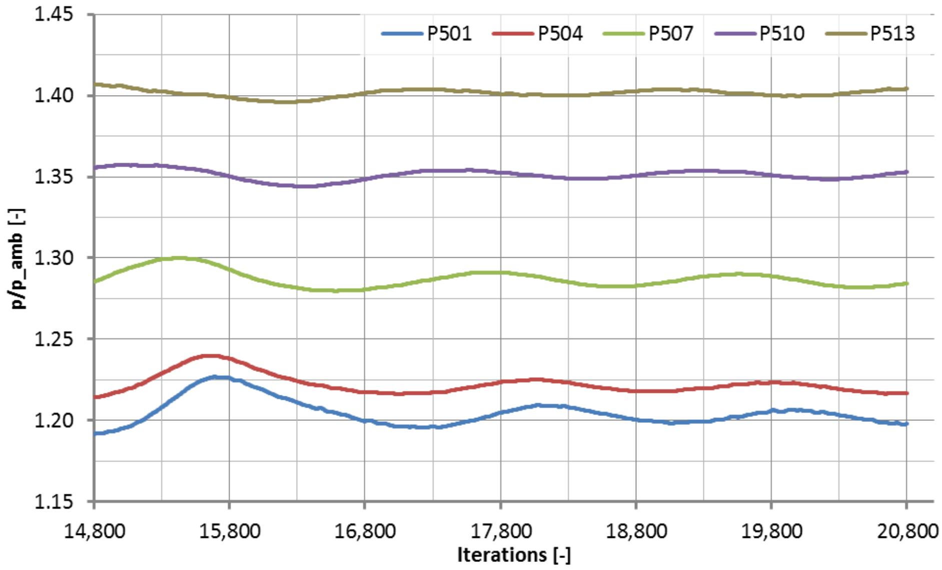

Figure B.7: Monitored pressure plot for simulation 4.2 (Boxer mesh) and pressure taps P501, P504, P507, P510 and P513

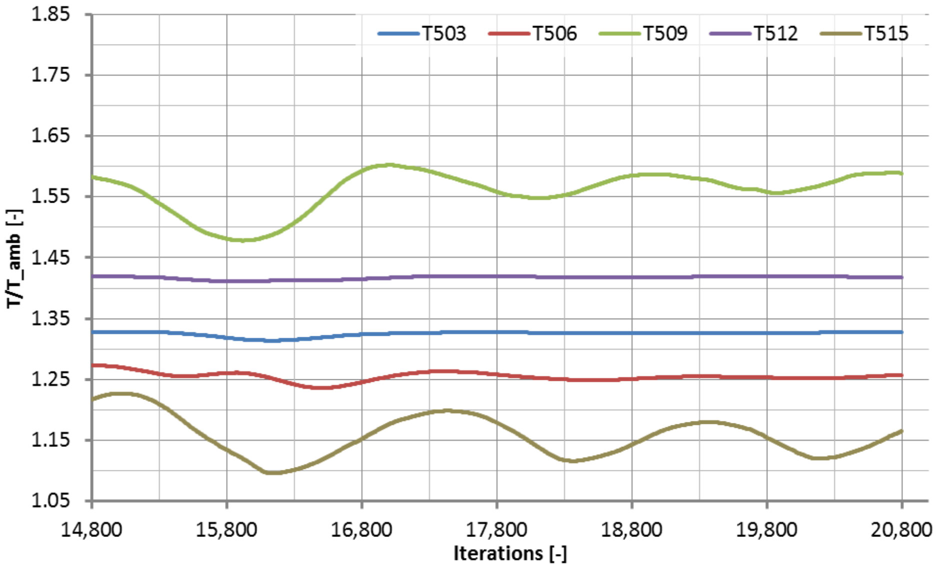

Figure B.8: Monitored temperature plot for simulation 4.2 (Boxer mesh) and thermocouples T503, T506, T509, T512 and T515